UNIVERSITY OF OKLAHOMA

GRADUATE COLLEGE

THERMAL CONDUCTIVITY ENHANCEMENT OF GRAPHENE POLYMER COMPOSITES THROUGH EDGE FUNCTIONALIZATION AND EXPANSION OF GRAPHITE

A DISSERTATION

SUBMITTED TO THE GRADUATE FACULTY

in partial fulfillment of the requirements for the

Degree of

DOCTOR OF PHILOSOPHY

By

FATEMA TARANNUM
Norman, Oklahoma
2022

THERMAL CONDUCTIVITY ENHANCEMENT OF GRAPHENE POLYMER COMPOSITES THROUGH EDGE FUNCTIONALIZATION AND EXPANSION OF GRAPHITE

A DISSERTATION APPROVED FOR THE SCHOOL OF AEROSPACE AND MECHANICAL ENGINEERING

BY THE COMMITTEE CONSISTING OF

Dr. Jivtesh Garg, Chair

Dr. Liangliang Huang

Dr. Wilson Merchan-Merchan

Dr. Hamidreza Shabgard

Dr. Jie Cai

Dr. Keisha Walters

Acknowledgment

First and foremost, I am grateful to Allah Almighty for the blessings and knowledge bestowed upon me. My Lord has continuously strengthened me to carry on in my journey and helped me to achieve more through determination, courage, and integrity.

I sincerely appreciate and express my gratitude to my academic advisor and committee chair, Dr. Jivtesh Garg, for his continuous support, motivation, and remarkable guidance throughout my Ph.D. program. He always believed in my potential and helped me to bring the best out of me in my academic and research life. I am indebted to his patience while correcting my writing samples and reports and support in getting various awards from Gallogly College of Engineering and the School of Aerospace and Mechanical Engineering. I want to thank Dr. Jivtesh Garg for sharing his professional and personal life experiences with me that would enable me taking wiser decisions at various stages of my life.

I am so glad that all my dissertation committee members, Dr. Wilson Merchan-Merchan, Dr. Liangliang Huang, Dr. Hamidreza Shabgard, Dr. Jie Cai and Professor Keisha Walters, believe in my ability to do independent research work. I appreciate their commitment, time, and constructive comments throughout my PhD program that improved the quality of my work. I would also like to thank Professor Keisha Walters, especially for her support and helping hand in accessing her research facilities. I thank Professor Brian Grady for allowing me to access his laboratory equipment whenever needed. I want to thank Professor Farrokh Mistree for helping me improve my communication skills and providing opportunities to showcase my research work through Graduate Student Community services. I am also indebted to Professor Zahid Siddique for his guidance in my career and support without any time constraints. I am thankful to Dr. Preston

Larson for assisting in the SEM image processing. I want to acknowledge and thank the School of Aerospace and Mechanical Engineering staff for their continuous support.

I extend my humble regards to the School of Aerospace and Mechanical Engineering (AME) at the University of Oklahoma for providing me financial assistance in graduate teaching and research assistantships, travel support for conferences and awarded me with Jim Bee Close Engineering scholarship and Dolese teaching fellowship. These AME scholarships helped me concentrate on my research work without having to think much about my financial burdens and inspired me to progress with additional momentum. I also thank Gallogly College of Engineering for felicitating me with awards such as the Dissertation excellence award for my research accomplishment.

I do not have enough words to express my deep gratitude toward my mother, Hosne Ara Begum, and my sister, Morium Tabassum, for their encouragement and support throughout this journey. Especially, I would not be able to express thanks to my husband, Md Shah Jalal Uddin, for his companionship, understanding, sacrifices, and mental support throughout this journey to overcome the challenges. I am very grateful to my friend, Umama Shuhorah Taskia for her continuous support. I am also thankful to Rajmohan Muthaiah for his support, discussions on writing manuscripts, and valuable input during my study program. I also thank my friends and roommates for making my life in Norman pleasant. I feel indebted for their love and support that always helped me. Finally, I dedicate this dissertation to my father, Abdul Jabbar, who taught me to learn and grow in every aspect of life with love, kindness, and quality. Thank you!

Abstract

In this work, we report an ultra-high enhancement of 4030% in thermal conductivity of polyetherimide/graphene nanocomposite (k = 9.5 $Wm^{-1}K^{-1}$) prepared through the use of expanded graphite (EG) with hydrogen peroxide as an intercalating agent at 10 weights% composition (k of pure polyetherimide ~ 0.23 $Wm^{-1}K^{-1}$). This value represents the highest thermal conductivity ever measured in a polymer composite at this low filler loading and is more than a factor of 2 higher relative to earlier reported results. This ultra-high thermal conductivity value is found to be due to an expanded graphite mediated interconnected graphene network throughout the composite, establishing a percolative environment that enables highly efficient thermal transport in the composite. Comparative studies were also performed using sodium chlorate as an intercalating agent. At 10 wt% composition, sodium chlorate intercalated expanded graphite was found to lead to a smaller enhancement of 2190% in k of composite. These results highlight the distinct advantage of hydrogen peroxide as an intercalating agent in enhancing thermal conductivity. Detailed characterization performed to elucidate this advantage, revealed that hydrogen peroxide led to primarily edge oxidation of graphene sheets within expanded graphite, leaving the basal plane intact, thus preserving the ultra-high in-plane thermal conductivity of ~ 2000 $Wm^{-1}K^{-1}$. Sodium chlorate, on the other hand, led to a higher degree of oxidation, with a large number of oxygen groups on basal plane of graphene, dramatically lowering its in-plane thermal conductivity. To directly shed light on the effect of intercalating agents on thermal conductivity of graphene itself, we prepared expanded graphite paper by compressing expanded graphite particles together. Thermal diffusivity of hydrogen-peroxide prepared expanded graphite paper was measured to be 9.5 mm^2/s while that of sodium chlorate case measured to be 6.7 mm^2/s, thus directly confirming the beneficial impact of hydrogen peroxide on k of graphene itself. This study is the first to address

the role of intercalating agents on *k* of expanded graphite/polymer composites and has led to the discovery of hydrogen peroxide as an effective intercalating agent for achieving ultra-high thermal conductivity values.

The work is also the first to address the comparison between edge and basal plane functionalization of graphene for enhancement of *k* of graphene-nanoplatelet /polyetherimide (GnP/PEI) composites. Graphene nanoplatelets (GnPs) comprise of multiple layers of graphene stacked parallel to each other. Edge functionalization enables the advantage of coupling the edges of all sheets of GnP with the embedding polymer, thus enabling the entire nanoplatelet to efficiently conduct heat through the composite. Basal-plane functionalization only couples the outermost layers of GnP with the polymer, thus causing only part of the nanoplatelet to be effective in conducting heat. Another very important advantage of edge-functionalization lies in leaving the basal plane of graphene intact. This preserves the ultra-high in-plane *k* of graphene (k~ 2000 $Wm^{-1}K^{-1}$). Basal plane functionalization, on the other hand, introduces a large number of defects in the basal plane of graphene dramatically lowering its intrinsic *k* value. Molecular dynamics simulations have revealed that even 5% functionalization of the basal plane can lower graphene thermal conductivity by as much as 90%. In this work, we experimentally realized the outlined advantages of edge-functionalization on the enhancement of *k*. Edge functionalization was achieved by oxidizing graphene with an excess of carboxyl groups through use of sulfuric acid, sodium chlorate and hydrogen peroxide. Carboxyl groups are known to preferentially attach to edges of graphene leading to edge oxidation. Basal plane oxidation was achieved through Hummer's method by using sulfuric acid and potassium permanganate. Measurements reveal edge-oxidized graphene to enhance composite *k* by 18%, while basal-plane oxidized graphene reduced composite *k* by 57% at 10 wt% composition, clearly outlining the advantage of edge-

functionalization on enhancement of thermal conductivity. Detailed characterization was performed to confirm edge versus basal plane oxidation. X-ray photoelectron spectroscopy showed greater fraction of carboxyl groups in edge-oxidized graphene, while basal plane oxidized graphene had larger fraction of hydroxyl/epoxy oxygen groups. 2D Raman mapping was used to obtain I_D/I_G ratios separately on edge and basal plane of GnPs. Edge oxidized graphene demonstrated higher I_D/I_G ratio on edge, while basal plane oxidized graphene demonstrated higher I_D/I_G ratio on basal plane. These studies for the first time, comprehensively demonstrate that edge functionalization can lead to superior thermal conductivity enhancement. Unique breakthroughs outlined in this thesis will lead to promising new avenues to achieve next-generation ultra-high thermal conductivity polymer-graphene nanocomposites.

Keywords: Thermal conductivity, polymers, polymer composites, expanded graphite, solution casting, porous, interfacial resistance, functionalization

Table of Contents

Abstract vi

Table of Contents ix

List of Figures xiii

List of Tables xviii

CHAPTER 1 1

Introduction 1

1.1 OBJECTIVES 2

1.2 OUTLINE OF THIS RESEARCH 4

CHAPTER 2 9

Superior effect of edge relative to basal plane functionalization of graphene in enhancement of thermal conductivity of polymer-graphene composites 9

2.1 FUNCTIONALIZATION OF GRAPHENE 9

2.2 EXPERIMENTAL SECTION 16

2.2.1 Material Synthesis 17

2.2.2 Synthesis of Edge Functionalized Graphene Oxide (EGO) 17

2.2.3 Synthesis of Basal-Plane Functionalized Graphene Oxide (BGO) 18

2.2.4 Other Synthesis Routes 18

2.2.4.1 Step II Oxidation of Graphene Using Modified Hummers Method (GO-1) 18

2.2.4.2 Synthesis of Graphene Oxide Using Sodium Persulfate ($Na_2S_2O_8$) Activated by Ferrous (Fe^{2+}) Ion (GO-2) 19

2.2.5 Preparation of Polymer-Graphene Oxide Composites 20

2.3 RESULT & DISCUSSION 21

2.3.1 Measurement of Through-Thickness Thermal Conductivity 21

2.3.2 Thermal Conductivity Data 22

2.4 MOLECULAR STRUCTURE CHARACTERIZATION 24

2.4.1 Dispersion of Graphene Nanoplatelets within the Composite. 27

2.4.2 Raman Characterization 28

2.4.3 Effect of Functionalization on Interlayer Spacing through XRD Analysis 32
2.4.4 Chemical Group Analysis through FTIR Analysis 33
2.4.5 Thermogravimetric Analysis 34
2.4.6 XPS Analysis 34
2.4.7 FE-SEM & HR-TEM Images of GnP, EGO & BGO Fillers 39
2.5 CONCLUSION 40
CHAPTER 3 41
Large enhancement in thermal conductivity of solvent-cast expanded graphite/polyetherimide composites 41
3.1 INTRODUCTION AND LITERATURE REVIEW 41
3.2 EXPERIMENTAL DETAILS 47
3.2.1 Materials 47
3.2.2 Fabrication of the EG/Polymer Composites 47
3.3 CHARACTERIZATION 49
3.4 RESULT AND DISCUSSION 52
3.4.1 Thermal Conductivity Results 52
3.4.2 Effective Medium Model for Thermal Conductivity Prediction 58
3.4.3 Morphologies of EG Filler and EG/PEID Composite 61
3.4.4 Analysis of Crystal Structure by XRD and Raman Spectroscopy 63
3.4.5 XPS Analysis of GIC and EG Filler 64
3.5 CONCLUSION 64
CHAPTER 4 66
Thermally expanded graphite polyetherimide composite with superior electrical and thermal conductivity 66
4.1 INTRODUCTION 66
4.2 EXPERIMENTAL SECTION 71
4.2.1 Materials 71
4.2.2 Fabrication of the EG/PEI & GNP/PEI Composites 72
4.3 CHARACTERIZATION 72

4.4 RESULT & DISCUSSION 75
4.4.1 Electrical Properties 75
4.4.2 Effective Medium Theory to Predict Electrical Conductivity 77
4.4.3 Thermal Conductivity Data 81
4.4.4 Microstructures and Morphologies of Fillers & Polymer Composite through FE-ESEM: 84
4.4.5 XPS Analysis 86
4.4.6 XRD Analysis 87
4.4.7 Raman Analysis 88
4.5 CONCLUSION 89
CHAPTER 5 90
Comparative study of intercalating agents on thermal conductivity of expanded graphite/polyetherimide composite 90
5.1 GRAPHITE INTERCALATED COMPOUND (GIC) AND OXIDIZING AGENTS 90
5.2 EXPERIMENTAL SECTION 96
5.2.1 Materials 96
5.2.2 Synthesis of GIC-H_2O_2 & EG-H_2O_2 using Intercalation Route I 97
5.2.3 Synthesis of GIC-$NaClO_3$ & EG-$NaClO_3$ using Intercalation Route II 98
5.2.4 Preparation Method of Expanded Graphite-Polyetherimide (EG/PEI) Composite and Expanded Graphite (EG) Paper 98
5.3 CHARACTERIZATION 100
5.4 RESULT & DISCUSSION 101
5.4.1 Thermal Conductivity Measurement 101
5.4.2 Thermal Conductivity (*k*) Data Analysis 103
5.4.3 Formation and Expansion Volume of GICs and EG Fillers 108
5.4.4 Raman Analysis 113
5.4.5 Chemical Composition Analysis of GICs and EG Fillers by XPS 120
5.4.6 Analysis of Interlayer Spacing of GICS and EG Fillers through XRD 126
5.4.7 Structure and Morphology Characterization of GICs and EG Filler 131
5.5 CONCLUSION 138

CHAPTER 6 139
Conclusion 139
REFERENCES 145

List of Figures

Figure 2.1 Atomic structure of a) functionalized single graphene sheet with basal plane functional groups, b) functionalized single graphene sheet with edge functional groups. Atomistic structures for c) multilayer edge functionalized graphene (EFGnP) and d) multilayer basal-plane functionalized graphene (BFGnP), e) interactions between graphene-oxide and polyetherimide (PEI). 11

Figure 2.2 a) Schematic structure of GnP, EGO, and BGO (carboxyl & carbonyl group: -COOH/-C=O; epoxy: C-O-C; hydroxyl group: -OH), b) images of GnP nanopowder, PEI pellets and chemical structure of PEI; c) scheme for polymer-graphene composite preparation; DMAC-Dimethylacetamide 16

Figure 2.3 a) Through -thickness thermal conductivity value with 5, 7, 10, and 15 wt% filler content of GnP/PEI, EGO/PEI, BGO/PEI composites, and b) 7 wt% filler content of GnP/PEI, GO-1/PEI, GO-2/PEI composites 20

Figure 2.4 Images of composite films for a) pristine GnP/PEI, b) EGO/PEI, c) BGO/PEI & cross-sectional FE-ESEM images of 15 wt% composites for d) pristine GnP/PEI, e) EGO/PEI and f) BGO/PEI composites. 26

Figure 2.5 I_D/I_G ratio of edge and basal plane area of a) GnP, b) EGO, and c) BGO..... 28

Figure 2.6 a) Image of a graphene nanoplatelet under 100x magnification during 2D Raman mapping, b) Raman intensity profile showing intensity of G band and D band for a particular point in the red rectangle in Fig. 2.6a, c) super imposed Raman chemical image showing I_D/I_G ratios as color contours, d) representative Raman spectra for edge and basal plane area of graphene nanoplatelet. 29

Figure 2.7 Raman spectra of a) GnP, EGO and BGO, b) GO-1 and GO-2; c) Full XRD spectra, d) Inset of XRD spectra, (e) FTIR, and (f) TGA spectra of GnP, EGO and BGO. 30

Figure 2.8 XPS data showing the a) survey spectra, b) atomic percentage of C1s and O1s for GnP, EGO, and BGO, and the high resolution C1s spectra for c) EGO and d) BGO. 35

Figure 2.9 XPS spectra showing the a) survey spectra, b) atomic percentage of C1s and O1s for GnP, GO-1, and GO-2, and the high resolution C1s spectra for c) GO-1 and d) GO-2. 36

Figure 2.10 FE-SEM images of overall particle size of a) EGO, b) BGO; c) Frontal, d) Cross sectional view and e) Edge of EGO particle; f) Frontal view of BGO particle. 38

Figure 2.11 HR-TEM images of (a-b) GnP; (c-f) EGO; (g-h) BGO. 39

Figure 3.1 a) Schematic illustration of expanded graphite from graphite intercalated compounds through thermal expansion. SEM image of b) GIC, c) expanded graphite after thermal expansion. High−resolution FE−ESEM images of EG at magnification of d) ×100, e) ×1500, f) ×12,000, g) FE−ESEM images of 60 nm graphene nanoplatelet. FE−ESEM images of EG/PEID composite at h) ×350, (i & j) ×3500. 44

Figure 3.2 a) Schematic for the preparation process of EG/PEID composites, b) chemical structure of PEID. 49

Figure 3.3 *k* value of a) EG/PEID (experimental and effective medium theory (EMT)) and GnP/PEID composite with different filler content (2,5, 5, 7.5 & 10 wt%), b) EG/epoxy and GnP/epoxy composite with different filler content (0.5, 1, 1.5, and 2 wt%), c) EG/PEID composite with different sonication time at 20% ultrasonication power, d) EG/PEID composite with different ultrasonication power sonication for 40 s. e) Comparison of *k* value of polymer composites in previous works. 51

Figure 3.4 FE−ESEM images of EG/PEID composites with (a,b) 7.5 wt%, (c,d) 10 wt% fabricated at 20% amplitude for 40 s ultrasonication; (a,c) 350× magnification, (b,d,) 3500× magnification. 53

Figure 3.5 FE−ESEM images of (a,b) 10 wt% EG/PEID composite with ultrasonication for 3 min at 20% amplitude, (c,d) 10 wt% GnP/PEID composite with ultrasonication for 40 s at 20% amplitude; FE−ESEM images of EG at 20% sonication for (e) 40 s and (f) 3 min using montage large area mapping. 54

Figure 3.6 Predicted thermal conductivity value based on the effective medium theory (EMT) with different graphene–graphene interlayer thermal conductivity. 61

Figure 3.7 XRD spectra a), Raman spectra b), and XPS spectra c) of GIC and EG filler. 62

Figure 4.1 Schematic preparation of expanded graphite (EG) from graphite intercalated compound (GIC) at 900 °C with FE-ESEM images of GIC and EG filler. 67

Figure 4.2 a) Interaction between polyetherimide (PEI) and graphite nanosheet of EG through hydrogen bonding, b) schematic preparation of EG/PEI composite. 70

Figure 4.3 a) Electrical resistivity and b) electrical conductivity value of the PEI/EG nanocomposites as a function of EG, c) comparison of electrical conductivity value of polymer composites with previous work, and d) effective in-plane electrical conductivity in EG/PEI composites with respect to EG filler volume concentrations under perfect and imperfect interface conditions. 74

Figure 4.4 a) Thermal conductivity (*k*) value of EG/PEI and GNP/PEI composite with different filler content (2.5, 5, 7.5, and 10 wt%), b) *k* value of EG/PEI composite with different sonication time at 20% ultrasonication power. 81

Figure 4.5 a) Montage area mapping of EG filler. FE-ESEM image of EG filler at b) ×30, c) ×150, d) ×500, e) ×1500 & f) ×8000. FE-ESEM images of EG/PEI composite for g) 5 wt% at ×350, (h & i) 10 wt% at ×350 & ×3500. FE-ESEM images of j) GNP, (k & l) GNP/PEI composite for 10 wt% GNP filler at ×350 and ×1500. 82

Figure 4.6 a) Montage area mapping of EG filler and b) FE-ESEM image of single EG filler after 2min ultrasonication at 20% amplitude in DMAC solvent. 83

Figure 4.7 a) XPS spectra and b) XRD spectra of GNP, GIC, and EG filler. 86

Figure 4.8 Raman spectra of GIC and EG filler. 88

Figure 5.1 a) Preparation of graphite intercalation compound (GIC) in the presence of intercalants (acids & oxidizing agents), b) schematic illustration of different stages of intercalation. 91

Figure 5.2 Preparation method of expanded graphite (EG) paper using compression molding 100

Figure 5.3 a) *k* value of EG-H_2O_2 1/PEI & EG-$NaClO_3$ 1/PEI composite at 2.5, 5, 7.5 and 10 wt% filler concentration, b) α value of EG-H_2O_2 1 & EG-$NaClO_3$ 1 paper. 102

Figure 5.4 *k* value of 10 wt% EG-H_2O_2/PEI composites for a) different volume ratio of H_2SO_4:H_2O_2 for 20, 40, and 60 mL of H_2SO_4 respectively, b) different volume ratio of H_2SO_4:H_2O_2 for 2, 4, and 6 mL of H_2O_2 respectively. 104

Figure 5.5 *k* value of 10 wt% EG-$NaClO_3$ /PEI composites with the different volume ratio of H_2SO_4: $NaClO_3$ and reaction time. 105

Figure 5.6 a) Schematic illustration of the preparation process of a) GIC-H_2O_2 & EG-H_2O_2, b) GIC-$NaClO_3$ & EG-$NaClO_3$. 109

Figure 5.7 Expansion volume (EV) of a) GIC-H_2O_2 1, 2 & 3, b) GIC-H_2O_2 4, 5 & 6, c) EG-H_2O_2 1, 2 & 3, d) EG-H_2O_2 4, 5 & 6. 110

Figure 5.8 Expansion volume of a) GIC-$NaClO_3$ 1, 2 & 3, and b) EG-$NaClO_3$ 1, 2 & 3. 111

Figure 5.9 Raman spectra of a) GIC-H_2O_2 1, 2 & 3, and b) EG-H_2O_2 1, 2 & 3. c) G band line, d) D band line, e) 2D band line of GIC-H_2O_2 1, 2 & 3, f) G band line, d) D band line, e) 2D band line of EG-H_2O_2 1, 2 & 3. 114

Figure 5.10 Raman spectra of a) GIC-$NaClO_3$ 1, 2 & 3, and b) EG-$NaClO_3$ 1, 2 & 3. c) G band line, d) D band line, and e) 2D band line of GIC-$NaClO_3$ 1, 2 & 3, f) G band line, g) D band line, and h) 2D band line of EG-$NaClO_3$ 1, 2 & 3. 117

Figure 5.11 Raman spectra of a) GIC-H_2O_2 1 & GIC-$NaClO_3$ 1, and b) EG-H_2O_2 1 & EG-$NaClO_3$ 1. c) G band line, d) D band line, and e) 2D band line of GIC-H_2O_2 1 & GIC-$NaClO_3$ 1, f) G band line, g) D band line, and h) 2D band line of EG-H_2O_2 1 & EG-$NaClO_3$ 1. 119

Figure 5.12 a) XPS spectra of GIC-H_2O_2 1, 2 & 3 and b) EG-H_2O_2 1, 2 & 3. 120

Figure 5.13 a) XPS spectra of GIC-$NaClO_3$ 1, 2 & 3, and b) EG-$NaClO_3$ 1, 2 & 3..... 122

Figure 5.14 C1s core level XPS spectra for a) GIC-H_2O_2 1, b) GIC-$NaClO_3$ 1, c) EG-H_2O_2 1, and d) EG-$NaClO_3$ 1. 124

Figure 5.15 XRD spectra of a) GIC-H_2O_2 1, 2 & 3, b) EG-H_2O_2 1, 2 & 3; Inset of XRD spectra of c) GIC-H_2O_2 1, 2 & 3, and d) EG-H_2O_2 1, 2 & 3. 127

Figure 5.16 XRD spectra of a) GIC-$NaClO_3$ 1, 2 & 3, b) EG-$NaClO_3$ 1, 2 & 3; Inset of XRD spectra of c) GIC-$NaClO_3$ 1, 2 & 3 and d) EG-$NaClO_3$ 1, 2 & 3..... 128

Figure 5.17 XRD spectra of a) GIC-H_2O_2 1& GIC-$NaClO_3$ 1, b) EG-H_2O_2 1& EG-$NaClO_3$ 1. 129

Figure 5.18 FE-ESEM images of 10mesh graphite a) ×35, b) ×150. 131

Figure 5.19 FE-ESEM micrographs of a) GIC-H_2O_2 1 (×150), b) GIC-H_2O_2 1 (×800), c) GIC-H_2O_2 1 (×120), d) EG-H_2O_2 1 (×20), e) EG-H_2O_2 1 (×250), f) EG-H_2O_2 1 (×500), g) EG-H_2O_2 1 (×500), h) EG-H_2O_2 1 (×50), and i) EG-H_2O_2 1 (×150). 132

Figure 5.20 FE-ESEM micrographs of a) GIC-H_2O_2 2 (×120), b) GIC-H_2O_2 3 (×120), c) EG-H_2O_2 3 (× 35), d) EG-H_2O_2 3 (×200). 133

Figure 5.21 FE-ESEM micrographs of a) GIC-$NaClO_3$ 1 (×150), b) GIC-$NaClO_3$ 1 (×250), c) GIC-$NaClO_3$ 1 (×1000), d) EG-$NaClO_3$ 1 (×35), e) EG-$NaClO_3$ 1 (×120), f) EG-$NaClO_3$ 1 (×500), g) EG-$NaClO_3$ 1 (×1000), h) EG-$NaClO_3$ 1 (×800), i) EG-$NaClO_3$ 1(×5000)..... 134

Figure 5.22 FE-ESEM micrographs of a) GIC-$NaClO_3$ 2 (×80), b) GIC-$NaClO_3$ 2 (×200), c) GIC-$NaClO_3$ 2 (×150), d) GIC-$NaClO_3$ 2 (×250), e) GIC-$NaClO_3$ 2 (×500), f) GIC-$NaClO_3$ 2 (× 500), g) EG-$NaClO_3$ 2 (× 200), h) EG-$NaClO_3$ 2 (× 200), and i) EG-$NaClO_3$2 (×1200)..... 135

Figure 5.23 FE-ESEM micrographs of EG-H_2O_2 1/PEI composite for 10 wt% EG-H_2O_2 1 filler a) (×250), b) (×650) magnification; and FE-ESEM micrographs of GIC-$NaClO_3$ 1/PEI composite for 10 wt% GIC-$NaClO_3$ 1 filler c) (×250), d) (×650) magnification. 136

List of Tables

Table 2.1 Position and value of FWHM of D & G band of GnP, EGO and BGO..... 31

Table 2.2 Abundance of functional groups of EGO, BGO, GO-1 and GO-2 in atomic percentage 35

Table 3.1 Comparison of $k_{\perp}$ for different polymer graphene and EG−polymer composite..... 57

Table 3.2 The values of different parameters used in EMT calculations..... 59

Table 3.3 Atomic composition by XPS analysis of EG and GIC. 64

Table 4.1 Comparison of EC for different polymer-graphene and EG-polymer composite..... 76

Table 4.2 Physical values used in the theoretical calculation of the effective conductivity of nanocomposites..... 80

Table 4.3 Atomic composition by XPS analysis of GNP, EG and GIC 87

Table 5.1 Chemicals and their compositions used for the synthesis of GIC-H_2O_2 and EG-H_2O_2 97

Table 5.2 Chemicals and their compositions used for synthesis of GIC-$NaClO_3$ and EG-$NaClO_3$ 98

Table 5.3 Exfoliation volume and weight loss (%) for GICs & EG fillers. 112

Table 5.4 Raman peak positions and I_D/I_G of GIC-H_2O_2 & EG-H_2O_2 fillers..... 113

Table 5.5 Raman peak positions and I_D/I_G of GIC-$NaClO_3$ & EG-$NaClO_3$ fillers 116

Table 5.6 Atomic composition and C/O ratio by XPS analysis of graphite, GICs, and EG- fillers 123

Table 5.7 Relative atomic percent composition of functional groups of GICs & EG fillers 125

Table 5.8 2θ and d-spacing values of graphite, GICs and EG fillers using XRD analysis..... 126

CHAPTER 1

Introduction

Continuous miniaturization of electronic devices has led to increasing heat fluxes, exacerbating thermal management in the modern electronic industry. Efficient heat dissipation is required to prevent the failure of electronic components because of overheating resulting from increased power dissipation in electronic systems. High thermal conductivity materials can help to achieve efficient heat dissipation. Extensive research has been conducted to find suitable materials with high thermal conductivity to meet the demand for a higher heat dissipation rate. Polymeric materials offer several advantages such as light weight, low cost, high corrosion and chemical resistance, and ease of processability over metals. Polymeric materials have been used in various applications such as chemical and bio sensors[1], solar cells[2], supercapacitors[3], actuators[4] and separation membranes[5] because of the advantages. Due to these physical properties, polymers have been considered to replace metals in thermal management applications. However, low thermal conductivity of polymers (~0.5$Wm^{-1}K^{-1}$)[6] limits their heat transfer performance. This research focuses on exploring different techniques to enhance thermal conductivity of polymer nanocomposites.

Thermal conductivity is one of the intrinsic properties of materials that determines the operating temperature levels in response to a given heat flux. Metals have higher thermal conductivity than insulators such as polymers, glasses, ceramics. For steady state condition and one-dimensional heat flow, the heat conduction is determined by Fourier law and is given by-

$$Q = -kA\left(\frac{dT}{dx}\right) \quad (1.1)$$

where Q is the rate of heat transfer (W), k is thermal conductivity ($Wm^{-1}K^{-1}$), A is the cross-sectional area (m^2), and dT/dx is the temperature gradient.

In solids, energy carriers such as phonons or electrons transfer energy. Phonons transfer heat through lattice vibrations while free electrons are the dominant heat carriers in metals. In polymers, phonons are dominant in the heat conduction mechanism. To increase thermal conductivity, highly thermal conductive fillers[7-12] are added to polymer matrix, and the resultant composites typically exhibit better thermal conductivity than the pristine polymer. Phonon scattering at the interface between polymer and filler limits the thermal conductivity of polymer composites. Therefore, it is crucial to include the fillers with modified interface to improve heat conduction in polymer composites. Enhancing thermal conductivity of polymers through different schemes, considering above effects, is outlined in this work.

1.1 OBJECTIVES

Polymers are thermal insulators because of their low thermal conductivity (k< 0.5 $Wm^{-1}K^{-1}$)[13]. On the other hand, high thermal conductivity materials such as metals are known as thermal conductors, having k values >20 $Wm^{-1}K^{-1}$ [14,15]. High thermal conductivity polymer materials can improve thermal management in a wide range of applications, such as - water desalination[16], automotive control units[17], batteries[18], solar panels[19], supercapacitors[20], electronic packaging[21], and electronic cooling[22]. A key pathway to achieve high thermal conductivity polymers is addition of ultra-high thermal conductivity fillers such as graphene nanofillers[23-25]. The objectives of this work are to enhance effectiveness of graphene in facilitating thermal conductivity increase in polymers through three key effects outlined below.

a) Superior functionalization of graphene to improve interfacial thermal conductance between polymer and graphene: A key effect that limits the effectiveness of graphene in enhancing the thermal conductivity of polymer composites is the high interfacial thermal resistance between graphene and polymer. Functionalization of graphene with functional groups that are compatible with embedding polymer can reduce interfacial thermal resistance, thus improving overall thermal conductivity. To achieve the highest effective polymer composite thermal conductivity, a fundamental question that needs to be answered is – What is the relative effectiveness of functional groups located on the edge versus the basal plane of graphene in enhancing effective polymer-graphene nanocomposite thermal conductivity? It is shown in this work that, edge functionalization of graphene leads to superior enhancement in *k* value relative to basal plane functionalization. Functionalization schemes have been compared using oxidation of graphene. Relative to pure polyetherimide (PEI), edge-oxidized graphene was found to enhance composite *k* by 725% at 15 wt% composition, while the corresponding enhancement through basal plane oxidation was only ~75%.

b) Interconnected graphene networks through use of expanded graphite (EG): Thermal contact between graphene particles can allow bypassing the low *k* polymer matrix, thus leading to high thermal conductivity composite. Expanded graphite provides a natural way to achieve such interconnected graphene networks, providing avenues to enhance polymer *k*. Role of expanded graphite (EG) in enhancing thermal conductivity of polyetherimide and epoxy composites is explored.

c) Use of intercalating agents that leads to lower oxidation of EG: EG can be produced using different intercalating agents. Understanding of role of such intercalating agents in facilitating enhancement in thermal conductivity of polymer composites is lacking. In this work we compare

two intercalating agents – hydrogen peroxide (H_2O_2) and sodium chlorate ($NaClO_3$) and show that EG produced using H_2O_2 leads to higher enhancement in thermal conductivity. Detailed characterization is performed to show that this higher enhancement in thermal conductivity through H_2O_2 is due to lower oxidation of graphene which preserves its intrinsically high thermal conductivity.

1.2 OUTLINE OF THIS RESEARCH

Significant research has used Graphene Nanoplatelets (GnPs) as a promising nanofiller to enhance the thermal conductivity of polymers. This is due to the ultra-high thermal conductivity of graphene (~2000 $Wm^{-1}K^{-1}$)[26]. Powder blending[27], melt blending[28,29], solution blending[30-32] and in situ polymerization[33] have been used as common fabrication methods to prepare polymer-graphene nanocomposites. Graphene has limitations, due to its inhomogeneous dispersion and weak interface bonding with polymer, in maximizing the thermal transport[34,35]. Furthermore, re-agglomeration of graphene sheets induced by van der Waals forces between them also leads to poor dispersion[36]. Interfacial thermal resistance between polymer and graphene significantly diminishes thermal conductivity enhancement that can be achieved[37]. Polymer matrix with high surface area filler induces lot of interfaces and those interfaces hinder phonon transmission. Modification of graphene through chemical functionalization can significantly overcome inefficiency in thermal conductance leading to higher thermal conductivity. In this research, functionalization schemes to improve thermal conductance between graphene and polymer will be investigated and discussed in chapter 2.

A key hurdle in use of graphene is the large interfacial thermal resistance between graphene and polymer owing to the mismatch of their lattice vibrations. In this research we experimentally study functionalization scheme of graphene that can improve interaction with polymers, thus

diminishing the thermal resistance. Thermal conductivity enhancement with simple oxidation is studied. Edge oxidation of GnP offers the advantage of leaving the basal plane of graphene intact, preserving its high in-plane thermal conductivity (k_{in} > 2000 $Wm^{-1}K^{-1}$ [38,39]), while, simultaneously, the oxygen groups introduced on graphene edge enhance interfacial thermal conductance through hydrogen bonding with oxygen groups of polyetherimide (PEI). Therefore, *k* value of EGO/PEI (EGO= edge oxidized graphene or edge-functionalized graphene oxide) composite is higher than pristine GnP/PEI composite. Basal-plane oxidation of graphene, on the other hand, achieved through Hummers' method, distorts sp^2 carbon-carbon network of graphene, dramatically lowers its intrinsic thermal conductivity, causing the BGO/PEI (BGO = basal-plane oxidized graphene or basal-plane-functionalized graphene oxide) composite *k* to be even lower than pristine GnP/PEI composite *k* value. Raman spectra, X-ray diffraction (XRD), X-ray photoelectron spectroscopy (XPS), Fourier transform infrared (FTIR) spectroscopy, thermogravimetric analysis (TGA) , scanning electron microscopy (SEM) characterization of basal plane and edge oxidized graphene have been performed to correlate the observed enhancement to state of oxidation.

In chapter 3 we explore the role of expanded graphite or EG in enhancing thermal conductivity of polymer composites. Graphite intercalation using combination of acid molecules and oxidizing agent can produce graphite intercalated compound (GIC) or expandable graphite (EPG). Rapidly heating GIC at ~900 °C leads to higher interlayer spacing than graphene layer-to-layer distance because of increased pressure generated from evaporating intercalated compounds; this causes expanded graphite to turn into worm like structure as it expands. Expanded graphite has been added to polymer in this study to enhance thermal conductivity of composites. In chapter 3, we report ~28 times higher thermal conductivity value (6.6 $Wm^{-1}K^{-1}$) of EG/polymer composite compared to pure polyetherimide (~0.23 $Wm^{-1}K^{-1}$). In this study, GIC of +100 mesh (92%) with

lateral size of 180 μm was expanded at very high temperature of 900 °C. A simple effective solution casting technique is used to prepare the expanded graphite polyetherimide (EG/PEID) composite and measured *k* value is compared with graphene nanoplatelet (GnP)/PEID composite. Thermal conductivity of EG/PEID composite dramatically exceeds that of graphene-nanoplatelet (GnP)/PEID composites by 572% at low filler loading of 10 wt%. This extraordinary enhancement in thermal conductivity is shown to be due to a network of continuous graphene sheets over long length scales, resulting in low thermal contact resistance. Solvent casting offers the advantage of preserving the porous structure of expanded graphite in the composite, resulting in the above highly thermally conductive interpenetrating network of graphene and polymer composites. Effect of ultra-sonication time and power on thermal performance and microstructure of the composite is further studied. Field emission environmental scanning electron microscopy (FE-ESEM) is used to provide detailed understanding of interpenetrating graphene-polymer structure in the expanded graphite composite.

In chapter 4, we explore the electrical properties of expanded graphite/polymer composite and report very high electrical conductivity of 969 Sm^{-1} (almost 19 orders of magnitude higher than pure PEI). We have treated GIC of higher lateral size, +50mesh (lateral size = 300 μm) at 900 °C to prepare EG, followed by the solution casting technique at the optimum sonication time to fabricate the expanded graphite polyetherimide (EG/PEI) composite. Expanded graphite has the potential to enable larger enhancement in properties relative to graphene nanoplatelets, through creation of continuous graphitic networks in the composite. Solution casting technique enables preservation of worm structure of expanded graphite in the composite thus enabling development of continuous graphitic networks throughout the composite, enabling superior property enhancement. Measurements reveal ~19 orders of magnitude increase in electrical conductivity of

composite (yielding values up to 969 Sm^{-1}) through inclusion of the 10 wt% of EG filler, relative to pure PEI (1.2×10^{-17} Sm^{-1}). Theoretical prediction using effective medium approach reveals the impact of continuous graphitic network on electrical conductivity of the composites. We also find that the 10 wt% EG filler composition composite exhibits a thermal conductivity (k) value of 7.3 $Wm^{-1}K^{-1}$, representing a significant enhancement of 3070% compared to pure PEI ($k \sim 0.23$ $Wm^{-1}K^{-1}$). FE-ESEM reveals the preserved interconnected structure of EG within the composite allowing development of a conductive interpenetrating network of polymer and filler. Raman spectroscopy, XRD and XPS analysis are further used to characterize the expanded-graphite/PEI nanocomposites.

In Chapter 5, we study the effect of intercalation and oxidizing agents on thermal conductivity of expanded graphite polymer composites. Oxidizing agents, hydrogen peroxide (H_2O_2) (route I), and sodium chlorate ($NaClO_3$) (route II) were used as auxiliary intercalating agent separately with the intercalating agent- sulfuric acid to synthesize graphite intercalated compounds (GICs) with different degree of oxidation. EG fillers with different degree of expansion and oxidation were prepared. We investigated the influence of intercalant agents on the morphological and structural properties of EG, and, thus, the thermal properties of EG-polymer composites. ~4030% enhancement in k value of EG/PEI composite for route I was achieved compared to pure PEI whereas route II enhances the k value of composite up to ~2190% at 10 wt% expanded graphite filler content. Enhancement in composite's k value is found primarily because of the interconnected graphene network of expanded graphene throughout the composite. establishing a percolative environment that enables highly efficient thermal transport in the composite. Significant enhancement indicates the superior effect of auxiliary intercalating agent, H_2O_2 in enhancing k of composite than $NaClO_3$. FE-ESEM, XRD, Raman spectroscopy (RS), and XPS

have been utilized to differentiate the morphological structure, delamination, crystal structure, degree of oxidation and chemical composition of graphite intercalated compounds (GIC-H_2O_2 & GIC-$NaClO_3$) and expanded graphite fillers (EG-H_2O_2 & EG-$NaClO_3$) of intercalation routes I & II in detail. Detailed characterization revealed that H_2O_2 of route-I leads to dominant edge oxidation, while $NaClO_3$ of route-II causes basal plane oxidation to prepare expanded graphite. Due to edge oxidation of graphene sheets within EG-H_2O_2, the preserved basal plane structure enables the advantage ofin-plane *k* value of graphene (~ 2000 $Wm^{-1}K^{-1}$) in composite. On the other hand, higher degree of oxidation in the case of route II dramatically damages the basal plane structure of graphene sheets in EG-$NaClO_3$ due to the attachment of functional groups mostly on the basal plane, thus leading to reduced composite *k* value. We prepared expanded graphite paper by compressing EG particles together to directly understand the effect of intercalating agents on thermal conductivity of graphene itself. Thermal diffusivity of EG-H_2O_2 paper was measured to be 9.5 mm^2/s while that of EG-$NaClO_3$ paper measured to be 6.7 mm^2/s, which directly confirms the beneficial impact of H_2O_2 on *k* of graphene itself. The comparative study of auxiliary intercalating agents on *k* of expanded graphite/polymer composites reveals the superior effect of H_2O_2 compared to $NaClO_3$ for achieving high thermal conductivity.

CHAPTER 2

Superior effect of edge relative to basal plane functionalization of graphene in enhancement of thermal conductivity of polymer-graphene composites[1]

2.1 FUNCTIONALIZATION OF GRAPHENE

A key approach to enhance the thermal conductivity of polymers is the addition of high thermal conductivity fillers such as graphene (k > 2000 $Wm^{-1}K^{-1}$ [38,39]). Different approaches have been used to enhance the composite k value through graphene, such as the synergistic effect with multiple fillers[40,41] and alignment of graphene[24,42-44]. The success of these approaches is, however, limited by the large interface thermal resistance between graphene and the polymer in the range of 10^{-8} to 10^{-7} m^2 KW^{-1} [43,45] due to mismatch of phonons (lattice vibrations) between the two. To decrease the thermal interface resistance, graphene is chemically functionalized by groups that are compatible with the surrounding polymer[46,47]. Covalent functionalization[20] and non-covalent functionalization[48] of graphene can lead to higher interfacial thermal conductance. Two orders of magnitude increase in interface thermal conductance[47] and 156% enhancement[49] in composite thermal conductivity were achieved through grafting of polymer chains on graphene. Recent work

[1] The content of this chapter is an extension of a published paper by the author. The paper contains results of research which was solely conducted as partial fulfillment for the PhD requirement.

demonstrated that multilayer graphene is more efficient in enhancing thermal conductivity than single layer graphene[50]. For such multilayer graphene, it is critically important to understand the optimal location of functional groups (such as the edge or basal plane of graphene, Figure 2.1a-d) which can lead to highest composite thermal conductivity. In this work, we demonstrate that functionalization on the edges (Figures. 2.1b,c) can lead to significantly higher effective polymer thermal conductivity compared to functionalization on the basal plane (Figures. 2.1a,d). The functionalization scheme used in this work is oxidation of graphene because oxygen groups on graphene can interact with oxygen groups in polyetherimide (PEI) through hydrogen bonding (Figure 2.1e). Edge oxidation is achieved in this work using a recently introduced chemical pathway, by oxidizing graphene in the presence of sodium chlorate and hydrogen peroxide to introduce excess carboxyl moieties[51]. Oxidation of the basal plane is achieved through the Hummers method[52].

Several computational and experimental studies have reported the enhancement of thermal conductivity through functionalization. Theoretical studies on polymer-grafted graphene (performed by Wang *et al.*) showed 2-fold lower interfacial thermal resistance through attachment of functional groups[53].. Using molecular dynamics (MD) simulations, Konatham *et al.*[54] demonstrated almost 50% reduction in the interfacial thermal resistance between functionalized graphene and octane. Lin and Buehler[47] showed using MD simulations, a 22% increase in interface thermal conductance through the use of alkyl-pyrene functional groups. Ganguli *et al.*[55] showed that silane-functionalized graphene improved the thermal conductivity of graphene/epoxy composite by 50% compared to a pristine graphene composite with 8 wt% graphene content. A pyrene-end poly(glycidyl methacrylate) -functionalized graphene/epoxy composite was found to yield ~184% enhancement in thermal conductivity over pure epoxy[56]. A comparison between edge

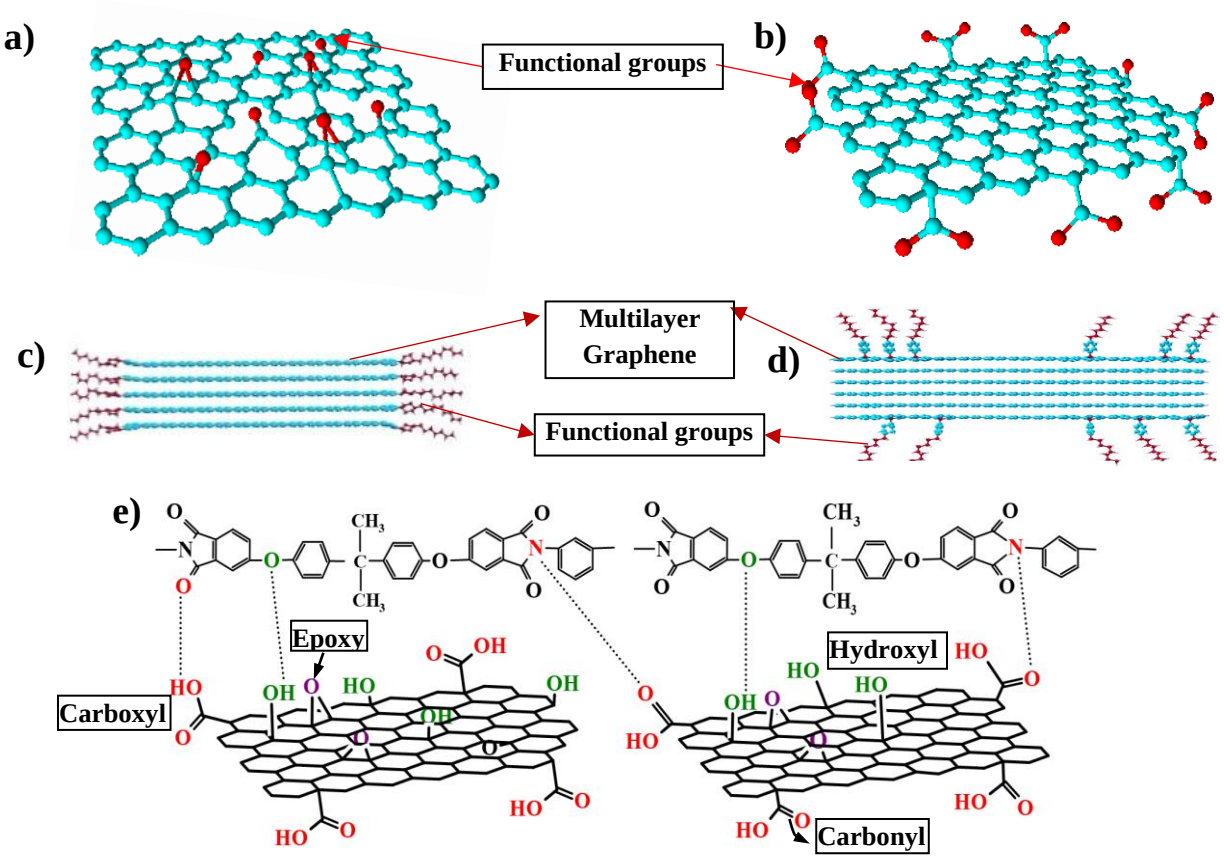

Figure 2.1 Atomic structure of a) functionalized single graphene sheet with basal plane functional groups, b) functionalized single graphene sheet with edge functional groups. Atomistic structures for c) multilayer edge functionalized graphene (EFGnP) and d) multilayer basal-plane functionalized graphene (BFGnP), e) interactions between graphene-oxide and polyetherimide (PEI).

and basal plane functionalization has also been carried out for several applications. Yang *et al.*[57] compared the role of edge and basal plane functionalization in modifying the interfacial tension between graphene and liquids. Mungse *et al.*[58] studied the lubrication potential of basal plane alkylated graphene nanosheets. In another study, the effect of an interconnected three-dimensional network structure of the edge- or basal plane-modified graphene oxide on electrical conductivity[59] was examined. Xiang *et al.*[60] compared edge versus basal plane functionalization of graphene for energy conversion and energy storage applications. There is, however, a lack of detailed

understanding of the relative effectiveness of edge versus basal plane functionalization in enhancing the thermal conductivity of polymer-graphene nanocomposites.

The advantage of edge-oxidation can be understood by observing that oxidation of the basal plane through the Hummers method[52] distorts the planar sp^2-sp^2 carbon network of the basal plane by requiring a transition to tetrahedral sp^3 hybridization needed to accommodate the extra bond for oxidation (Figure 2.1a). These sites of distortion act as phonon scatterers, dramatically lowering the intrinsic thermal conductivity of graphene. In general, a subsequent reduction reaction is required to partially restore the sp^2 carbon-carbon network, before graphene can be used to enhance the thermal conductivity of composites. The defective structure of basal plane oxidized graphene has been studied through X-ray diffraction (XRD), scanning tunneling microscopy (STM), and Raman scattering[61-63]. The oxidation-related defects are found to be mainly due to the presence of hydroxyl (-OH) and epoxy (C-O-C) functional groups on the basal plane of graphene[61,63]. Bagri *et al.* also studied the defective state of GO and indicated the presence of hydroxyl and epoxy groups on the basal plane as the main defect sites[64]. We later show the presence of these functional groups in basal plane oxidized graphene through Fourier Transform Infrared (FTIR) spectroscopy, thermogravimetric analysis (TGA), and X-Ray photoelectron spectroscopy (XPS) in sections 2.4.4, 2.4.5, and 2.4.6, respectively. Reduction in thermal conductivity through such functionalization of the basal plane has been well studied computationally. While the intrinsic thermal conductivity of graphene is ~ 2000 $Wm^{-1}K^{-1}$, Fugallo *et al.* used first-principles computations to report that this value dropped by a factor of 2 in hydrogenated graphene and by one order of magnitude in fluorogenated graphene [65]. Mu *et al.* [66] used molecular dynamics simulations to predict a dramatic decrease in thermal conductivity of basal plane oxidized graphene. An oxygen coverage of mere 5% was shown to reduce the *k* value

of basal-plane oxidized graphene dramatically by 90% and a coverage of 20% lowered it further to ~8.8 $Wm^{-1}K^{-1}$, even lower than the amorphous limit. Shenogin *et al.*[67] similarly used MD simulations to show a decrease in *k* of carbon nanomaterials through functionalization. The much lower thermal conductivity of basal plane functionalized graphene limits its effectiveness in enhancing the thermal conductivity of the polymer composite and can even result in a decrease in composite thermal conductivity relative to the case of pristine graphene. A reduction reaction with different reactants[68,69] or simultaneous amination[70,71] is used to partially restore the thermal conductivity of graphene. 15.8 wt% thermally reduced-RGO/epoxy composites (prepared using a modified Hummers method, followed by a two-step reduction reaction) yielded a *k* value of 1.27 $Wm^{-1}K^{-1}$ (relative to 0.275 $Wm^{-1}K^{-1}$for pure epoxy)[72]. An amine-functionalized GO/PEI composite reached thermal conductivity values up to 0.33 $Wm^{-1}K^{-1}$ at 3 wt% phenyl aminated graphene-oxide filler concentration[73] (showing an enhancement of 43% relative to pure PEI thermal conductivity of 0.23 $Wm^{-1}K^{-1}$). Bernal *et al.* prepared graphene nano paper from phenol-functionalized graphene and linked this phenol-functionalized graphene with dianiline and directly measured a *k* value of 0.672 $Wm^{-1}K^{-1}$, demonstrating 190% enhancement with respect to the pristine GnP nanopaper[74].

Edge oxidation of graphene offers the advantage of leaving the basal plane intact (Figure 2.1b), preserving its ultra-high thermal conductivity (~ 2000 $Wm^{-1}K^{-1}$)[45]. Using MD simulations, the thermal conductivity of edge-functionalized graphene has been shown to be within 90% of the pristine graphene value[75]. Simultaneously, hydrogen bonding interaction between oxygen groups of graphene (on edge) and polyetherimide enhances interfacial thermal conductance between graphene and polyetherimide (PEI). The preserved high thermal conductivity of graphene coupled

with superior interfacial thermal conductance of a polymer can lead to superior enhancement in thermal conductivity of polymer composite through edge oxidation, compared to the case of BGO.

In our recent computational work[75], we also demonstrated other advantages of edge functionalization for enhancement of composite thermal conductivity. We showed that edge-bonding couples polymer to the high in-plane (k_{in} > 2000 $Wm^{-1}K^{-1}$)[38] thermal conduction pathway of all graphene sheets within a nanoplatelet (Figure 2.1c), thus establishing a very efficient thermal conduction path through the composite. Basal plane bonding, on the other hand, primarily couples functional groups only to the outermost surface layers of the nanoplatelet (Figure 2.1d). The weak van der Waals' coupling of outer layers with inner layers renders the inner layers of the GnP to be less efficient in conducting heat due to the poor through-thickness thermal conductivity of graphite (~10 $Wm^{-1}K^{-1}$)[43,76] (Figure 2.1d). It was further demonstrated that edge bonding leads to weak damping of vibrations within the graphene sheets, while for basal plane bonding, the coupling of the entire basal plane with an embedding polymer was found to strongly dampen vibrations, further promoting the advantage of edge bonding. Finally, Muthaiah *et al.* used *ab initio* atomistic Green's function computations[77], to demonstrate that interfacial thermal conductance at an individual junction between a functional group and graphene is higher, when the functional group is located on the edge, as opposed to on the basal plane of graphene. This higher interfacial conductance is explained in terms of higher transmission to in-plane phonons of graphene for the edge-bonding case.

The above computational results provide a comprehensive understanding of the advantage of edge bonding in enabling superior thermal conductivity enhancement of composite. In this work, we demonstrate this advantage of edge bonding experimentally. Selective edge oxidation of graphene is obtained in this work by using the scheme outlined by Miao *et al.*[51] involving oxidizing

graphene in the presence of sodium chlorate and hydrogen peroxide in sulfuric acid. Miao *et al.*[51] showed that such a scheme leads to an excess of carboxyl groups on the edge of oxidized graphene. We confirm the presence of excess of carboxyl groups through the above oxidation scheme using FTIR and XPS analysis in sections 2.4.4 and 2.4.6, respectively. Carboxyl groups are known to preferentially form on the edge of graphene, yielding edge-oxidized graphene. To experimentally show the edge localization of carboxyl groups, Yuge *et al.*[78], stained carboxyl groups using a Pt-amine complex and found Pt-amine clusters to mainly exist at the edges of graphene sheets. Computations based on density-functional theory also showed through geometric arguments that carboxyl groups are more likely to form on graphene edges[79]. This work is the first to report enhancement in thermal conductivity through the use of the chemical edge oxidation pathway discussed above. Basal plane oxidation was achieved by using the Hummers method[52] by oxidizing graphene in the presence of sodium nitrate and potassium permanganate. Basal plane oxidation was achieved by using the Hummers method[52] by oxidizing graphene in the presence of sodium nitrate and potassium permanganate.

The preferential edge functionalization through Miao's scheme[51] is confirmed in this work through location-dependent two-dimensional (2D) Raman mapping of GnPs. Functionalized graphene is further characterized using X-ray diffraction (XRD), X-ray photoelectron spectroscopy (XPS), thermogravimetric analysis (TGA), Fourier transform infrared (FTIR) spectroscopy, and scanning and transmission electron microscopy (SEM and TEM) to examine the physical and chemical differences between the pristine, EGO and BGO.

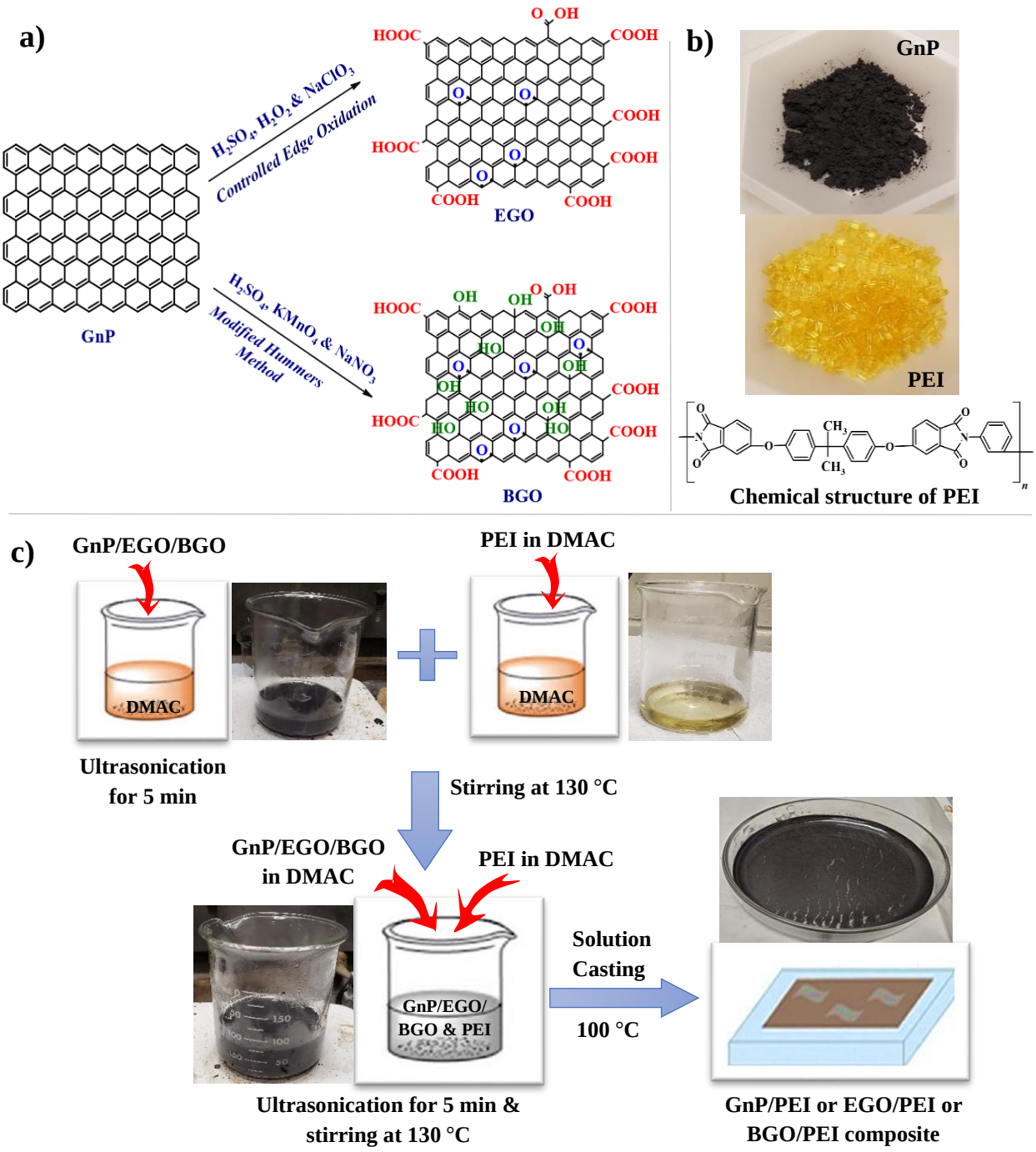

Figure 2.2 a) Schematic structure of GnP, EGO, and BGO (carboxyl & carbonyl group: -COOH/-C=O; epoxy: C-O-C; hydroxyl group: -OH), b) images of GnP nanopowder, PEI pellets and chemical structure of PEI; c) scheme for polymer-graphene composite preparation; DMAC- Dimethylacetamide

2.2 EXPERIMENTAL SECTION

2.2.1 Material Synthesis

GnPs used in this work have an average thickness of ~60nm and a lateral size of ~7μm. The graphene nanopowder was purchased from Graphene supermarket[80]. Potassium permanganate ($KMnO_4$, 99%), sulfuric acid (H_2SO_4, 95–98%), hydrogen peroxide (H_2O_2, 30%), sodium chlorate ($NaClO_3$,99%), Sodium nitrate ($NaNO_3$), N, N-dimethylacetamide (DMAC), hydrochloric acid (HCl, 35.0 -37.0%), PEI (PEI pellets, melt index 18 g/10 min) were purchased from Sigma Aldrich[81].

2.2.2 Synthesis of Edge Functionalized Graphene Oxide (EGO)

The synthesis of edge oxidized graphene was performed with a controlled oxidation reaction using $NaClO_3$, H_2SO_4 and H_2O_2 (Figure 2.2a) according to the approach outlined by Miao *et al.*[51]. 80 mL of H_2SO_4 was cooled down to 0 °C temperature using an ice bath and 1 g of graphene-nanopowder was dispersed into the H_2SO_4 using bath sonication for 15 min. After dispersing graphene into H_2SO_4, approximately 6 mL of 30% H_2O_2 solution was added to the mixture and stirred at 0 °C for few minutes. Then 4 g of $NaClO_3$ was added very slowly and carefully into this mixture for 2 h. This mixture was kept stirring at room temperature for 8 h. The reaction mixture was then poured into 500 ml of cold DI water. The mixture was centrifuged at 4000 rpm to separate the particles from acidic solution. The separated particles were then washed twice with 800 ml of HCl aqueous solution (HCl:DI water = 1:9), followed by repeated filtration with ethanol, acetone and DI water until the pH reached neutral condition. The product was then kept in vacuum oven at 60 °C for 24 h. These oxidized particles are edge oxidized graphene, denoted as EGO.

2.2.3 Synthesis of Basal-Plane Functionalized Graphene Oxide (BGO)

The Hummers method[52] was used to prepare basal-plane functionalized graphene oxide (Figure 2.2a). For this synthesis, 1 g graphene nanopowder was added into a mixture of 46 mL of sulfuric acid and 1 g of $NaNO_3$. This reaction was stirred for 4 h at 0 °C in an ice-cold bath to get a homogeneous dispersion. 6g $KMnO_4$ was added very slowly into this mixture. To maintain the temperature at 0 °C, the addition of $KMnO_4$ was done for 1 h. Then the reaction mixture is kept stirring at 35 °C. After 6 h, the reaction mixture was added to 92 mL of DI water at 95 °C and stirred for 15 min. In the last step, this mixture was mixed with 20% H_2O_2 aqueous solution. The final product was washed several times with HCl aqueous solution, ethanol, acetone and DI water repeatedly to remove ions and impurities. The separated particles were dried in a vacuum oven at 60 °C for 24 h to obtain the basal plane oxidized graphene, named as BGO.

2.2.4 Other Synthesis Routes

To prepare the edge oxidized graphene, different synthesis routes have been experimented and analyzed as described below-

2.2.4.1 Step II Oxidation of Graphene Using Modified Hummers Method (GO-1)

Step II oxidation of modified Hummers Method, developed by Kang *et al.*[82] has been utilized to prepare graphene oxide. 138 ml of H_2SO_4 was cooled down to 0 °C before adding 3.0 g of GnP. 18.0 g of $KMnO_4$ was mixed in 200 ml of cold deionized (DI) water, using an ice bath to cool it down. 50 ml of cold DI water was very carefully added to prevent the temperature from rising above 70 °C, and aqueous $KMnO_4$ was poured, followed by 50 ml of DI water. The reaction mixture was stirred at 70 °C bath for 6 h. After this stirring process, 10 ml of H_2O_2 was added to the reaction mixture. This mixture was ultra-centrifuged three times at 13000 rpm with 3.4% HCl

repeatedly using ultra-centrifugation at 12000 rpm to obtain the particles. The precipitant was washed for five times to reach at pH 7 using DI water and particles were collected using ultra-centrifugation at 4000 rpm. The particles were finally dried in a vacuum oven at 80 °C, named GO-1.

2.2.4.2 Synthesis of Graphene Oxide Using Sodium Persulfate ($Na_2S_2O_8$) Activated by Ferrous (Fe^{2+}) Ion (GO-2)

Han *et al.* prepared the edge oxidized graphene using oxidizing radicals (SO_4^-) generated from sodium persulfate ($Na_2S_2O_8$) using ferrous ion (Fe^{2+}) activation. The synthesis process was carried out in a 500 mL round-bottomed with a constant pressure funnel under magnetic stirring. The stirring speed and temperature were kept at 300 rpm and 25 °C, respectively. 30 g of $Na_2S_2O_8$ was added to a mixture of 200 ml deionized (DI) water and 1 g of GnP. The mixture was continuously stirred under the purged nitrogen to remove the produced oxygen and carbon dioxide. 15 min later, 100 mL of 1 $molL^{-1}$ $FeSO_4$ solution was added with continuous diffusion through a constant pressure funnel in 12, 24 and 48 h. Then, DI water was used 4-5 times to wash the particles and remove the by-products. Finally, graphene aqueous dispersion was obtained by 15 min bath sonication, followed by vacuum filtration, and collected in acetone. The graphene oxide particles were dried in a 60 °C vacuum oven for 24 h. The obtained graphene oxide particles are identified as GO-2. This scheme, used to produce edge oxidized graphene using oxidizing radicals (SO_4^-) generated from sodium persulfate ($Na_2S_2O_8$) using ferrous ion (Fe^{2+}) activation, has been developed by Han *et al.*[83].

2.2.5 Preparation of Polymer-Graphene Oxide Composites

A solution casting method was used to prepare the composites, and the through-thickness thermal conductivity values of these samples were then measured and compared. Pristine 60 nm GnPs were

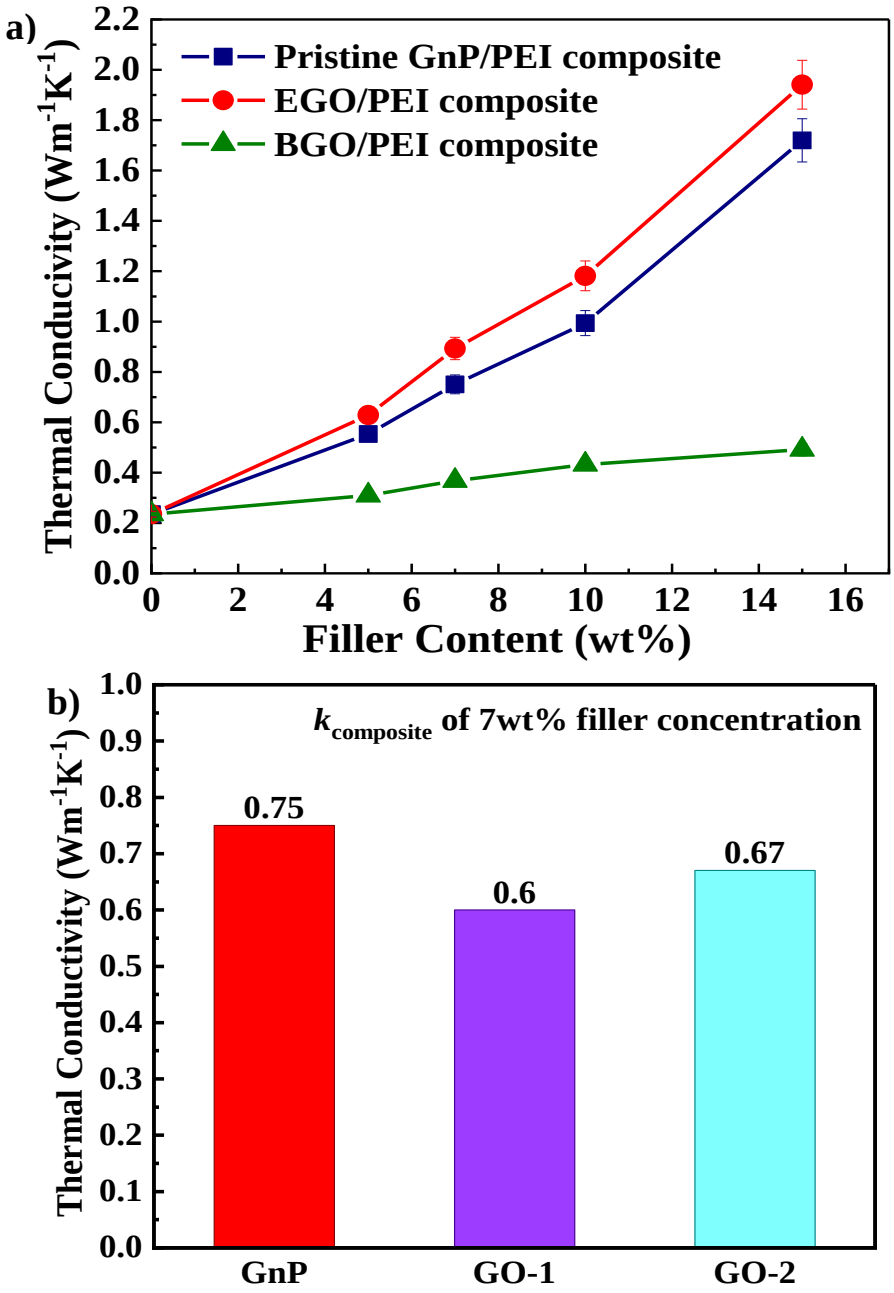

Figure 2.3 a) Through -thickness thermal conductivity value with 5, 7, 10, and 15 wt% filler content of GnP/PEI, EGO/PEI, BGO/PEI composites, and b) 7 wt% filler content of GnP/PEI, GO-1/PEI, GO-2/PEI composites

dispersed into 20 mL DMAC for 30 min using a probe sonicator (Figure 2.2c). PEI pellets were separately dissolved into 50 mL DMAC at 130 °C for 1 h. Dispersed graphene solution was blended into dispersed polymer solution for 3 h at 130 °C. To disperse the graphene into polymer properly, graphene and polymer solutions were mixed and ultrasonicated for 5 min. The homogenized solution was cast into a petri dish and held at 100 °C for 24 h producing a graphene-PEI composite film. 7, 10, and 15 wt% GnP/PEI, EGO/PEI, and BGO/PEI composite films were prepared using the same procedure. Similarly, 7 wt% GO-1/PEI & GO-2/PEI composites were also prepared to compare the thermal conductivity data.

2.3 RESULT & DISCUSSION

2.3.1 Measurement of Through-Thickness Thermal Conductivity

Thermal conductivity measurements were performed by the laser flash technique. A Netzsch LFA 467 Hyperflash laser was used to measure the through-thickness thermal diffusivity of the samples. A short, pulsed laser beam is impinged on one side of the sample and the temperature is measured on the opposing side of the sample as a function of time. The film samples were cut into a 12.5 mm diameter circles and coated with a thin layer of graphite paint. Measurements were performed at room temperature (23 °C) and a total of 6-8 shots per sample were taken. The thermal diffusivity was determined using the following equation:

$$\alpha = (0.1388\ d^2)/t_{1/2} \quad (2.1)$$

where, α is the thermal diffusivity (mm^2/s), $t_{1/2}$ is the time to obtain half of the maximum temperature on the rear surface, and d denotes the sample thickness (mm). The thermal conductivity was calculated based on the following equation:

$$k = \alpha \rho Cp \quad (2.2)$$

where *k*, ρ, and Cp represent the thermal conductivity, density, and specific heat constant of the sample, respectively. In this work, density and specific heat of the sample are calculated from the rule of mixtures.

2.3.2 Thermal Conductivity Data

Figure 2.3a presents the comparison of *k* values of GnP/PEI, EGO/PEI and BGO/PEI composites for different GnP filler loadings. The thermal conductivity (*k*) value of pure PEI is measured to be 0.23 $Wm^{-1}K^{-1}$ (in good agreement with literature value[84]), while thermal conductivity of pristine graphene-PEI composite (shown by blue curve in Figure 2.3a) is measured to be 1.72 $Wm^{-1}K^{-1}$ for 15 wt% filler content. Figure 2.3a further shows that the highest thermal conductivity values are achieved through the use of edge-oxidized graphene (EGO), clearly demonstrating the advantage of edge-oxidation. Enhancements in the *k* value of 18% and 13% are achieved for the EGO/PEI composite relative to pristine GnP/PEI composite, resulting in high *k* values of 1.14 $Wm^{-1}K^{-1}$ and 1.94 $Wm^{-1}K^{-1}$ for the EGO/PEI composite for 10 wt% and 15 wt% graphene, respectively. The *k* value of 1.94 $Wm^{-1}K^{-1}$ achieved for 15 wt% EGO/PEI composite, represents a large ~725% enhancement compared to that of pure PEI.

On the other hand, the *k* value of BGO/PEI composite is found to be diminished relative to that of the pristine GnP/PEI composite. At 15 wt% composition, the *k* value of BGO/PEI composite (0.48 $Wm^{-1}K^{-1}$) is lowered by almost 72% and 75% relative to those of pristine GnP/PEI and EGO/PEI composites, respectively. The BGO/PEI composite's *k* value is still found to be enhanced with respect to the pure PEI by ~104% at 15 wt% composition. This enhancement is, however, much smaller than the enhancement of 725% achieved for EGO/PEI composite.

The lower *k* value of the BGO/PEI composite is due to the defects introduced by the Hummers method on the basal plane of GnP[85-87] (as discussed before), which dramatically lowers the intrinsic

thermal conductivity of graphene. We later provide evidence (through I_D/I_G ratio obtained via Raman analysis in section 2.4.2) for the presence of a much larger number of functional groups on the basal plane of graphene for BGO compared to pristine GnP and EGO. XRD analysis (presented in section 2.4.3) further shows that these oxygen functional groups lead to an increase in the interlayer spacing of BGO to 0.717 nm (relative to the value of 0.336 nm for pristine GnP) indicating that the oxygen groups intercalate the spacing between the graphene layers within the GnP for BGO and attach to the basal planes of all graphene sheets constituting the GnP. Previous computations have shown that such BGO has a dramatically diminished *k* value compared to that of pristine graphene (by up to 90% lower for 5% coverage)[66]. The significantly lower *k* of BGO compared to that of pristine graphene causes the *k* of the BGO/PEI composite to become even lower than that of the pristine GnP/PEI composite.

For edge bonding (EGO), however, we show through Raman analysis (in section 2.4.2), a much smaller presence of functional groups on the basal plane of graphene. XRD analysis (discussed in section 2.4.3) further shows that interlayer spacing of EGO (0.337 nm) is very similar to that of pristine graphene (0.336 nm), providing more evidence of the presence of oxygen groups on the edges of graphene for EGO. XPS analysis (section 2.4.6) further shows a stronger intensity of the C-C/C=C peak in EGO compared to that of BGO. These analyses point to superior structural integrity of the basal plane of graphene for EGO relative to BGO. Computational analysis reveals that *k* of such structurally preserved EGO can be close to the high intrinsic *k* of pristine graphene. Simultaneously, hydrogen bonding between oxygen groups of EGO and PEI enhances interfacial thermal conductance between the two. Significantly superior *k* of EGO (and close to the value of pristine graphene) compared to BGO, combined with improved interfacial thermal conductance between EGO and PEI (relative to between pristine GnP and PEI) causes the *k* of EGO/PEI to

exceed those of both the pristine GnP/PEI and BGO/PEI composites (Figure 2.3a). These results can enable new avenues to achieve higher thermal conductivity polymer/graphene nanocomposites. Below, we provide the details of dispersion of graphene in the prepared composite. We further provide understanding of differences in oxidation in EGO and BGO through detailed characterization.

k value of graphene oxide polymer composite as obtained from other synthesis routes has been measured as well. Composites with 7 wt% filler concentration have been prepared to compare the *k* value of GO-1/PEI and GO-2/PEI composites. Figure 2.3b displays the through-thickness *k* value of GO-1/PEI, GO-2/PEI composites for 7 wt% GO-1 & GO-2 filler compared to GnP/PEI composite. For both the cases, the composite *k* value is lower than GnP/PEI composite. A decrease in *k* value demonstrates that attached oxygen groups do not provide any beneficial property, but rather degrade the basal plane structure as seen in XPS analysis and Raman characterization. Raman (section 2.4.2) and XPS analysis (section 2.4.6) were performed to understand the structural defect and chemical composition to compare GO-1 & GO-2 with EGO and BGO.

2.4 MOLECULAR STRUCTURE CHARACTERIZATION

A DXR3 Raman microscope from Thermo Fisher Scientific was used to collect the Raman spectra (shown in Figure 2.5). The following parameters were used to collect the spectra□a laser wavelength λL of 532 nm, a laser power at the sample of 0.5 mW, and a microscope objective of 100×. A 25 mm confocal pinhole aperture and 10 s collection for each spectrum were used. The Raman spectra shown in Figure 2.7a have been obtained using a Horiba Jobin-Yvon labRam HR instrument. Data were collected over the range from 2400 to 1000 cm^{-1} using a laser wavelength λL of 633 nm, a spectral resolution of 0.16 cm^{-1}, and an imaging resolution of 702 nm. An

Olympus BX 41 microscope with a 5× objective, an exposure time of 10 s for 15 accumulations, and three scans per sample was used to collect the spectra.

A Rigaku SmartLab 3kW (Rigaku Corporation, Japan) was used to produce the XRD patterns of GnP, EGO, and BGO at room temperature using Cu Kα radiation (λ = 1.5406 Å) with a scan range of 2-8° min^{-1} and a step size of 0.02°. The Bragg−Brentano configuration was used to collect the data at room temperature, and the operating parameters were applied over 2θ = 5 to 70°.

GnP, EGO, and BGO were analyzed by Thermo Scientific K-alpha XPS, where an Al Kα gun source was used to excite the sample and measurement was carried out for an acquisition time of ~48 s at a spot size of 400 μm. A passing energy of 50 eV was utilized to find the C, O peak in this analysis spectrum. The elemental composition of C and O as well as the abundance of functional groups were investigated using the Avantage software. To determine the functional groups' peak position, full width at half-maximum (FWHM), and atomic percentage, Avantage software was used to do curve fitting utilizing Gaussian and Lorentzian functions.

The FT-IR spectra were collected on the GnP, EGO, and BGO samples using a Paragon 1000 FT-IR Spectrometer (PerkinElmer, Inc) with a germanium crystal in attenuated total reflectance (ATR) mode. Data were measured over a wavenumber range of 4000 to 500 cm^{-1} and OMNIC software was used for spectral analysis.

TGA was performed using NETZSCH TG 209 F1 Libra to evaluate the thermal stability of the graphene samples and functional groups attached during the oxidation process. Data were collected over the temperature range of 50−800°C. N_2 gas atmosphere was used with a heating rate of 10 °C/min.

Field Emission Environmental Scanning Electron Microscopy (FE-ESEM) was used to characterize the composite structure. A ThermoFisher Quattro S FE-ESEM was operated at 20 kV to perform the analysis of the samples. Morphological characterization of pristine GnP, EGO and BGO was carried out using scanning electron microscopy (SEM) and high-resolution transmission electron microscopy (HR-TEM). A Zeiss NEON 40 EsB Crossbeam instrument and JEOL 2000-

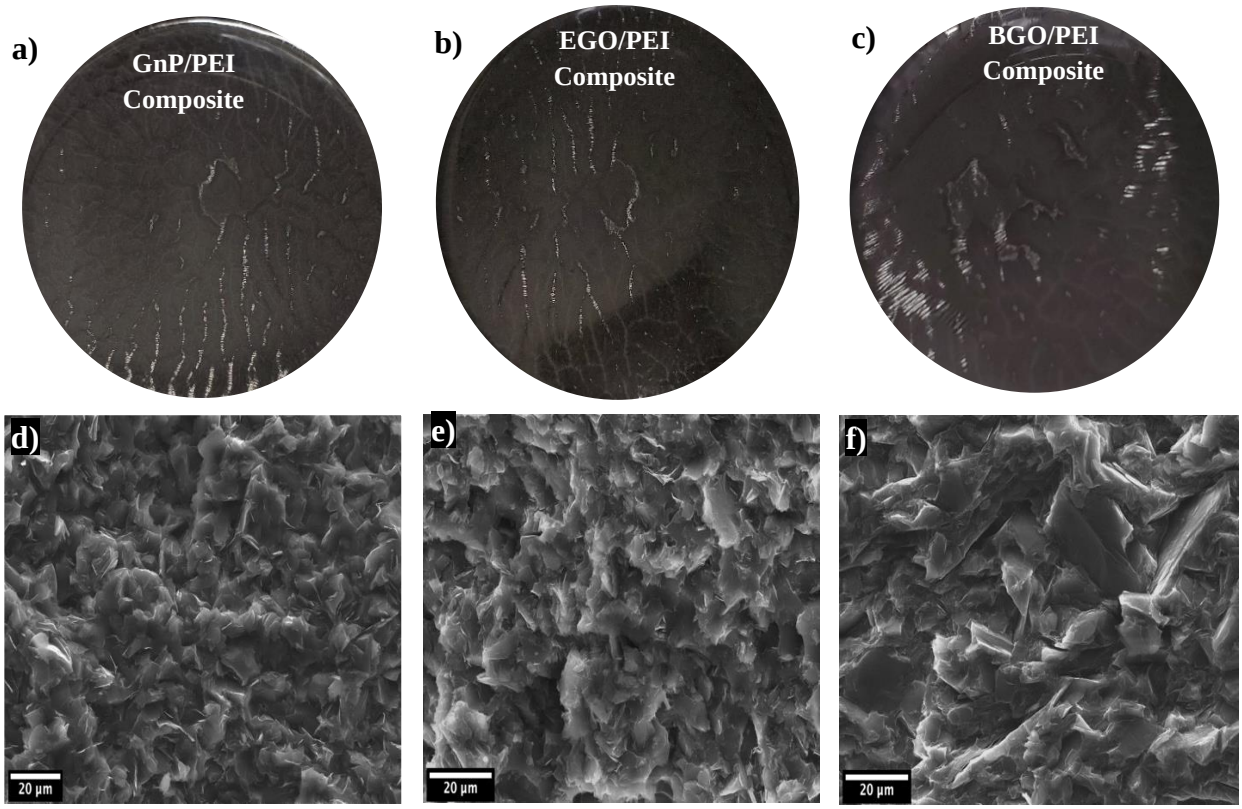

Figure 2.4 Images of composite films for a) pristine GnP/PEI, b) EGO/PEI, c) BGO/PEI & cross- sectional FE-ESEM images of 15 wt% composites for d) pristine GnP/PEI, e) EGO/PEI and f) BGO/PEI composites.

FX 200kV transmission electron microscope with a camera for acquisition of DE (Direct Electron)-12 were used to perform the high-resolution SEM and TEM analysis, respectively. This field-emitting scanning electron microscope was operated at an accelerating voltage of 5 kV. To

prepare the samples for SEM imaging, the DMAC solvent was used to coat the smooth silicon surface, and a 300 mesh lacy carbon copper grid was used for TEM.

2.4.1 Dispersion of Graphene Nanoplatelets within the Composite.

Uniform dispersion of graphene in the polymer matrix is critical for achieving high thermal conductivity. In this work, we used N, N-dimethylacetamide (DMAC) to both dissolve polyetherimide and disperse graphene nanoplatelets. DMAC is a highly polar aprotic solvent and has a very strong dispersing power. This enables significantly lower aggregation compared to other solvents such as acetone or ethanol. Figure 2.4(a-c) show that GnPs were uniformly dispersed in all three composites – pristine GnP/PEI, EGO/PEI and BGO/PEI. While Figure 4a-c shows dispersion of graphene in bulk samples, we also performed cross-sectional FE-SEM analysis to study dispersion of graphene on a microscopic scale. These images are shown in Figure 2.4d-f for 15 wt% GnP/PEI, EGO/PEI and BGO/PEI composites. These images clearly indicate that pristine GnP, EGO and BGO fillers are all similarly well dispersed into polymer matrix even at a microscopic level. The similar uniform dispersion of graphene for all three cases (pristine, edge-oxidized and basal-plane oxidized) indicates that the advantage of edge-bonding in enhancing k relative to pristine graphene, can be attributed to superior interfacial thermal interaction with the surrounding PEI.

2.4.2 Raman Characterization

To provide evidence for selective edge oxidization of graphene, 2D Raman mapping of EGO and BGO (Figure 2.5a-c) was performed. Raman spectroscopy characterizes the graphene's unique structure through two conventional peaks, one at ~1586 cm^{-1} and another one at ~1345 cm^{-1}, attributed to the G band and D band respectively[88]. The presence of the G band is related to the

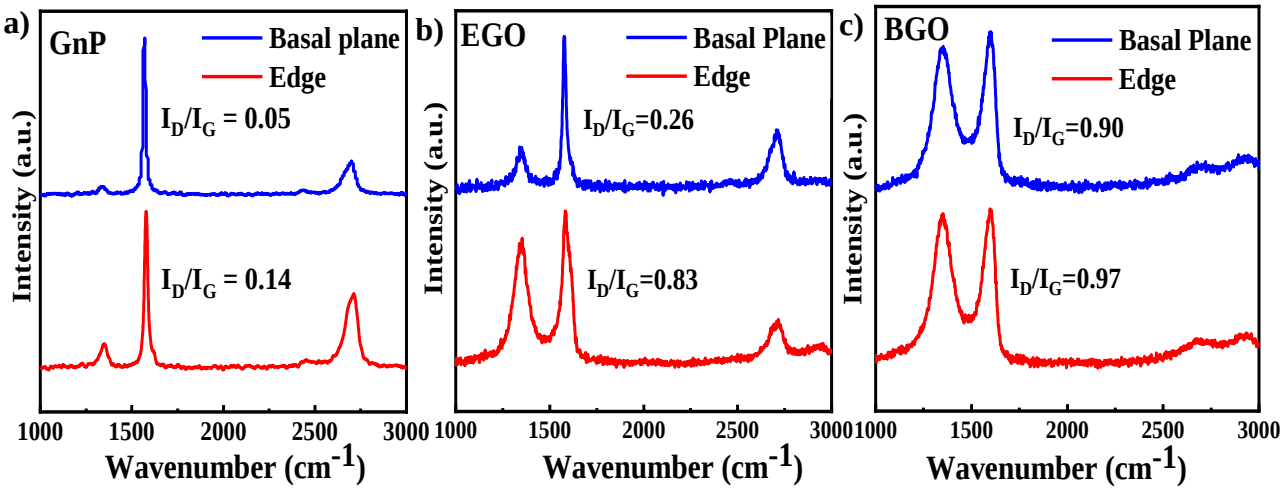

Figure 2.5 I_D/I_G ratio of edge and basal plane area of a) GnP, b) EGO, and c) BGO.

stretching mode of defect-free sp^2 carbon through the first order E_{2g} scattering mode and the D band is induced by the disordered structure of sp^3 hybridized carbon[89]. I_D/I_G (the ratio of the intensity of the D band and G band)[90] thus provides an understanding of the structural disorder of the graphitic structure.

To examine and compare the I_D/I_G ratio at the "edge" versus. "basal plane" of both EGO and BGO, a DXR3 Raman microscope is used and graphene nanoplatelets (pristine graphene/EGO/BGO) are transferred on a glass slide on top of a piece of double-sided tape to ensure that they do not move/drift during the Raman mapping. For treated/untreated graphene, one

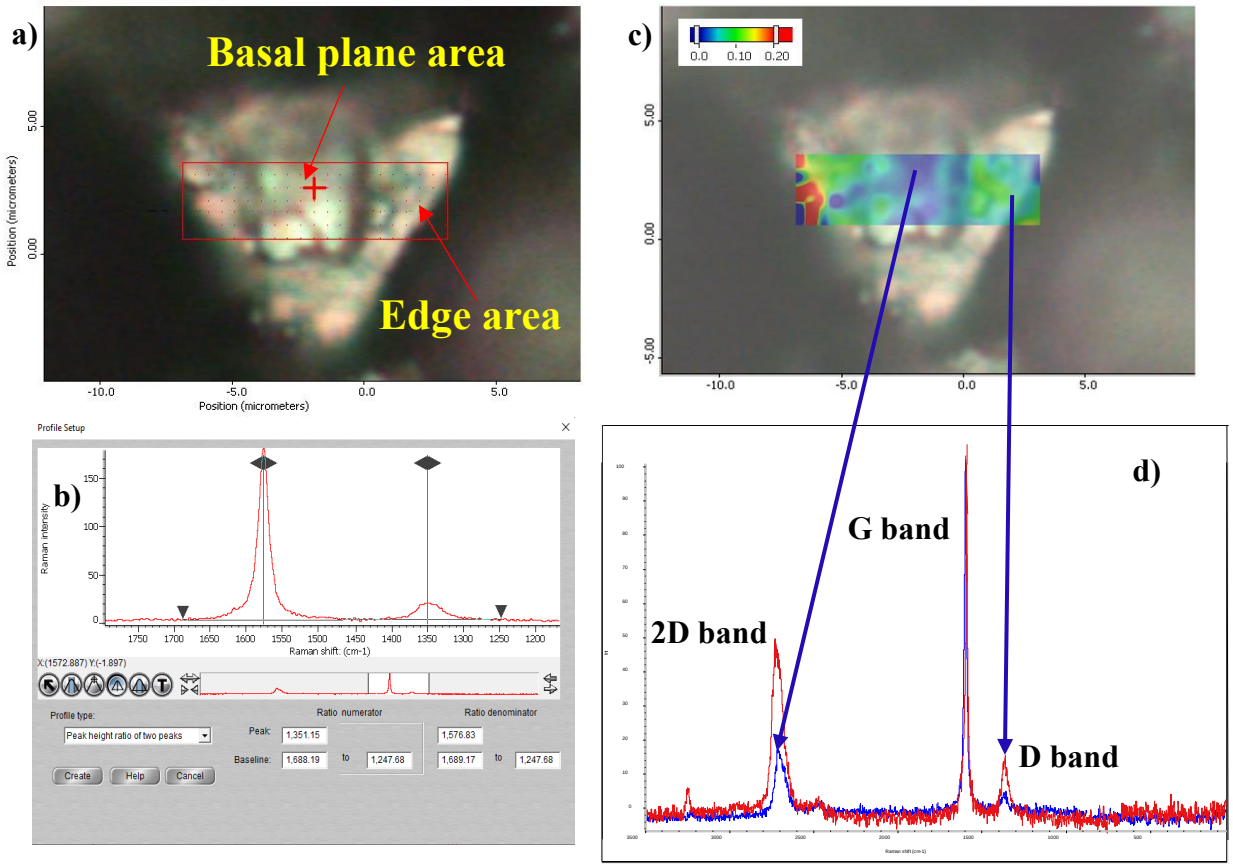

Figure 2.6 a) Image of a graphene nanoplatelet under 100x magnification during 2D Raman mapping, b) Raman intensity profile showing intensity of G band and D band for a particular point in the red rectangle in Fig. 2.6a, c) super imposed Raman chemical image showing I_D/I_G ratios as color contours, d) representative Raman spectra for edge and basal plane area of graphene nanoplatelet.

to two GnPs are selected for Raman area mapping. A snapshot of pristine GnPs captured during the 2D Raman mapping using a 100× objective is shown in Figure 2.6a. The red rectangle (as shown in Figure 2.6a is the area (10 μm × 4.2 μm) selected for Raman mapping, with each red dot representing a spot for Raman spectral collection (total 147 points, with a step size of 0.5 μm). Intensities of D and G bands are shown for a particular point in Figure 2.6b. Values of I_D/I_G ratios for different points are assembled and shown as color contours to generate Raman chemical image as seen in Figure 2.6c. The spectra were collected from points on the edge and averaged. These

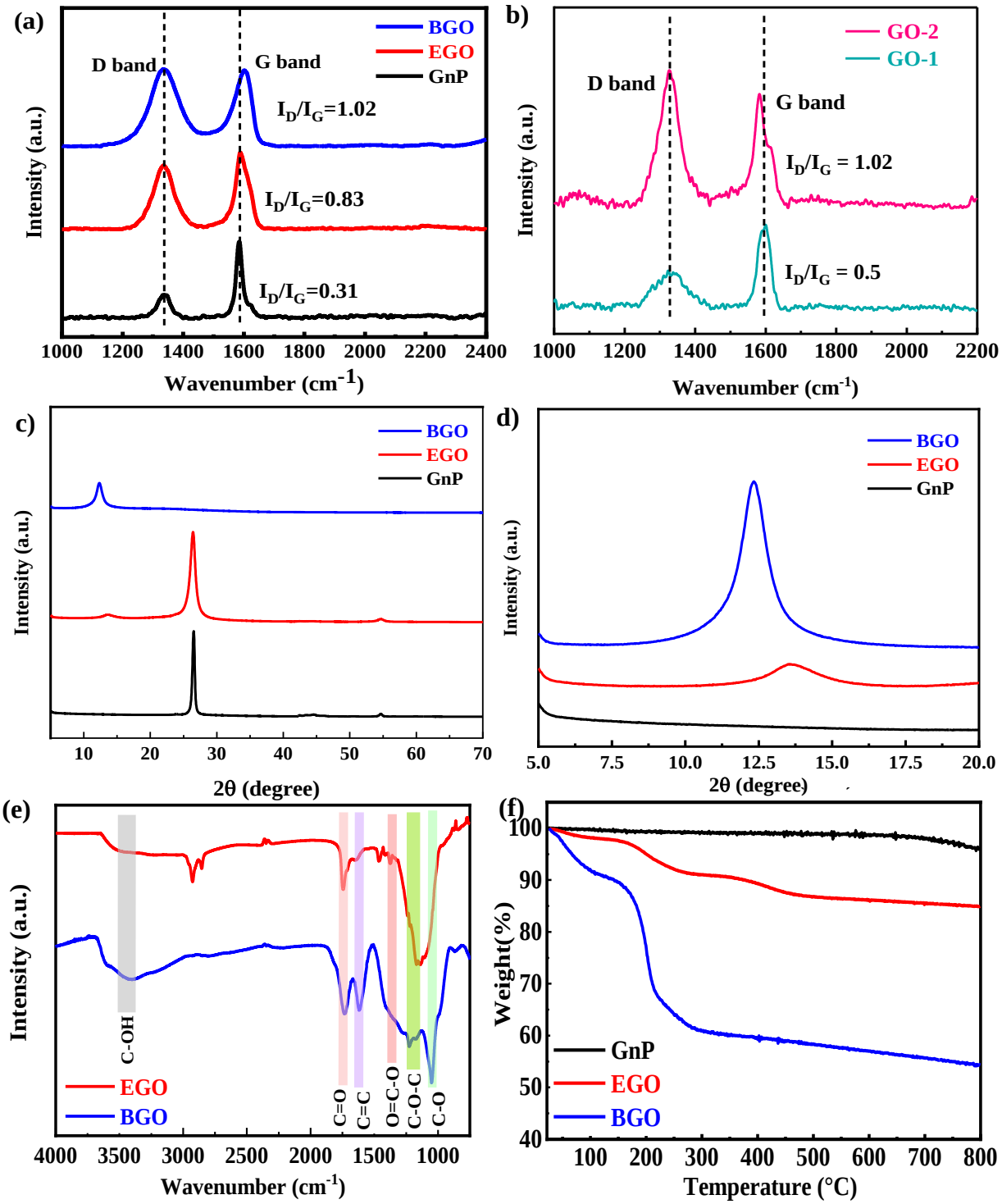

Figure 2.7 Raman spectra of a) GnP, EGO and BGO, b) GO-1 and GO-2; c) Full XRD spectra, d) Inset of XRD spectra, (e) FTIR, and (f) TGA spectra of GnP, EGO and BGO.

values were reported as the edge I_D/I_G ratio and shown in Figure 2.5a, b and c. Similarly, I_D/I_G

ratios of points in the center area (Figure 2.6 c) of the nanoplatelet were averaged and reported as the basal plane I_D/I_G ratio in Figure 2.5a, b and. I_D/I_G ratios of two points, close to edge and basal plane are represented using red and blue spectra respectively as shown in Figure 2.6d.

These I_D/I_G ratios for the center area and edge are compared in Figures. 2.5(a-c) for pristine GnP, EGO) and BGO. The I_D/I_G ratio increases more dramatically on edges (from 0.14 for pristine graphene to 0.83 for EGO) relative to the basal plane (from 0.05 for the pristine graphene to 0.26 for EGO) for EGO. This much larger increase of the I_D/I_G ratio on edges suggests that selective edge oxidation has taken place at the edges of EGO. However, for BGO, an increase in the I_D/I_G ratio on the basal plane is more significant (from 0.05 for pristine graphene to 0.90 for BGO), suggesting basal plane oxidation for BGO.

Table 2.1 Position and value of FWHM of D & G band of GnP, EGO and BGO.

Sample name	**G band (cm^{-1})**	**D band (cm^{-1})**	**FWHM (cm^{-1}) of G band**	**FWHM (cm^{-1}) of D band**
GnP	1585	1335	28.76	48.32
EGO	1588	1335	56.92	85.89
BGO	1601	1339	122.91	74.43
GO-1	1595	1330	35.13	89.79
GO-2	1587	1327	48.20	61.66

The higher I_D/I_G ratio on the central area of BGO (0.90) compared to EGO (0.25) indicates a greater number of functional groups on the central area of BGO relative to EGO; these functional groups distort the basal plane of graphene in BGO[57,91], causing a reduction in its thermal conductivity which in turn decreases the overall thermal conductivity of the BGO/PEI composite (Figure 2.5c). Overall, the I_D/I_G ratio (for the entire GnP) of EGO (0.83) is also significantly lower

than that of BGO (1.02), indicating overall less structural damage in EGO compared to BGO (Figure 2.7a).

The Raman spectra of GO-1 & GO-2 have been analyzed to find the I_D/I_G ratio for the other two GO synthesis procedure as shown in Figure 2.7b. The I_D/I_G ratio of GO-1(0.5) is lower than the overall I_D/I_G ratio of EGO (0.83), but the shift in G peak position and the broader D band peak of GO-1 suggests the exfoliation during the reaction process. The I_D/I_G ratio of GO-2 (1.02), similar to the BGO indicates the disorder in graphitic structure due to the attachment of functional groups. Such higher disorder leads to lower *k* value of composite.

2.4.3 Effect of Functionalization on Interlayer Spacing through XRD Analysis

To further provide evidence for distortion of the graphitic structure in BGO, we performed XRD analysis to understand the interlayer spacing for the two different oxidation schemes. The interlayer spacing is measured from Bragg's law[92] by using,

$$n\lambda = 2d \sin\theta \quad (2.3)$$

where, λ is the X-ray wavelength (0.15404 nm), and θ is the diffraction angle (radians). The XRD diffraction pattern of pristine GnP shows a sharp reflection peak (002) at $2\theta = 26.5°$ [93] (Figure 2.7c), pointing to an interlayer spacing (d) of 0.336 nm (computed from Eq. 2.3) for pristine GnP. For the GnPs of EGO, the diffraction peak is still sharp and intense at the same location (2θ = 26.4°) the same as the pristine nanoplatelet, indicating that EGO has a similar interlayer spacing of 0.337 nm as in pristine graphene. This indicates that the functionalization scheme based on Miao's approach[51] mostly accessed the edge of graphene without penetrating the interlayer spacing. The XRD pattern for EGO also exhibits a very weak peak at $2\theta = 13.5°$ [94] (Figure 2.7d), this corresponds to the introduction of oxygen groups at the edge of graphene. This localization of

functional groups on graphene edges for EGO, leaves the basal plane mostly intact, preserving the high thermal conductivity of graphene.

For graphene oxidized by the Hummers method (BGO), it is observed that the reflection peak at 2θ = 26.5° completely disappears and shifts to 12.33° indicating a higher interlayer spacing of 0.717 nm; this higher spacing is due to the intercalation of oxygen functional groups in between graphene layers in the nanoplatelets, suggesting oxidation of the basal plane of all graphene sheets within the nanoplatelets for BGO, resulting in a disordered graphitic structure[95]. Such BGO has a dramatically lower thermal conductivity relative to pristine graphene[66].

According to Table 2.1, it can be noticed that the G band of pristine GnP is located at 1585 cm^{-1}. The G band of BGO is, however, found to be shifted to 1601 cm^{-1}, whereas G band of EGO does not change its peak position much. The smaller shift of G band indicates lower number of defects and structural deformation in a sample[57,94,96]. Full width at half maximum (FWHM) values from peak analysis of Raman spectra in Table 2.1 indicate that the functionalization scheme of BGO introduces higher degree of oxidation on both basal plane and edge of graphene, as opposed to the case of EGO. Lower value of ~56 cm^{-1} FWHM of G band for EGO can only be attributed to initial edge functionalization as claimed by different literature studies[94,97] .

2.4.4 Chemical Group Analysis through FTIR Analysis

FTIR analysis was carried out in attenuated total reflection (ATR) mode to observe the difference in functional groups for EGO and BGO. Oxidation of graphene leads to the presence of epoxy(C−O−C) and hydroxyl (C−OH) functional groups on the basal plane and carbonyl (C□O) and carboxyl (−COOH) functional groups on the edge according to the Lerf−Klinowski model[98] (see Figure 2.1e). Figure 2.7e shows that EGO exhibits an intense peak at ~1740 cm^{-1} [95] and a peak at ~1380 cm^{-1} [99], corresponding to stretching vibrations of (C=O) and (C-O), confirming the

presence of carboxyl (-COOH) groups. BGO shows a sharp and intense peak for the epoxy group (C-O-C) at ~1231 cm^{-1}, [73] and a comparatively broader peak for the hydroxyl (-OH) group at ~3400 cm^{-1} [100], which is quite dissimilar from EGO. Outlined FTIR analysis reveals the difference in functional groups present in EGO and BGO. Carboxyl group formation is strongly noticeable in EGO confirming the introduction of an excess of carboxyl groups through the Miao's oxidation scheme (involving use of sodium chlorate and hydrogen peroxide)[51].

2.4.5 Thermogravimetric Analysis

Functionalization behavior is also observed with TGA (thermogravimetric) analysis in Figure 2.7f d. Pristine GnP exhibits minor weight change with temperature indicating the presence of a very small quantity of functional groups. Lower total weight loss for EGO (15 wt%) compared to BGO (~45%) represents smaller quantities of functional groups present in EGO compared to BGO. Weight loss in EGO is found to occur very slowly up to 800 °C, indicating removal of highly stable oxygen groups which are usually edge functional groups[101]. Quick degradation in BGO in the 110-300 °C temperature range is not observed in EGO, which implies that BGO possesses a higher amount of less stable epoxy and hydroxyl groups in comparison to EGO[59]

2.4.6 XPS Analysis

XPS analysis (seen in Figure 2.8) is further used to investigate the differences in oxidation in EGO and BGO samples. Figure 2.8a shows the presence of a C1s peak around 285 eV for pristine GnP, and strong peaks of O1s around 533eV for EGO and BGO[73]. The intensity of the oxygen peak in BGO is higher than that in EGO, suggesting a higher atomic percentage of oxygen

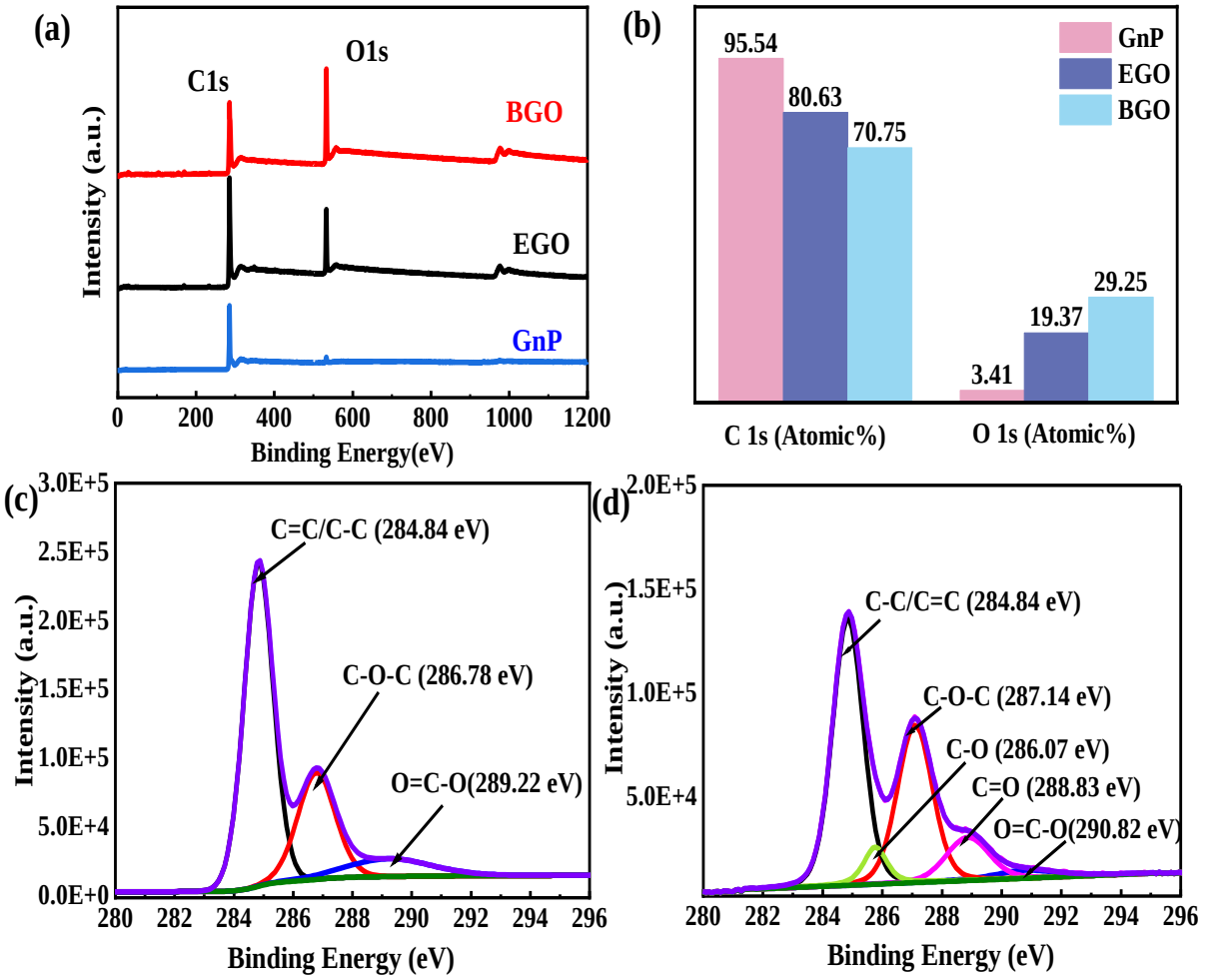

Figure 2.8 XPS data showing the a) survey spectra, b) atomic percentage of C1s and O1s for GnP, EGO, and BGO, and the high resolution C1s spectra for c) EGO and d) BGO.

functional groups in BGO compared to EGO (Figure 2.8b). The O/C ratios for EGO and BGO are 0.24 and 0.41 respectively.

Table 2.2 Abundance of functional groups of EGO, BGO, GO-1 and GO-2 in atomic percentage.

Sample name	C-C/C=C	C-OH	C-O-C	C=O	O=C-OH
EGO	62.99	-	26.87	-	10.14
BGO	46.28	8.49	33.48	10.25	1.51
GO-1	63.31	12.37	8.73	7.11	8.48
GO-2	36.05	37.97	11.20	4.81	9.97

To understand the differences in functional groups in EGO and BGO, the C1s high-resolution XPS spectra were further analyzed. The deconvoluted spectra of BGO (shown in Figure 2.8d) reveal the presence of non-oxygenated peak of C-C/C=C at 284.84 eV, C-O-C (epoxy) at 287.14 eV, C-OH (hydroxyl) at 286.07 eV, C=O (carbonyl) at 288.83 eV, and O=C-OH (carboxyl) at 290.82 eV[102,103]. Table 2.2 reveals that the atomic percentage of epoxy and hydroxyl functional groups in BGO is higher than that in EGO. These functional groups penetrate the graphitic structure modifying the basal plane of BGO, as indicated by the weaker intensity of C-C/C=C in

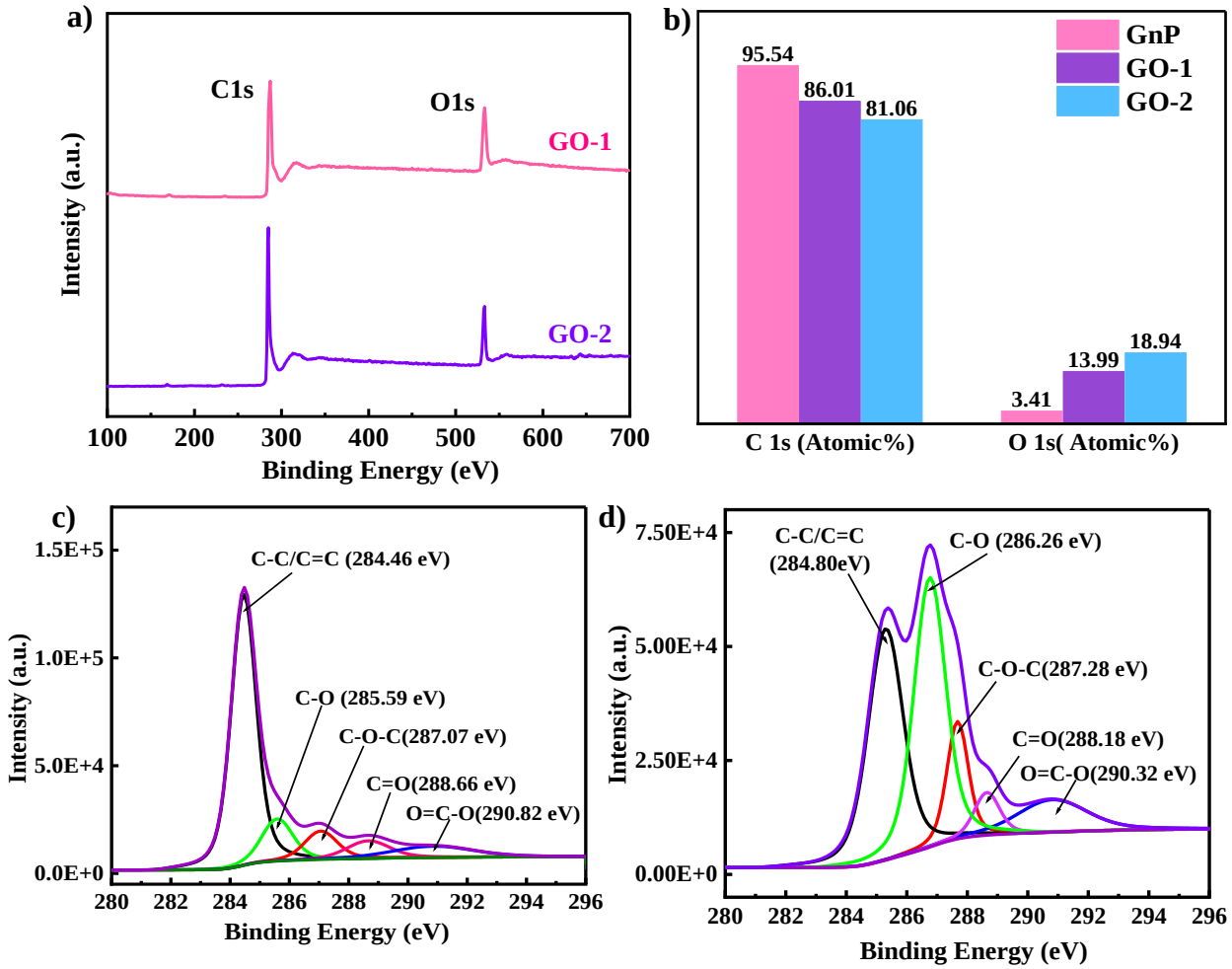

Figure 2.9 XPS spectra showing the a) survey spectra, b) atomic percentage of C1s and O1s for GnP, GO-1, and GO-2, and the high resolution C1s spectra for c) GO-1 and d) GO-2.

BGO relative to EGO. Such a modification of the basal plane in BGO lowers the thermal conductivity of BGO relative to pristine GnP.

Contrary to the case of BGO, Figure 2.8c shows that EGO exhibits a significant presence of carboxyl groups which are known to be predominantly located at the edges of graphene[78,79]. This combined with the presence of a smaller quantity of epoxy groups (C-O-C peak at 286.78 eV[103,104]) and the absence of hydroxyl groups (C-OH) in EGO, preserves the structural integrity of the basal plane of graphene in EGO. The stronger intensity of the C-C/C=C peak in EGO (Table 2.2) further confirms the superior integrity of graphene in EGO through the controlled edge oxidation scheme[51] used in this work. The minimal distortion of the basal plane of graphene in EGO preserves its high intrinsic thermal conductivity.

Figure 2.9a presents XPS spectra of GO-1, and GO-2 showing the of C1s peak around 285 eV for pristine GnP, and strong peaks of O1s around 533eV for EGO and BGO[73]. The atomic percentage of C and O is presented in Figure 2.9b, referring to the O/C ratio of 0.16 and 0.23 of GO-1 and GO-2 respectively. The O/C ratio of GO-1 is lower than EGO but the intensity of carbon peak is much lower than EGO (Figures 2.8c & 2.9c), suggesting lots of functional groups attached to the graphene's structure, that causing lower value *k* for the composite. The intensity of carbon peak of GO-2 shows the weakest intensity due to highest amount of oxygen functional groups (Figure 2.9d). Further investigation of deconvoluted carbon peak reveals the presence of C-OH functional groups, for GO-1 and GO-2, attributing to the fact of basal plane oxidation. Further investigation of the deconvoluted carbon peak indicates the presence of C-OH & C-O-C functional groups in GO-1 and GO-2 in substantial amounts, indicating that the basal plane has been highly oxidized. As a result of such basal plane oxidation, the graphene structure is significantly degraded, and the composite's *k* value drops severely compared to pristine graphene/PEI composite.

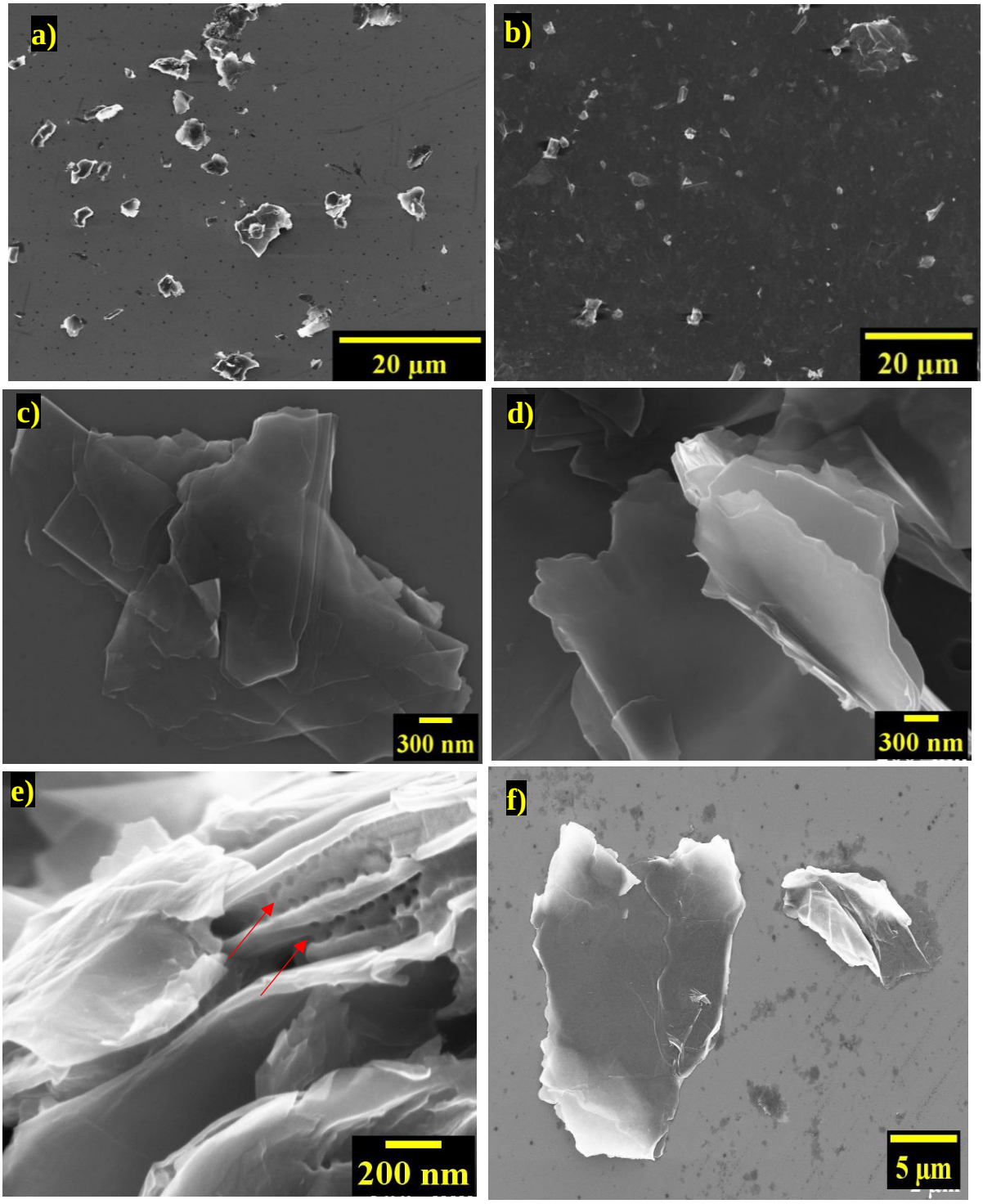

Figure 2.10 FE-SEM images of overall particle size of a) EGO, b) BGO; c) Frontal, d) Cross sectional view and e) Edge of EGO particle; f) Frontal view of BGO particle.

2.4.7 FE-SEM & HR-TEM Images of GnP, EGO & BGO Fillers

SEM and TEM images of pristine and functionalized graphene nanoplatelets are shown in Figures. 2.10. & 2.11.

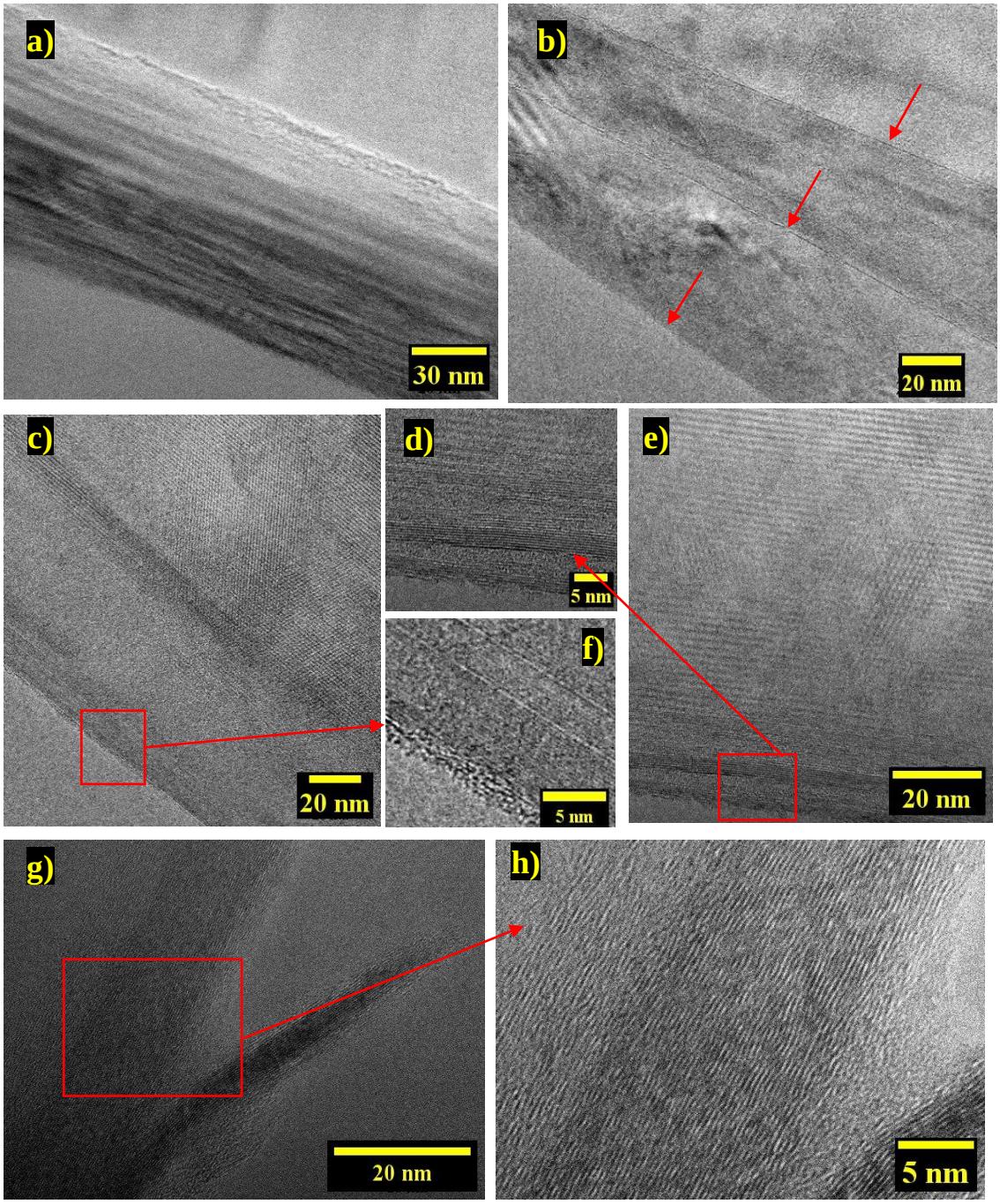

Figure 2.11 HR-TEM images of (a-b) GnP; (c-f) EGO; (g-h) BGO.

2.5 CONCLUSION

In summary, we have demonstrated the superiority of edge-oxidation of graphene (EGO) in enhancing the thermal conductivity of graphene-nanoplatelet (GnP)/polyetherimide (PEI) composite, relative to oxidation of the basal plane (BGO). To achieve edge-oxidation, graphene was oxidized with sodium chlorate and hydrogen peroxide in sulfuric acid, introducing an excess of carboxyl groups on graphene edges. Basal plane oxidation was achieved using the Hummers method. The combined effects of the preservation of high intrinsic thermal conductivity of graphene and an enhancement in interfacial thermal conductance between polyetherimide and graphene through edge oxidation, caused the thermal conductivity of EGO/PEI composite to exceed that of pristine GnP/PEI composite by almost 18% at 10 wt% graphene composition. Oxidation of the basal plane, however, dramatically lowers the intrinsic thermal conductivity of graphene, causing the *k* of BGO/PEI composite to be diminished by 57% and 63% relative to those of pristine GnP/PEI and EGO/PEI composites, respectively at the same composition. EGO was found to enhance composite *k* by 725% at 15 wt% composition, while the corresponding enhancement through basal plane oxidation was only ~75%, relative to pure PEI. Raman spectroscopy, XPS analysis, XRD and FTIR provided evidence for the preferential edge oxidation in EGO through the presence of an excess of carboxyl (-COOH) functional groups on graphene edges. These results open up new avenues to achieve higher thermal conductivity polymer-graphene nanocomposites, with important implications for a wide range of thermal management technologies.

CHAPTER 3

Large enhancement in thermal conductivity of solvent-cast expanded graphite/polyetherimide composites[2]

3.1 INTRODUCTION AND LITERATURE REVIEW

Increased thermal dissipation in modern electronic devices has led to a demand for thermally conductive materials with superior thermal conductivity (*k*) [11,105,106]. The light weight, high corrosion resistance, and excellent processability of polymeric materials make them attractive for thermal management applications[107,108]. However, poor thermal conductivity (<0.5 $Wm^{-1}K^{-1}$)[13,42] of polymers limits their application in the efficient heat removal process. The addition of high thermal conductivity fillers such as graphene or carbon nanotubes has been shown to significantly enhance the thermal conductivity of polymer graphene nanocomposites [38,45,109-113] . Different effects have been investigated to enhance the effectiveness of graphene in enhancing *k*, such as alignment and percolation effects. Alignment of carbon nanomaterials [24,114-119] takes advantage of their thermal conductivity in one direction (in−plane for graphene nanoplatelets and along the axis for carbon nanotubes). However, the enhancement achieved in *k* through alignment effects is anisotropic, potentially limiting the application of such composites. One of the most promising approaches has been the percolative effect, where graphene–graphene contact is used to bypass

[2] The content of this chapter is an extension of a published paper by the author. The paper contains results of research which was solely conducted as partial fulfillment for the PhD requirement.

the polymer, leading to significantly higher thermal conductivity enhancement [113,120]. More recently, expanded graphite has been shown to yield very high composite *k* values [121-126]. In this paper, we explore the use of expanded graphite (EG) for enhancing the thermal conductivity of polyetherimide (PEID) due to the unique applications of this polymer in electrical systems [127-129] , which can benefit from efficient heat dissipation. In particular, we show that expanded graphite/polymer composites prepared through solvent casting can lead to more efficient heat transfer due to an almost continuous network of graphitic sheets over long−length scales, which overcomes the problem of low interfacial thermal conductance at graphene–graphene contact in typical percolation environments. We have measured a composite thermal conductivity of 6.6 $Wm^{-1}K^{-1}$ at just 10 wt% filler concentration. This value represents the highest *k* value measured in a polymer composite at this low weight fraction of filler. Presented results provide new avenues for achieving efficient thermal management in a wide range of applications.

Intercalation of acid molecules and oxidizing agents into graphite followed by rapid heating (900 °C) causes intercalated agents to gasify, producing enough pressure to push the adjacent graphite layers apart, resulting in expanded graphite (Figure 3.1a). Figure 3.1b shows the graphite intercalated compounds (GICs), while Figure 3.1c shows expanded graphite with a worm−like structure. EG achieved through such expansion has a highly porous (Figure 3.1d,e), lightweight structure with a very low density (0.002–0.02 gcm^{-3}) and exhibits high mechanical strength (10 MPa), thermal conductivity (25–470 $Wm^{-1}K^{-1}$), and electrical conductivity (10^6–10^8 Scm^{-1}) [130]. As a result, EG has emerged as a promising material with applications such as flame retardancy [131], phase−change material[132,133] , electrodes [26,134], electrochemical sensors [135], fuel cells [136,137], batteries [138,139]and supercapacitors [140,141].

Significant research has been performed into the use of EG in enhancing the thermal conductivity of polymer graphene nanocomposites. Wu *et al.* [142] measured the thermal conductivity of individual expanded graphite particles using a T−type method and reported a value ~335 $Wm^{-1}K^{-1}$ for EG particles. Tao *et al.*[143] prepared EG/PDMS composite using a hot−press technique and reported a high thermal conductivity value of 4.7 $Wm^{-1}K^{-1}$ at 10 wt% EG composition. Zhao *et al.* [144] measured a high thermal conductivity of 3.5 $Wm^{-1}K^{-1}$ in EG/paraffin wax composites at 25 wt% composition. Song *et al.* [145] measured a thermal conductivity of 1.66 $Wm^{-1}K^{-1}$ at 20 wt% composition in EG/$MgCl_2 \cdot 6H_2O$ composite. Wei *et al.* [146] created a network of expanded graphite particles using stearic acid and polyethylene wax and measured a high thermal conductivity of 19.6 $Wm^{-1}K^{-1}$ using ~25 vol% expanded graphite. Che *et al.* [147] employed synergistic effects between expanded graphite and carbon nanotubes to achieve a high thermal conductivity of ~3.0 $Wm^{-1}K^{-1}$ at ~20 t% composition in high−density polyethylene (HDPE) composites.

In this work, we show that expanded graphite can lead to a remarkable increase in the thermal conductivity of polyetherimide composites prepared via the approach of solvent casting. Expanded graphite has a highly porous structure with interconnected graphitic walls, as seen in the SEM image of expanded graphite in the air in Figure 3.1e. Figure 3.1f shows the separation of adjacent graphite layers, which occurs due to the release of gases during the expansion procedure. Such a porous structure is absent in graphene nanoplatelets, also used in this work, and presented in Figure 3.1g. The graphitic sheets form a continuous network over long−length scales, allowing efficient conduction of heat. The approach of solvent casting offers the advantage of preserving this porous structure of expanded graphite as seen in the field emission environmental scanning electron microscopy (FE−ESEM) images of expanded graphite while it is embedded in the polymer

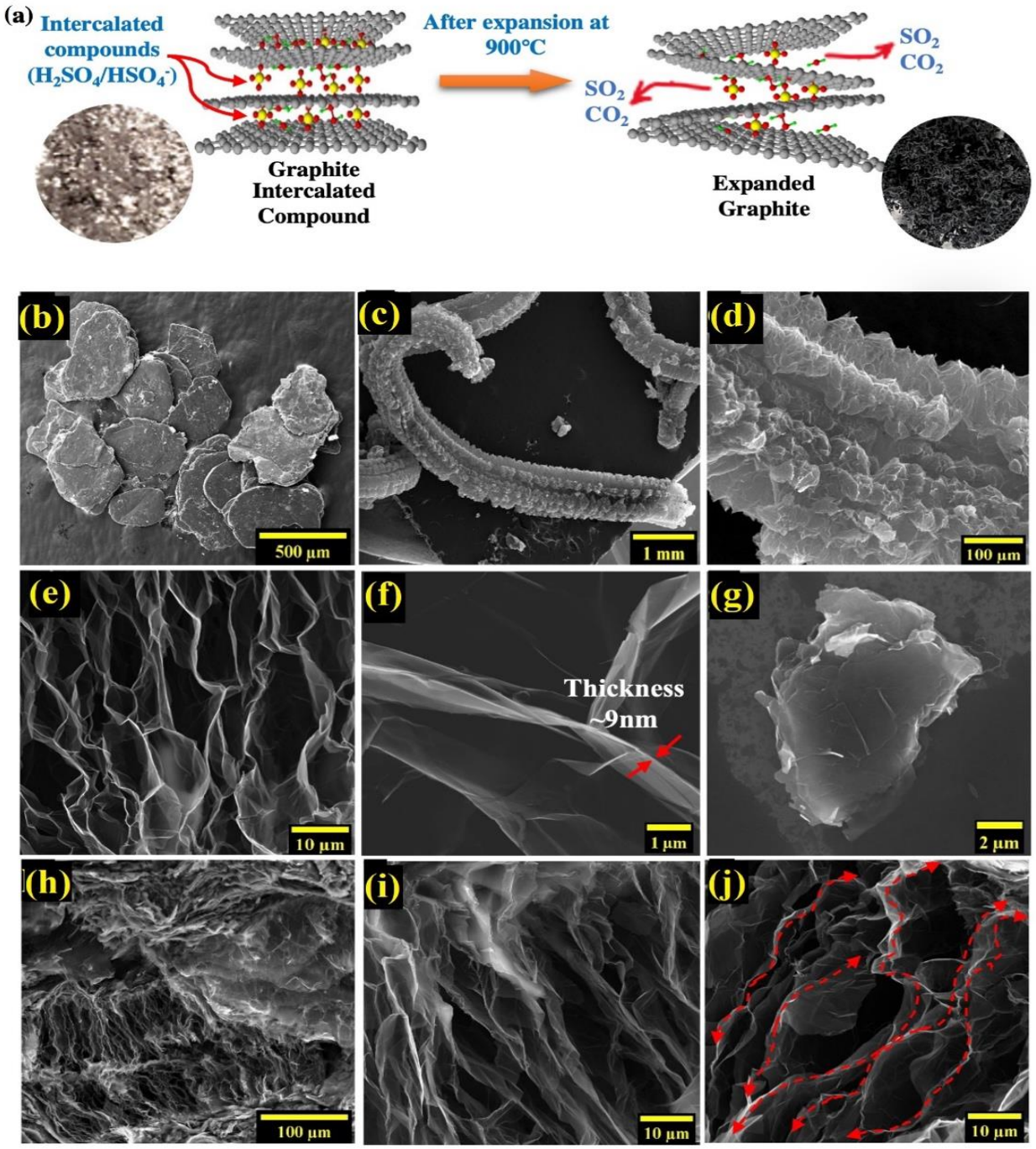

Figure 3.1 a) Schematic illustration of expanded graphite from graphite intercalated compounds through thermal expansion. SEM image of b) GIC, c) expanded graphite after thermal expansion. High−resolution FE−ESEM images of EG at magnification of d) ×100, e) ×1500, f) ×12,000, g) FE−ESEM images of 60 nm graphene nanoplatelet. FE−ESEM images of EG/PEID composite at h) ×350, (i & j) ×3500.

composite, in Figure 3.1h–j. The comparison of Figure 3.1e (showing EG in the air) and Figure 3.1h–j (showing EG in the composite) clearly show that the porous structure of EG is retained within the composite. This is due to the use of solvent casting, which does not exert large forces on expanded graphite, preserving its porous structure, unlike microcompounding, where large shear forces distort this structure [146,148]. Such a porous structure gets infused with the dissolved polymer during the casting process resulting in a highly thermally conductive interpenetrating network of graphene and polymer.

The resulting interpenetrating polymer graphene structure from the solvent casting method allows for very efficient heat transfer. This can be seen by observing that graphitic nanosheets in this network are continuous for very long−length scales (the lateral dimensions of these expanded graphite particles can range from a few hundred to thousands of microns), as shown in Figure 3.1j (arrows indicate heat flow over long continuous paths). The high in−plane thermal conductivity (k ~ 2000 $Wm^{-1}K^{-1}$)[38] of graphene nanosheets forming this network allows very efficient heat transfer over long−length scales, resulting in high composite thermal conductivity. We later show through X−ray diffraction and Raman analysis that the graphitic layers forming the walls of this network retain the chemical structure and exact interlayer spacing of graphite and can thus be expected to have the high thermal conductivity values reported for graphite nanoplatelets (k_{in} ~ 2000 $Wm^{-1}K^{-1}$, and k_{out} ~ 10 $Wm^{-1}K^{-1}$) [38] .

A unique advantage of this continuous network can be understood by noticing that even at bends/turns, the graphitic sheets are still continuous, allowing for a very high thermal conductance (low interfacial thermal resistance) at such junctions. The above effect of low interfacial resistance at bends/turns in an expanded graphite network offers an advantage over the effect of percolation[113,120,147,149-151]. Percolation involves enhancing heat transfer through establishing

discrete particle–particle contact resulting in efficient heat conduction along a network of graphene particles. While this enhances thermal conduction by bypassing the low thermal conductivity polymer, the interfacial thermal resistance at the contact between discrete graphene particles in percolative networks can still be significant. Konatham *et al.* [152] performed molecular dynamics simulations to show that thermal contact resistance at graphene–graphene contact is 5.5×10^{-8} K/W, which is comparable to graphene−polymer interfacial thermal resistance[45]. In expanded graphite composites, however, the continuous nature of graphene sheets at bends/turns results in much more efficient interfacial thermal transport at junctions, resulting in a superior thermal conductivity enhancement overall. Another advantage of expanded graphite−mediated *k* enhancement over percolation effect is that typically very high-volume concentrations are required to achieve particle–particle contact for percolation. In the case of solvent−cast expanded graphite/polymer composites, however, the continuous graphitic networks are present at all volume fractions, enabling achieving high *k* even at low particle concentrations.

The polymers chosen for this work, namely polyetherimide and epoxy, enable the advantage of superior thermal interaction with graphene[73,153] . Both polyetherimide and epoxy have oxygen groups in their molecular structure that can enable strong thermal interaction through hydrogen bonding with the oxygen groups [154-156] in expanded graphene. Such oxygen groups are introduced in expanded graphite during intercalation (with an oxidizing agent) and the expansion process. Evidence for the presence of oxygen groups in expanded graphite is provided through X−ray photoelectron spectroscopy (XPS)[157-159] .

We further investigated the effect of sonication parameters on thermal conductivity enhancement and showed that lower sonication time and power result in larger expanded graphite particles in the composite, which allows for heat to be conducted efficiently along longer lengths

scales, resulting in higher thermal conductivities. Finally, we also compare the measured thermal conductivity results with a recently introduced effective medium model that takes graphene–graphene contact into account for thermal conductivity prediction.

3.2 EXPERIMENTAL DETAILS

3.2.1 Materials

Graphite intercalated compound (GIC) or expandable graphite (EPG), with an average particle size of ≥ 180 μm (+100 mesh size: ~92%) and expansion ratio 290:1 (ASB−3570), were bought from a graphite store[160] . Graphene Nanoplatelets AO−4 (60 nm thickness and lateral size < 7 μm) were acquired from a graphene supermarket [161] . The epoxy resin used for the study was EPIKOTE RESIN MGS RIMR 135, and the hardener used was EPIKURE CURING AGENT MGS RIMH 137, both purchased from Hexion[162] . Commercially available N, N−dimethylacetamide (DMAC), and polyetherimide (PEID) with a melt index of 18 g/10 min (337 °C/6.6 kg) and a density of 1.27 g/mL were obtained from Alfa Aesar [163] and Sigma Aldrich [164]. The organic solvents N−N, Dimethylformamide (DMF), and Acetone were purchased from the University of Oklahoma chemical stock room.

3.2.2 Fabrication of the EG/Polymer Composites

The fabrication procedure of the EG/PEID composite is illustrated in Figure 3.2a and the chemical structure of PEID is presented in Figure 3.2b. For EG/PEID composite preparation, expandable graphite was first placed into a furnace at 900 °C for approximately 30–60 s in a crucible to obtain the required quantity of EG filler. EG so obtained was then dispersed into 20 mL DMAC. Separately PEID pellets were dissolved into 50 mL DMAC at 130 °C for 1 h.. The DMAC solution with EG was mixed with a polymer solution and blended for 3 h at 130 °C,

followed by a short−time (~40 s) probe sonication at 20% amplitude using probe−sonicator (VCX 750 Sonicator, PRO Scientific Inc., Oxford, Connecticut, USA; power output: 750 W, frequency: 20 kHz). The EG blended with a polymer solution of ~25–30 mL was cast into a petri dish. Lastly, the petri dish was kept at 100 °C for 24–48 h to produce the composite film. Likewise, 2.5 wt%, 7.5 wt%, and 10 wt% EG/PEID composite films were prepared using this same procedure. For comparison, the graphene nanoplatelet (GnP)/PEID composite films were also prepared using the same solution casting technique for graphene with 60 nm thickness, respectively.

To prepare epoxy/expanded graphite composites, resin was added to 90 mL N,N−dimethylformamide (DMF) solution and stirred while heating at 150 °C to obtain a homogeneous mixture. Expanded graphite was added to this solution and stirred for one hour. The solution was then tip sonicated for 40 s followed by stirring at 150 °C until the solvent completely evaporated. After the solvent evaporated, a thick mixture of EG/epoxy was obtained. This mixture was then spread over a PTFE sheet and kept in a vacuum oven at 140 °C for 15 h to remove any residual solvent present in the mixture. On cooling the mixture to room temperature, a hardener was added to it and mixed to obtain a homogeneous viscous paste. This paste was then transferred to aluminum molds and cured at 90 °C for 20 h.

3.3 CHARACTERIZATION

Thermal Conductivity (*k*): *k* of EG/polymer composites was measured by the laser flash technique. A Netzsch LFA 467 Hyperflash (Netzsch, Selb, Germany) laser was used to measure the through−thickness thermal diffusivity of the samples. We measured average thermal diffusivity

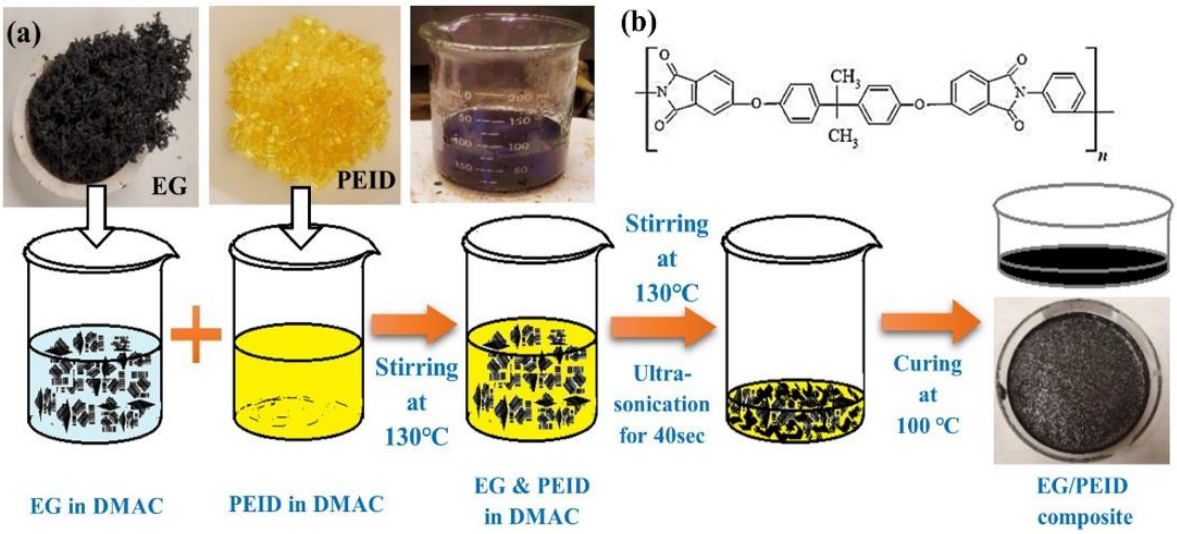

Figure 3.2 a) Schematic for the preparation process of EG/PEID composites, b) chemical structure of PEID.

(α) of 8–12 samples of 12.5 mm diameter and 0.3–0.4 mm thickness at room temperature (23 °C). The samples were coated with graphite spray before the measurement to efficiently absorb heat from a flash lamp, and an average of 6–8 measurements was reported. This laser flash technique induces heat by a laser pulse on one surface of the sample, and the temperature rise is captured on the other surface of the sample as a function of time. α is determined by LFA using the following equation: $\alpha = (0.1388\ d^2)/t_{1/2}$, where α is the thermal diffusivity (mm^2/s), $t_{1/2}$ is the time to obtain half of the maximum temperature on the rear surface, and d denotes the sample thickness (mm). The thermal conductivity was calculated using $k = \alpha \times \rho \times Cp$, where k, ρ, and Cp represent the thermal conductivity, density, and specific heat constant of the sample, respectively. In this work, the density and specific heat of the composite samples were calculated using a gas pycnometer

(AccuPyc II 1340, Micromeritics Instrument Corporation, Norcross, Georgia, USA) and differential scanning calorimetry (DSC) (DSC 204F1 Phoenix, Netzsch, Selb, Germany).

Scanning Electron Microscopy (SEM): Morphological characterization of EG filler and EG/polymer composites was carried out by high−resolution field emission environmental scanning microscopy (Quattro S FE−ESEM, Thermofisher Scientific, Waltham, Massachusetts, USA). This SEM was operated in secondary electron (SE) mode at an accelerating voltage of 20 kV. To prepare the samples for SEM imaging, liquid nitrogen was used to crack down the composite to image over the cross−sectional area. Montage large area mapping of EG fillers has been captured using MAPS software of FE−ESEM.

Raman Spectroscopy: Raman spectroscopy was performed using a DXR3 SmartRaman Spectrometer (Thermofisher Scientific, Waltham, Massachusetts, USA) to collect the data over the range from 3250 to 250 cm^{-1}, laser wavelength λ_L = 633 nm, spectral resolution = 0.16 cm^{-1}, and imaging resolution = 702 nm for the EG and GIC samples. An Olympus BX 41 microscope with 5× objective, 10 s exposure time for 15 accumulations, and 3 scans per sample were used to collect the spectra.

X−ray Diffraction (XRD): A PANalytical Empyrean Diffractometer (Malvern Panalytical Ltd., Grovewood Rd, Malvern WR14 1XZ, United Kingdom) produced the information regarding the crystal structure of EG compared to GIC using Bragg−Brentano focusing geometry at room temperature. A total of 3 kW Cu Kα radiation (λ = 1.5406 Å) with a scan range of 2θ = 5 to 80°and step size of 0.013°.

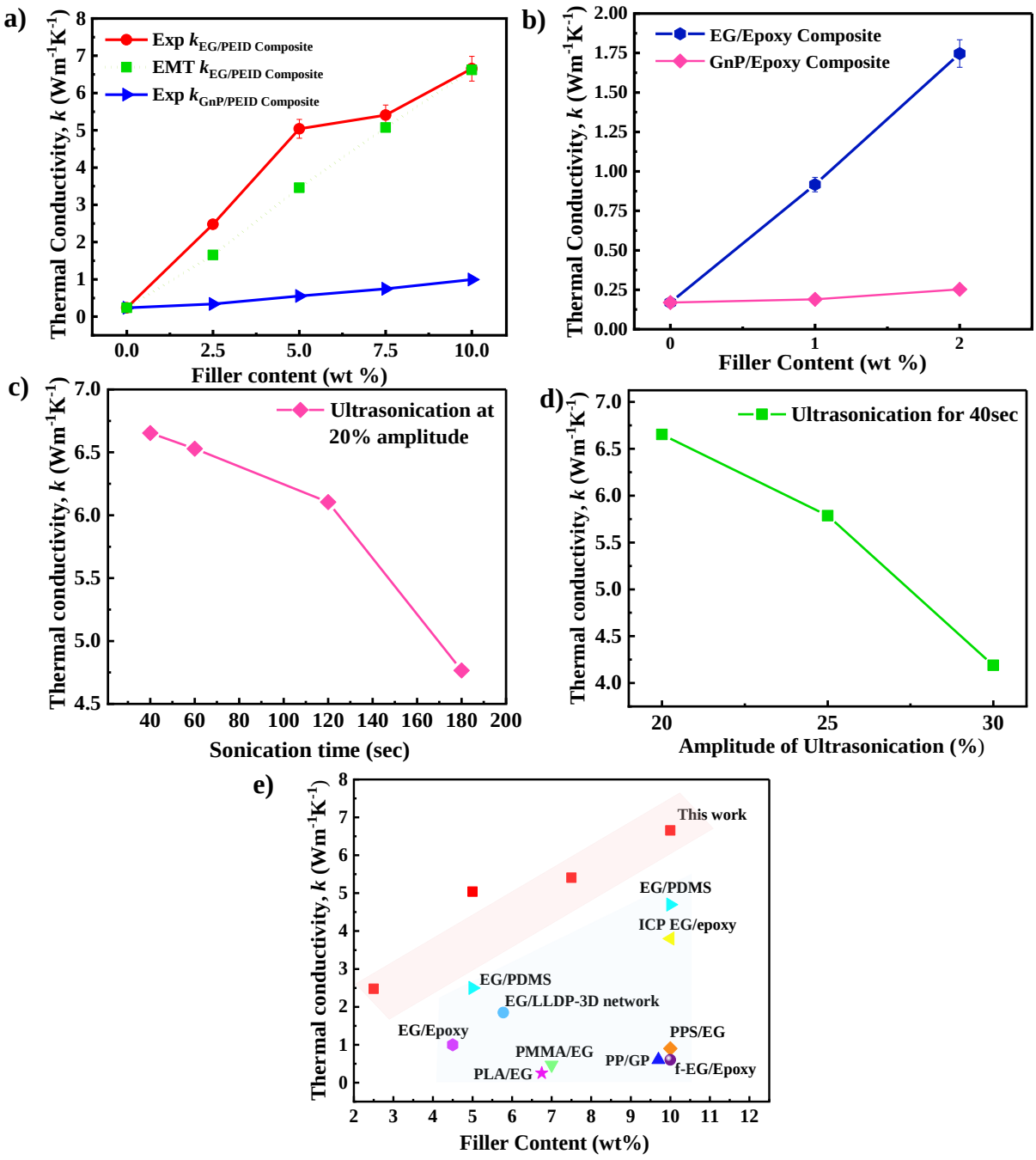

Figure 3.3 *k* value of a) EG/PEID (experimental and effective medium theory (EMT)) and GnP/PEID composite with different filler content (2,5, 5, 7.5 & 10 wt%), b) EG/epoxy and GnP/epoxy composite with different filler content (0.5, 1, 1.5, and 2 wt%), c) EG/PEID composite with different sonication time at 20% ultrasonication power, d) EG/PEID composite with different ultrasonication power sonication for 40 s. e) Comparison of *k* value of polymer composites in previous works.

X−ray Photoelectron Spectroscopy (XPS): X−ray Photoelectron Spectroscopy (XPS) was performed for GIC and EG samples by Thermo Scientific K−alpha XPS (Thermofisher Scientific, Waltham, Massachusetts, USA). A Kα gun source was used to excite the sample, and the data were collected for an acquisition time of ~70 s at 400 µm spot size. The passing energy of 200 eV was used to find the carbon c), oxygen(O), and sulfur (S) peak in this analysis spectrum. The atomic percentage of C, O, and S were investigated using the Avantage software. To determine the atomic percentage, this software was used to perform the curve fitting in accordance with Gaussian and Lorentzian functions.

3.4 RESULT AND DISCUSSION

3.4.1 Thermal Conductivity Results

The measured thermal conductivities of EG/PEID and EG/epoxy composites are shown in Figure 3.3 a & b. Thermal conductivity of solvent−cast EG/PEID composites is measured to be around 6.6 $Wm^{-1}K^{-1}$ at 10 wt% filler composition. This value represents a remarkable 2770% enhancement over the *k* (0.23 $Wm^{-1}K^{-1}$) of pristine PEID, providing new avenues for high thermal conductivity composites. Similarly, the measured thermal conductivity of EG/epoxy composites also shows remarkable enhancement at very low loadings of EG. At just 2 wt% EG composition, a thermal conductivity value of 1.74 $Wm^{-1}K^{-1}$ is achieved for the epoxy composite, representing an enhancement of 1025% over pristine epoxy (0.16 $Wm^{-1}K^{-1}$). Table 3.1 and Figure 3.3e show that the measured value is significantly higher than similar graphene/polymer composites either based on a) uniformly dispersed graphene, b) other expanded graphite−based methods, and c) graphene−based percolative networks.

We first compare the measured values against previous results reported for the percolation effect based on establishing a graphene–graphene network. A key advantage of expanded graphite is that a large enhancement in *k* value is achieved even at low graphene loading, as opposed to the case of percolation, where typically much higher particle concentrations are required to achieve particle–particle contact. Kargar *et al.* achieved around 6 $Wm^{-1}K^{-1}$ in graphene/epoxy composites

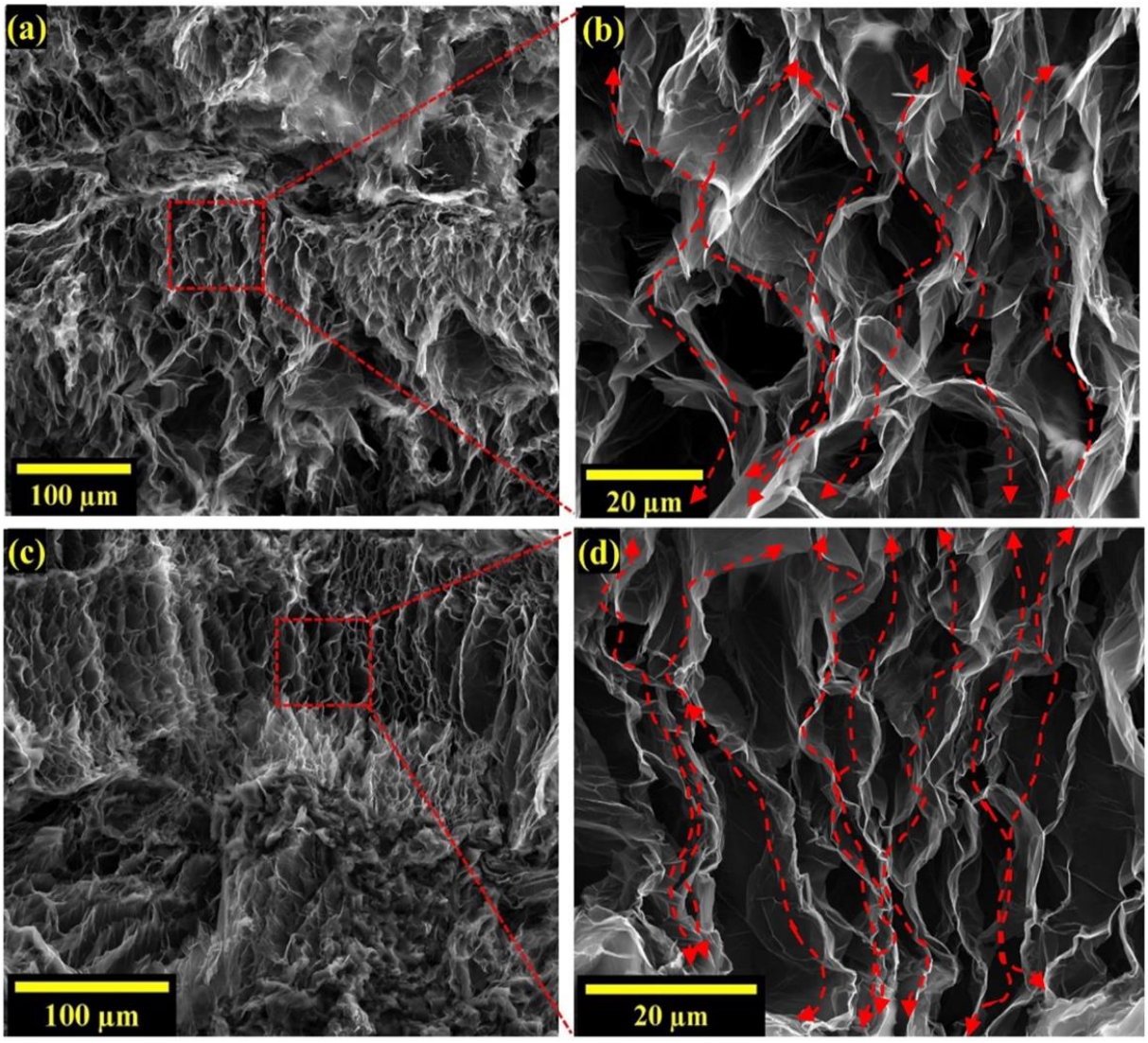

Figure 3.4 FE−ESEM images of EG/PEID composites with (a,b) 7.5 wt%, (c,d) 10 wt% fabricated at 20% amplitude for 40 s ultrasonication; (a,c) 350× magnification, (b,d,) 3500× magnification.

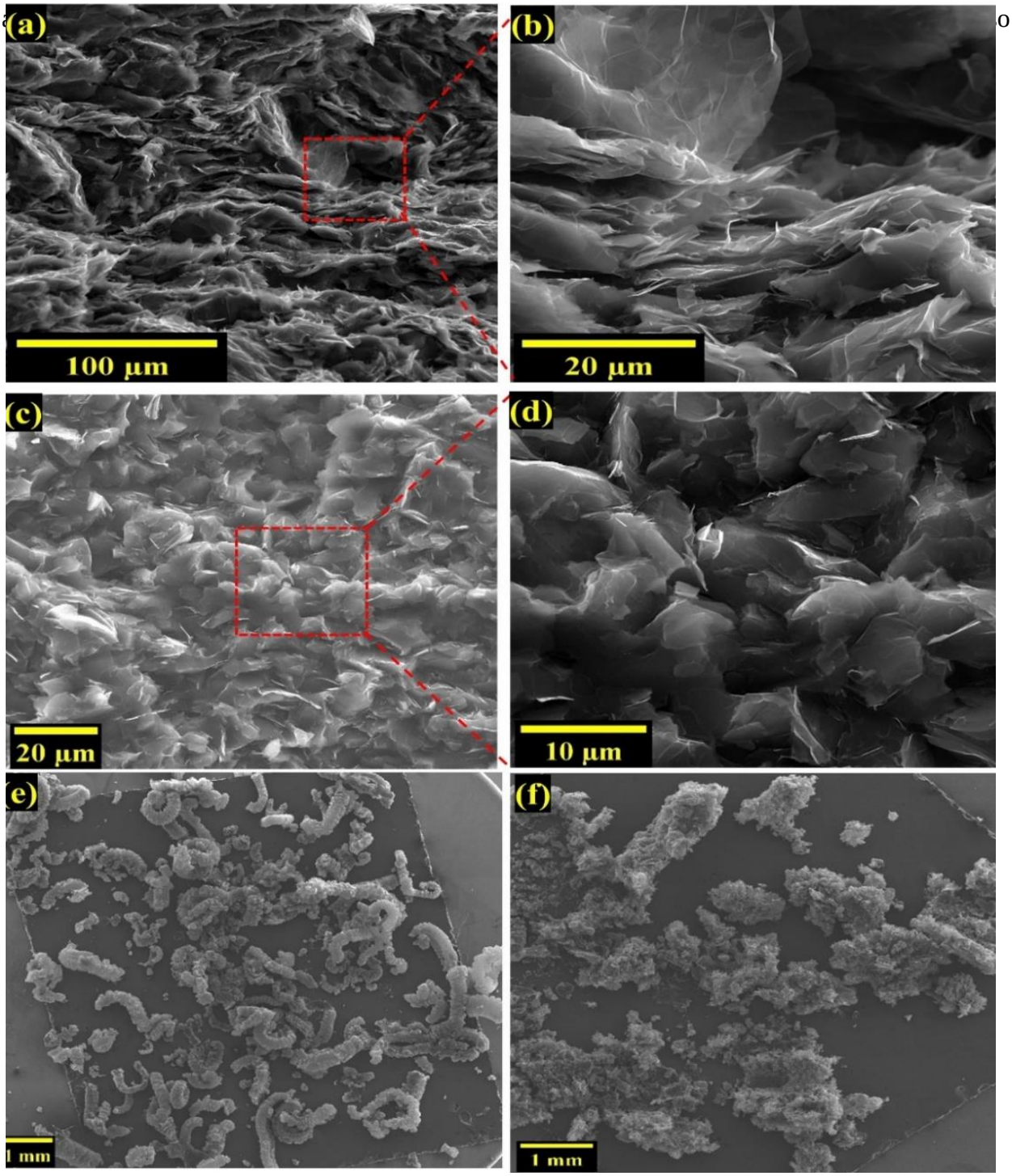

Figure 3.5 FE−ESEM images of (a,b) 10 wt% EG/PEID composite with ultrasonication for 3 min at 20% amplitude, (c,d) 10 wt% GnP/PEID composite with ultrasonication for 40 s at 20% amplitude; FE−ESEM images of EG at 20% sonication for (e) 40 s and (f) 3 min using montage large area mapping.

found to yield a thermal conductivity of ~5.5 $Wm^{-1}K^{-1}$ in Boron–Nitride/epoxy composites [120]at a volume loading of 45 vol%. A high *k* of 6.6 $Wm^{-1}K^{-1}$ is achieved in this work through the use of just 10 wt% EG content. Even in percolative *k* enhancement, the thermal interfacial resistance at particle–particle contact can be relatively high. Konatham *et al.* reported a thermal boundary resistance of 5.5×10^{-8} K/W, almost as high as at the graphene−polymer contact [152]. Expanded graphite, achieved through the solvent casting approach, leads to continuous graphite networks (Figure 3.4a-d), overcoming the issue of low particle–particle interfacial thermal conductance in percolative environments. Significant enhancement in *k* value of EG/PEID composite has been achieved due to such continuous graphitic network of EG as presented in Figure 3.4b,d throughout the composite film.

The higher *k* achieved in this work is also due to the use of solvent casting, which offers the advantage of preserving the porous structure of expanded graphite within the composite (seen in Figure 3.1 f, i & j). This is due to only moderate forces being exerted on expanded graphite during the solvent casting approach. Figure 3.1 f &,i compare the porous structure of expanded graphite before and after it is embedded into the composite and show that the porous structure of EG is largely retained within the composite. This is in contrast to microcompounding (melt‑blending), where large shear forces during the compounding process can exfoliate expanded graphite, converting it into a nanoplatelet‑like morphology. Mokhtari *et al.* [165] discussed such exfoliation of expanded graphite through microcompounding.

We also compare measured *k* values of EG/PEID composite with those of GnP/PEID composites in Figure 3.3a & b. The measured thermal conductivity of EG/PEID composites is dramatically higher relative to that achieved using graphite nanoplatelets. At 10 wt% composition, the *k* of EG/PEID composite (6.6 $Wm^{-1}K^{-1}$) is higher by 572% relative to GnP/PEID composite

(1.0 $Wm^{-1}K^{-1}$). Similarly, at 2 wt% composition, *k* of EG/epoxy composite (1.74 $Wm^{-1}K^{-1}$) is higher by ~600% relative to GnP/epoxy composite (0.25 $Wm^{-1}K^{-1}$). At the low graphene content used in this work, GnPs are well separated by polymer; high interfacial thermal resistance between GnPs and polymer then restricts the enhancement achievable through the use of graphene nanoplatelets. These results highlight the large advantage of expanded graphite over graphene nanoplatelets in enhancing composite thermal conductivity.

We further investigated the effect of sonication parameters used during composite preparation on *k* enhancement. Figure 3.3c,d show that lower sonication time and amplitude lead to the higher thermal conductivity of EG/PEID composite. To understand the effect of sonication parameters on the structural integrity of EG, we performed an FE–ESEM analysis. As the porous interpenetrating network has a beneficial impact on thermal conductivity enhancement (shown in Figure 3.4a–d), high–resolution images are obtained to visualize the effect of sonication time on this porous network structure (Figure 3.5a,b). The image of 10 wt% EG/PEID composite (Figure 3.5a,b) prepared with 3 min sonication time at 20% amplitude shows an absence of porous structure within the composite, suggesting that longer sonication time causes the porous structure to be damaged. FE–SEM images of 10 wt% GnP/PEID composite are also presented in Figure 3.5c,d.

Table 3.1 Comparison of $k_{\perp}$ for different polymer graphene and EG−polymer composite.

Filler	Matrix	Fraction	$k_{\perp}$ ($Wm^{-1}K^{-1}$)	k_{matrix} ($Wm^{-1}K^{-1}$)	Enhancement (%)	Preparation Method	Ref.
GnPs/MWCNT	PS	(3.5/1.5) vol%	1.02	0.19	437	Melt mixing + Synergistic effect	166
Graphite	PP	40 wt%	5.4	0.25	2060	Compression molding	167
Multilayer GnP	Epoxy	10 vol%	5.1	0.21	2300	Solvent casting, higher sheer mixing	45
fGO	Epoxy	5 wt%	0.21	0.16	34	Solution casting	168
EG	LLDP	5.78 wt%	1.85	0.33	461	Melt mixing, 3D network formation	146
EG	PMMA	7 wt%	0.47	0.125	276	Water–−−assisted melt extrusion	169
EG	LDPE	10 wt%	0.5	0.32	56	Melt mixing	170
EG	PDMS	10 wt%	4.7	0.18	2511	Solvent casting, hot press	143
EG	PEG	10 wt%	1.324	0.298	344	Melt mixing	171
EG	Paraffin	25 wt%	3.16	0.18	1695	Melt mixing	144
EG	PEID	30 wt%	1.6	0.2	700	Solvent mixing, melt mixing followed by injection molding	172
EG	PEID	10 wt%	6.6	0.23	2770	Solution casting	This work

PS—polystyrene; PP—polypropylene; PMMA—Poly(methyl methacrylate); LDPE—low−density polyethylene; PDMS—polydimethylsiloxane; PEG—Polyethylene glycol.

While the above images show the expanded graphite embedded in the polymer, we also show expanded graphite before it is embedded into the polymer in Figure 3.5e,f. These images show that fragile, porous graphite is broken into nanosheets after 3 min sonication time, whereas 40 s sonication time has a negligible effect on EG filler structure. Short−time sonication thus offers the advantage of preserving the structure of expanded graphite while also allowing uniform dispersion into the polymer matrix.

In the next section, we compare measured *k* values of EG/PEID composite with theoretical predictions based on a recently introduced effective medium model by Su *et al.* [173] . Comparison with theoretical predictions highlights the advantage of expanded graphite and provides evidence for the outlined mechanism of heat conduction along continuous graphitic paths.

3.4.2 Effective Medium Model for Thermal Conductivity Prediction

The effective medium model introduced by Su *et al.* [173]includes the effect of both graphene−polymer and graphene–graphene thermal contact resistance. Effective composite thermal conductivity k_e through this model is computed by solving the following equation:

$$c_0\frac{k_0-k_e}{k_e+(k_0-k_e)/3}+\frac{c_1}{3}\left[\frac{2(k_{11}-k_e)}{k_e+S_{11}(k_0-k_e)}+\frac{(k_{33}-k_e)}{k_e+S_{33}(k_3-k_e)}\right]=0 \qquad (3.1)$$

where c_0 and c_1 are the concentrations of the embedding matrix and filler material, respectively, k_{11} and k_{33} are the effective in−plane and through−plane thermal conductivities of graphitic nanosheets. The effective thermal conductivities take into account the effect of interfacial thermal resistance. S_{11} and S_{33} are the shape parameters related to the aspect ratio of graphitic nanosheets, given by the following equations.

$$S_{11}=S_{22}=\frac{\alpha}{2(1-\alpha^2)^{3/2}}\left[\arccos\alpha-\alpha(1-\alpha^2)^{1/2}\right],\ \alpha<1$$

$$S_{33}=1-S_{11}$$

In the above equations, α is the aspect ratio (thickness/lateral dimension) of the graphitic nanosheets, and k_0 is the thermal conductivity of an interlayer surrounding graphene sheets. The role of this interlayer is to include the effect of interfacial thermal resistance at graphene−polymer and graphene–graphene contacts.

The effective thermal conductivities k_{11} and k_{33} are computed using the in−plane and through−plane thermal conductivities of graphene (k_1 and k_3, respectively) and the interlayer properties through the following equations,

$$k_{11} = k_0[1 + \frac{(1-c_{int})(k_1-k_0)}{c_{int}S_{11}(k_1-k_0)+k_0}] \quad (3.2)$$

$$k_{33} = k_0[1 + \frac{(1-c_{int})(k_3-k_0)}{c_{int}S_{11}(k_3-k_0)+k_0}] \quad (3.3)$$

In the above equations, c_{int} is the concentration of the interlayer. The values of different parameters used in this effective medium model are described below.

Table 3.2 The values of different parameters used in EMT calculations.

Material Parameters	Values
Average graphene lateral length, l,	10 μm
Average graphene thickness	10 nm
Aspect ratio of the graphene filler	0.001
Thermal conductivity of polymer phase $Wm^{-1}K^{-1}$	0.23
Thermal conductivity of graphene filler, k_1 and k_3, $Wm^{-1}K^{-1}$	2000 and 10
Thermal conductivity of interlayer with Kapitza resistance, $Wm^{-1}K^{-1}$	0.04
Thermal conductivity of the interlayer with a firmly developed graphene–graphene contact state, $Wm^{-1}K^{-1}$	0.17

In the Table 3.2, graphene thickness and length are the thickness and length of the graphitic sheets forming the walls of the interpenetrating network. Average values of these parameters were obtained from microscopy to be 10 μm for lateral length and 10 nm for thickness. The thermal conductivity of the polymer phase is taken to be 0.23 $Wm^{-1}K^{-1}$ from our measurements (in suitable agreement with the literature). The in−plane (k_1) and through−plane thermal conductivities (k_3) of graphene were taken to be 2000 $Wm^{-1}K^{-1}$ and 10 $Wm^{-1}K^{-1}$, respectively[38,174].

The interfacial resistance between graphene and polymer is modeled as an interlayer in the above theory. The thickness of this interlayer was nominally taken to be 2 nm, and its thermal conductivity was assumed to be 0.04 $Wm^{-1}K^{-1}$, resulting in an interfacial resistance between graphene and polymer of 5×10^{-8} m^2K/W[45], a well−accepted value for interfacial thermal resistance between graphene and polymer.

A key parameter in the above model is the interfacial resistance at graphene–graphene contact. This value was determined by fitting the measured values to the effective medium model. A suitable agreement between measured thermal conductivities and predicted values was obtained by using a graphene–graphene interlayer thermal conductivity of 0.17 $Wm^{-1}K^{-1}$ (see Figure 3.3a and Figure 3.6), which is more than four times higher than the interlayer thermal conductivity of polymer graphene (0.04 $Wm^{-1}K^{-1}$). This interlayer thermal conductivity of 0.17 $Wm^{-1}K^{-1}$ at graphene–graphene contact corresponds to a graphene–graphene interfacial thermal resistance of 1.17×10^{-8} m^2K/W. This value is significantly smaller than the interfacial resistance predicted for regular graphene–graphene contact [152] (5×10^{-8} m^2K/W), providing evidence that graphene sheets are in superior contact (covalently bonded) at bends/turns in an expanded graphite network, compared to the contact between discrete graphene particles. The analysis points to the advantage of the continuous graphitic network achieved through the use of expanded graphite via solvent casting technique in enhancing the thermal conductivity of polymer composites. We further show the effect of lower graphene–graphene contact conductance by decreasing the graphene–graphene

contact thermal conductivity in the model. It is seen that as the graphene–graphene contact thermal conductivity is decreased from 0.17 to 0.10, the effective composite thermal conductivity is decreased from 6.6 $Wm^{-1}K^{-1}$ to 4.4 $Wm^{-1}K^{-1}$ (by almost 33.3%), indicating the importance of

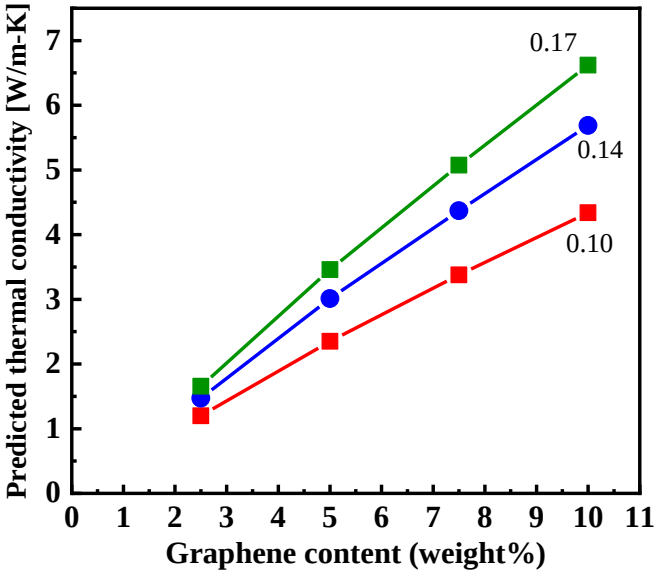

Figure 3.6 Predicted thermal conductivity value based on the effective medium theory (EMT) with different graphene–graphene interlayer thermal conductivity.

superior graphene–graphene contact conductance for achieving overall high composite *k* values. We next discuss the characterization of EG filler and EG/PEID composites.

3.4.3 Morphologies of EG Filler and EG/PEID Composite

Analysis through FE–ESEM reveals the structural integrity of EG structure before and after the preparation of polymer composite. SEM (Scanning electron microscopy) images enable understanding of morphological differences between graphene nanoplatelets (GnPs), Graphene Intercalation compound (GIC), and thermally expanded graphite (EG) (Figure 3.1a). Thermal expansion of GIC with an average diameter of ~180 μm and thickness of 1–150 μm turns it into a worm–like structure. Uneven expansion resulting from the expansion of the intercalation compound at 900 °C leads to the separation of expandable graphite into multiple layers resulting

in a porous network with an average edge size of 10–20 μm. These pores allow the formation of the interpenetrating graphene–polymer network where the pores are wetted with PEID polymer. While Figure 3.1f shows expanded graphite before it is used to prepare composite, FE–SEM also is used to study the structure of EG even within the polymer composite. EG structures in EG/PEID composites with 7.5 and 10 wt% filler are presented in Figure 3.4a–d. These figures show that solvent casting clearly preserves the porous network structure of expanded graphite, enabling the creation of the highly thermally conductive interpenetrating graphene–polymer network within the composite.

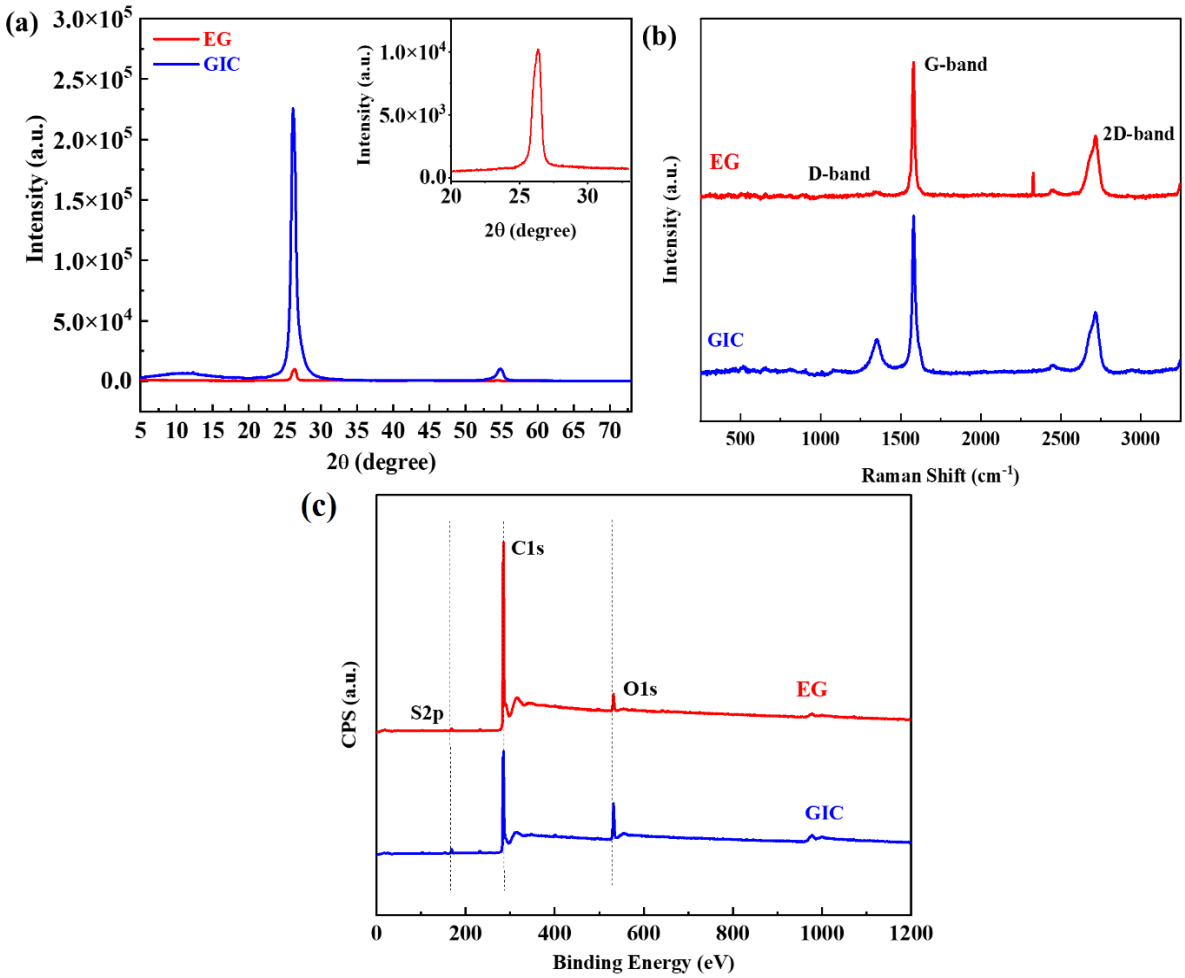

Figure 3.7 XRD spectra a), Raman spectra b), and XPS spectra c) of GIC and EG filler.

3.4.4 Analysis of Crystal Structure by XRD and Raman Spectroscopy

X–ray diffraction (XRD) analysis was performed to determine the crystal structure and interlayer spacing of GIC and EG. Figure 3.7a shows a strong diffraction peak at 2θ = 26.133° (002) for GIC, slightly shifted from the case of natural graphite 2θ = 26.5° [175-178] . A weaker peak (004) is observed at 2θ = 54.37°[179] for GIC. The small shift in peak for GIC is attributed to the presence of intercalated compounds. On the contrary, a reduced sharp peak is visible at 2θ= 26.35° (002) [180] for EG (the inset of Figure 3.7a), closer to the (002) graphitic carbon structure. A clear diminution is observed in the intensity at (002) peak, which is caused due to disorder in graphitic morphology[181] after the expansion process. Still, a mostly aligned peak position in EG indicates the existence of intact chemical structure of graphite and interlayer order [182,183].This interconnected and stacked structure of EG enables better thermal transport throughout the polymer composite [124]

Nondestructive Raman analysis was also performed to further analyze the crystal structure before and after the thermal expansion. Raman spectroscopy of Figure 3.7b exhibits two inherent peaks of G band and D band at ~1580 cm^{-1} and ~1350 cm^{-1} for graphitic material [184]. The G band signifies the stretching of defect−free sp^2 carbon of hexagonal ring due to in−plane tangential stretching of the carbon-carbon bonds [185], and the D band represents the vibrational mode caused by the amorphous disordered structure of sp^3 hybridized carbon [157].The 2D band also can be seen at around 2700 cm^{-1} and represents a second−order two−photon process [186]. Raman spectra of GIC clearly show those characteristic peaks (G, D, and 2D bands). In contrast, G and 2D bands are present, but the presence of the D band is negligible in EG Raman spectra. I_D/I_G ratio is typically used to characterize the defective state of graphene. The absence of a D band in EG suggests the presence of a highly ordered defect−free graphite structure in EG. This high degree of the ordered structure of graphite, even after thermal expansion, has a strong beneficial impact on the thermal

conductivity enhancement of polymer graphene composite as it preserves the intrinsic high thermal conductivity of graphene itself.

3.4.5 XPS Analysis of GIC and EG Filler

XPS analysis was further performed to investigate the concentration of carbon c), oxygen (O), and sulfur (S) elements before and after the thermal expansion of GIC, as presented in Table 3.3. Figure 3.7c shows that two peaks of C1s and O1s at ~285 eV and ~532 eV are present for GIC and EG filler, but the S2p peak (~169 eV)[187] is only visible in GIC spectra because of the included intercalated compounds. The atomic percentage of carbon increases from 85.14% to 95.76%, and oxygen reduces from 13.16% to 4.24% after expansion. This is attributed to the fact that thermal expansion at 900 °C releases oxygen contents. The presence of small amounts of oxygen groups in EG allows favorable interactions with oxygen groups in PEID through hydrogen bonding, leading to efficient interfacial thermal transport. This further enhances the thermal conductivity of EG/PEID composite.

Table 3.3 Atomic composition by XPS analysis of EG and GIC.

Sample name	**Atomic Composition by XPS (at%)**		
	C (285.08 eV)	**O (532.08 eV)**	**S (169.11eV)**
GIC	85.14	13.16	1.7
EG	95.76	4.24	–

3.5 CONCLUSION

In summary, we demonstrate that expanded graphite (EG) can lead to a large enhancement in the thermal conductivity of EG/PEID composites prepared through solvent casting. At 10 wt% EG composition, a high thermal conductivity of 6.6 $Wm^{-1}K^{-1}$ is measured, representing an

enhancement of 2770% over pristine polyetherimide. This large enhancement in thermal conductivity is found to be due to a network of continuous graphene sheets over long−length scales achieved through the solvent casting technique, which preserves the interconnected porous structure of expanded graphite within the composite. Even at bends/turns in graphene sheets in such a network, the sheets are covalently bonded, which minimizes the interfacial thermal resistance at junctions, enhancing heat transfer. Overall, the resulting structure allows highly efficient heat conduction over long−length scales along the continuous graphitic sheets. This results in the observed high thermal conductivity of the composite through the use of EG. The thermal conductivity of EG/PEID composite is also found to dramatically exceed that of graphene nanoplatelet (GnP)/PEID composites by 572% for 10 wt% filler composition. At low filler loading, GnPs are well separated by polymer and the resulting high graphene−polymer interfacial thermal resistance results in low effective GnP/PEID thermal conductivity. Presented results highlight the advantage of expanded graphite in enhancing the thermal conductivity of polymer composites and can lead to novel avenues for achieving efficient thermal management in a wide array of technologies.

CHAPTER 4

Thermally expanded graphite polyetherimide composite with superior electrical and thermal conductivity

4.1 INTRODUCTION

Polymer materials offer advantages such as low cost, low weight, and excellent processability but exhibit poor electrical (10^{-18}- 10^{-7} Scm^{-1})[188] and thermal conductivity (<0.5 $Wm^{-1}K^{-1}$)[189]. To manufacture polymer composites with superior electrical and thermal performance, carbon-based fillers are typically added to the polymer matrix. These carbon fillers (such as graphene, carbon nanotubes) based polymeric composites have a wide range of applications, including sensors[190,191], electromagnetic interference shielding[192,193], batteries[194,195], supercapacitors[196,197], and functional materials[198,199].

The electrical conductivity of composites is significantly influenced by the composite preparation methods, embedded filler, dispersion quality, and size and amount of filler[200]. The addition of graphene nanoplatelets has been shown to significantly improve electrical conductivity[116,201-203]. However, graphene nanoplatelets within the composite are separated by the embedded polymer matrix having low electrical conductivity which leads to overall low composite conductivity. To achieve high electrical conductivity, it is desirable for graphene particles to be in contact with each other, leading to a percolative network. Graphene nanosheet (2D) or carbon nanotubes (CNT) with a rod or disk-like shape, can enable a continuous conductive network in

composites due to their high surface area and aspect ratio[204-206]. However, a drawback of this approach is the requirement of high filler concentrations to achieve the percolation threshold. 3D continuous networks using 2D fillers have been developed using chemical vapor deposition[207-210] or solution-based synthesis[211] for outstanding electrical and thermal properties of composites. Kashi *et al.*[212] reported an electrically percolative 3D network of graphene /polylactide (PLA) nanocomposite at 6–9 wt% graphene filler composition. In another study, Moghaddam et al[59] developed an interconnected 3D network within graphene oxide (GO)/epoxy composite using functionalized GO filler and demonstrated an increase in electrical conductivity due to successful 3D network formation. Such a 3D network of filler can be utilized for continuous electron transfer in composite, thus overcoming the barrier resulting from the polymer medium.

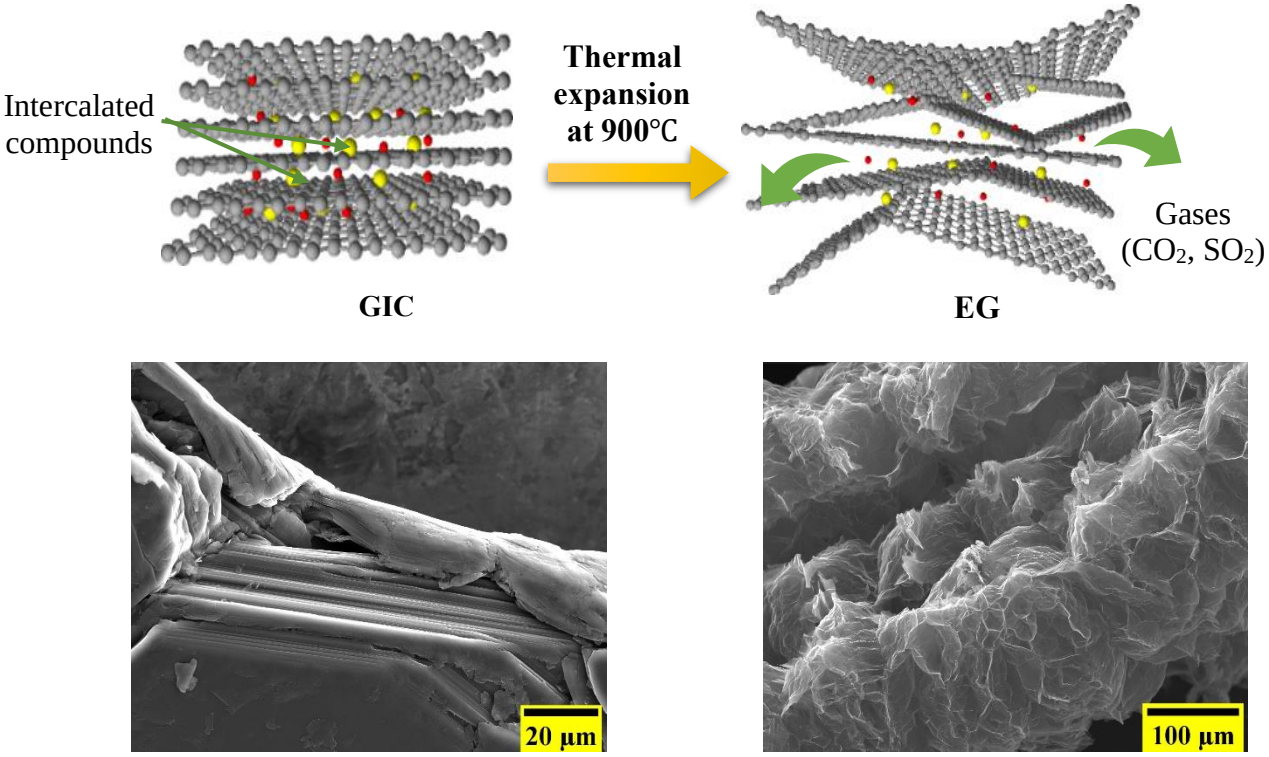

Figure 4.1 Schematic preparation of expanded graphite (EG) from graphite intercalated compound (GIC) at 900 °C with FE-ESEM images of GIC and EG filler.

Thermally expanded graphite (EG) provides another avenue to establish percolative networks within a composite, resulting in high electrical and thermal conductivity. EG has been a promising 3D filler with a lightweight, porous structure and has excellent electrical conductivity (10^6–10^8 Sm^{-1})[130] and thermal conductivity (>300 $Wm^{-1}K^{-1}$)[146]. EG is utilized in this experimental study as filler to establish a hierarchical porous structure with an interconnected network of graphene nanosheets within the composite to achieve a large enhancement in thermal and electrical conductivity.EG can be easily obtained from graphite intercalated compound (GIC)[213,214] through thermal treatment[215-217], as shown in Figure 4.1. More detail of EG preparation technique is provided in the earlier chapter 3. In this work, we use EG filler to fabricate EG/polymer composite via the solution casting technique. A high electrical conductivity value of 969 Sm^{-1} is achieved at a very low concentration of 10 wt% EG filler content. We also report *k* value of 7.3 $Wm^{-1}K^{-1}$ for the same filler composition sample of EG polymer composite.

Melt mixing[144,171,218], high shear mixing[219,220], ball milling technique[122,221] have been applied in past studies to fabricate EG/polymer composites. The melt mixing technique was not found suitable in several studies due to the poor dispersion and segregation issue[222,223]. According to Wei *et al*[146], 13.33 vol% expanded graphite filler, pre-melt blended with stearic acid and polyethylene wax, was melt-mixed with low-density polyethylene (LDPE) to obtain electrical conductivity of 1345 Sm^{-1}. Yang *et al.*[148] fabricated multilayer plastic packaging waste (MPW)/EG composite using powder mixing technique, followed by compression molding, and achieved electrical conductivity of 253 Sm^{-1} for 31.6 vol% EG filler.

Significant research has led to the development of EG-based polymer composites with high electrical conductivity at low percolation thresholds. She *et al.* embedded expanded graphite into high-density polyethylene (HDPE) matrix via melt-extrusion and found a percolation threshold of

~5.7 wt% for HDPE/EG composite for electrical conductivtiy[224] . Thermally expanded graphene oxide polycarbonate nanocomposites exhibited percolation effect at 1.25 wt % for surface resistance and surface resistance reached up to $2\times10^5\ \Omega$ at 3 wt% nanocomposites[29]. Piao and his co-workers developed a EG polymer composites using a conducting polymer poly(3,4-ethylenedioxythiophene) poly-(styrene sulfonate) (PEDOT:PSS) with electrical conductivity up to 10^4 Sm^{-1} for 50 wt% EG filler[225]. The graphene−polyimide nanocomposites exhibited an ultra-low graphene percolation threshold of 0.03 vol % and maximum direct current (dc) conductivity of 0.94 Scm^{-1} [226]. Li *et al.* prepared poly(vinylidene fluoride)PVDF/EG composites and found a percolation threshold of 6.3 vol% for electrical conductivity[227]. Several studies also report the *k* value of EG/polymer composite. Sari *et al.* [228] found that using 10 wt% EG, the thermal conductivity of the paraffin/EG composite material was increased to 0.82 $Wm^{-1}K^{-1}$ at 10 wt% filler due to proper absorbance of paraffin wax into the expanded graphite. The inclusion of EG filler into polyethylene glycol (PEG) improved thermal conductivity by ~4.4-fold compared to the pure PEG thermal conductivity of 0.2985 $Wm^{-1}K^{-1}$ [171]. Kim *et al.*[123] achieved 10.77 $Wm^{-1}K^{-1}$for EG/epoxy composite at 20 wt% EG filler amount using ultrasonication for 30min. Incorporating a lower amount of filler to achieve higher electrical and thermal performance has been presented in this study along with a detailed morphological analysis of the EG filler and composite.

Polyetherimide (PEI) (a polar polymer) is chosen as the polymer matrix in this work. It is a high-performance polymer with excellent flame retardancy, chemical resistance, and high-temperature stability[229]. High melting temperature of PEI, 340−360 °C makes the fabrication process challenging[230] through the melt mixing approach. Organic solvent such as N,N-dimethylacetamide (DMAC) has the potential in processing this polymer at low temperature of

130 °C, which makes the solution casting technique suitable for this work. Furthermore, this strategy allows the homogeneous solution of PEI (in solvent) to fill the pores of EG with polymer

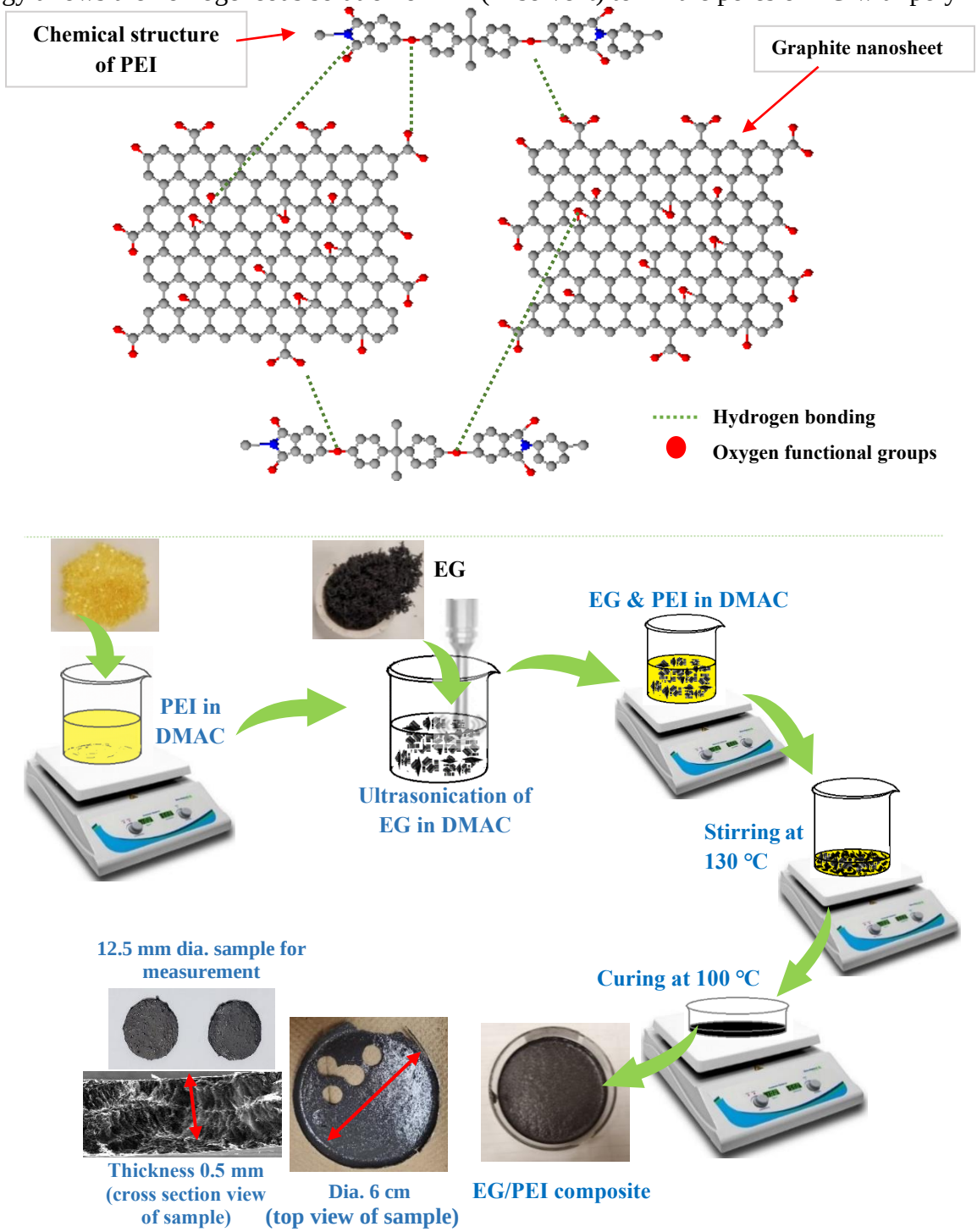

Figure 4.2 a) Interaction between polyetherimide (PEI) and graphite nanosheet of EG through hydrogen bonding, b) schematic preparation of EG/PEI composite.

and preserve the porous 3D structure of EG in the composite. Particularly, the solution casting technique enables the advantage of minimal distortion due to minimal shear forces during sample making. Additionally short time ultrasonication disperses the EG filler well into the polymer matrix. Oxygen groups of EG interact with imide groups of PEI through hydrogen bonding (as shown in Figure 4.2a), enabling superior interaction between polymer matrix and filler. XPS analysis provides the evidence of the presence of oxygen content in EG filler.

In this paper, we demonstrate an effective solution mixing route with short time ultrasonication for fabricating EG/PEI composite with in-plane electrical conductivity of 969 Sm^{-1}. In addition, we have investigated the thermal properties of the solution-cast EG/PEI composites. Thermal conductivity of the EG/PEI composite is found to reach values up to 7.3 $Wm^{-1}K^{-1}$, almost ~32-fold higher relative to the thermal conductivity of pure PEI (0.23 $Wm^{-1}K^{-1}$). The dispersion and morphology of the expanded graphite/PEI composite have been investigated using Field Emission Environment Scanning Electron Microscopy (FE-ESEM). The presence of functional groups, structural integrity, and defective state of expanded graphite and graphite intercalated compound were characterized by XPS, XRD, and Raman analysis to understand the resulting electrical and thermal properties.

4.2 EXPERIMENTAL SECTION

4.2.1 Materials

Graphite intercalated compound (GIC), with an average lateral size of ≥300 μm (+50 mesh size: ~92%) and expansion ratio 280:1 (ASB-3772) were bought from Graphite store[231]. Graphene Nanoplatelets (GNPs) of ~15 nm thickness and lateral size of ~25 μm were purchased from Sigma Aldrich[81]. Polyetherimide (PEI) pellets (melt index of 18 g/10 min and a density of 1.27 g/mL)

and N, N-dimethylacetamide (DMAC) were purchased from Sigma Aldrich[81] and Alfa Aesar[232] respectively.

4.2.2 Fabrication of the EG/PEI & GNP/PEI Composites

Thermal expansion of GIC was carried out using a hot furnace at 900 °C, to obtain expanded graphite (EG) with a worm-like structure. The GIC was kept inside the furnace for a very short time, ~1 min to achieve the highest expansion. Figure 4.2b shows the fabrication procedure of the EG/polyetherimide composite, described next. EG fillers obtained above through thermal expansion were dispersed into 20-30 mL DMAC. Separately PEI pellets were dissolved using 50 mL DMAC at 130 °C for 1 h. The DMAC solution with EG filler and dissolved polymer were mixed and blended for 3 h at 130 °C followed by ultrasonication at 20% amplitude for ~ 120 s. Then, the mixture was cast into a glass petri dish and kept at 100 °C. The composite film was peeled off after 24 to 48 h. The composite films were prepared for different concentrations of filler, including- 2.5, 5, 7.5, and 10 wt% EG content. The preparation process was optimized using different ultra-sonication time (30 s -150 s). To compare the electrical and thermal property with graphene-nanoplatelet-based polymer composite, the composite films were also prepared using graphene nanoplatelet following the same procedure.

4.3 CHARACTERIZATION

Measurement of electrical conductivity: In-plane electrical conductivity of EG/PEI and GnP/PEI composites was measured using a four-point probe setup. Keithley Multimeter 2100 (Keithley Instruments, Solon, OH, USA), coupled with an in-house built four probe point set up, was arranged to measure the resistance of composite film. EG/PEI films were cut into pieces with length = 4.3 mm, width = 1 cm, and thickness = 0.3-0.5 mm to determine the average resistivity

using the resistance,(Ω), and dimensions of the flat strips. Volume resistivity was calculated using the following equation,

$$\rho = \frac{R \times A}{L} = \frac{R \times w \times t}{L}$$

where, R, w, t, and L represent the resistance, width, thickness and length of the sample respectively. Electrical conductivity is the inverse of resistivity, calculated by $\sigma = \frac{1}{\rho}$.

Through-thickness thermal conductivity (k) measurement: k of EG/polymer composites was measured by using the laser flash technique. A Netzsch LFA 467 Hyperflash (Netzsch, Germany) laser was used to measure the through-thickness thermal diffusivity of the prepared samples. 8-12 samples of 12.5 mm diameter and 0.3-0.4 mm thickness were used to measure the thermal diffusivity (α) at room temperature (23 °C). The samples were coated with a thin layer of graphite paint before the measurement to increase emissivity for efficiently absorbing heat from a flash lamp. An average of 6-8 measurements is reported in this work. The laser flash technique induces heat through a flash lamp pulse on one surface of the sample and the temperature rise is captured on the other surface of sample as a function of time. α is determined by LFA using the following equation: $\alpha = (0.1388\ d^2)/t_{1/2}$, where, α is the thermal diffusivity (mm^2/s), $t_{1/2}$ is the time to obtain half of the maximum temperature on the rear surface, and d denotes the sample thickness (mm). The thermal conductivity was calculated using $k = \alpha \times \rho \times Cp$, where *k*, ρ, and C_p represent the thermal conductivity, density, and specific heat constant of the sample, respectively. In this work, the density and specific heat of the composite samples were measured using a gas pycnometer (AccuPyc II 1340, Micromeritics Instrument Corporation, USA) and Netzsch differential scanning calorimetry (DSC) (DSC 204F1 Phoenix, Netzsch, USA).

Scanning Electron Microscopy (SEM): Morphological characterization of EG filler and EG/polymer composites was carried out by using high-resolution Field Emission Environmental Scanning Microscopy (Quattro S FE-ESEM, ThermoFisher Scientific, USA). This SEM was operated in secondary electron (SE) mode at an accelerating voltage of 20 kV.

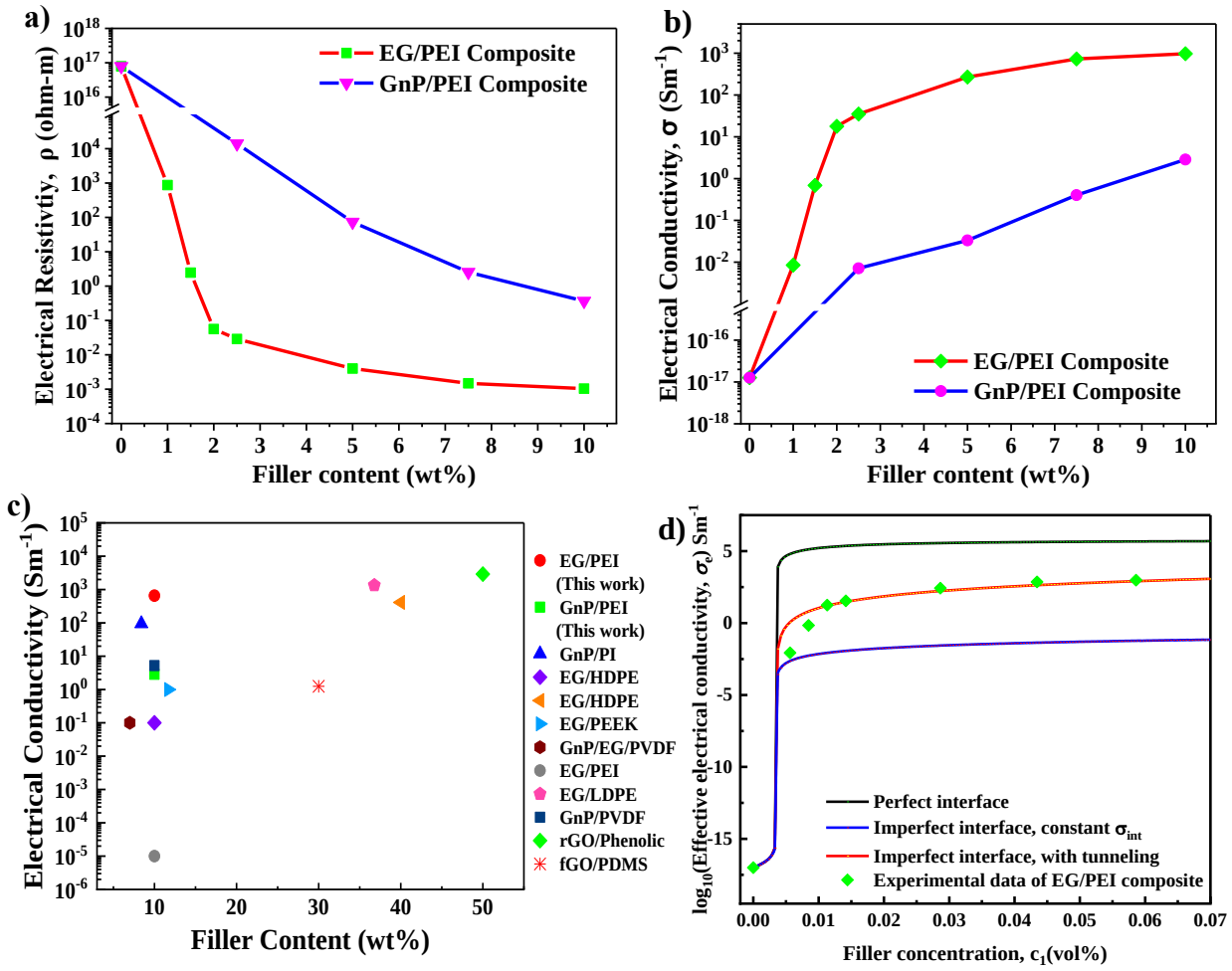

Figure 4.3 a) Electrical resistivity and b) electrical conductivity value of the PEI/EG nanocomposites as a function of EG, c) comparison of electrical conductivity value of polymer composites with previous work, and d) effective in-plane electrical conductivity in EG/PEI composites with respect to EG filler volume concentrations under perfect and imperfect interface conditions.

Raman Spectroscopy (RS): Raman spectroscopy (RS) was performed using a DXR3 SmartRaman Spectrometer (Thermofisher Scientific, USA) to collect the data over the range from 3000 to 1000 cm^{-1}, laser wavelength λ_L = 633 nm, spectral resolution = 0.16 cm^{-1}, and imaging resolution = 702 nm for the EG and GIC samples.

X-ray Diffraction (XRD): A PANalytical Empyrean Diffractometer (Malvern PANalytical Ltd, UK) produced the information regarding the crystal structure of EG compared to GIC using Bragg-Brentano focusing geometry at room temperature. 3 kW Cu Kα radiation (λ = 1.5406 Å) with a scan range of 2θ = 5 to 80°and step size of 0.013°.

4.4 RESULT & DISCUSSION

4.4.1 Electrical Properties

Figure 4.3a and b show the resistivity and conductivity of EG/PEI and GnP/PEI composites as a function of the filler content. While the electrical conductivity of pure PEI is about 1.2×10^{-17} Sm^{-1} [230,233], it increases with an increase in filler content. The addition of 1 wt% EG filler amount causes electrical conductivity to rise sharply from 1.2×10^{-17} Sm^{-1} (for pure polymer) to 8.3×10^{-3} Sm^{-1}. In contrast, the GNP/PEI composite reaches a similar electrical conductivity value of 7.1×10^{-3} Sm^{-1} for higher filler content of 2.5 wt%. From EG concentration of 2.5 wt% onwards, the electrical conductivity value of EG/PEI composite increases at a slower rate up to 10 wt% filler concentration. The electrical conductivity of the EG/PEI composite reaches a value of 969 Sm^{-1} at 10 wt% EG content, representing a ~10^{19}-fold increase in electrical conductivity relative to that of pure PEI. At a similar composition of 10 wt%, the GNP/PEI composite exhibits an electrical conductivity of 2.86 Sm^{-1}, significantly lower than that achieved for EG/PEI composite. Such higher enhancement of electrical conductivity for EG/PEI composite is due to the interpenetrating

network of graphene and polymer resulting from expanded graphite as a filler. Understanding of morphology of EG filler within the composite is achieved through FE-ESEM analysis (described in section 4.4.4). The solution casting technique followed by short-time sonication helps to disperse the filler and simultaneously fills the pores of expanded graphite with dissolved polymer. The dependence of electrical conductivity values for different filler content and preparation methods is presented in Figure 4.3c and table 4.1.

Table 4.1 Comparison of EC for different polymer-graphene and EG-polymer composite.

Filler	Matrix	Fraction	**ρ** (Sm^{-1})	Preparation method	ref
GnP	PI	5 vol%	94	solvent casting using N-methyl-2-pyrrolidone (NMP)	[226]
EG	PEI	10 wt%	1E-5	Ultrasonic melt-extrusion	[234]
EG	LDPE	36.78 wt%	1345	Melt mixing	[146]
EG	PDS	10 wt%	2500	Solvent casting	[235]
EG	HDPE	10 wt%	0.1	Melt mixing	[236]
EG	HDPE	40 wt%	410	Melt mixing	[237]
EG	PEEK	11.7 wt% (7vol%)	2.40×10^{-3}	Melt mixing	[165]
Graphite/EG	PVDF	7/0.5 wt%/wt%	0.1	Melt Crystallization and quenching in water	[238]
GnP	PVDF	10 wt%	5.2	Solvent blending–casting	[239]
GnP	PS	30 wt%	1.25	Solution mixing	[240]
rGO	Phenolic	50 wt%	2900	Solution mixing	[241]
rGO	PDMS	0.4 wt%	0.32	Bidirectional freeze-casting	[242]
EG	PEI	10 wt%	969	Solution mixing	This work
GnP	PEI	10 wt%	2.86		

PI: Polyimide; PEEK: Poly(ether ether ketone); HDPE: High density polyethylene; LDPE: Low density polyethylene; PS: Polystyrene; PVDF: Polyvinylidene fluoride; PDMS: Polydimethylsiloxane

In EG/PEI composite, a continuous graphitic network of 3D filler is present as shown in FE-ESEM images, allowing us to take advantage of in-plane electrical conductivity value (10^7 – 10^8)[130] of graphene nanosheets, thus leading to a high electrical conductivity value of composite. Simultaneously, 3D interconnected network reduces the percolation threshold of composite avoiding the need for use of higher filler content. The large graphite nanosheets are covalently bonded even at the bend or turns within this worm like structure of EG, minimizing the contact resistance, thus enhancing overall composite conductivity. In addition, PEI inherently has oxygen and nitrogen groups that interact with oxygen functional groups present in the EG (as shown in XPS analysis) through hydrogen bonding, leading to the strong interaction between polymer and graphene nanosheets of the EG.

4.4.2 Effective Medium Theory to Predict Electrical Conductivity

The significant enhancement in electrical conductivity of EG/PEI composite is mainly due to the continuity of large graphite nanosheets over a long length scale of EG. Below we compare the measured electrical conductivity of EG/PEI composite with predictions from an effective medium model (Figure 4.3d).

Xia *et al.*[243] calculated the effective electrical conductivity tensor, L_e, of the two-phase medium considering polymer matrix as phase 0 and EG inclusions as phase 1 using the following equation:

$$c_0[(L_0 - L_e)^{-1} + S_0 L_e^{-1}]^{-1} + c_1 \langle [(L_1 - L_e)^{-1} + S_1 L_e^{-1}]^{-1} \rangle^* (\theta) = 0 \quad (4.1)$$

where c_0 and c_1 are the volume fractions of phase 0 and 1 respectively. S_i and L_i represent the Eshelby's S-tensor and electrical conductivity tensor of phase i and subscript 'e' refers to the 'effective' properties of the composites. The in-plane and out-of-plane effective electrical conductivities σ_1^e and σ_3^e can be obtained by solving the following nonlinear equations:

$$c_0 \frac{\sigma_1^e(\sigma_0-\sigma_1^e)}{\sigma_1^e+S_{11}^0(\sigma_0-\sigma_1^e)} + c_1\left\{A(\theta)\frac{\sigma_1^e(\sigma_1-\sigma_1^e)}{\sigma_1^e+S_{11}(\sigma_1-\sigma_1^e)} + B(\theta)\frac{\sigma_3^e(\sigma_3-\sigma_3^e)}{\sigma_3^e+S_{33}(\sigma_3-\sigma_3^e)}\right\} = 0 \quad (4.2)$$

$$c_0 \frac{\sigma_3^e(\sigma_0-\sigma_3^e)}{\sigma_3^e+S_{33}^0(\sigma_0-\sigma_3^e)} + c_1\left\{A(\theta)\frac{\sigma_1^e(\sigma_1-\sigma_1^e)}{\sigma_1^e+S_{11}(\sigma_1-\sigma_1^e)} + B(\theta)\frac{\sigma_3^e(\sigma_3-\sigma_3^e)}{\sigma_3^e+S_{33}(\sigma_3-\sigma_3^e)}\right\} = 0 \quad (4.3)$$

where θ indicates orientational average of the angle, and the subscripts '1' and '3' refer to the components of in-plane and out-of-plane directions, respectively. σ_0, σ_1 and σ_3 indicate the electrical conductivity of the polymer matrix, and in-plane and out-of-plane conductivities of EG filler respectively. Also, the θ-dependent coefficients, $A(\theta)$, $B(\theta)$ and $C(\theta)$ are presented below:

$$A(\theta) = \frac{9+2\cos\theta+\cos 2\theta}{12},\ B(\theta) = \frac{3-a\cos\theta-\cos 2\theta}{12},\ C(\theta) = \frac{3+2\cos\theta+\cos 2\theta}{6} \quad (4.4)$$

S_{11}^0 and S_{33}^0 are the two components of the S-tensor for the matrix phase. Assuming the statistical distribution of EG fillers to be isotropic, these matrix elements are computed to be S_{11}^0 = 1/3 and S_{33}^0 = 1/3. Two independent components S_{11} and S_{33} are the shape factors related to aspect ratio and can be calculated using following equations:

$$S_{11} = S_{22} = \frac{\alpha}{2(1-\alpha^2)^{3/2}}\left[\arccos\alpha - \alpha(1-\alpha^2)^{1/2}\right];\ \alpha<1 \quad (4.5)$$

$$S_{33} = 1 - S_{11} \quad (4.6)$$

where, α is the aspect ratio of graphite nanosheet.

Two major sources of interfacial effects are mainly responsible for reducing the electrical conductivity of polymer composite. The first one refers to the imperfect interface between the inclusions and the polymer matrix, which lowers the overall conductivity. Introducing a thin interfacial layer around the inclusions can be implemented to treat the interface effect. Overall

electrical conductivity for an imperfect interface can be obtained by assuming the interfacial layer as isotropic, and using the equations presented below:

$$\sigma_i^{(C)} = \sigma^{(int)}\left[1 + \frac{(1-c_{int})(\sigma_1-\sigma^{(int)})}{c_{int}s_{11}(\sigma_1-\sigma^{(int)})}\right] \quad (4.7)$$

where $\sigma^{(int)}$ is the isotropic electrical conductivity of the interfacial layer, and c_{int} is the volume fraction of the interfacial layer around the inclusions.

$$c_{int} = 1 - \frac{\lambda}{2}\left(\frac{\lambda}{2\alpha}\right)^2 / \left(\frac{\lambda}{2} + h\right)\left(\frac{\lambda}{2\alpha} + h\right)^2 \quad (4.8)$$

The second important source of interfacial effect is the tunneling. According to Wang *et al.*[244,245], the effect starts to develop with increase in filler loading and decrease in distance between inclusive filler, causing greater probability of electrons tunneling across particle-particle gaps in the start-up zone of percolative regime. The tunneling-assisted interfacial conductivity can be evaluated using the equation below:

$$\sigma^{(int)} = \sigma_0^{(int)} / \tau\,(c_1, c_1^*(\theta), \gamma_\sigma) \quad (4.9)$$

where $\sigma_0^{(int)}$, τ, γ_σ and $c_1^*(\theta)$ represents the intrinsic electrical conductivity of the interfacial layer, resistance-like function, electron tunneling scale parameter, and θ-dependent percolation threshold respectively.

Table 4.2 Physical values used in the theoretical calculation of the effective conductivity of nanocomposites.

Material Parameters	Values
Aspect ratio of the graphene filler, α	1.00×10^{-3}
Graphene half thickness, λ	8.00×10^{-9}
Thickness of the interlayer, h (m)	10.00×10^{-9}
In-plane electrical conductivity of EG, σ_1 (Sm^{-1})	8.32×10^{7}
Out-of-plane electrical conductivity of EG, σ_3 (Sm^{-1})	8.32×10^{2}
Electrical conductivity of the PEI polymer, σ_0 (Sm^{-1})	1.2×10^{-17}
Electrical conductivity of the interface at c_1=0, $\sigma_0^{(int)}$(Sm^{-1})	9.5×10^{-3}
Scale parameter of the electronic tunneling at the interface, γ_σ	1.3×10^{-5}

Electrical conductivity of EG/PEI composite is predicted using the above effective medium model. Effective electrical conductivity of composite for three different interface conditions is plotted in Figure 4.3d for randomly oriented EG filler by assuming $\theta = \pi/2$. Table 4.2 presents values of the parameters involved in calculation of the effective electrical conductivity. A perfect interface between the EG filler and polymer matrix (assuming zero interfacial resistance between filler and polymer) results in the highest EC value shown by the black curve in Fig. 4.3d. Blue curve in Figure. 4.3d is related to the case of imperfect interface with a constant $\sigma_0^{(int)}$ (value presented in Table 4.2), and shows a significant drop in the effective electrical conductivity. The calculated electrical conductivity value for imperfect interface reveals that the contribution of the electron tunneling effect adds a positive impact, as indicated by the red curve. Figure 4.3d shows

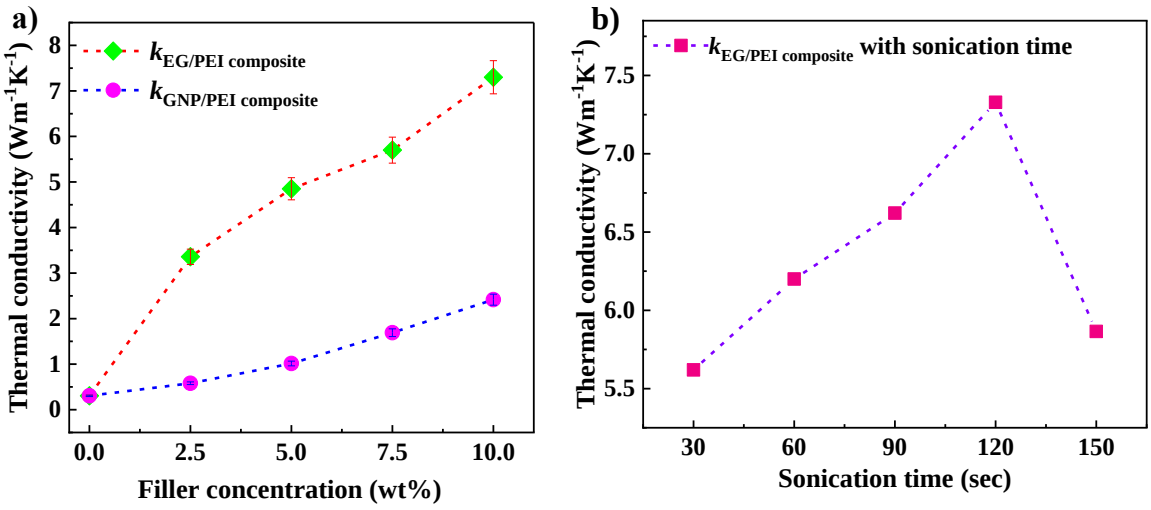

Figure 4.4 a) Thermal conductivity (*k*) value of EG/PEI and GNP/PEI composite with different filler content (2.5, 5, 7.5, and 10 wt%), b) *k* value of EG/PEI composite with different sonication time at 20% ultrasonication power.

that the theoretical approach of imperfect interface with tunneling effect is in good agreement with the experimental value of EG/PEI composite.

4.4.3 Thermal Conductivity Data

Figure 4.4a shows the measured through-thickness thermal conductivities of EG/PEI and GNP/PEI composites as a function of filler concentration. *k* of pure PEI is measured to be 0.23 $Wm^{-1}K^{-1}$, in good agreement with literature[73,246]. The inclusion of only 2.5 wt% EG filler increases the $k_{EG/PEI}$ value to 3.4 $Wm^{-1}K^{-1}$, representing 1378% enhancement with respect to pure PEI. On the contrary, the $k_{GNP/PEI}$ value (0.58 $Wm^{-1}K^{-1}$) shows a much smaller enhancement of 152% for 2.5 wt% GNP filler. The addition of 10 wt% EG filler enhances the composite *k* value to 7.3 $Wm^{-1}K^{-1}$ which represents a large ~3100% enhancement in *k* value compared to pure polymer. In contrast, *k* of GNP/PEI composite is enhanced by 947% for similar content of GNP filler. Such

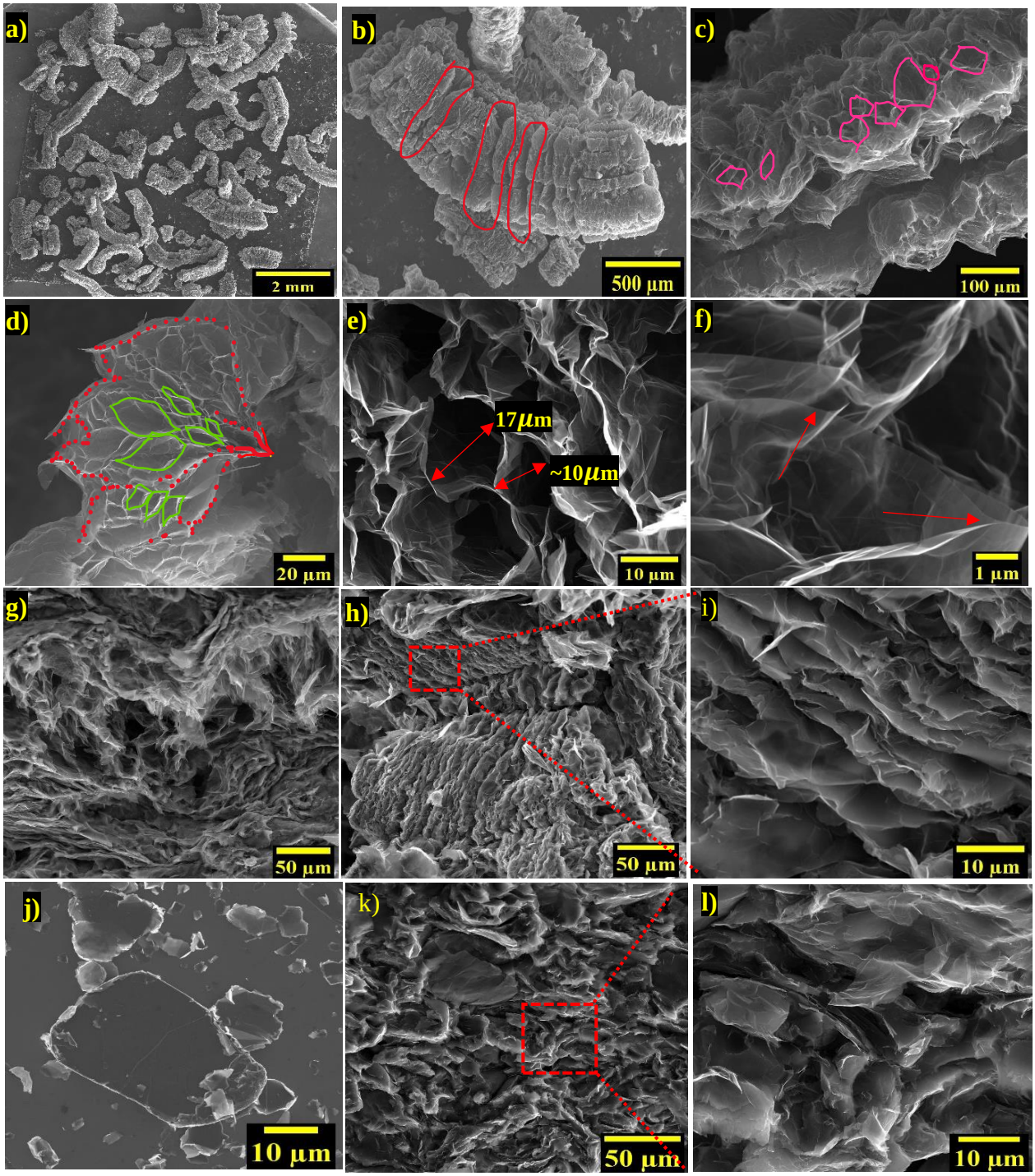

Figure 4.5 a) Montage area mapping of EG filler. FE-ESEM image of EG filler at b) ×30, c) ×150, d) ×500, e) ×1500 & f) ×8000. FE-ESEM images of EG/PEI composite for g) 5 wt% at ×350, (h & i) 10 wt% at ×350 & ×3500. FE-ESEM images of j) GNP, (k & l) GNP/PEI composite for 10 wt% GNP filler at ×350 and ×1500.

significant enhancement in EG/PEI composite is attributed to 3D interconnected continuous network of EG filler, creating an efficient heat transfer pathway in the composite.

We investigated the effect of ultrasonication on the *k* value of composite by preparing the 10 wt% EG/polymer composite at different ultrasonication times. The measured $k_{EG/PEI}$ values reveal that ultra-sonication time of EG filler into polymer solution directly influences thermal conductivity value, as shown in Figure 4.4b. The increase in sonication time from 30 s to 120 s leads to an increase in the value of $k_{EG/PEI}$ from 5.6 $Wm^{-1}K^{-1}$ to 7.3 $Wm^{-1}K^{-1}$; further increase in sonication time to 150 s reduces the *k* value to 5.7 $Wm^{-1}K^{-1}$.

Lower $k_{GNP/PEI}$ implies higher effective interfacial resistance between polymer and graphene due to low conductivity polymer between graphene particles. Overall, the high $k_{EG/PEI}$ value supports the presence of a continuous conductive network of EG in the composite via the solution casting technique.

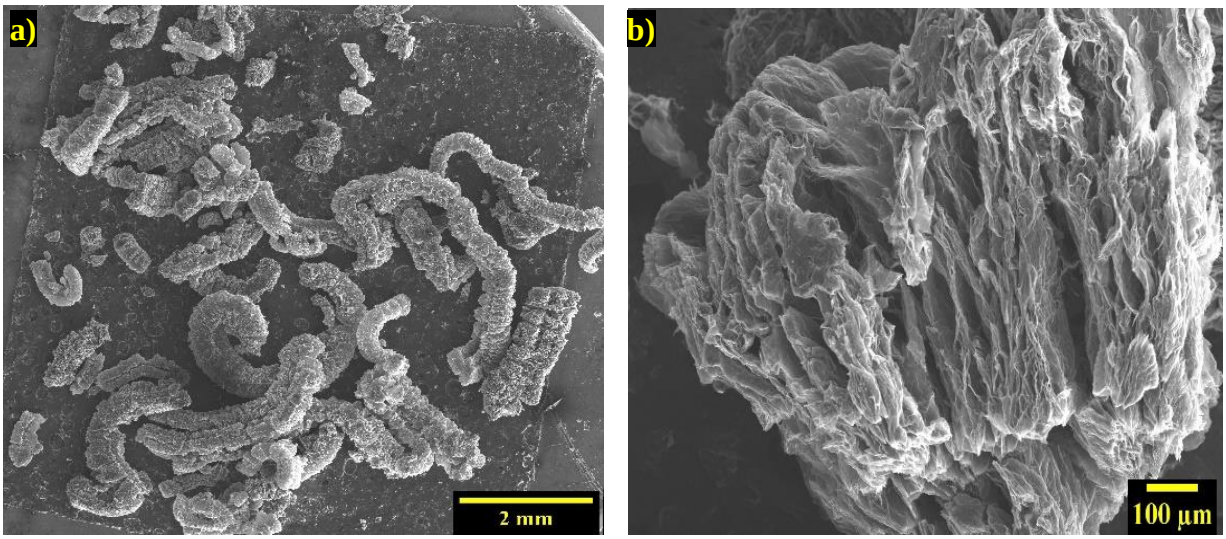

Figure 4.6 a) Montage area mapping of EG filler and b) FE-ESEM image of single EG filler after 2min ultrasonication at 20% amplitude in DMAC solvent.

4.4.4 Microstructures and Morphologies of Fillers & Polymer Composite through FE-ESEM:

FE-ESEM analysis allows a detailed understanding of the morphology of the fillers (EG & GNP) and composites (EG/PEI & GNP/PEI). The GIC expands in through-thickness direction and expands up to the highest expansion ratio of 280. GIC used in this work is made from +50mesh particles (lateral size = 300 μm); the through-thickness structure of the used GIC is presented in Figure 4.1. After the expansion process, the intercalated graphite compound turns into worm-like structure of EG, as shown in Figure 4.5a. Montage area mapping is used to measure the average length and diameter of the EG filler achieved after the expansion.

At a magnification of ×20, EG's average length and diameter are found to be 6-8 mm and ~250 μm, respectively. Intercalation and expansion create a multilevel hierarchical structure as shown in Figure 4.5b with red circles. The puffed-up, worm-shaped material exhibits beneficial interconnection between the graphene sheets throughout the entire length of the particle. At higher magnification shown in Figure 4.5c, the diamond-shaped pores (indicated by pink color) are visible throughout the single EG filler, and pores are measured to have length scales ranging from a few nanometers to ~20-30 micron scale. Figure 4.5d shows the interconnected graphene sheets in between the EG. Figure 4.5e shows the magnified view of EG pores of length (~10-20 micron) and wall thickness (~10 nm), creating a continuous 3D network of graphene sheets. Such formation of a network within the EG filler leads to the high electrical and thermal conductivity of composite after mixing with the polymer. The thickness of the graphene sheet in the network is found to be ~10-20 nm as shown in the magnified view in Figure 4.5f. The thickness is significantly smaller than the length of the graphene nanosheet in EG, leading to a high aspect ratio.

FE-ESEM analysis of EG/PEI & GNP/PEI composites has been performed to examine the morphology of the fractured surface of solution cast nanocomposites. FE-ESEM images of 5 and 10 wt% EG filler composition with PEI are presented in Figure 4.5g & h at a magnification of ×350, and in Figure 4.5i at a magnification of ×3500. Even at lower magnification, the porous structure is visible, and a graphitic network is seen to be formed over the entire composite. Figure 4.5i displays the higher magnification SEM images of 10 wt% EG/PEI composites, where the connected graphitic layers are clearly visible. The pores formed by graphene sheets inside EG adsorb the dissolved PEI polymer during the stirring and curing process of the composite. Initial absorbance of DMAC solvent in EG makes the dispersion of EG filler into polymer solution easier through wetting of the porous structure. Furthermore, agitation in the mixture of dissolved PEI and EG filler in DMAC solvent through ultrasonication leads to better diffusion of polymer into EG pores. Sonication parameters were optimized to achieve good dispersion of EG in polymer, while at the same time preserving the interconnected structure of EG. A sonication time of 2 min and an amplitude of 20% was found to result in good dispersion and preserve EG structure. Montage area mapping confirms that 2 min sonication of the EG filler in DMAC solvent preserves the porous structure (as shown in Figure 4.6a & b) to a large extent. For comparison, the morphology of GNP filler and GNP/PEI composite is also presented in Figure 4.5j and 4.5k-l respectively. The average diameter of GNP filler is measured to ~25 μm, significantly smaller than EG filler.

4.4.5 XPS Analysis

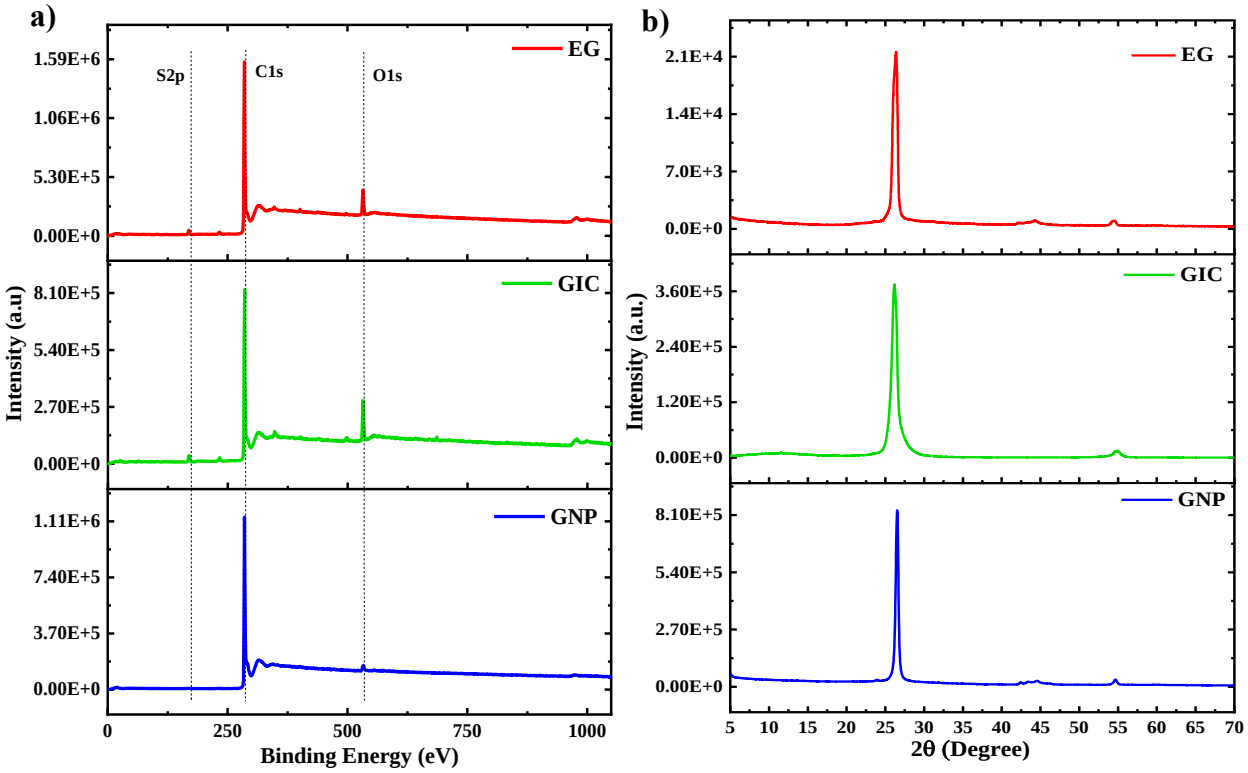

Figure 4.7 a) XPS spectra and b) XRD spectra of GNP, GIC, and EG filler.

XPS analysis was further performed to investigate the concentration of carbon c), oxygen (O), and sulfur (S) elements before and after the thermal expansion of GIC; these data are presented in Table 4.3. Figure 4.7a shows that two peaks of C1s and O1s at ~285 eV and ~532 eV[247] are present for GIC and EG filler. S2p peak at ~169 eV is visible in GIC and EG filler spectra because of the included intercalated compounds. Due to the expansion process, the sulfur content decreases from 1.95 at% (in GIC) to 1.24 at% (in EG). The atomic percentage of carbon increases from 87.85% to 91.85%, and oxygen reduces from 10.2% to 6.91% after expansion. Oxygen content decreases due to the thermal expansion at 900°C, and the increased atomic percentage of carbon content indicates the presence of more graphitic content in EG. XPS spectra of GNP are also presented in Figure 4.7a and Table 4.3, indicating the presence of 97.48 at% C1s and 2.52 at% O1s. Increased

oxygen groups in EG allow favorable interactions with oxygen groups in PEI through hydrogen bonding, leading to efficient interfacial thermal transport. This further enhances the conductivity of EG/PEI composite.

Table 4.3 Atomic composition by XPS analysis of GNP, EG and GIC.

Sample name	Atomic Composition by XPS (at%)		
	C (~285 eV)	O (~532 eV)	S (~169 eV)
GIC	87.85	10.2	1.95
EG	91.85	6.91	1.24
GNP	97.48	2.52	-

4.4.6 XRD Analysis

X-ray diffraction (XRD) analysis was performed to determine the crystal structure and interlayer spacing of GIC, EG, and GNP filler. Figure 4.7b shows a strong diffraction peak at 2θ = 26.2° (002) for GIC, slightly shifted from the case of natural graphene case 2θ= 26.5° [175-178], implying highly oriented carbon material. The slight shift in peak for GIC is attributed to the presence of intercalated compounds. From Bragg's diffraction equation, $n\lambda = 2d \sin\theta$, the interlayer spacing, d, changes from 0.335 nm for pristine graphite to 0.339 nm for GIC. A broad, weak peak at 2θ = 11.2° (001) in GIC spectra indicates the attachment of functional groups through the intercalation process between graphene layers. The slight shift in peak for GIC is attributed to the presence of intercalated compounds.

On the contrary, a reduced sharp peak is visible at 2θ = 26.35° (002)[180] for EG, still presenting interlayer spacing of 0.337 nm, closer to the graphitic carbon structure. A weaker peak (002) is

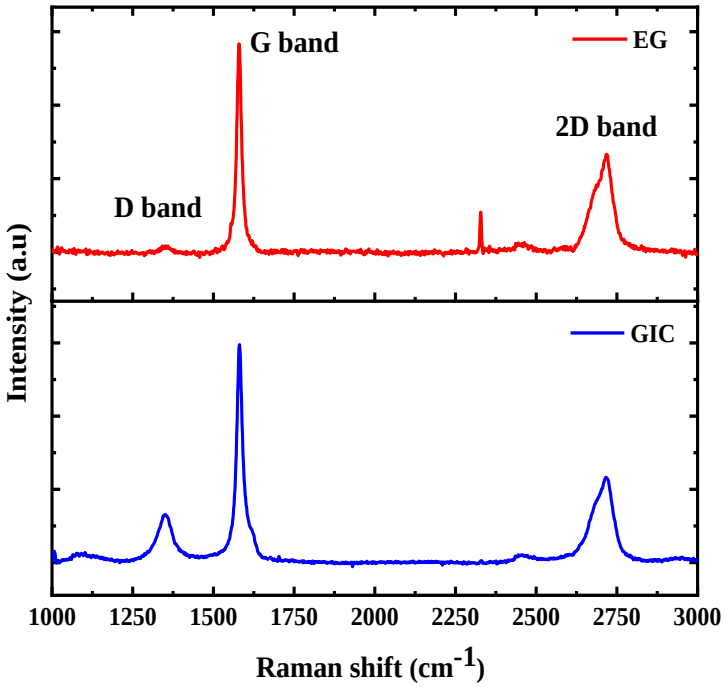

Figure 4.8 Raman spectra of GIC and EG filler.

observed for EG case than GIC, which is caused due to disorder in graphitic morphology [181] after the expansion process. Still, a mostly aligned peak position in EG indicates the intact chemical structure of graphite and interlayer order[182,183]. EG's interconnected and stacked structure enables better thermal transport throughout the polymer composite[124].

4.4.7 Raman Analysis

Raman spectroscopy has been performed to further investigate the crystal structure before and after the thermal expansion. Figure 4.8 exhibits three characteristic peaks corresponding to G-band, D-band, and 2D-band at ~1580 cm^{-1}, ~1350 cm^{-1}, and ~2700 cm^{-1} for graphite[184]. The G band denotes the in-plane vibration of the carbon-carbon bonds, resulting from the stretching of defect-free sp^2 carbon of hexagonal ring [185]. The D band signifies the vibrational mode caused due to the amorphous, disordered structure of sp^3 hybridized carbon[157]. The 2D band also can be seen at around 2700 cm^{-1} and represents a second-order two phonon process[186]. Raman spectra of GIC and EG clearly shows the representative peaks of G, D & 2D bands.

Broad D band in GIC and large I_D/I_G ratio of 0.21, suggests the presence of structural defects due to intercalation process. On the contrary, the D band is negligible in EG Raman spectra and

refers to a highly ordered defect-free graphite structure. The peak shape of the 2D band varies with the number of graphene layers. The 2D peak position and shape of GIC and EG filler show slight change after thermal treatment, indicating a reduction in van der Waals interaction between graphene layers and increase of the interlayer distance between these layers[248]. Because of this change in graphitic structural order, EG imparts strong electrical and thermal properties in EG/PEI composite through the graphitic nanosheets.

4.5 CONCLUSION

In summary, a high electrical and thermal conductivity EG/PEI composite has been developed using a solution casting technique followed by short time ultrasonication. Even at a low filler content of 10 wt% EG filler, the composite displays a superior electrical conductivity of 969 Sm^{-1}, almost ~19 orders of magnitude higher relative to pure polyetherimide (electrical conductivity ~ 1.2×10^{-17} Sm^{-1}). Measured values matched well with an effective medium approach by including the effects of electron tunneling and interface resistance on the electrical conductivity of EG/polymer composite. A dramatic enhancement of ~3074% has also been achieved for the thermal conductivity of EG/PEI composite (7.3 $Wm^{-1}K^{-1}$), with respect to pure polymer. The EG/PEI *k* value is also 3 times higher than the GNP/PEI composite *k* value at 10 wt% inclusion of filler. FE-ESEM images show that a 3D continuous network of EG filler is responsible for enabling superior performance in electrical and thermal properties. Developed polymeric materials have potential applications in a wide range of thermo-electronic technologies.

.

CHAPTER 5

Comparative study of intercalating agents on thermal conductivity of expanded graphite/polyetherimide composite

5.1 GRAPHITE INTERCALATED COMPOUND (GIC) AND OXIDIZING AGENTS

In this chapter, the role of intercalating agents in modifying thermal properties of expanded graphite is explored with the goal of developing high thermal conductivity polymer/expanded-graphite nanocomposites. Graphite comprises of multiple layers of graphene which are stacked along the c-axis by weak van der Waals force with an interlayer spacing of 3.35 Å[249] . Due to the weak van der Waals force and the interlayer spacing, the insertion of atoms, ions, and molecules between the graphene layers can quickly initiate the intercalation process. Graphite intercalated compound (GIC) is the form of graphite with intercalated chemical species such as atoms, ions, and molecules between the graphene layers[250,251] as shown in Figure 5.1a. GIC has been studied for various applications including- superconductors, fuel cells, battery cells, heterogeneous catalysts, electrodes, hydrogen storage, and polarizers[252-255]. GICs are also of interest for obtaining large lateral size[256-258] and single/bilayer/few layers of graphene using liquid-phase exfoliation[249,259].

Concentrated H_2SO_4 serves as the acidic environment and has been the most common intercalating agent for the preparation technique of GIC; however, the intercalation process also

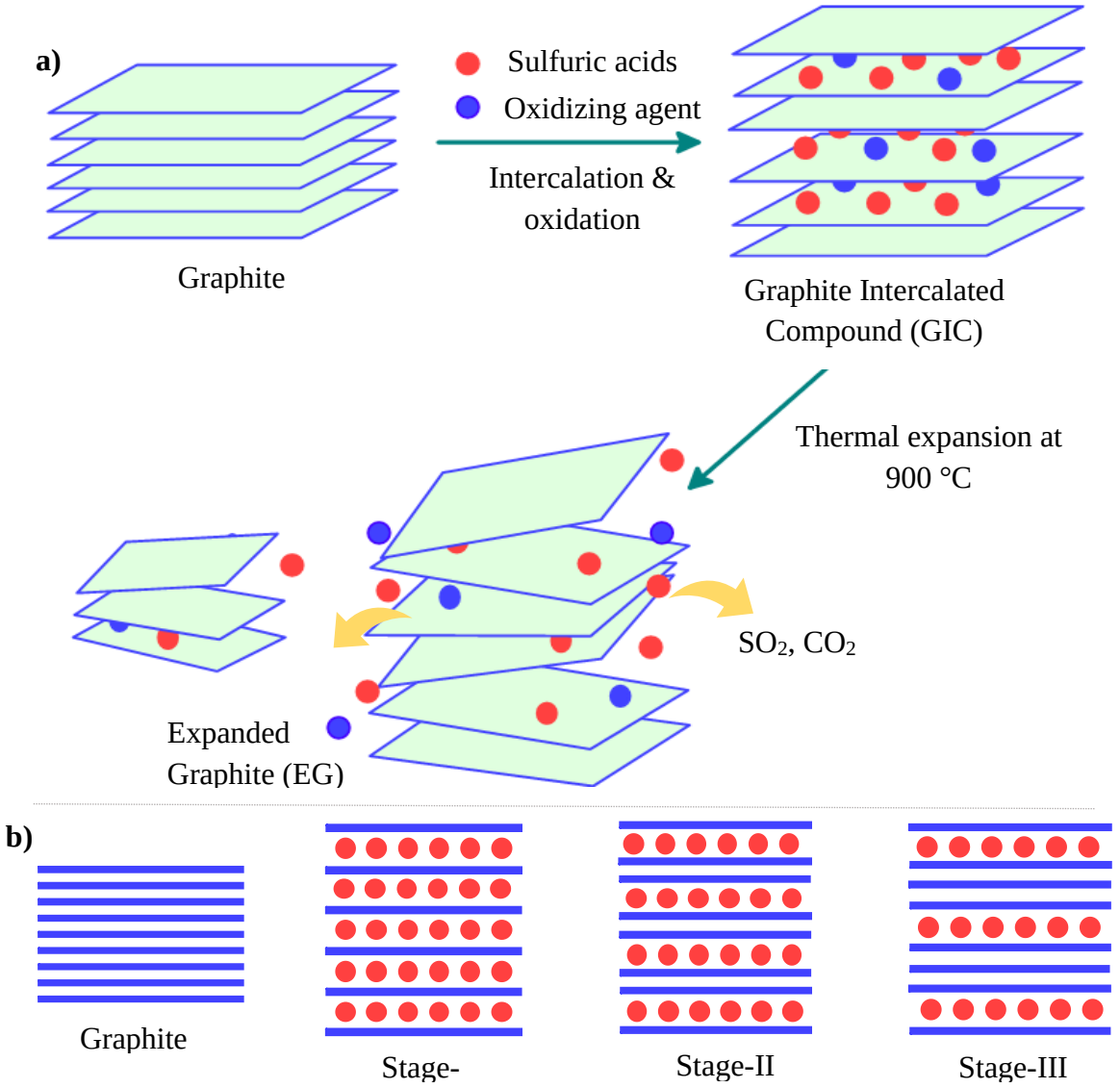

Figure 5.1 a) Preparation of graphite intercalation compound (GIC) in the presence of intercalants (acids & oxidizing agents), b) schematic illustration of different stages of intercalation.

requires an anodic or strong oxidizing agent. According to Cai *et al.*[260], even though the van der Waals force between the graphene layers is weak, it is still strong enough to make the intercalation process difficult. Oxidizing agents coupled with H_2SO_4 reduce these forces significantly, enabling the interlayer separation to be increased, which leads to a high degree of intercalation of GIC[260,261]. Intercalation degree is directly related to a parameter known as staging index which is equal to the

number of graphite layers between two intercalated regions[262]. Several studies emphasize the role of staging index of GIC[263,264] in understanding the intercalation process.

According to the Rudorff model, a single layer, bilayer, or tri-layer graphene can be alternated regularly with intercalated species in stages I, II, or III. In stage-I of the intercalation process, each graphene sheet is separated from the others by intercalated compounds, and in stage II, GIC has two adjacent graphene sheets contained between intercalated compounds[265] as shown in Figure 5.1b.

GIC possesses a well-stacked graphitic structure containing acceptor, donor, or neutral type intercalant species. An acceptor type GIC is produced when electronegative species accept an electron and form an ionic bond with the π-electron network[264] denoted by C_x.

$$C_x + A \rightleftharpoons C_x^{m+} \cdot A^{m-} \quad (5.1)$$

Here A accepts m electron from the π-electron network. A donor type GIC is produced when an electron is donated to the network[25,264]; this happens with metal atoms as shown in the following equation.

$$C_x + A \rightleftharpoons C_x^{m-} \cdot A^{m+} \quad (5.2)$$

The intercalation process allows simultaneous oxidation or reduction of starting graphite sheets. Through this method, the positive or negative charges of the acceptor or donor type GIC cause repulsion between the graphite layers that increase their relative distance, and the intercalating agents can enter in between the graphite gaps. Donor and acceptor type intercalants cause the carbon-carbon bonds in the bonding layers to have stage-dependent stiffening nature for acceptors or softening for donors, respectively, due to the electron transfer process[266]. Another main structural characteristic of GIC is strong intraplanar binding and weak interplanar bonding,

which causes the graphite and intercalant layers to stay separated and maintain the inherent properties of graphite.

A class of graphite intercalated compounds known as graphite bisulfates, are an acceptor type intercalated compound, and can be synthesized using sulfuric acid and oxidizing agents such as concentrated nitric acid, potassium permanganate, potassium dichromate and chromium trioxide[216,267].

Synthesis of graphite bisulfate is obtained using the following reaction scheme[215]:

$$24nC + O_x^z + mH_2SO_4 \rightarrow C_{24n}^{+} \cdot HSO_4^{-} \times (m-1)\, H_2SO_4 + HO_x^{(z-1)} \quad (5.3)$$

where O_x is the oxidizing agent, C is the carbon atoms in the graphite, n and m are the numbers of moles of C and H_2SO_4 respectively. Intercalation of graphite produces intercalated graphite bisulfate compound. Simultaneously, oxidizing agents cause the anionic and molecular insertion between the carbon layered structure along with the formation of C_n^+ through their high redox potential. Upon synthesis, GIC contains carbon, oxygen, and sulfur with different ratios. Due to the insertion of intercalated species and oxygen groups, GIC has huge potential to expand significantly by thermal heating, along the graphite c-crystallographic direction because of weak adhesive forces between adjacent graphene layers. Thus, GIC provides an efficient route to obtain expanded graphite (EG). Camino *et al.* have proposed that the expansion occurs due to the formation of carbon dioxide (CO_2), sulfur dioxide (SO_2), and water vapor (H_2O) produced by the reaction (5.5), yielding expanded graphite[268,269] (Figure 5.1a).

$$C + 2H_2SO_4 \rightarrow CO_2 + SO_2 + H_2O \quad (5.4)$$

The properties of expanded graphite have been shown to be highly dependent on the GIC production processes related to intercalation, chemical oxidation, and electrochemical

intercalation[270-272]. The characteristics of EG are substantially influenced by the sulfuric acid concentration, oxidizing agent, and intercalation period used in the intercalation process.

Numerous GICs with different intercalants have been synthesized and reported. In recent years, after discovering the fascinating properties of graphene, and the higher-temperature superconductivity in CaC_6[273], GICs started gaining renewed interest[274]. Significant research has been performed on the synthesis process and characterization of graphite intercalated compound. The intercalation process is complicated, and studies are still ongoing to better understand it. Hong *et al.* developed a simple method for producing graphene from sulfuric acid intercalated graphite oxide by fast reduction and expansion exfoliation at temperatures just above 100 °C in ambient air[275]. Salvatore *et al.*[276] explored the morphology and intercalation effect of intercalated graphite bisulfate synthesized using various oxidizing agents and sulfuric acid. Parvez *et al.*[277] investigated electrochemical exfoliation using several organic salts ($(NH_4)_2SO_4$, Na_2SO_4, K_2SO_4) to create GICs using sulfate ions, and found that the EG, produced has better electrical properties including 11 Ω sq^{-1} conductivity of graphene films and high yield exfoliation[277].

EG filler has recently attracted a lot of interest in polymer composite applications. While integrated with the polymer, EG filler improves thermal characteristics significantly. Huang *et al.*[157] found that two-step intercalation with hydrogen peroxide and phosphoric acid improved the flame retardancy of expandable graphite (EG). They found that 30 wt% EG composition EG/ethylene-vinylacetate copolymer (EVM) matrix composite had a high limited oxygen index (LOI) of 30.4% [157]. Hou *et al.* used hydrogen peroxide and sulfuric acid to make an exfoliated or expanded graphite film with an in-plane thermal conductivity of 575 $Wm^{-1}K^{-1}$ at density of 2 gcm^{-3}. Liu *et al.*[278] reported thermal conductivity of 12.95 $Wm^{-1}K^{-1}$ of 3D-EG/ polydimethylsiloxane (PDMS) composite containing 31.9 wt% EG and graphene oxide (GO). Wang *et al.* demonstrated

superior electrical properties of 1719 Sm^{-1} of chemically expanded graphite poly(methyl methacrylate) (PMMA) composite through interlayer polymerization at 10 wt% EG filler content[182]. Kuan *et al.* compared different preparation techniques to observe the flame retardant property and found that hydrothermally H_2O_2 processed EG high density polyethylene composite showed superiority over other procedures[159]. However, no work has addressed the role of intercalating agents in the thermal conductivity enhancement of expanded graphite polymer composites.

To synthesize intercalated graphite, two distinct oxidizing agents, namely, hydrogen peroxide (H_2O_2) and sodium chlorate ($NaClO_3$) are used in this work, and the influence of thermally expanded graphite (EG) on the thermal characteristics of EG polymer composites is investigated in this work. Theoretical studies have revealed that Na ions possess strong intercalating power between graphene layers, resulting in lower stage number at a higher degree of oxidation[279]. Recently Kang *et al.*[280] theoretically studied the role of alkali metal sodium (Na) on the intercalation behavior of expanded graphite oxide with different amounts and ratios of oxygen functional groups. Wang *et al.* [281] also reported that oxidation leads to enlarged interlayer spacing of graphite to accommodate sodium ion and microchannels of oxidized graphite significantly help in Na ion diffusion. Intercalation behavior and effect on the thermal properties of EG using such alkali metal base and strong oxidizer, namely, $NaClO_3$ will be investigated here. On the other hand, Vittore *et al.*[282] developed a simple approach for preparing edge oxidized graphite utilizing H_2O_2 treatment at 60 °C and also claimed an additional benefit of eliminating amorphous carbon fraction from starting graphite. Edge oxidized graphite can lead to superior thermal and electrical properties to the polymer composites. In this work, we utilize another intercalation route of H_2O_2 to prepare expanded graphite from intercalated graphite bisulfate.

Polyetherimide (PEI) has significantly low thermal conductivity of 0.23 $Wm^{-1}K^{-1}$. Thermally expanded graphite (EG) produced from GICs functions as a useful 3D carbon filler for the thermosetting polymer, PEI. The thermal conductivity of an EG/polymer composite made of H_2O_2 expanded graphite (EG-H_2O_2) was found to be significantly higher than that of $NaClO_3$ expanded graphite (EG-$NaClO_3$). Compared to pure PEI, the *k* value of EG-H_2O_2/PEI composite for H_2O_2 intercalation increased by ~ 4030%, whereas EG-$NaClO_3$ fillers increased the *k* value by ~2190% at 10 wt% expanded graphite filler concentration. We have also made compressed EG sheets out of EG-H_2O_2 and EG-$NaClO_3$ to compare the thermal conductivity of graphene paper attained via the two intercalation processes addressed above. In this study, the impact of oxidizing agent concentrations, reaction duration, and interlayer spacing on EG structure, chemical composition, and structural integrity of GIC and EG is thoroughly examined. To perform the investigation and provide evidence to demonstrate the remarkable improvement of EG-H_2O_2/PEI composites, characterization methods such as Raman, XPS, XRD, and FE-ESEM were utilized. As described in the previous chapter, the solvent casting approach was used to prepare the composite as it helps to preserve the EG structure during the composite preparation.

5.2 EXPERIMENTAL SECTION

5.2.1 Materials

Natural flake graphite (-10 mesh graphite, 99.9%) and N, N-dimethylacetamide (DMAC) were purchased from Alfa aesar[232], US. Sulfuric acid (H_2SO_4, 95–98%), hydrogen peroxide (H_2O_2, 30%), sodium chlorate ($NaClO_3$, 99%), and polyetherimide (PEI pellets, melt index 18 g/10 min) were purchased from Sigma Aldrich[81].

5.2.2 Synthesis of GIC-H_2O_2 & EG-H_2O_2 using Intercalation Route I

10 mesh graphite was intercalated using H_2SO_4 and H_2O_2 under the mechanical stirring in the intercalation route I. Initially, cold water bath was used for 10-15 min to run the reaction then we ran the reaction at room temperature. 20 ml of H_2SO_4 was added to the flask and slowly cooled it down below 20 °C using a cold-water bath. Then 2 g graphite was added to the H_2SO_4 solution, followed by a very slow addition of H_2O_2. 300 ml cold deionized water was added to the mixture slowly at the end of the reaction time. Then we filtered and separated the particles from acidic solution. We dried the filtered graphite at 60 °C for 24 h to obtain the intercalation compound GIC, denoted as GIC-H_2O_2. Then, the EG particles, named as EG-H_2O_2, was obtained from GIC-H_2O_2 through the rapid heat treatment at 900 °C. To achieve the highest thermal properties, we optimized the amount of H_2SO_4 and H_2O_2 using different quantity of H_2SO_4 and H_2O_2 in the reaction. Performed reaction condition and obtained sample names are given in Table 5.1.

Table 5.1 Chemicals and their compositions used for the synthesis of GIC-H_2O_2 and EG-H_2O_2.

Sample name (GIC & EG)	**10 Mesh Graphite (g)**	**Amounts of reactants used**		**Volume ratio (H_2SO_4: H_2O_2)**	**Time**
		H_2SO_4 (mL)	**H_2O_2 (mL)**		
GIC-H_2O_2 1 & EG-H_2O_2 1	2	20	6	3.33:1	30 min
GIC-H_2O_2 2 & EG-H_2O_2 2	2	40	6	6.67:1	30 min
GIC-H_2O_2 3 & EG-H_2O_2 3	2	60	6	10:1	30 min
GIC-H_2O_2 4 & EG-H_2O_2 4	2	20	2	10:1	1 h
GIC-H_2O_2 5 & EG-H_2O_2 5	2	20	4	5:1	1 h
GIC-H_2O_2 6 & EG-H_2O_2 6	2	20	6	3:33:1	1 h

5.2.3 Synthesis of GIC-$NaClO_3$ & EG-$NaClO_3$ using Intercalation Route II

In intercalation route II, H_2SO_4 and $NaClO_3$ were used to intercalate the 10 mesh graphite particles. using mechanical stirring. Cold water bath was used for 10-15 min to run the reaction then ambient temperature has been used. At first, H_2SO_4 was taken into a flask and slowly cooled it down below 20 °C using cold water bath, then 2 g 10 mesh graphite particles were dispersed in H_2SO_4 and $NaClO_3$ was added to H_2SO_4 solution slowly. 300 ml cold deionized water was added to mixture slowly at the end of the reaction time and then washed with deionized water. The filtered graphite particles were then dried at 60 °C for 24 h to obtain the intercalation compounds GIC, named as GIC-$NaClO_3$. To obtain the EG-$NaClO_3$ fillers, GICs were thermally expanded at 900 °C. 20-40 ml H_2SO_4 and 0.25-0.5 g $NaClO_3$ were utilized to optimize the amounts of reactants for the preparation of EG. Performed reaction conditions are mentioned in Table 5.2.

Table 5.2 Chemicals and their compositions used for synthesis of GIC-$NaClO_3$ and EG-$NaClO_3$.

Sample name	10 Mesh Graphite (g)	Amounts of reactants used		Volume Ratio H_2SO_4: $NaClO_3$	Time
		H_2SO_4 (mL)	$NaClO_3$ (g)		
GIC-$NaClO_3$ 1 & EG-$NaClO_3$ 1	2	20	0.25	200:1	30 min
GIC-$NaClO_3$ 2 & EG-$NaClO_3$ 2	2	20	0.25	200:1	1 h
GIC-$NaClO_3$ 3 & EG-$NaClO_3$ 3	2	20	0.5	100:1	30 min

5.2.4 Preparation Method of Expanded Graphite-Polyetherimide (EG/PEI) Composite and Expanded Graphite (EG) Paper

Thermal expansion of graphite intercalated compound was carried out to obtain the worm structured EG filler using a hot furnace at 900 °C. To achieve the maximum expansion, the reacted

GIC particles were kept inside the furnace for a ~1 min. The solution casting technique was used to prepare the expanded graphite polymer composite, and polyetherimide (PEI) was chosen as polymer matrix to mix with the EG filler. We have followed a similar fabrication procedure as described in section 4.2.2 and Figure 4.3 to prepare EG/PEI composite. GIC-H_2O_2 and GIC-$NaClO_3$ were separately expanded by using the thermal expansion technique to obtain the EG-H_2O_2 and EG-$NaClO_3$ particles. EG fillers were then dispersed into 20 mL DMAC. Separately PEI pellets were dissolved using 50 mL DMAC at 130 °C for 1 h. The DMAC solution with EG filler and dissolved polymer were mixed and blended for 3 h at 130 °C, followed by ultrasonication at 20% amplitude. Ultra-sonication time (1 min – 3 min) was optimized for the composite preparation process. Then, the mixture was cast into a glass petri dish and kept at 100 °C. The composite film was peeled off after 24-48 h. Composite films were prepared using different concentrations of EG filler- 2.5, 5, 7.5, and 10 wt%. The EG-H_2O_2/PEI and EG-$NaClO_3$/PEI composite films at 10 wt% filler loading were prepared using the same solution casting technique for different reaction condition to compare the thermal conductivity value.

We also prepared the expanded graphite paper or EG paper using compression molding technique on EG particles as illustrated in Figure 5.2. Carver hot press was used to compress 2 g of EG particles together at room temperature under a pressure of 1-2 MPa and ~0.3 mm thick EG papers were fabricated. We prepared EG-H_2O_2 1 and EG-$NaClO_3$ 1 papers separately, using EG-H_2O_2 1 and EG-$NaClO_3$ 1 particles, respectively.

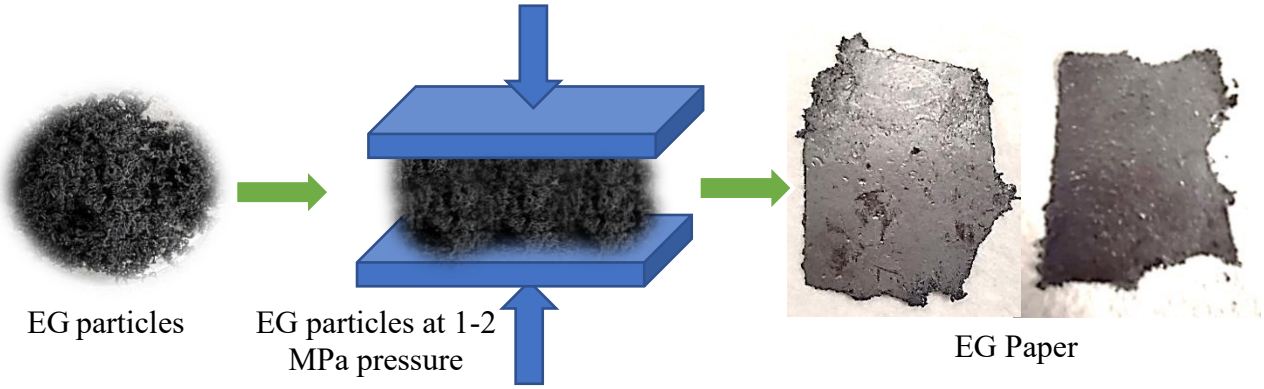

Figure 5.2 Preparation method of expanded graphite (EG) paper using compression molding

5.3 CHARACTERIZATION

The expansion volume (EV) was determined by exfoliating 1 g of GIC at a temperature of 900 °C for 30-60 s, and its volume was measured using a graduated cylinder. Then volume was recorded, and this datum was considered as EV value. To ensure accuracy, measurements were carried out in triplicate, and the average value was reported.

The Raman spectra was obtained using a Horiba Jobin-Yvon labRam HR instrument (HORIBA Scientific, France). Data were collected over the range from 3000 to 1000 cm^{-1} using a laser wavelength λ_L of 632 nm and a spectral resolution of 1.5 cm^{-1}. An Olympus BX 41 microscope with a 50× objective, a beam cross-sectional diameter of 25 μm, and 3 scans per sample was used to collect the spectra.

Rigaku SmartLab diffractometer (Rigaku Corporation, Japan) was used to produce the X-ray powder diffraction (XRD) patterns of GICs, and EGs at room temperature. A Cu Kα radiation (λ = 1.5406 Å) at 40 KV and 30 mA with a scan range of 5 to 80° and step size of 0.02° was used to collect the spectra. Bragg-Brentano configuration was used to collect the data at room temperature.

GICs and EGs were analyzed by Thermo Scientific K-alpha X-ray Photoelectron Spectroscopy (XPS) (ThermoFisher Scientific, Waltham, Massachusetts, USA), where Al Kα gun source was used to excite the sample, and measurement was carried out for acquisition time of ~68 s at 400 µm spot size. The passing energy of 200 eV was utilized to find the C, O and S peaks in this analysis spectrum. The elemental analysis of C, O & S and the abundance of functional groups were investigated using the Avantage software. To determine the functional group's peak position and atomic percentage, Avantage software was used for deconvoluting C1s curve fitting utilizing Gaussian and Lorentzian functions.

Morphological characterization of EG filler and EG/polymer composites was carried out by high-resolution Field Emission Environmental Scanning Electron Microscopy (Quattro S FE-ESEM, ThermoFisher Scientific, USA). This SEM was operated in secondary electron (SE) mode at an accelerating voltage of 20 kV.

5.4 RESULT & DISCUSSION

5.4.1 Thermal Conductivity Measurement

A Netzsch LFA 467 Hyperflash was used to measure the through-thickness thermal diffusivity of the samples. The composite film samples of 0.5-0.8 mm thickness were cut into 12.5 mm diameter discs and coated with a thin layer of graphite paint. Thermal diffusivity measurements were performed at room temperature (23 °C) for 8-12 samples. Then, the thermal conductivity was calculated using $k = \alpha \times \rho \times Cp$, where k, ρ, and Cp represent the thermal conductivity, density, and specific heat constant of the sample, respectively. The density of composite sample was measured using the Pycnometer (Accu-Pyc II 1340, Micromeritics, US instrument). Rule of mixture formula was used to calculate the specific heat of composite where the specific heat of pure polymer and

expanded graphite were obtained from differential scanning calorimetry (DSC) (DSC 204F1 Phoenix, Netzsch, Selb, Germany). We measured the through-thickness thermal diffusivity (α) of EG paper using LFA 467 Hyperflash for 18-20 samples and averaged them to determine the thermal diffusivity value of EG paper.

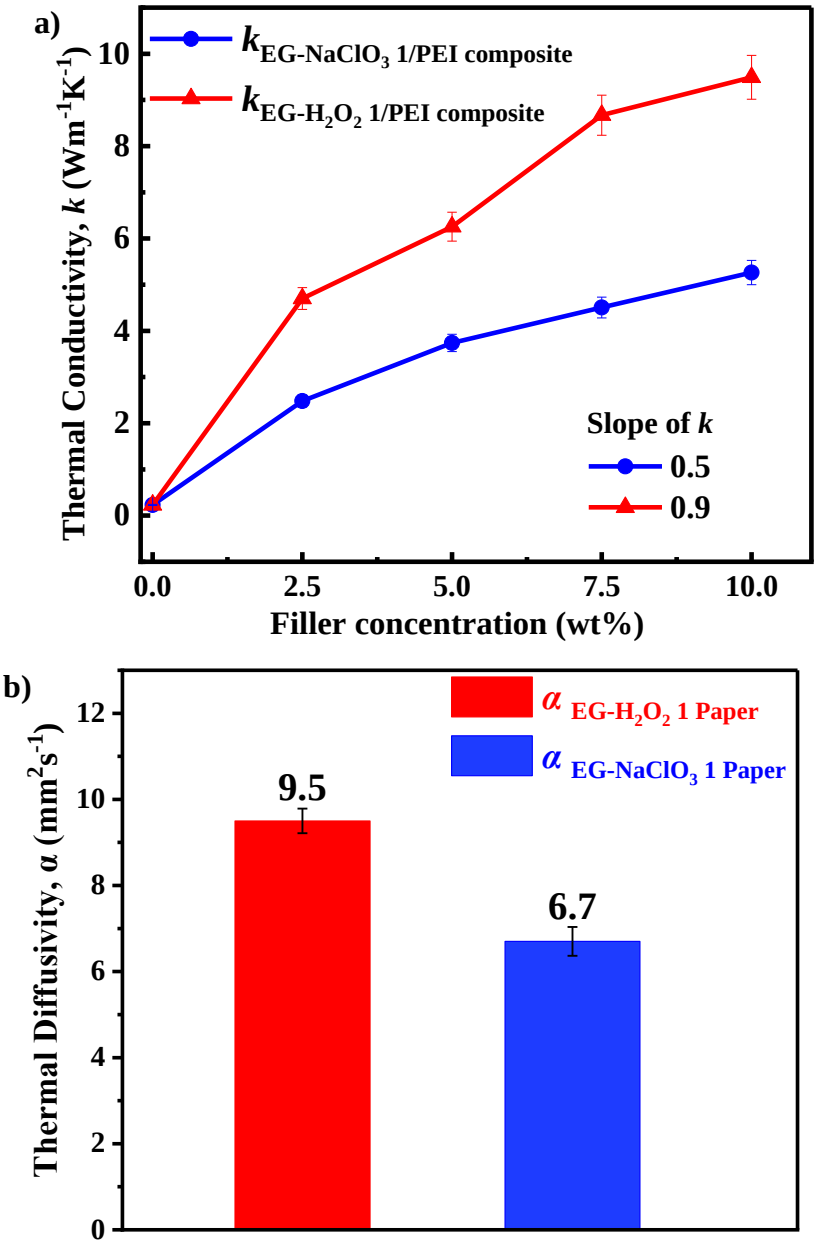

Figure 5.3 a) *k* value of EG-H_2O_2 1/PEI & EG-$NaClO_3$ 1/PEI composite at 2.5, 5, 7.5 and 10 wt% filler concentration, b) *α* value of EG-H_2O_2 1 & EG-$NaClO_3$ 1 paper.

5.4.2 Thermal Conductivity (*k*) Data Analysis

To compare the thermal properties of EG-H_2O_2 and EG-$NaClO_3$, the through-thickness thermal conductivity of expanded graphite polymer composite was measured. Comparison in thermal conductivity (*k*) value of EG/polymer composites for two auxiliary intercalating agents (H_2O_2 & $NaClO_3$) at different weight percentages-2.5, 5, 7.5 & 10 wt% of EG filler content has been presented in Figure 5.3a. With the addition of 2.5 wt% filler, the *k* of EG-H_2O_2 1/PEI composites significantly increased to 4.7 $Wm^{-1}K^{-1}$ (representing an increase of ~1944% with respect to pure PEI), while the *k* of EG-$NaClO_3$ 1/PEI composites only increased to 2.3 $Wm^{-1}K^{-1}$. Increasing the EG-H_2O_2 1 filler concentration to 5 and 7.5 wt%, increased *k* enhancement of EG-H_2O_2 1/PEI composites by ~2620% and ~3670% respectively,. The slope of the EG-H_2O_2 /PEI composite's *k* value (as shown in Figure 5.3a) is 0.9, on the other hand, the slope of the EG-$NaClO_3$ 1/PEI composite's *k* is relatively low (0.5). *k* value of EG-H_2O_2 1/PEI composites reaches up to 9.5 $Wm^{-1}K^{-1}$ for 10 wt% EG-H_2O_2 1 filler concentration, indicating a remarkable enhancement of ~4030% with respect to *k* of pure PEI (0.23 $Wm^{-1}K^{-1}$). In comparison, a *k* value of 5.3 $Wm^{-1}K^{-1}$ is achieved for EG-$NaClO_3$ 1/PEI composite with 10 wt% EG-$NaClO_3$ 1 filler concentration, showing ~2190% enhancement in *k* value compared to pure PEI polymer. Such outstanding enhancement of *k* for EG-H_2O_2 1/PEI relative to EG-$NaClO_3$ 1/PEI composite reveals the superior effect of EG-H_2O_2 1 filler over the EG-$NaClO_3$ 1 filler. This superior effect of EG-H_2O_2 filler can be explained in terms of structural integrity, optimum expansion volume, and presence of higher C=C/C-C bonding. Most importantly, H_2O_2 leads to edge oxidation during the intercalation route I, whereas $NaClO_3$ leads to basal plane oxidation during the intercalation route II, as shown in XPS analysis (shown in section 5.4.5). To verify the thermal conductivity of the expanded graphite prepared from the two intercalation routes, EG papers have been prepared to measure the through-thickness thermal

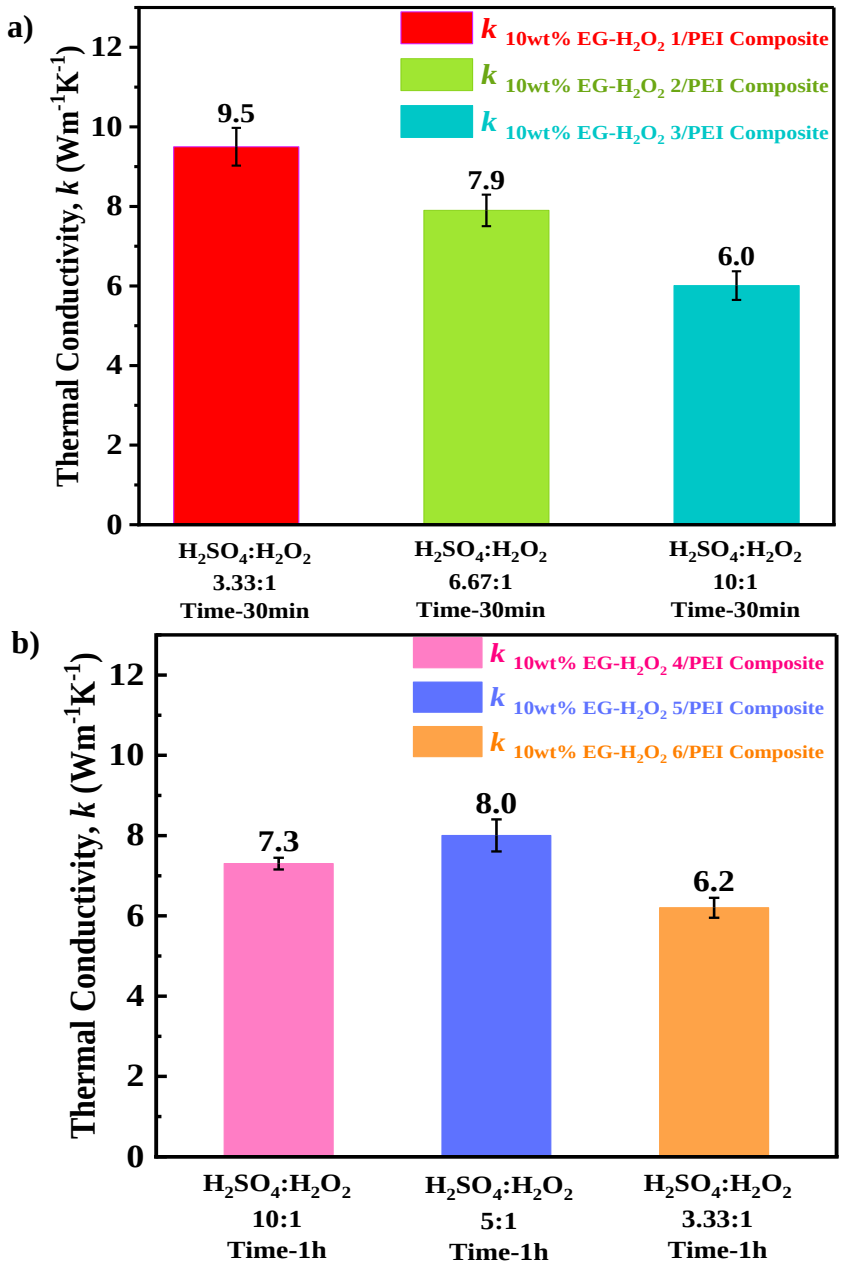

Figure 5.4 *k* value of 10 wt% EG-H_2O_2/PEI composites for a) different volume ratio of H_2SO_4:H_2O_2 for 20, 40, and 60 mL of H_2SO_4 respectively, b) different volume ratio of H_2SO_4:H_2O_2 for 2, 4, and 6 mL of H_2O_2 respectively.

diffusivity (α) and a higher α value has been found for EG-H_2O_2 1 paper as shown in Figure 5.3b. ~42% enhancement in α value for EG-H_2O_2 1 paper has been achieved compared to EG-$NaClO_3$ 1 filler.

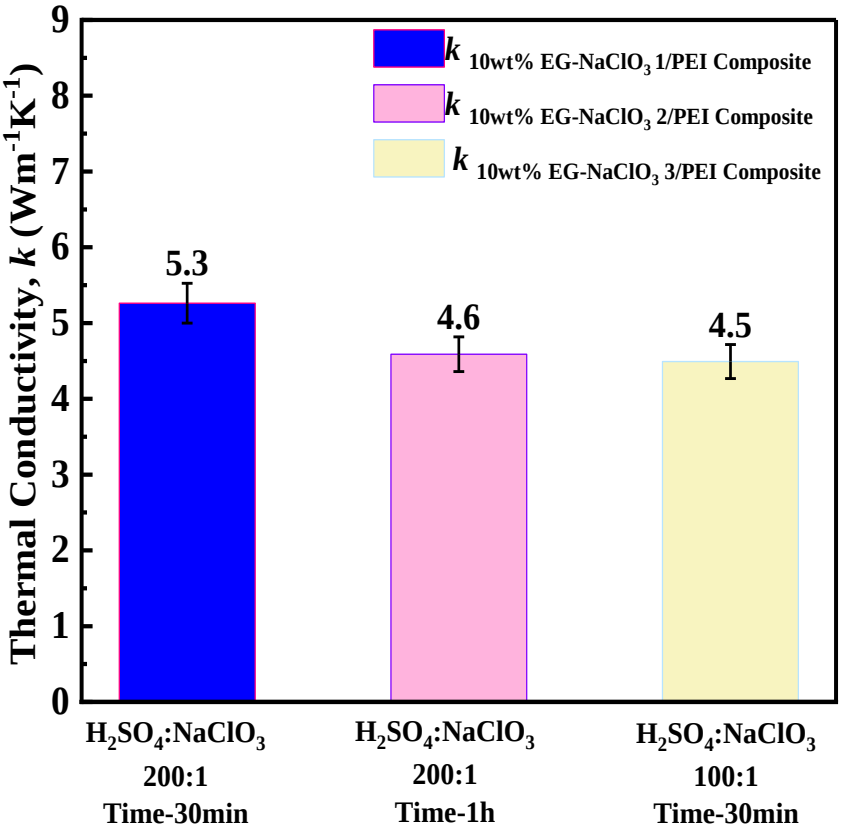

Figure 5.5 *k* value of 10 wt% EG-$NaClO_3$ /PEI composites with the different volume ratio of H_2SO_4: $NaClO_3$ and reaction time.

We have performed multiple reactions to optimize the volume ratio of H_2SO_4:H_2O_2 and reaction timeto achieve highest thermal conductivity. Initially, keeping the amount of H_2O_2 the same, the quantity of H_2SO_4 was changed to 20 ml, 40 ml & 60 ml, and 10 wt% EG-H_2O_2/PEI composite composites were prepared for different volume ratios of H_2SO_4 : H_2O_2 such as 3.33:1, 6.67:1 & 10:1. Figure 5.4a presents the *k* value of 10 wt% EG-H_2O_2 /PEI composite for different volume ratios of H_2SO_4:H_2O_2, and shows a decrease in composite *k* with increase in H_2SO_4 quantity. This is due to strong intercalation with higher amount of H_2SO_4, resulting in lower stage number in GIC-H_2O_2 and higher expansion volume of EG. The *k* value of 10 wt% EG-H_2O_2 1/PEI composite at a volume ratio of H_2SO_4:H_2O_2 (3:33:1) is found to be 9.5 $Wm^{-1}K^{-1}$; this decreases to 6 $Wm^{-1}K^{-1}$ for 10 wt% EG-H_2O_2 3/PEI composite at a volume ratio of 10:1. Due to the strong

intercalation, the defective structural morphology of EG filler is responsible for such reduction in *k* value as shown through Raman analysis (section 5.4.4).

We have also observed a change in the *k* value of EG-H_2O_2/PEI composite with an increase in H_2O_2 quantity at a similar dosage of H_2SO_4 .Figure 5.4b presents the thermal conductivity value of EG-H_2O_2/PEI composites for different volume ratios of 10:1, 5:1 & 3.33:1 at 2 ml, 4 ml and 6 ml of H_2O_2, respectively and 1 h of intercalation time. *k* value of EG-H_2O_2 4/PEI composite is 7.3 $Wm^{-1}K^{-1}$ for 10 wt% EG-H_2O_2 4 filler loading and *k* value increases to 8 $Wm^{-1}K^{-1}$ for 10 wt% EG-H_2O_2 5 filler loading. In contrast, 10 wt% EG-H_2O_2 6 filler composition sample leads to a reduced *k* value of 6.2 $Wm^{-1}K^{-1}$. For the case of 2 ml & 4 ml H_2O_2, the intercalation process does not complete with 20 ml H_2SO_4 for 60 min reaction time to reach optimum expansion volume. Optimum synthesis condition of 20 ml H_2SO_4 , 6 ml H_2O_2, and 30 min leads to optimum expansion volume and superior thermal conductivity of 9.5 $Wm^{-1}K^{-1}$ for 10 wt% EG-H_2O_2 1/PEI composite.

We also have studied variation in *k* value of EG-$NaClO_3$/PEI composite with different quantities of H_2SO_4 & $NaClO_3$ and for different intercalation times. Figure 5.5 represents the *k* value of EG-$NaClO_3$/PEI composite for different volume ratios of 200:1 and 100:1. For a minimal amount of 0.25 g $NaClO_3$ and at volume ratio of H_2SO_4 : $NaClO_3$ (200:1), *k* value of EG-$NaClO_3$ 1/PEI composite reaches 5.3 $Wm^{-1}K^{-1}$ for 10 wt% EG-$NaClO_3$ 1 filler composition. The *k* value of EG-$NaClO_3$ 2/PEI composite is decreased to 4.6 $Wm^{-1}K^{-1}$ as the intercalation time increases from 30 min to 1 h. Higher intercalation time to prepare the GIC-$NaClO_3$ for the same amount of oxidant leads to more intercalation and lower stage number, leading to higher expansion volume. On the other hand, higher oxidation leads to higher structural defects as shown in XPS and Raman analysis, resulting in lower *k* value. Also, a higher amount of $NaClO_3$ at volume ratio of H_2SO_4 : $NaClO_3$ (100:1) has negative impact on EG-$NaClO_3$ 3/PEI composite's *k* value, leading to lower

k value of 4.5 $Wm^{-1}K^{-1}$ compared to EG-$NaClO_3$ 1/PEI composite. The measured *k* value does not increase at higher quantity of H_2SO_4 used in the reaction. Optimum reaction condition at a volume ratio of H_2SO_4: $NaClO_3$ (200:1) and 30 min intercalation time reveals a *k* value of to 5.3 $Wm^{-1}K^{-1}$.

Additionally, the nature of oxidation greatly impacts the EG filler's structural integrity as well as the thermal conductivity of EG/PEI composite, as discussed in chapter 2 in detail. According to the XPS analysis as discussed in section 5.4.5, we have found significant differences in oxidation degree and the presence of functional groups for GIC-H_2O_2 1& EG-H_2O_2 1 in contrast to GIC-$NaClO_3$ 1& EG-$NaClO_3$ 1.

Furthermore, the degree and location of oxidation have a significant impact on the structural integrity of the EG filler as well as the thermal conductivity of the EG/PEI composite, as explored in detail in Chapter 2. We noticed a substantial difference in oxidation degree and the location-dependent functional groups for GIC-H_2O_2 1& EG-H_2O_2 1 in comparison to GIC-$NaClO_3$ 1& EG-$NaClO_3$ 1 in the XPS study reported in section 5.4.5. According to location of functional groups of graphite oxide, the percentage of bassal plane functional groups (C-O-C & C-O) are larger in quantity than edge functional groups (C=O, O=C-O) for $NaClO_3$. The GIC-H_2O_2 1 & EG-H_2O_2 1, on the other hand, contain a higher percentage of edge functional groups than basal plane functional groups.

It is important to mention that basal plane oxidation leads to distortion of sp^2 carbon structure due to attachment of the functional groups on the basal plane, increasing phonon scattering, and dramatically reducing intrinsic thermal conductivity of graphene. On the contrary, edge oxidation avoids distortion of the basal plane area leading to higher intrinsic *k* of graphene.

5.4.3 Formation and Expansion Volume of GICs and EG Fillers

To intercalate graphite, H_2O_2 and H_2SO_4 were used to prepare GIC-H_2O_2, where H_2SO_4 was used as a primary intercalating agent and H_2O_2 as an auxiliary intercalating agent or oxidizing agent for the intercalation route I. The addition of oxidant, H_2O_2 into H_2SO_4 raises the temperature and causes self-decomposition of H_2O_2 according to Eq. 5.5. For the case of intercalation using H_2O_2, the synthesis was carried out using a cold ice bath to maintain the temperature at 20-25 °C. We have utilized the strategy to intercalate graphite using oxidant H_2O_2 so that H_2O_2 helps to open up the edges of graphite with simultaneous insertion of HSO_4^- and SO_4^{2-} ions into graphite from H_2SO_4. Such intercalation process leads to a separation of graphene layers releasing O_2 (Eq. 5.6) and yielding GIC-H_2O_2 as shown in Figure 5.6a. Self-decomposition of H_2O_2 leads to a pre-expansion phenomenon before the GIC-H_2O_2 is exposed to high-temperature treatment for expansion.

The effect of different volume ratios of H_2SO_4: H_2O_2 on optimum expansion volume to achieve superior thermal conductivity is studied and described in the next section. The expansion volume of GIC and EG was recorded for different volume ratios of H_2SO_4: H_2O_2 in Table 5.3 as presented in Figure 5.7a-d and surface morphology through expansion was investigated using FE-ESEM in section 5.4.7. Intercalation process of graphite with an increased amount of H_2SO_4 produces more O_2 without allowing much time for this generated O_2 to escape, pushing the microchannels of graphite layers apart. Thus, an increased volume of graphite particles GIC-H_2O_2 is obtained after different reaction processes of 2 g 10 mesh graphite as shown in Figure 5.7a-d. The expansion volume after thermal shock increases with an increasing amount of H_2O_2 up to 3.33:1(20 ml:6 ml) volume ratio but the increased amount of H_2O_2 also produces a significant amount of O_2, which

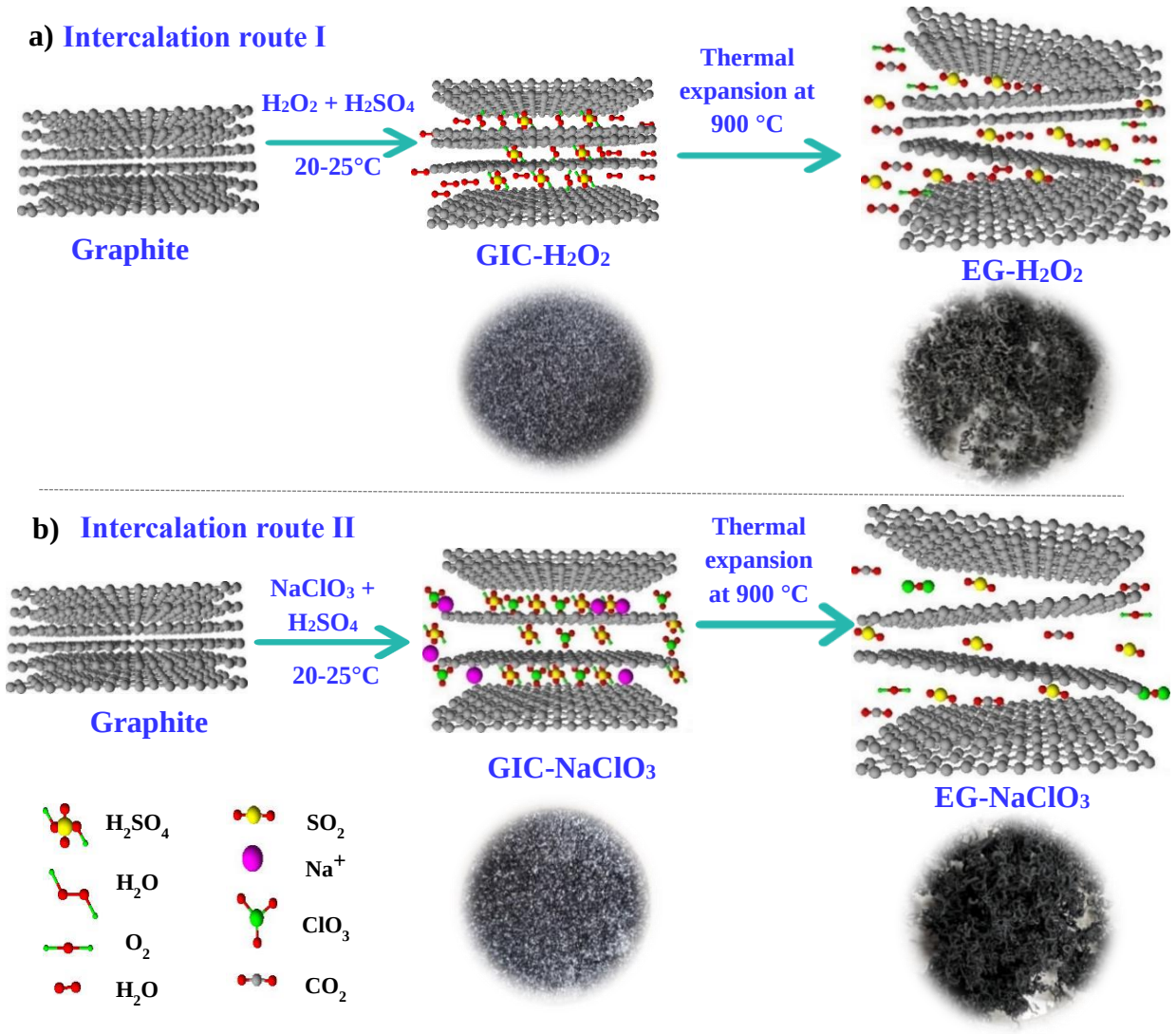

Figure 5.6 a) Schematic illustration of the preparation process of a) GIC-H_2O_2 & EG-H_2O_2, b) GIC-$NaClO_3$ & EG-$NaClO_3$.

causes excessive exfoliation of graphite. Furthermore, higher amount of H_2SO_4 leads to more intercalation, following the reaction below, so the volume of graphite particles increases even after the reaction because of pre-expansion.

$$2H_2O_2 \rightarrow 2H_2 + O_2 \quad (5.5)$$

$$H_2SO_4 + H_2O_2 \rightarrow H_3O^+ + HSO_4^- + O \cdot \quad (5.6)$$

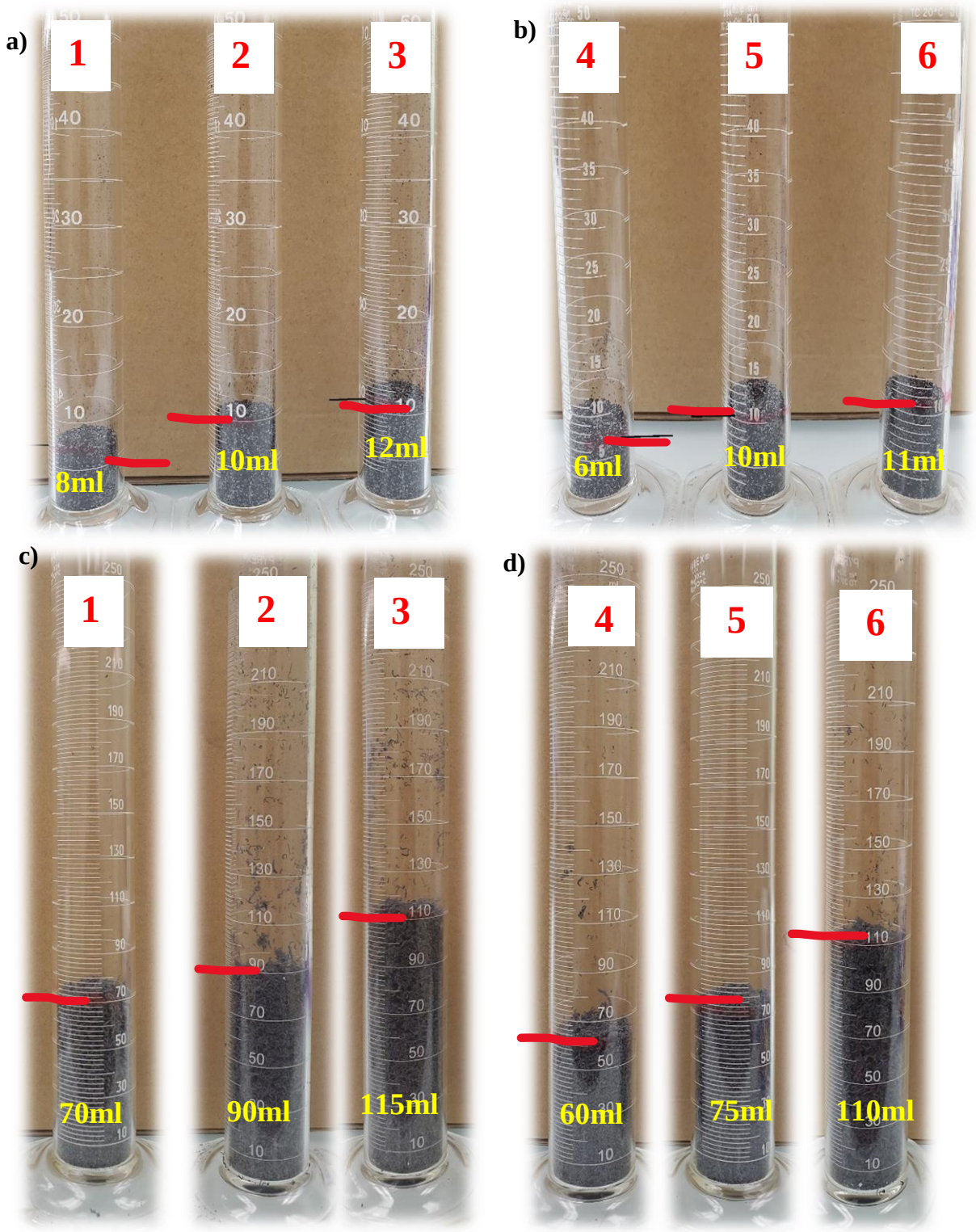

Figure 5.7 Expansion volume (EV) of a) GIC-H_2O_2 1, 2 & 3, b) GIC-H_2O_2 4, 5 & 6, c) EG-H_2O_2 1, 2 & 3, d) EG-H_2O_2 4, 5 & 6.

Oxidant H_2O_2, known as a green oxidizer, allows oxidation to graphite with non-toxic bi-products and involves an easy washing procedure. Such oxidation process causes insignificant damage to graphite and provides optimum expansion volume to achieve higher thermal conductivity.

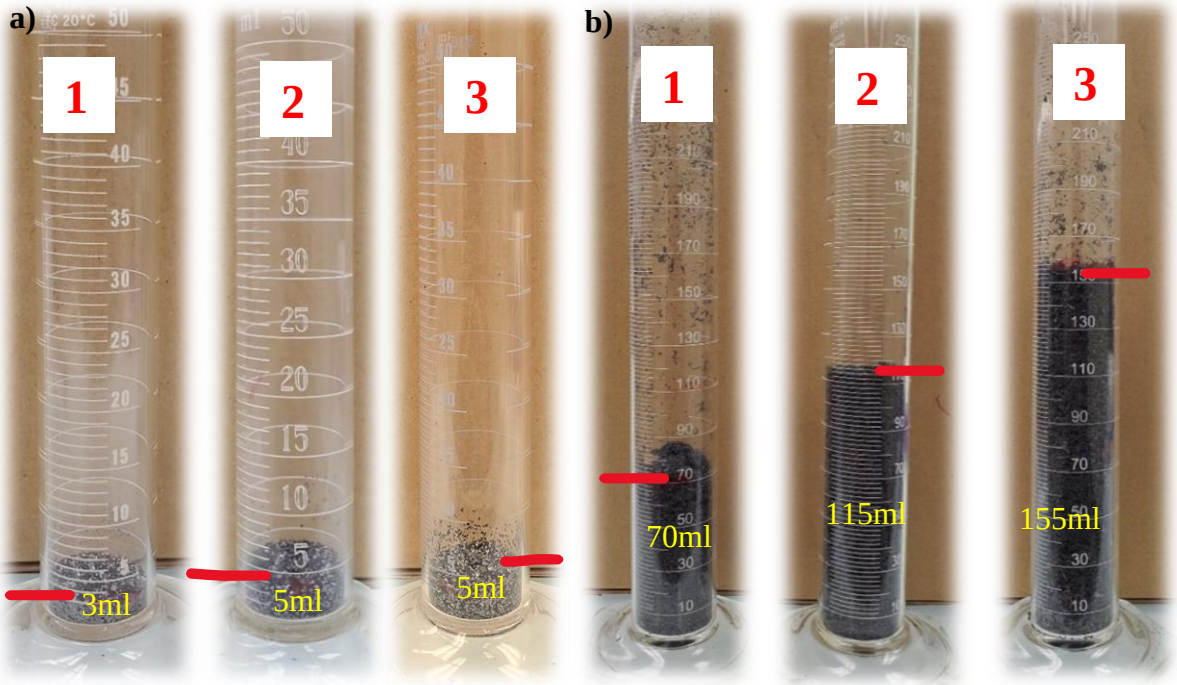

Figure 5.8 Expansion volume of a) GIC-$NaClO_3$ 1, 2 & 3, and b) EG-$NaClO_3$ 1, 2 & 3.

Another oxidant, sodium chlorate ($NaClO_3$) has been employed with H_2SO_4 to obtain sodium chlorate intercalated graphite compound (GIC-$NaClO_3$) and thermally expanded graphite, EG-$NaClO_3$ to observe the effect on thermal conductivity of EG-$NaClO_3$ polymer composite. The preparation process of GIC-$NaClO_3$ also involves performing reactions at room temperature of 20-25 °C. $NaClO_3$ has been used as a strong oxidizer for Brodie's and Staudenmaier's methods with other oxidizing agents[283,284]. With respect to previous work, the intercalation and oxidation effect of this oxidizer on EG has been observed in this work. With the intercalation of acceptor bisulfate compound, sodium ion gets diffused into the interlayer spacing as shown in Figure 5.6b and results

in strong intercalation with lower stage number as evident through characterization analysis. During the reaction, oxygen groups attach to the basal plane structure and delamination possibly occurs. The reaction takes place during intercalation route II as mentioned below.

$$3NaClO_3 + 2H_2SO_4 \rightarrow 2NaHSO_4 + 2ClO_2 + NaClO_4 + H_2O \quad (5.7)$$

Table 5.3 Exfoliation volume and weight loss (%) for GICs & EG fillers.

Sample name	Expansion volume (ml/g)	Weight loss (%)
GIC-H_2O_2 1	8	-
EG-H_2O_2 1	70	17
GIC-H_2O_2 2	10	-
EG-H_2O_2 2	90	20
GIC-H_2O_2 3	12	-
EG-H_2O_2 3	115	42
GIC-H_2O_2 4	6	-
EG-H_2O_2 4	60	14
GIC-H_2O_2 5	10	-
EG-H_2O_2 5	75	24
GIC-H_2O_2 6	11	-
EG-H_2O_2 6	110	45
GIC-$NaClO_3$ 1	3	-
EG-$NaClO_3$ 1	70	21
GIC-$NaClO_3$ 2	5	-
EG-$NaClO_3$ 2	115	40
GIC-$NaClO_3$ 3	5	-
EG-$NaClO_3$ 3	155	55

Different volume ratios have been explored to achieve the optimum reaction condition for enhancing the thermal conductivity of EG-$NaClO_3$/PEI composites. The expansion volume of GICs and EGs with different volume ratios of H_2SO_4: $NaClO_3$ is presented in Figure 5.8a & b and

recorded in Table 5.3. At a very small amount of $NaClO_3$, the expansion volume of EG is 70 ml/g indicating higher intercalation effect than EG-H_2O_2. Controlling the reaction process allows variation in the volume ratio. Optimum expansion volume of 70 ml/g of EG-H_2O_2 1 and EG-$NaClO_3$ 1 has been utilized for preparing the composite to achieve the highest thermal conductivity in both the case.

5.4.4 Raman Analysis

Raman spectroscopy is used to investigate the structural and chemical changes of graphite structure because of the intercalation & oxidation process. Typically, the Raman spectra of graphite exhibit the characteristic G, D & 2D peaks at ~1572 cm^{-1}, ~1330 cm^{-1}, and ~2680 cm^{-1} [285-287] respectively as presented in Figure 5.9a and Table 5.4 for 10 mesh graphite. The strong G peak is attributed to the vibration due to sp^2 hybridized carbon structure; the D peak is caused due to sp^3 hybridized carbon lattice defects[157]. The prominent 2D peak is the second order of the D peak caused by in-plane transverse optical phonons near the boundary of the Brillouin zone due to the electronic band structure, and always shows the double peak structure for graphite[288]. This shape and position of the 2D peak are useful for understanding the thickness of graphite[289].

Table 5.4 Raman peak positions and I_D/I_G of GIC-H_2O_2 & EG-H_2O_2 fillers.

Sample name	G band (cm^{-1})	D band (cm^{-1})	2D band (cm^{-1})	I_D/I_G
10 Mesh Graphite	1572	1332	2680	0.13
GIC-H_2O_2 1	1572	1326	2677	0.05
EG-H_2O_2 1	1573	1331	2680	0.04
GIC-H_2O_2 2	1571	1324	2676	0.06
EG-H_2O_2 2	1572	1324	2679	0.05
GIC-H_2O_2 3	1571	1331	2680	0.09
EG-H_2O_2 3	1582	1335	2687	0.1

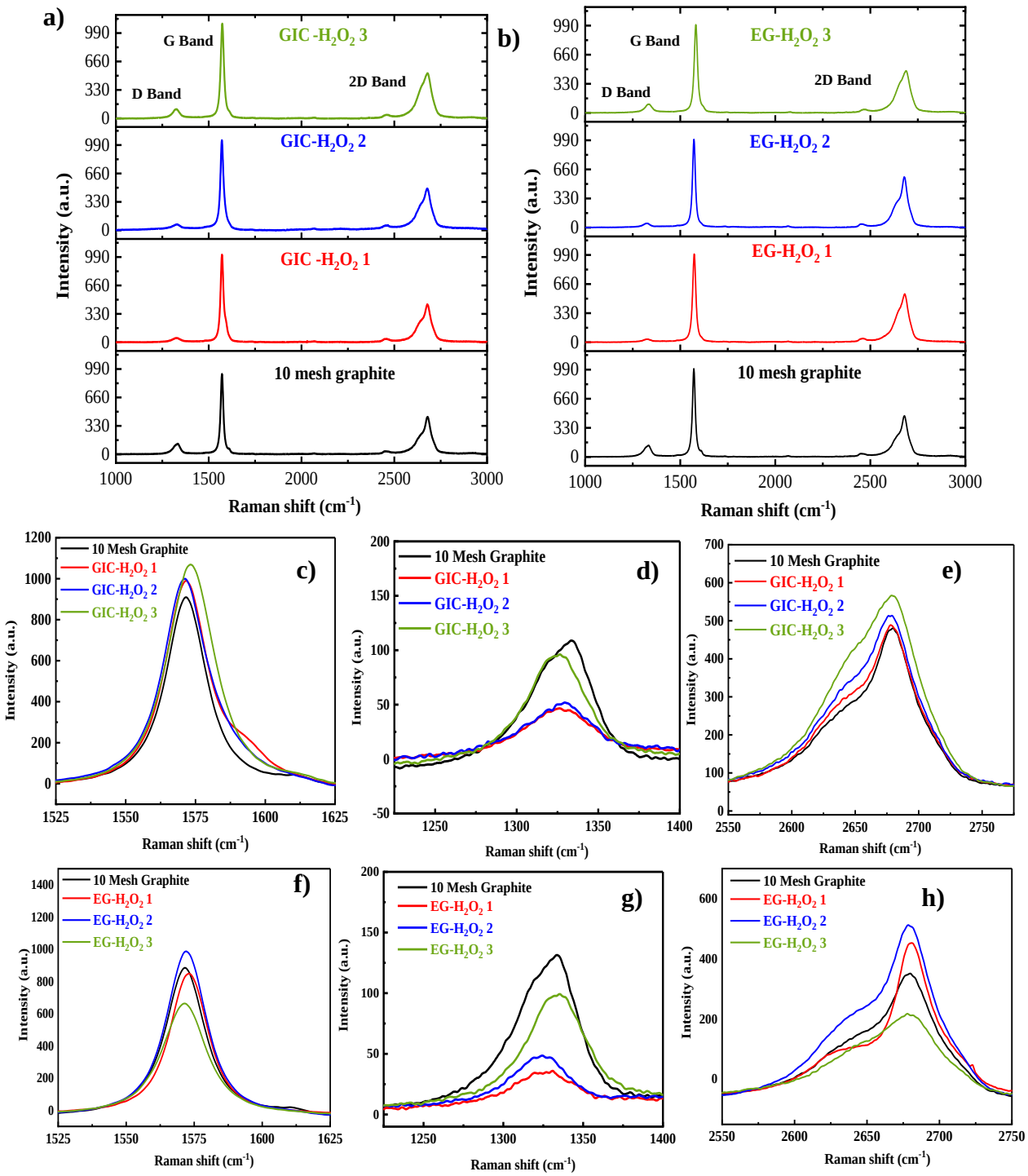

Figure 5.9 Raman spectra of a) GIC-H_2O_2 1, 2 & 3, and b) EG-H_2O_2 1, 2 & 3. c) G band line, d) D band line, e) 2D band line of GIC-H_2O_2 1, 2 & 3, f) G band line, d) D band line, e) 2D band line of EG-H_2O_2 1, 2 & 3.

The peak positions for GICs and EG fillers for intercalating agent H_2O_2 are presented in Table 5.4. We have estimated the I_D/I_G ratio for the GICs and EG fillers after the intercalation and thermal expansion to analyze the defective state of structure in graphite layers as reported in Table 5.4. I_D/I_G of 10 mesh graphite indicates the presence of defects in graphite structure as associated with the functional groups attached to the graphite shown in XPS analysis. Figure 5.9a & b present the Raman spectra of GIC-H_2O_2 1, 2 & 3 and EG-H_2O_2 1, 2 & 3 respectively to compare the change in carbon material due to the intercalation process and heat treatment. Figure 5.9 c, d & e show the G, D & 2D peak intensity of GIC-H_2O_2 1, 2 & 3 with an increase in the amount of H_2SO_4 respectively, and Figure 5.9 f, g & h show the G, D & 2D peak intensity of EG-H_2O_2 1, 2 & 3 after the thermal treatment. Figure 5.9 c-h clearly depict the change in intensity with the increase of H_2SO_4 for intercalation with H_2O_2. I_D/I_G ratios for GIC-H_2O_2 1, 2 & 3 are 0.05, 0.06, and 0.09, indicating an increase in degree of defect with the higher amount of H_2SO_4. Due to self-decomposition of H_2O_2, GICs have even lower I_D/I_G ratio than 10 mesh graphite. Similarly, I_D/I_G ratios for EG-H_2O_2 filler show similar trend in the degree of defect. I_D/I_G ratio increases from 0.04 to 0.1 with the change in the amount of H_2SO_4 from 20 ml to 40 ml. Additionally, the change in peak position and asymmetric broader peak for GICs and EG fillers compared to 10mesh graphite as shown in Figure 5.9 c-h refers to the oxidation effect. In Figure 5.9 e and h, the 2D peak position does not degrade to much lower wavenumber compared to 2D peak position of 10mesh graphite indicating higher stage number for the intercalation route with H_2O_2. The stronger G peak intensity in EG-H_2O_2 1, 2 & 3 fillers refers to the better structural integrity, consistent with the XRD (Section 5.4.6) and XPS analysis (Section 5.4.5). The thermal conductivity value of EG-H_2O_2 1, 2 & 3 PEI composites appears to be similarly decreased with higher degree of defect in graphite's structure.

Table 5.5 Raman peak positions and I_D/I_G of GIC-$NaClO_3$ & EG-$NaClO_3$ fillers.

Sample name	G band (cm^{-1})	D band (cm^{-1})	2D band (cm^{-1})	I_D/I_G
10 Mesh Graphite	1572	1332	2680	0.13
GIC-$NaClO_3$1	1574	1326	2680	0.35
EG-$NaClO_3$ 1	1574	1332	2676	0.25
GIC-$NaClO_3$ 2	1578	1325	2667	0.75
EG-$NaClO_3$ 2	1575	1332	2678	0.28
GIC-$NaClO_3$ 3	1577	1332	2678	0.62
EG-$NaClO_3$ 3	1573	1324	2680	0.26

The peak positions and I_D/I_G ratio for GICs and EG fillers for intercalating agent $NaClO_3$ are presented in Table 5.5. Figure 5.10a & b portray the Raman spectra of GIC-$NaClO_3$ 1, 2 & 3 and EG-$NaClO_3$ 1, 2 & 3 indicating the change in the defective state of carbon material due to the intercalation process and heat treatment respectively. Figure 5.10 c, d & e show the G, D & 2D peak intensity of GIC-$NaClO_3$ 1, 2 & 3 with the increase in the quantity of $NaClO_3$ and intercalation time. Figure 5.10 f, g & h show the G, D & 2D peak intensity of EG-$NaClO_3$ 1, 2 & 3 after the thermal treatment compared to pristine graphite. Figure 5.10 c-h clearly illustrate the change in intensity with the increase of H_2SO_4 for intercalation with $NaClO_3$. I_D/I_G ratio increases from 0.35 to 0.75 for GIC-$NaClO_3$ 1 and 2, indicating an increase in the degree of defect with the higher intercalation time. An increase in I_D/I_G ratio (0.62) for GIC-$NaClO_3$ 3 signifies an increased degree of defect with the higher amount of $NaClO_3$. I_D/I_G ratios of EG-$NaClO_3$ 1, 2 & 3 are 0.25, 28 & 0.23, show the similar trend in degree of defect. Overall, the I_D/I_G ratio for EG-$NaClO_3$ is higher

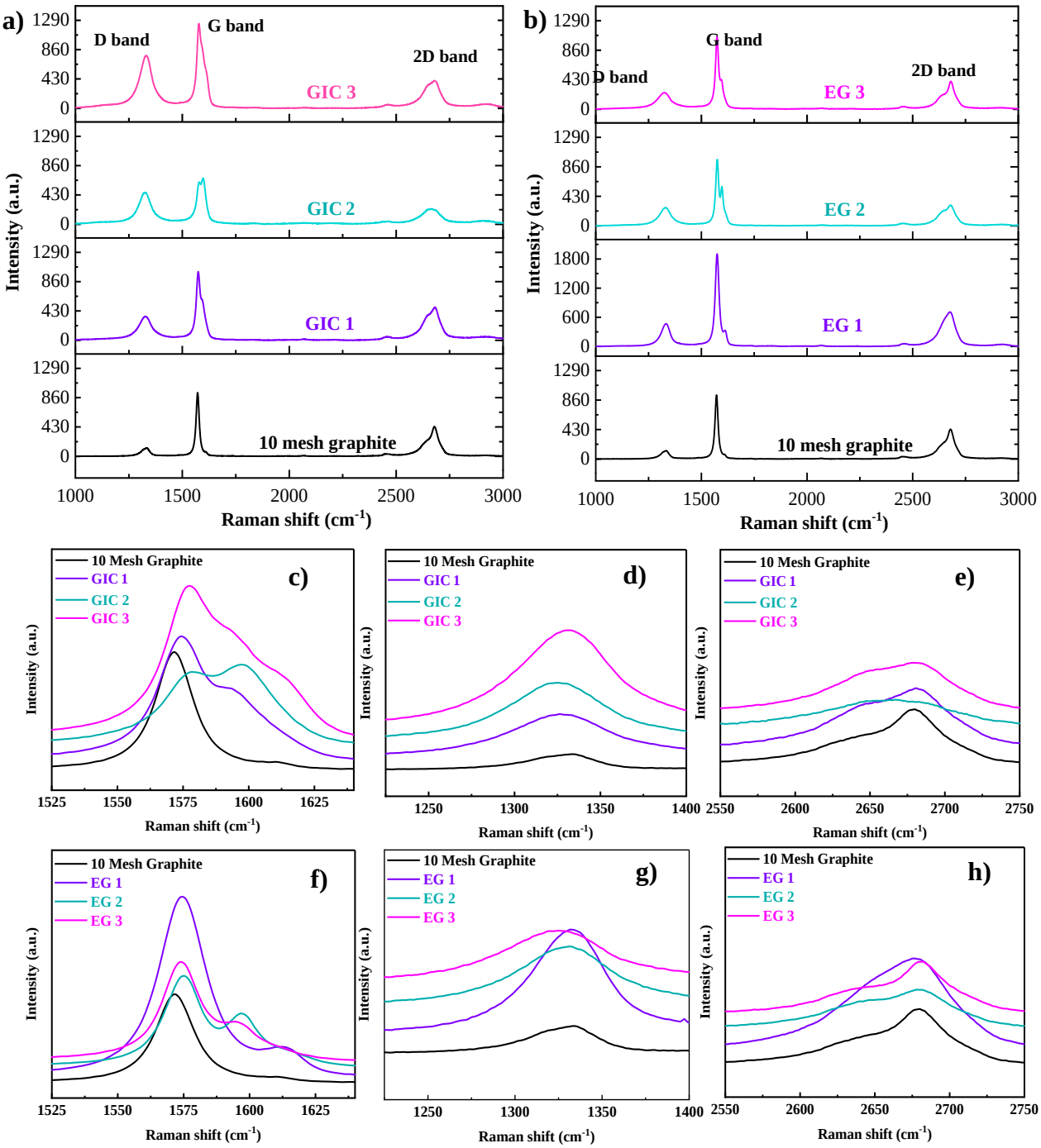

Figure 5.10 Raman spectra of a) GIC-$NaClO_3$ 1, 2 & 3, and b) EG-$NaClO_3$ 1, 2 & 3. c) G band line, d) D band line, and e) 2D band line of GIC-$NaClO_3$ 1, 2 & 3, f) G band line, g) D band line, and h) 2D band line of EG-$NaClO_3$ 1, 2 & 3.

due to the effect of stronger intercalating agent, $NaClO_3$. Figure 5.10 c & f show the broader G

peak and change in peak position and Figure 5.10 d & g show the broader D peak of GIC-$NaClO_3$ 1, 2 & 3 and EG-$NaClO_3$ 1, 2 & 3 because of higher disorder in the graphite structure. Also, another peak ~1600 cm^{-1} close to the G peak (shown in Figure 5.10 d & g) suggests large-scale damage and deformation to the graphitic crystalline structure due to oxidation [refer]. The comparison of I_D/I_G ratios of EG-$NaClO_3$ 2 and 3 reveals that the intercalation time affects more than the amount of $NaClO_3$. Therefore, the higher thermal conductivity value of EG-$NaClO_3$ 1 PEI composite than other EG-$NaClO_3$/PEI composite is due to such a lower I_D/I_G ratio.

Raman spectra of GIC-H_2O_2 1 & GIC-$NaClO_3$ 1 and EG-H_2O_2 1 & EG-$NaClO_3$ 1 fillers for intercalating agent H_2O_2 and $NaClO_3$ are depicted in Figure 5.11a &b to observe graphitic structural damage, happened during the intercalation and expansion process. We can see I_D/I_G ratio (0.25) of EG $NaClO_3$ 1 is higher than I_D/I_G ratio (0.04) for EG-H_2O_2 1. Figure 5.11 c, d & e show the G, D & 2D peak intensity of EG-H_2O_2 1 & EG-$NaClO_3$ 1. The D peak of Figure 5.11 d & f shows the higher intensity of EG-$NaClO_3$ 1 than EG-H_2O_2 1 filler. Another peak, ~1610 cm^{-1} close to G band, is visible in Figure 5.11c & f for GIC-$NaClO_3$ and EG-$NaClO_3$, which can be explained as the induced defect due to the strong oxidation effect is absent in GIC-H_2O_2 & EG-H_2O_2 spectrum. A broader 2D peak of EG-$NaClO_3$ 1 suggests a lower stage number than EG-H_2O_2 1 Figure 5.11 e & h. The structural integrity of carbon material plays a key role in the thermal properties of carbon-based polymer composites field[155,290]. Incorporation of EG-H_2O_2 1 filler with lower I_D/I_G ratio results in superior thermal conductivity due to less defective carbon structure.

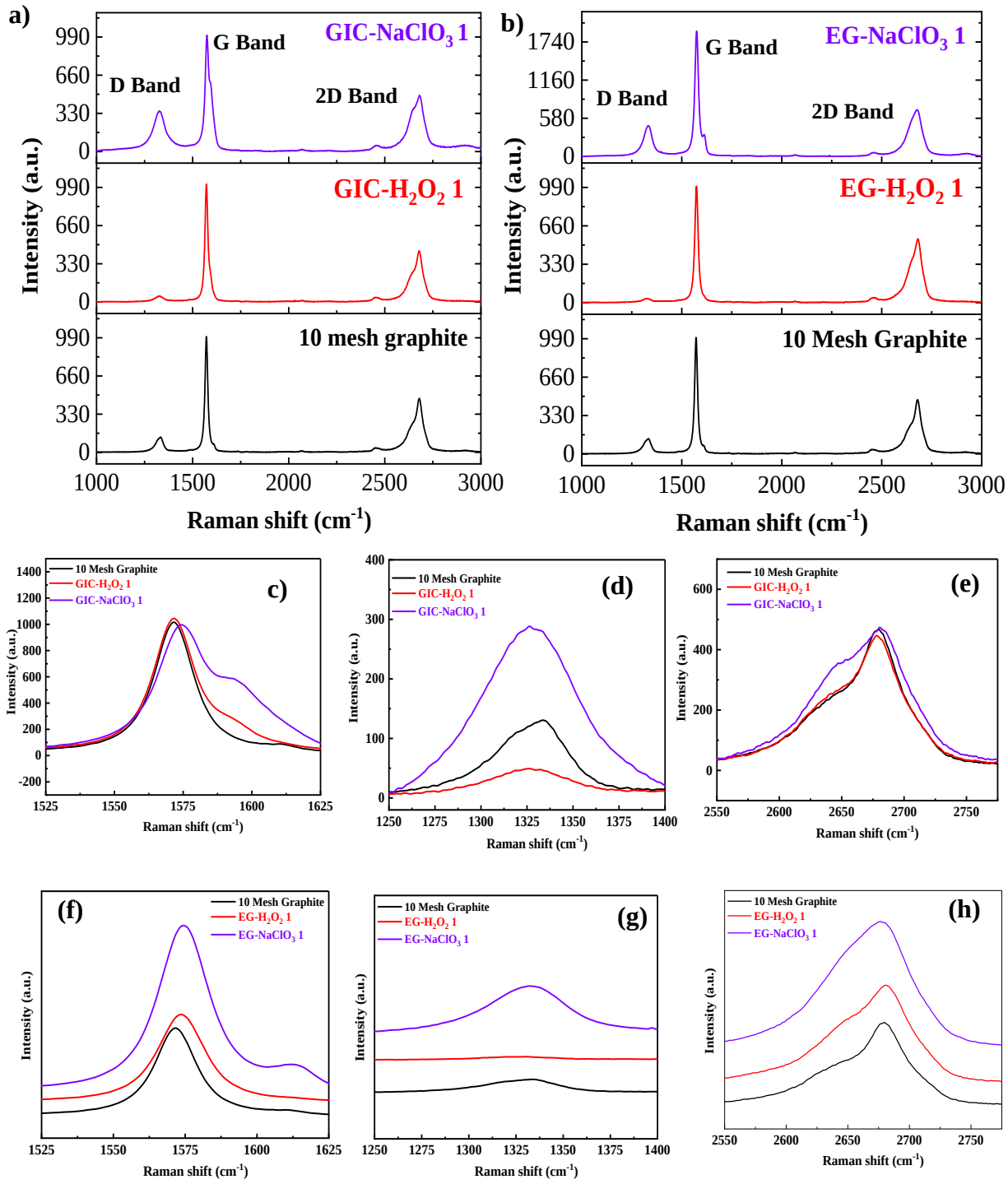

Figure 5.11 Raman spectra of a) GIC-H_2O_2 1 & GIC-$NaClO_3$ 1, and b) EG-H_2O_2 1 & EG-$NaClO_3$ 1. c) G band line, d) D band line, and e) 2D band line of GIC-H_2O_2 1 & GIC-$NaClO_3$ 1, f) G band line, g) D band line, and h) 2D band line of EG-H_2O_2 1 & EG-$NaClO_3$ 1.

5.4.5 Chemical Composition Analysis of GICs and EG Fillers by XPS

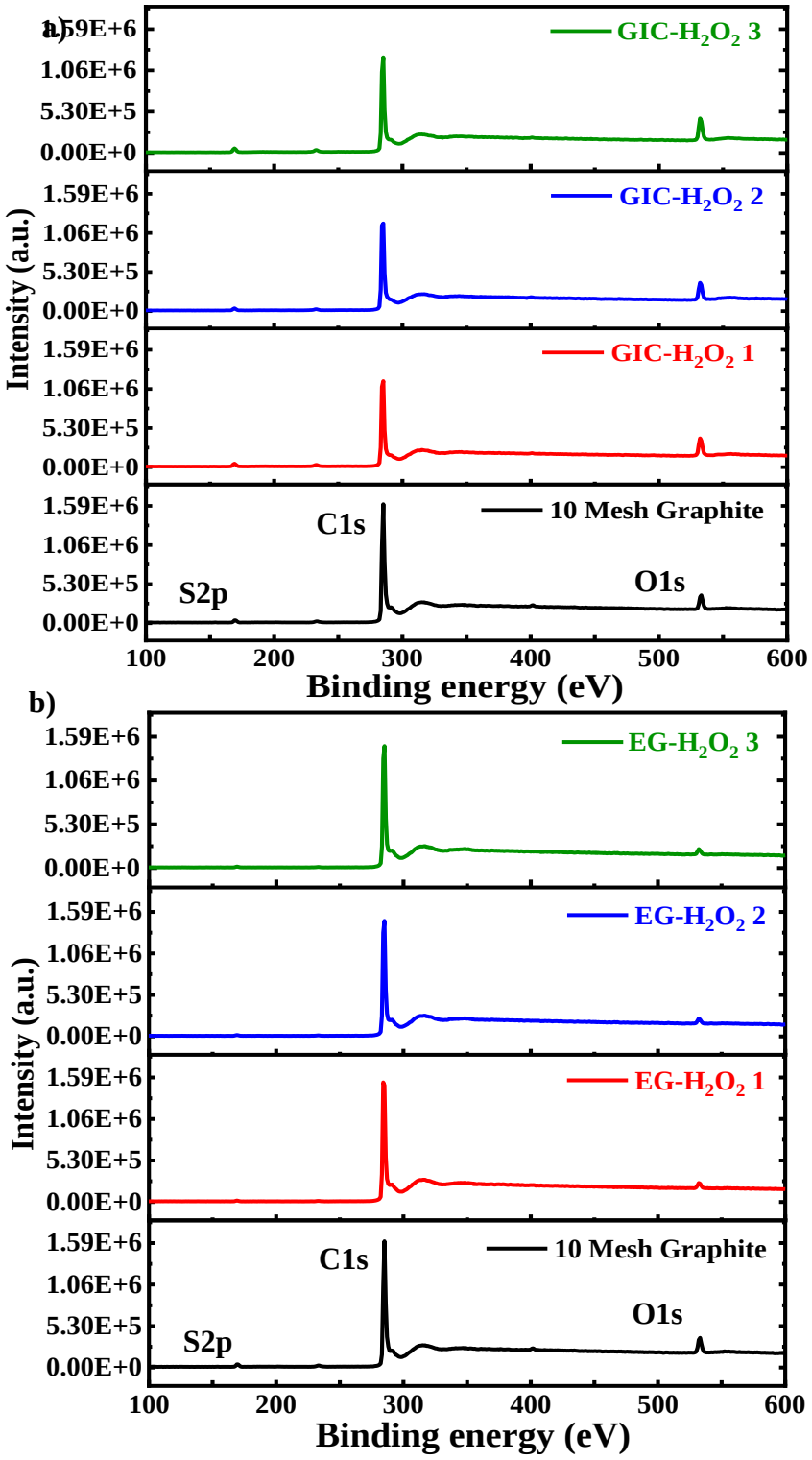

Figure 5.12 a) XPS spectra of GIC-H_2O_2 1, 2 & 3 and b) EG-H_2O_2 1, 2 & 3.

X-ray photoelectron spectroscopy (XPS) analysis reveals the chemical composition and binding states of GICs and EG fillers. Figure 5.12a & b and Figure 5.13a &b show the presence of C1s peak at ~285 eV, strong O1s peaks at ~532 eV, and weaker S2p peak at ~169 eV[157,291] for 10 mesh graphite, GICs, and EG fillers because of intercalation using H_2O_2 & $NaClO_3$ and thermal expansion. Table 5.6 presents the atomic percentage of C, O, and S, and C/O ratio for GICs and EG fillers. The atomic percentage of C shows that the C content decreases and O increases with higher intercalation using a larger quantity of H_2SO_4. The increase in H_2SO_4:H_2O_2 volume ratio from 3.33 to 10 results in a reduction in C/O ratio from 10.8 for GIC-H_2O_2 1 to 8.8 for GIC-H_2O_2 3. After thermal expansion, the C/O ratio similarly decreases from 44.2 for EG-H_2O_2 1 to 25.3 for EG-H_2O_2 3. We have achieved higher *k* value (9.5 $Wm^{-1}K^{-1}$) for EG-H_2O_2 1 composition, which decreases to 6 $Wm^{-1}K^{-1}$ for EG-H_2O_2 3 due to higher oxidation.

Figure 5.13 a & b present the XPS spectra of GICs and EG fillers, respectively showing three characteristic peaks of C, O, and S for intercalation route, $NaClO_3$. Analysis of the C/O ratio of GIC 1, 2 & 3 suggests a decrease in carbon content with the use of the higher quantity of strong oxidant, $NaClO_3$ and higher intercalation time, which also raises the content of sulfur. For optimum thermal conductivity, the C/O ratio is found to be 6.7 at a lower amount of $NaClO_3$ and lower intercalation time of 30 min. After thermal treatment, the C/O ratio of EG shows a similar trend as for GIC. EG-$NaClO_3$1 has the highest carbon content of almost 95% and provides a higher *k* value relative to other EG-$NaClO_3$ fillers. In addition, sulfur content still is present in EG-$NaClO_3$ fillers due to the substantial intercalation effect. C/O ratio of EG-H_2O_2 1 (44.2) is significantly higher than that of EG-$NaClO_3$ 1 (22.7), indicating that higher carbon content is preserved in intercalation route I after thermal expansion, resulting in superior *k* value of EG-H_2O_2 1/PEI composite than that of EG-$NaClO_3$1/PEI composite.

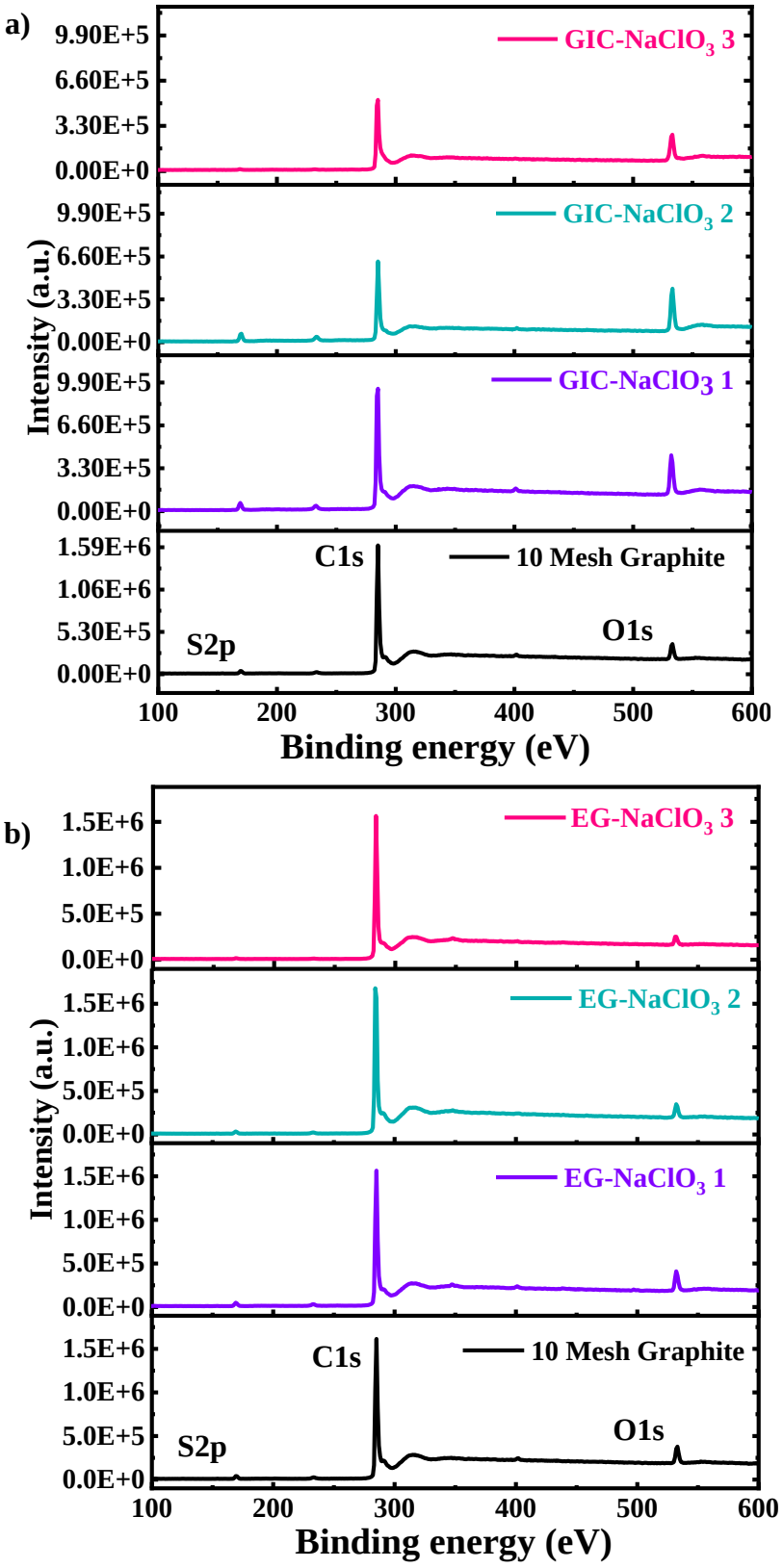

Figure 5.13 a) XPS spectra of GIC-$NaClO_3$ 1, 2 & 3, and b) EG-$NaClO_3$ 1, 2 & 3.

Table 5.6 Atomic composition and C/O ratio by XPS analysis of graphite, GICs, and EG- fillers.

Samples	Atomic Composition by XPS (at%)			C/O ratio
	C (~285 eV)	O (~532 eV)	S (~169 eV)	
10 mesh graphite	93.44	5.47	1.09	17.1
GIC-H_2O_2 1	90.4	8.35	1.24	10.8
EG-H_2O_2 1	97.79	2.21	-	44.2
GIC-H_2O_2 2	89.47	8.81	1.72	10.1
EG-H_2O_2 2	96.5	3.5	-	27.6
GIC-H_2O_2 3	87.84	9.99	2.17	8.8
EG-H_2O_2 3	96.2	3.8	-	25.3
GIC-$NaClO_3$ 1	84.85	12.63	2.52	6.7
EG-$NaClO_3$ 1	94.97	4.18	0.85	22.7
GIC-$NaClO_3$ 2	75.8	19.94	4.26	3.8
EG-$NaClO_3$ 2	91.85	6.81	1.34	13.5
GIC-$NaClO_3$ 3	80.73	16.59	2.68	4.9
EG-$NaClO_3$ 3	92.52	7.09	0.4	18.6

We have also shown the comparison in atomic precentage of functional groups between the GICs and EG fillers for H_2O_2 and $NaClO_3$ at their optimum condition in Table 5.7. To further analyze, the high-resolution carbon spectra of GIC-H_2O_2 1, GIC-$NaClO_3$ 1, EG-H_2O_2 1, and EG-$NaClO_3$ 1 are shown in Figure 5.14a-d. Sharper peaks are visible for both the GIC and EG filler case for H_2O_2 intercalation compared to $NaClO_3$. To understand the differences in functional groups achieved through the two intercalation routes (H_2O_2 and $NaClO_3$), the C1s high-resolution XPS spectra were further analyzed and resolved by curve fitting. The deconvoluted spectra of GIC-H_2O_2 1 (shown in Figure 5.14a) reveal the presence of C-C/C=C graphitic carbon (284.84 eV), the hydroxyl/epoxide group (~286 eV), and the carbonyl/carboxyl group (~288 eV),

respectively[102,103]. Basal plane functional groups (hydroxyl/epoxide groups) are present in higher quantities in GIC-$NaClO_3$ 1 and EG-$NaClO_3$ 1 (Figure 5.14b & d), due to the fact that $NaClO_3$ mostly attacks the basal plane of the graphite structure . In comparison, deconvoluted XPS spectra of GIC-H_2O_2 1 & EG-H_2O_2 1 show that the edge functional groups are more prominent as seen in Figure 5.14 a and c. It is noticeable that EG-H_2O_2 1 displays a stronger intensity peak of graphitic carbon (C-C/C=C) compared to EG-$NaClO_3$ 1; this directly correlates to better structural integrity

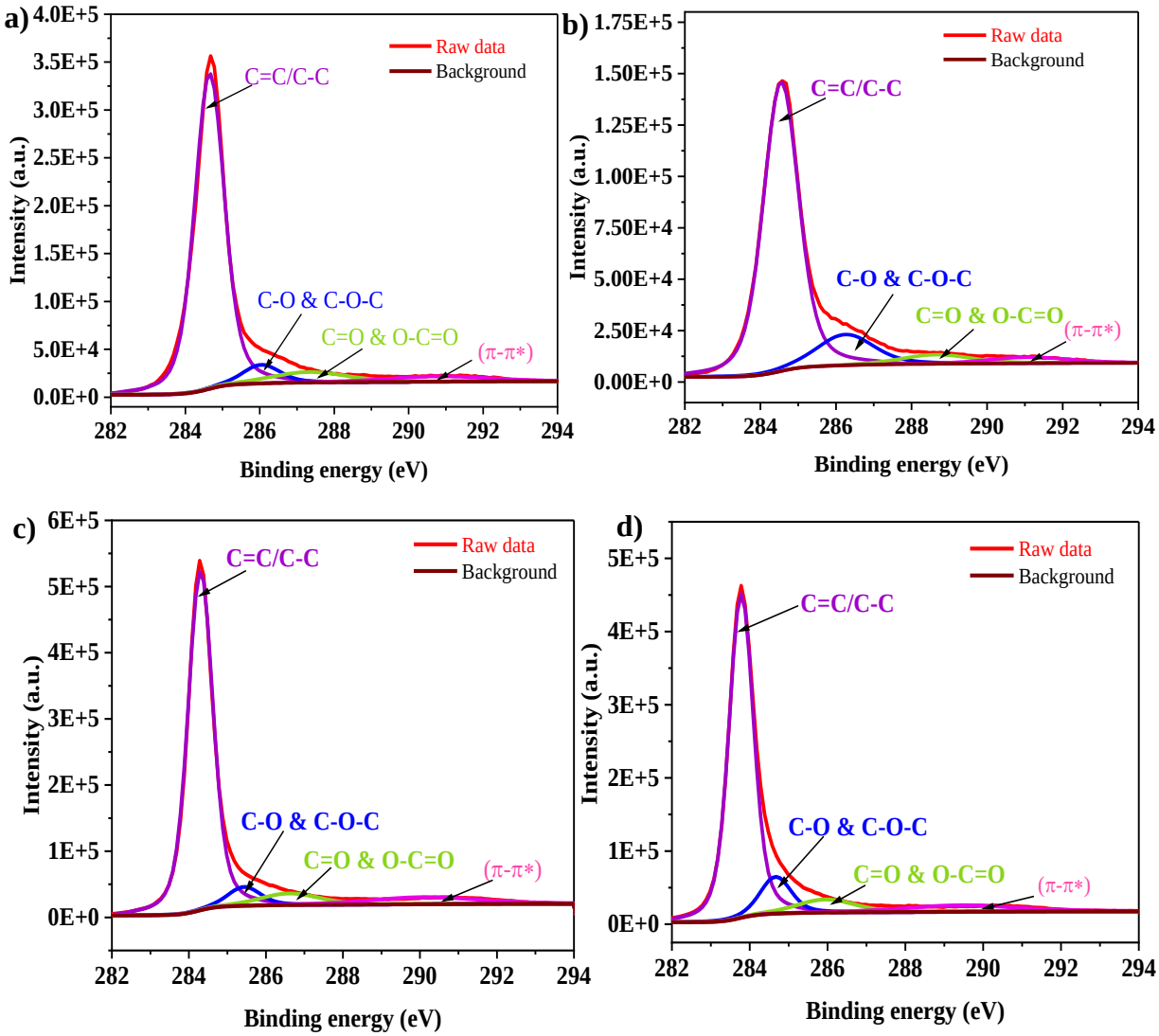

Figure 5.14 C1s core level XPS spectra for a) GIC-H_2O_2 1, b) GIC-$NaClO_3$ 1, c) EG-H_2O_2 1, and d) EG-$NaClO_3$ 1.

of expanded graphite prepared from oxidant H_2O_2. The atomic percentage of epoxy and hydroxyl functional groups (C-O-C/C-OH) as well as the edge functional groups (C=O/O=C-OH) (as shown in Table 5.7) reveal higher degree of edge functionalization in the case of EG-H_2O_2 1. The presence of higher degree of edge functional groups relative to basal plane functional groups in graphite's structure limits the structural damage in EG-H_2O_2 1 sample while presence of higher degree of basal plane functional groups lead to higher damage for $NaClO_3$ intercalation. The scheme of intercalation with H_2O_2, thus drastically preserves the basal plane structure which leads to superior thermal transport in EG-H_2O_2 1 sample.

Table 5.7 Relative atomic percent composition of functional groups of GICs & EG fillers.

Sample name	**C-C/C=C**	**C-OH & C-O-C**	**C=O & O=C-OH**
GIC-H_2O_2 1	82.4	5.91	7.16
GIC-$NaClO_3$ 1	75.11	13.54	6.22
EG-H_2O_2 1	80.31	5.9	6.56
EG-$NaClO_3$ 1	73.8	10.78	8.75

5.4.6 Analysis of Interlayer Spacing of GICS and EG Fillers through XRD

XRD analyzes the structural characteristics of the obtained GICs and EG fillers. XRD allows us to understand oxidation and intercalation effects on GICs and EG filler through the two auxiliary intercalating agents, H_2O_2 and $NaClO_3$. For the 10 mesh graphite, the sharp diffraction peak at 2θ = 26.3° corresponds to an interlayer spacing of 3.38 Å. This peak position is present at a lower angle than 2θ =26.6° for pristine graphite[175-178], corresponding to the standard 3.34 Å interlayer spacing of the (002) crystal phase for untreated graphite. Table 5.8 represents the peak position and d-spacing values of graphite GICs and EG fillers for both the intercalation routes.

Table 5.8 2θ and d-spacing values of graphite, GICs and EG fillers using XRD analysis.

Sample name	**10 Mesh Graphite**	**GIC-H_2O_2 1**	**GIC-H_2O_2 2**	**GIC-H_2O_2 3**
2θ	26.3	25.5, 26.4	25.2, 25.4	25.3, 26.3
d-spacing (Å)	3.38	3.49, 3.37	3.53,3.51	3.52, 3.38
Sample name	**10 Mesh Graphite**	**EG-H_2O_2 1**	**EG-H_2O_2 2**	**EG-H_2O_2 3**
2θ	26.3	26.5	26.5	26.5
d-spacing (Å)	3.38	3.36	3.36	3.36
Sample name	**10 Mesh Graphite**	**GIC-$NaClO_3$ 1**	**GIC-$NaClO_3$ 2**	**GIC-$NaClO_3$ 3**
2θ	26.3	25.8	24.7	25.6
d-spacing (Å)	3.38	3.45	3.6	3.48
Sample name	**10 Mesh Graphite**	**EG-$NaClO_3$ 1**	**EG-$NaClO_3$ 2**	**EG-$NaClO_3$ 3**
2θ	26.3	26.4	26.3	26.4
d-spacing (Å)	3.38	3.37	3.38	3.37

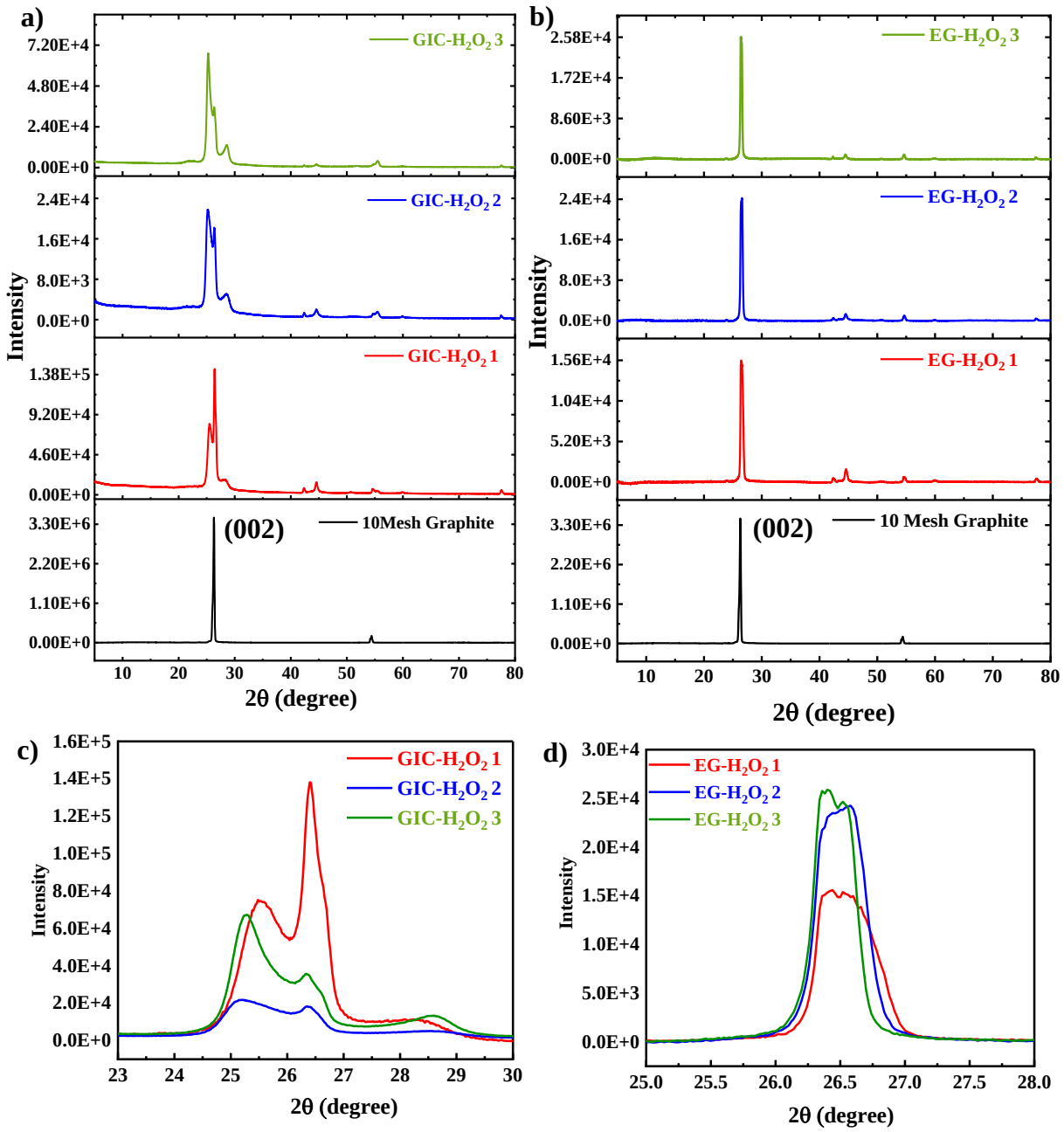

Figure 5.15 XRD spectra of a) GIC-H_2O_2 1, 2 & 3, b) EG-H_2O_2 1, 2 & 3; Inset of XRD spectra of c) GIC-H_2O_2 1, 2 & 3, and d) EG-H_2O_2 1, 2 & 3.

Figure 5.15 a & b illustrate the diffraction peaks of GIC-H_2O_2 and EG-H_2O_2, respectively, and demonstrate the XRD pattern before and after the thermal treatment for an increasing amount of H_2SO_4. The only signal observable in the XRD pattern of natural graphite is (002), which shows

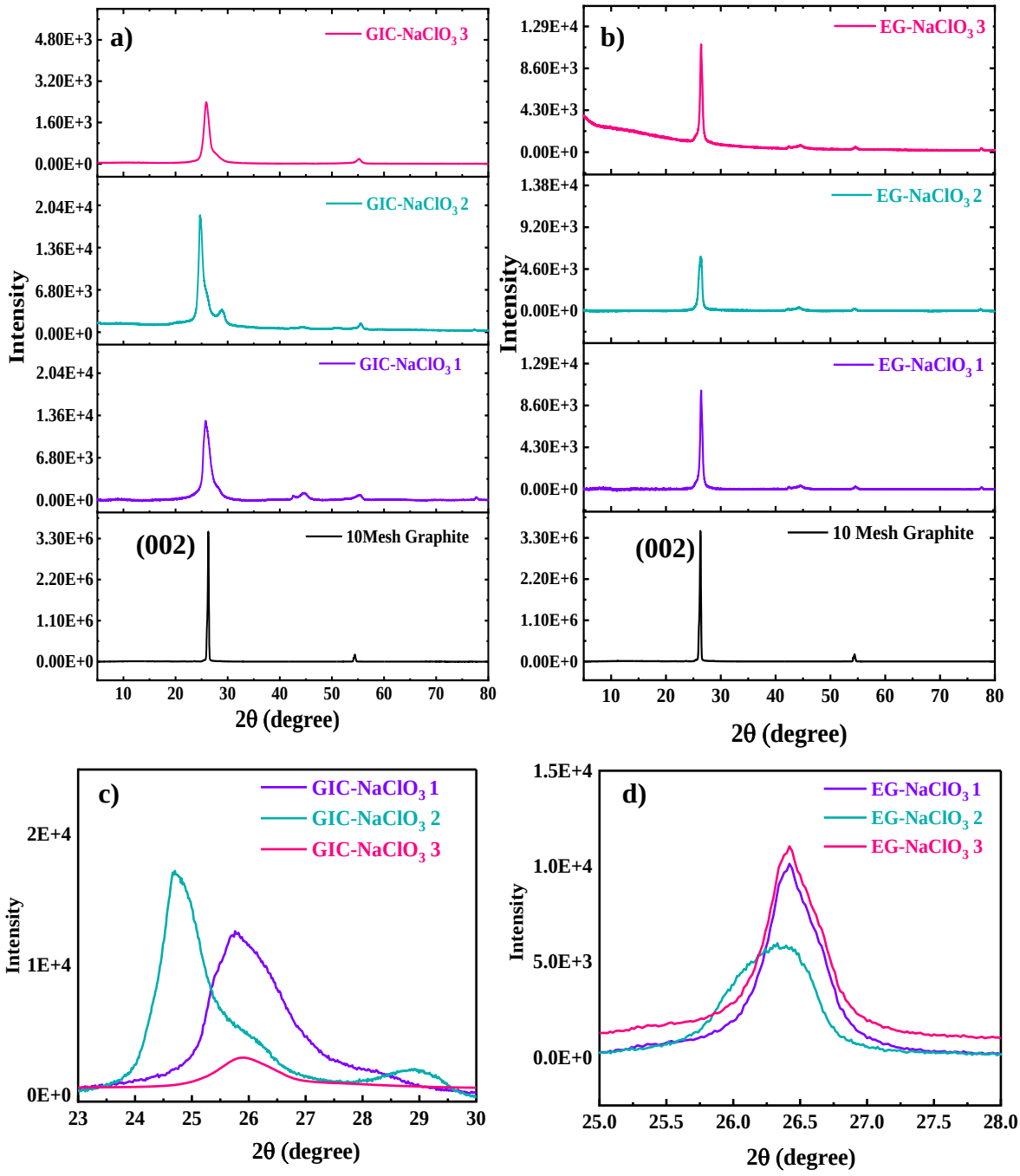

Figure 5.16 XRD spectra of a) GIC-$NaClO_3$ 1, 2 & 3, b) EG-$NaClO_3$ 1, 2 & 3; Inset of XRD spectra of c) GIC-$NaClO_3$ 1, 2 & 3 and d) EG-$NaClO_3$ 1, 2 & 3.

reflections in the perpendicular direction (c-axis) of the hexagonal planes of graphite. Compared to 10 mesh graphite, the (002) peaks in the GIC-H_2O_2 1, 2 & 3, are noticeably widened. The 002

peak is seen at 2θ angle (around ~26.4°) for GIC-H_2O_2 1 and intensity becomes weaker (as exhibited in Figure 5.15c) with the increased amount of intercalating agents due to the disorder in

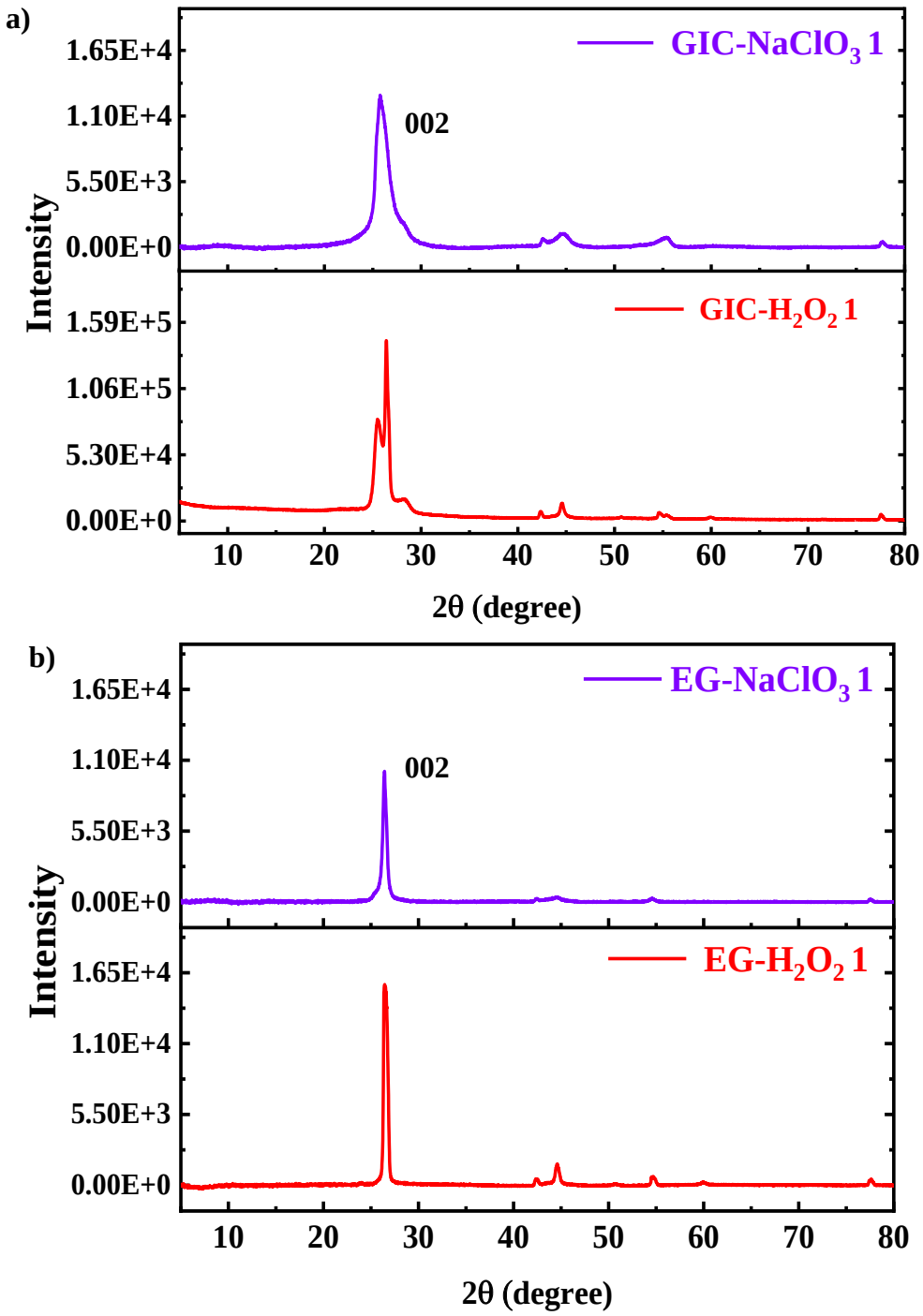

Figure 5.17 XRD spectra of a) GIC-H_2O_2 1& GIC-$NaClO_3$ 1, b) EG-H_2O_2 1& EG-$NaClO_3$ 1.

graphitic morphology[181] after the pre-expansion process. Also, the double peak nature in GIC-H_2O_2 1, 2 & 3 is attributed to the presence of intercalated compounds. Interlayer spacing critically becomes higher with the intercalation effect as indicated by a clear diminution in intensity of (002) peaks (visible in Figure 5.15c). After thermal expansion, the intensity becomes even weaker than the GICs. Comparatively stronger peaks of EG-H_2O_2 1, 2 & 3 at $2\theta = 25.5°$ are regained (as shown in Figure 5.15b) as the intercalated compounds evaporate in gaseous form during thermal treatment. Such aligned peak position of EG fillers also indicates the existence of intact chemical structure of graphite and ordered morphology[182,183]. The interlayer spacing between graphene layers is 3.36 Å which is slightly higher than pristine graphite layers. In addition, the (002) peak intensity is still wider (Figure 5.15d) than the untreated graphite suggesting the expanded nature of EG filler. This interconnected and stacked structure of EG enables better thermal transport throughout the polymer composite[124].

In contrast, the peak shape and position of GICs and EG filler obtained from $NaClO_3$ intercalation route are displayed in Figure 5.16 a &b. The reflection peaks of GIC-$NaClO_3$ 1, 2 & 3 at $2\theta = 25.8°$, 24.7°, and 25.6°, lead to interlayer spacings of 3.45, 3.6, and 3.48 Å, respectively. The asymmetric but intense peak shape of GIC-$NaClO_3$ 2 shifts to a lower 2θ angle, reflecting the insertion of many intercalating species. Higher intercalation time causes insertion of higher intercalated compounds between the layers and maximum peak shift as observed for GIC-$NaClO_3$ 2 (Figure 5.16c). After expanding the GICs at 900 °C, the EG-$NaClO_3$ 1, 2 & 3 are subjected to the change in peak position at 2θ = 26.4, 26.5 and 26.5 as discussed earlier, resulting in the interlayer spacing of 3.37, 3.38 and 3.37 Å respectively.

We have compared the XRD spectra of GICs and EG fillers, obtained at optimum conditions for the two intercalation routes in Figure 5.17 a & b. It is noticeable that the interlayer spacing is

higher for the case of EG-$NaClO_3$ 1 than EG-H_2O_2 1 filler and the broader peak in EG-$NaClO_3$ 1 compared to EG-H_2O_2 1 (Figure 5.17 b) reveals the effect of higher intercalation, and lower stage number in EG-$NaClO_3$ 1. Also the broader peak in EG-$NaClO_3$ 1 is caused due to the reduced crystalline structure and an increase in amorphous regions[292]. The larger change in peak position for GIC-$NaClO_3$ is attributed to the presence of higher oxygen moieties in $NaClO_3$ case, resulting in lower thermal conductivity of EG-$NaClO_3$ 1. On the other hand, stronger intensity accompanied with only a slight change in peak position of EG-H_2O_2 1 filler is attributed to lower disorder in the crystal structure of graphite layers[293] leading to higher thermal conductivity of EG-H_2O_2 1 filler.

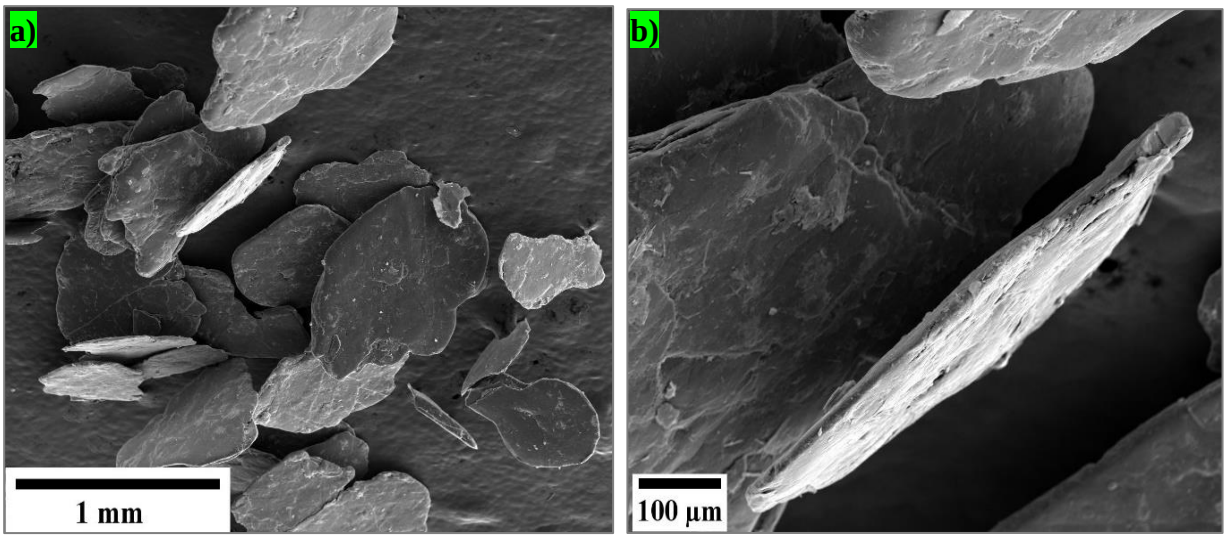

Figure 5.18 FE-ESEM images of 10mesh graphite a) ×35, b) ×150.

5.4.7 Structure and Morphology Characterization of GICs and EG Filler

The morphology and porosity of the graphite structure due to intercalation and worm-like thermally expanded graphite have been studied using FE-ESEM. The FE-ESEM image of 10 mesh graphite particles with an average lateral size of 800 µm is shown in Figure 5.18. Figure 5.19-5.22. illustrate the structural change in GICs, resulting from chemical intercalation of 10 mesh graphite

using H_2O_2 and $NaClO_3$ separately and thermally treated expanded graphites, observed by FE-ESEM.

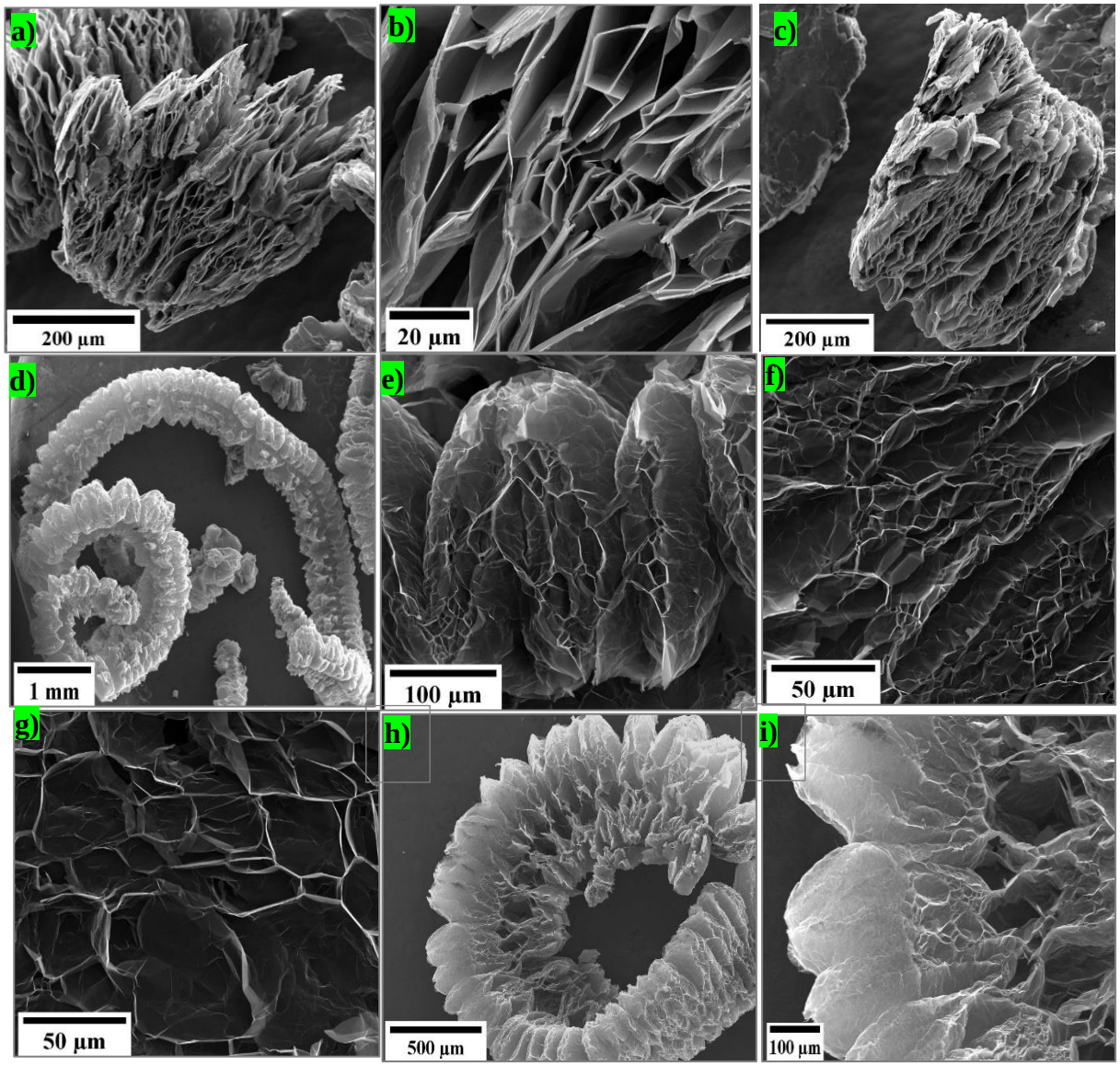

Figure 5.19 FE-ESEM micrographs of a) GIC-H_2O_2 1 (×150), b) GIC-H_2O_2 1 (×800), c) GIC-H_2O_2 1 (×120), d) EG-H_2O_2 1 (×20), e) EG-H_2O_2 1 (×250), f) EG-H_2O_2 1 (×500), g) EG-H_2O_2 1 (×500), h) EG-H_2O_2 1 (×50), and i) EG-H_2O_2 1 (×150).

Figure 5.19 a, b & c show images of GIC-H_2O_2 1 highlighting the expansion phenomenon as generated from H_2O_2 intercalation reaction. Magnified images of GIC-H_2O_2 1 (Figure 5.19 b) show a highly porous structure with sharp edges that emerge, as a result of the reaction scheme between H_2SO_4 and H_2O_2 producing a large amount of O_2 that tries to escape from the graphite layers. The measured average lateral size of GICs and thickness of the graphite walls are ~500 µm and ~1 µm respectively. The intercalated chemicals are decomposed by heating GICs to 900 °C,

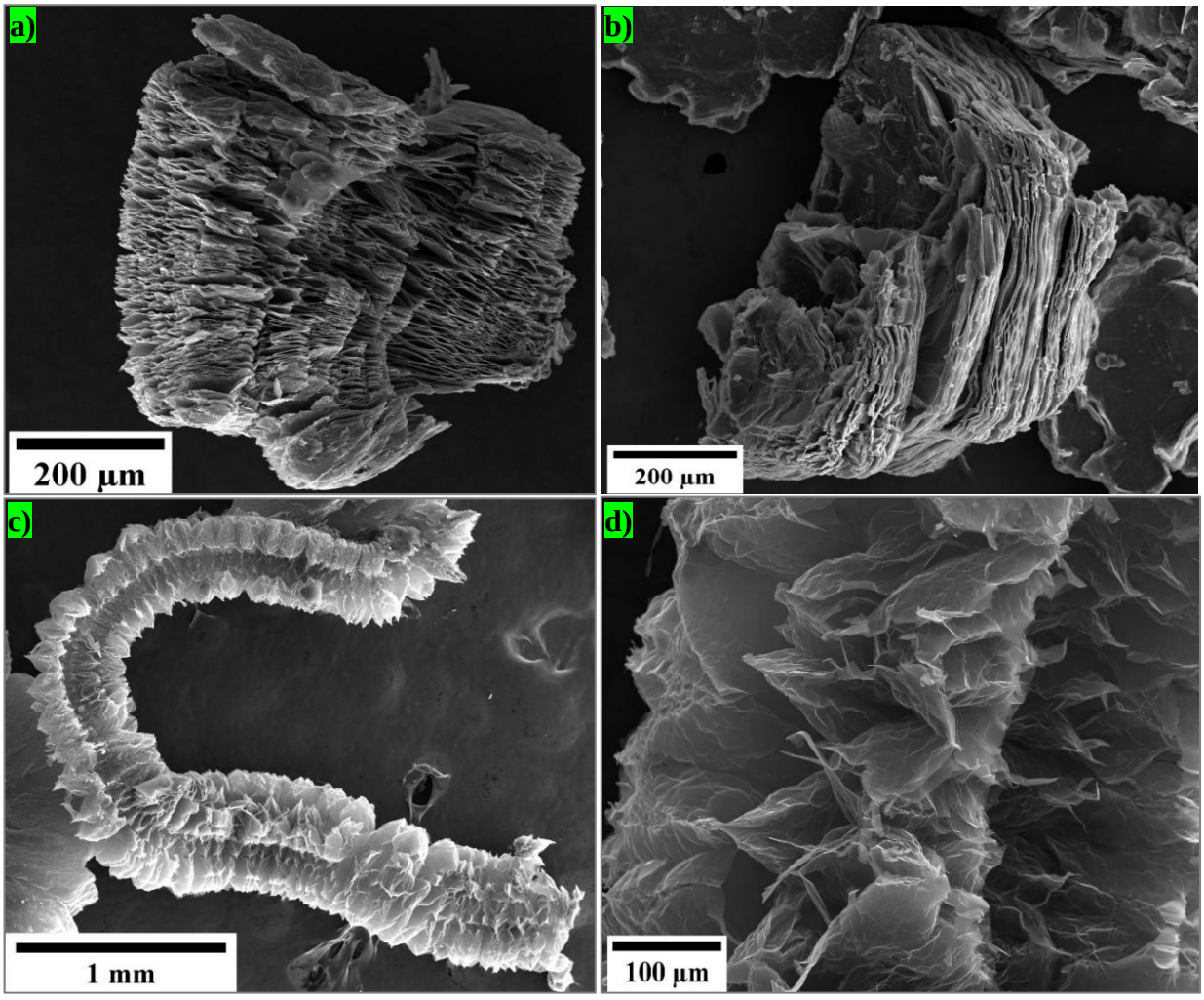

Figure 5.20 FE-ESEM micrographs of a) GIC-H_2O_2 2 (×120), b) GIC-H_2O_2 3 (×120), c) EG-H_2O_2 3 (× 35), d) EG-H_2O_2 3 (×200).

resulting in puffed up materials (Figure 5.19 d & h) with a very porous structure (as shown in Figure 5.19e-i).

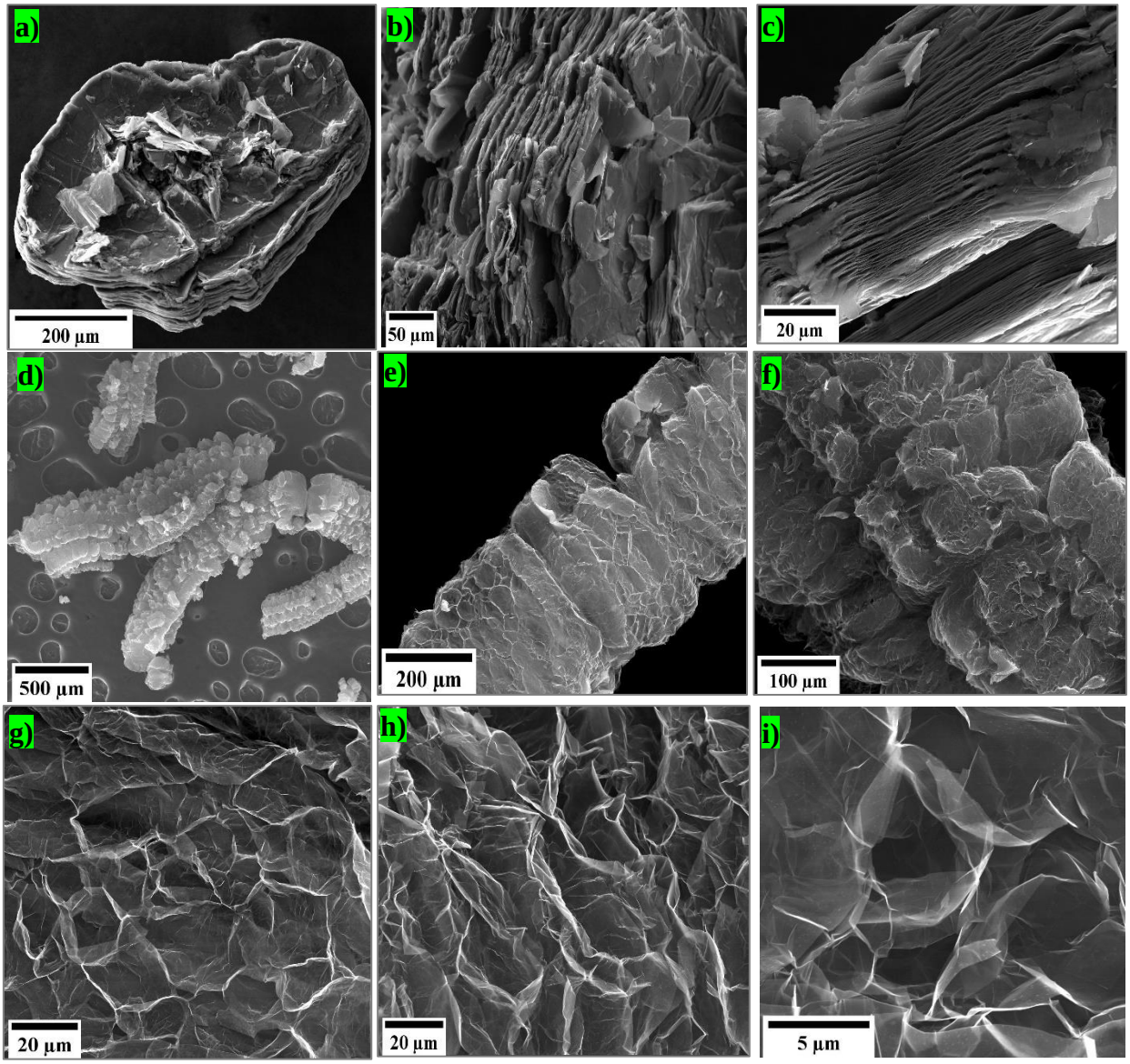

Figure 5.21 FE-ESEM micrographs of a) GIC-$NaClO_3$ 1 (×150), b) GIC-$NaClO_3$ 1 (×250), c) GIC-$NaClO_3$ 1 (×1000), d) EG-$NaClO_3$ 1 (×35), e) EG-$NaClO_3$ 1 (×120), f) EG-$NaClO_3$ 1 (×500), g) EG-$NaClO_3$ 1 (×1000), h) EG-$NaClO_3$ 1 (×800), i) EG-$NaClO_3$ 1(×5000).

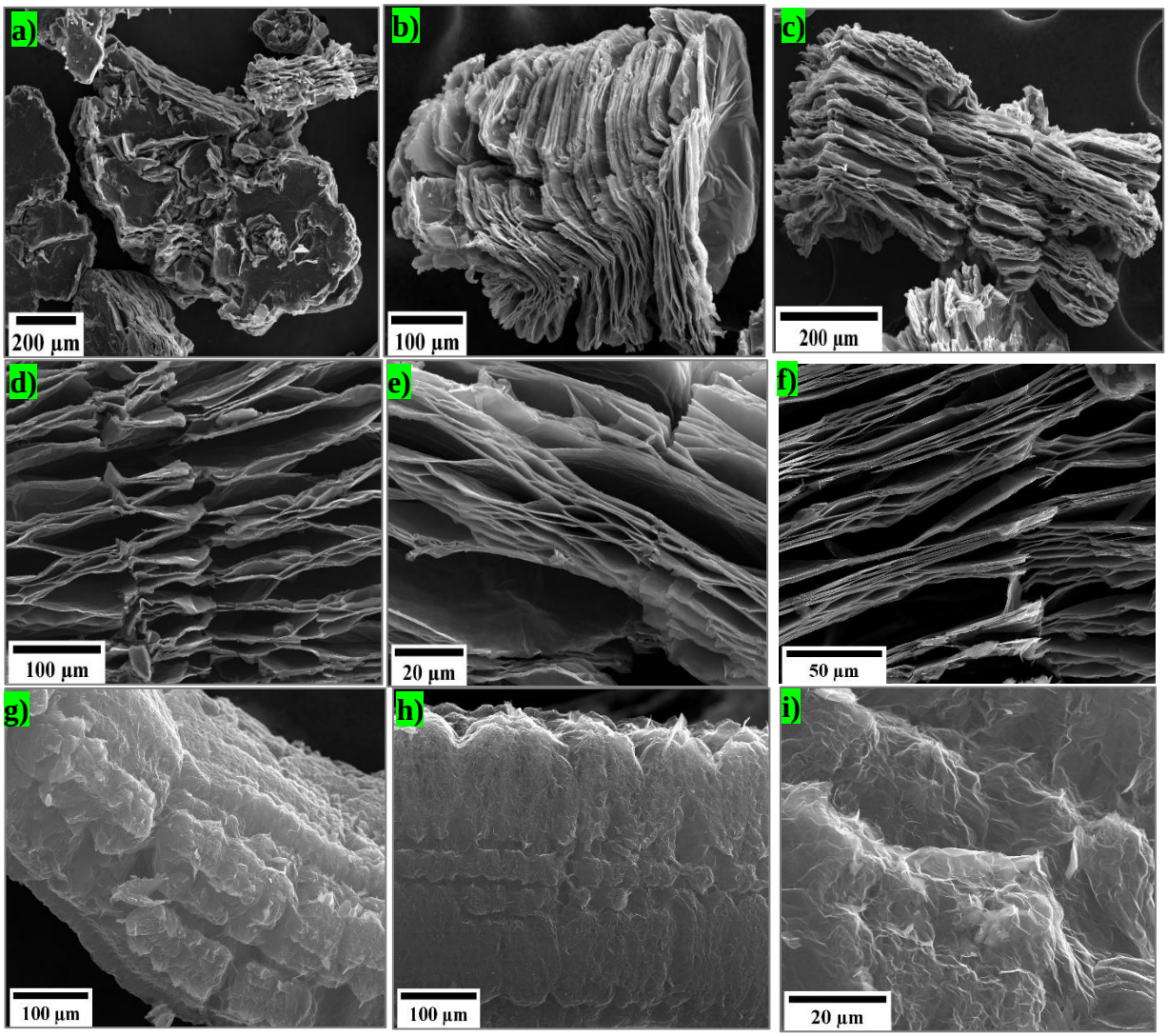

Figure 5.22 FE-ESEM micrographs of a) GIC-$NaClO_3$ 2 (×80), b) GIC-$NaClO_3$ 2 (×200), c) GIC-$NaClO_3$ 2 (×150), d) GIC-$NaClO_3$ 2 (×250), e) GIC-$NaClO_3$ 2 (×500), f) GIC-$NaClO_3$ 2 (× 500), g) EG-$NaClO_3$ 2 (× 200), h) EG-$NaClO_3$ 2 (× 200), and i) EG-$NaClO_3$2 (×1200)

The EG-H_2O_2 1 filler's edges are wide open (Figure 5.19 e), allowing the polymer to be absorbed properly into the EG-H_2O_2 1 filler. This interconnected porous structure (seen in Figure 5.19 h & i), allows creation of an interpenetrating 3D polymer/graphene network in the composite. We have observed the effect on H_2O_2 intercalation route with a higher amount of H_2SO_4. As a result, we discovered that GIC-H_2O_2 2 has a larger volume and a more ordered porous structure (Figure 5.20a), but EG-H_2O_2 3 has a higher structural defect because of lateral breakage and

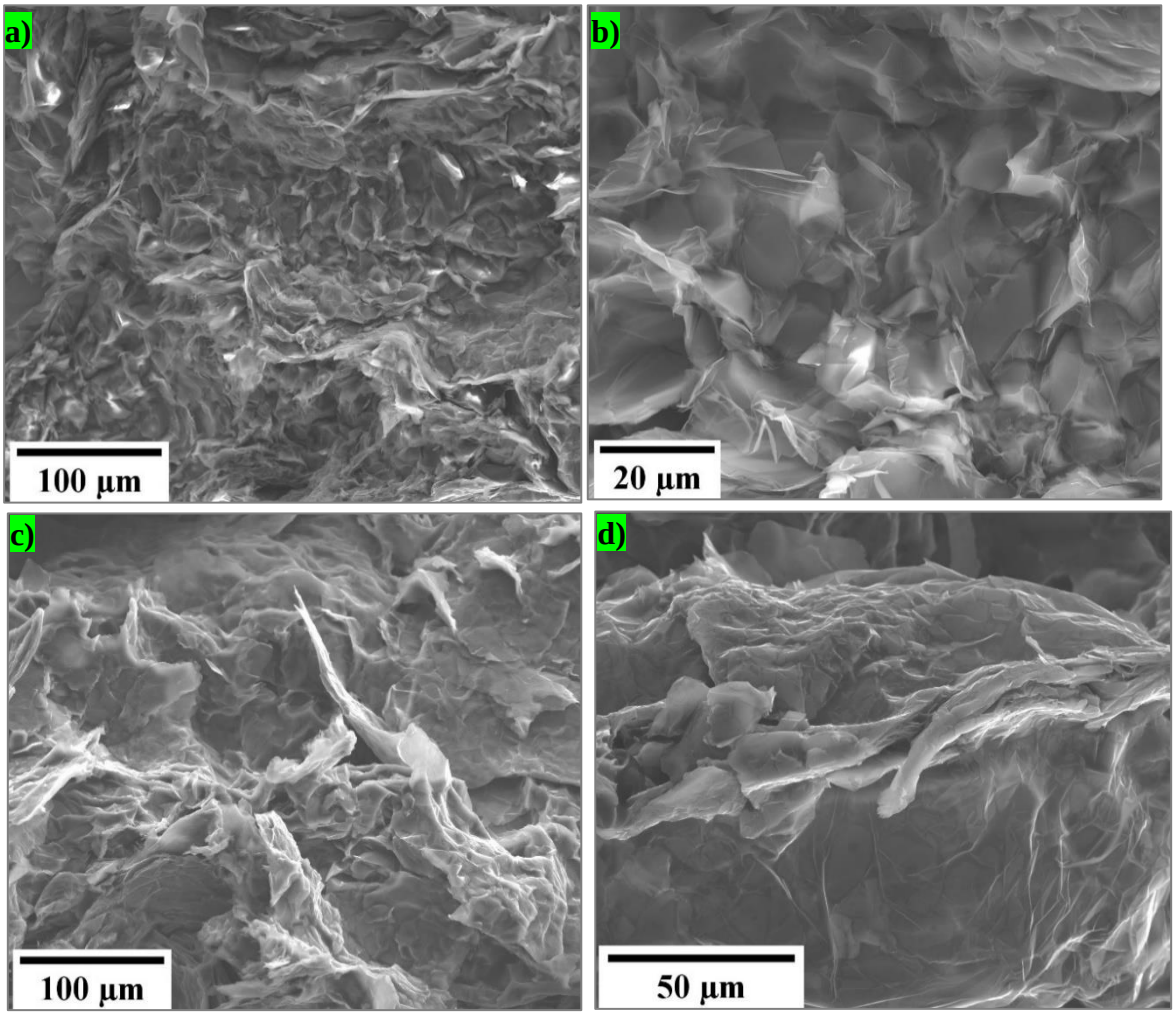

Figure 5.23 FE-ESEM micrographs of EG-H_2O_2 1/PEI composite for 10 wt% EG-H_2O_2 1 filler a) (×250), b) (×650) magnification; and FE-ESEM micrographs of GIC-$NaClO_3$ 1/PEI composite for 10 wt% GIC-$NaClO_3$ 1 filler c) (×250), d) (×650) magnification.

delamination in GIC-H_2O_2 3 (Figure 5.20b). Figure 5.20 c & d show the images of EG-H_2O_2 3 after the thermal treatment.

We have also observed the structural changes of GIC-$NaClO_3$ and EG-$NaClO_3$ while using $NaClO_3$ as an auxiliary intercalating agent to analyze the impact on thermal properties of composite. Figure 5.21a shows a fractured section at the center or basal plane area, as well as a crack across the GIC-$NaClO_3$ 1 particle. Figure 5.21b & c show highly stacked but delaminated area through the thickness, which can be explained as the result of vigorous intercalation.

The graphite layers expand when the intercalating chemicals transform into CO_2 and SO_2, and the length or surface of the GICs can be readily broken due to the loosely connected layers or fractured surface along the graphite layers (Figure 5.21 d). The expanded graphite image with the cleavage area because of the fractured nature is shown in Figure 5.21 e & f. Magnified view of comparatively smaller pores are visible in Figure 5.21 g-i.

We also observe the effect of longer intercalation time in the images of resulting GIC-$NaClO_3$ 2 and EG-$NaClO_3$ 2 in Figure 5.22 a-i. Figure 5.22 a, b & c represent the basal plane and cross-sectional area of a GIC -$NaClO_3$ 2 particle respectively. The structures seem to have a significant number of cracks and defects. Such structure leads to a reduction in the lateral size of the filler even after expansion.

To investigate the composite structure after composite fabrication, FE-ESEM images of EG-H_2O_2 1/PEI composite (Figure 5.23 a & b) for 10 wt% EG-H_2O_2 1 filler and EG-$NaClO_3$ 1/PEI composite (Figure 5.23 c & d) for 10 wt% GIC-$NaClO_3$ 1 filler were also observed. Because the pores of the EG-H_2O_2 1 filler are filled with polymer, the surface appears smooth and homogenous, lowering the overall thermal resistance of polymer composites (Figure 5.23 a & b).

There are obvious differences between the two intercalated graphite's structure and thermally treated EG fillers. The important factor for EG-H_2O_2/PEI composite's higher thermal conductivity over EG-$NaClO_3$/PEI composite is insignificant structural flaws with ordered texture of EG-H_2O_2.

5.5 CONCLUSION

In summary, two distinct intercalation methods have been employed to prepare GIC and EG filler using H_2SO_4 as principle intercalator and two auxiliary intercalating agents, H_2O_2 and $NaClO_3$ as oxidizers. With optimized conditions, EG-H_2O_2 1/PEI composites exhibit a *k* value of 9.5 $Wm^{-1}K^{-1}$ when the EG-H_2O_2 1 filler content is increased to 10 wt%, showing ~4030% enhancement relative to the pure PEI (*k* ~0.23 $Wm^{-1}K^{-1}$). In comparison, the EG-$NaClO_3$ 1/PEI composite shows *k* value of 5.3 $Wm^{-1}K^{-1}$ at 10 wt% EG-$NaClO_3$ 1 filler content, showing ~2190% enhancement relative to the PEI. Using the solution casting technique, the interconnected continuous network is established for the EG-H_2O_2 1/PEI composites, whereas the continuous structure is not quite apparent in EG-$NaClO_3$ 1/PEI composites as compared by FE-ESEM analysis. The developed interconnected network of high-quality larger graphene nanosheet in EG-H_2O_2 relative to EG-$NaClO_3$ leads to superior composite thermal conductivity. Analysis of the morphology, structural integrity, and crystal structure through FE-ESEM, Raman and XRD has validated the superiority of the intercalation route involving H_2O_2. XPS analysis of the chemical composition of the products from the two intercalation routes reveals the preferential edge oxidation in EG-H_2O_2 1, which leads to lower structural disorder relative to EG-$NaClO_3$ 1, caused by basal plane oxidation. Higher thermal diffusivity value of EG-H_2O_2 1 filler than that of EG-$NaClO_3$ 1 filler further confirms the beneficial effect of auxiliary intercalating agent, H_2O_2 used in the intercalation route I. With this superior thermally conductive composite, we have shed light on the potential use of EG filler in achieving an efficient thermal management system.

CHAPTER 6

Conclusion

Efficient thermal management systems have emerged as a critical challenge due to increasing heat fluxes in electronic devices driven by continuous miniaturization. There is an increasing demand for flexible, cost-effective, and lightweight high thermal conductivity materials to efficiently dissipate these heat fluxes. The fabrication of thermally conductive polymeric materials using graphene nanofiller and graphite as filler is a promising approach for achieving high thermal conductivity materials. However, the effectiveness of the fillers can be diminished by factors such as large interfacial thermal resistance between polymer and graphene, aggregation of graphene particles, and presence of polymer in between graphene particles. Mismatch in phonon vibrational spectra of polymer and graphene leads to high interfacial thermal resistance between polymer and graphene. This research focused on investigating the effect of the functionalization of graphene on the thermal conductivity of polymer composites.

We have utilized functionalization strategy to modify graphene's structure via oxidation to enhance the interfacial thermal conductance between polymer and graphene and prepared graphene-nanoplatelet (GnP)/polyetherimide (PEI) composites using the solution mixing technique. Different oxidation schemes have been employed to observe the superiority of edge functionalization over the basal plane functionalization of graphene on the *k* value of composites. Our experiments show that oxidation at the graphene edges can lead to a significant increment in the *k* of graphene nanoplatelet (GnP)/polyetherimide (PEI) composites than oxidation at the basal plane of graphene. Edge oxidation of graphene retains the basal plane and allows it to preserve its high in-plane thermal conductivity (k_{in} > 2000 $Wm^{-1}K^{-1}$) in EGO/PEI composite. A further

advantage of the edge oxygen groups is that they provide interfacial thermal conductance through hydrogen bonding with PEI oxygen groups, improving the overall thermal conductivity of the EGO (Edge oxidized graphene)/PEI composite. Hummers method attaches the oxygen groups mainly on the basal plane, which distorts the sp^2 carbon−carbon network of graphene and leads to lower thermal conductivity. Therefore, the BGO (Basal-plane oxidized graphene)/PEI composite's *k* value to significantly lower than the pristine GnP/PEI composite's *k* value. The resulting thermal conductivity of the EGO/PEI composite is enhanced by 18%, whereas that of the BGO/PEI composite is diminished by 57%, with respect to the pristine GnP/PEI composite with 10 wt% GnP content. Also, at 15 wt% filler content, the EGO/PEI composite of *k* is enhanced by 725% compared to pure PEI, while *k* of BGO/PEI composite is increased by only ~104% with respect to pure polymer. The preferential location of functional groups in the edge and basal plane case is confirmed by Raman mapping and spectroscopy, XPS, XRD, and FTIR analysis showing the presence of an excess of carboxyl (−COOH) functional groups on graphene edges. The evidence supports the superior effect of edge functionalization can lead to fundamentally novel pathways for achieving high thermal conductivity polymer composites.

Expanded graphite (EG) is the resultant material from intercalation of graphite, followed by heat treatment, and can be referred to as another kind of functionalized graphite. EG exhibits 3D interconnected graphene network with different degree of separation between graphene layers along the through-thickness direction. This separation does not occur throughout the entire plane or for all carbon layers. We use thermal treatment to expand the 100-mesh graphite intercalated compound and obtain EG. Using the solvent casting technique, we embedded the expanded graphite into a polymer matrix, PEI, and determined the composite thermal conductivity. It is

noteworthy to mention that the *k* value of EG/PEI composite linearly increased with the addition of EG filler. The *k* value of EG/PEI composite at 2.5 wt% composition sample was measured to be 2.5 $Wm^{-1}K^{-1.}$ This value is increased to 6.6 $Wm^{-1}K^{-1}$ when the filler content was increased to 10 wt%, representing a remarkable enhancement of ~2770% over pristine polyetherimide (*k*~0.23 $Wm^{-1}K^{-1}$). This extraordinary enhancement in thermal conductivity is due to a network of continuous graphene sheets over long−length scales, resulting in low thermal contact resistance at bends/turns due to the graphene sheets being covalently bonded at such junctions. Solvent casting offers the advantage of preserving the porous structure of expanded graphite in the composite, resulting in the highly thermally conductive interpenetrating network of graphene and polymer. Also, the solvent casting technique does not break down the expanded graphite particles due to minimal forces involved, allowing for efficient heat transfer over long−length scales, further enhancing overall composite thermal conductivity. We optimized the sonication time and power to achieve the highest thermal conductivity of the EG/PEI composite. The *k* value of composite is presented as a function of sonication time and energy. Comparisons with a recently introduced effective medium model show a very high value of predicted particle-particle interfacial conductance, providing evidence for efficient interfacial thermal transport in expanded graphite composites. Field emission environmental scanning electron microscopy (FE−ESEM) provides a detailed understanding of the interpenetrating graphene−polymer structure in the expanded graphite composite. XRD, Raman spectroscopy, and XPS analysis represent the crystal structure, defects, and functional groups of the EG filler before and after the thermal expansion.

A variety of EG filler-based polymer composites have also been developed to study the electrical conductivity of the composite. This dissertation also considered the electrical

performance of the EG/PEI composites. We report electrical conductivity enhancement of expanded graphite polyetherimide (EG/PEI) composite fabricated using a simple solution mixing technique. Expanded graphite can significantly enhance the properties relative to graphene nanoplatelets by creating continuous graphitic networks in the composite. Here we treat a larger mesh size (50 mesh) graphite intercalated compound at high temperature to measure the electrical properties. Solution casting technique allows the preservation of worm structure of expanded graphite in the composite, thus enabling the development of continuous graphitic networks throughout the composite, leading to superior property enhancement. Measurement reveals ~19 orders of magnitude increase in electrical conductivity of composite (yielding values up to 969 Sm^{-1}) through the inclusion of the 10 wt% of EG filler relative to pure polyetherimide (1.2×10^{-17} Sm^{-1}). Theoretical prediction using an effective medium approach reveals the impact of a continuous graphitic network on the composites' electrical conductivity. We also find that the 10 wt% EG filler composition composite exhibits a thermal conductivity (k) value of 7.3 $Wm^{-1}K^{-1}$, representing a significant enhancement of 3070% compared to pure PEI ($k \sim 0.23$ $Wm^{-1}K^{-1}$). FE-ESEM reveals the preserved interconnected structure of EG within the expanded-graphite/PEI composite, allowing the development of a conductive interpenetrating network of polymer and filler. Raman spectroscopy, XRD, and XPS analysis are further used to characterize the expanded-graphite filler.

Furthermore, we studied the preparation techniques of graphite intercalated compounds using different chemical synthesis routes. We obtain two different expanded graphite fillers by intercalation of 10 mesh graphite using H_2SO_4 as the primary intercalating agent and two different auxiliary intercalating agents or oxidizing agents (H_2O_2 and $NaClO_3$), followed by thermal heating

in this study. We use the two expanded graphite EG-H_2O_2 and EG-$NaClO_3$ filler to prepare the composite using polyetherimide as matrix and measure the thermal conductivity value of EG-H_2O_2/PEI and EG-$NaClO_3$/PEI composites. To identify the optimal reaction conditions, we perform several reactions with different quantities of intercalating and oxidizing agents for different time periods. The trend in the *k* value of composite reveals the effect of intercalating agents and intercalation time for both synthesis routes. We have found that the *k* value of EG-H_2O_2/PEI and EG-$NaClO_3$/PEI decreases with the increased volume of intercalating agents (H_2SO_4 /H_2O_2/$NaClO_3$) and reaction time. We obtain a *k* value of 9.5 $Wm^{-1}K^{-1}$ for EG-H_2O_2 1/PEI composites at a low filler content of 10 wt% at H_2SO_4:H_2O_2 volume ratio of 3:33:1 and reaction time of 30 min. On the other hand, the EG-$NaClO_3$ 1/PEI composite achieves a *k* value of 5.3 $Wm^{-1}K^{-1}$ at 10 wt% filler content at H_2SO_4:H_2O_2 volume ratio of 200:1 and reaction time 30 min. ~41 times higher *k* value (relative to pure PEI) of EG-H_2O_2 1/PEI is achieved for 10 wt% EG-H_2O_2 filler content at 70 ml/g expansion volume. But, for the same expansion volume of EG-$NaClO_3$ 1 filler, the *k* value is higher by only ~23 times relative to neat polymer. Self-decomposition of H_2O_2 and bi-product O_2 for the intercalation route H_2O_2 expands the EG filler before thermal heating. Such a combined effect opens the pore of EG-H_2O_2 more than EG-$NaClO_3$, where delamination or breakage is caused. Furthermore, H_2O_2 gently oxidizes graphite leaving minimal defects on the basal plane and introducing the functional groups mainly at the edges, while $NaClO_3$ shows a strong oxidation effect distorting the basal plane of the graphite structure, attaching functional groups on the basal plane area. XPS analysis supports the impact of functionalization on the filler and helps explain the subsequent higher *k* value of EG-H_2O_2/PEI composite than EG-$NaClO_3$ /PEI composite. Because of the edge functionalization, I_D/I_G ratio reveals superior structural integrity for EG-H_2O_2 filler compared to EG-$NaClO_3$ filler. This is also realized by XPS and XRD. Field

emission scanning electron microscopy (FE-SEM), X-ray powder diffraction (XRD), Raman spectroscopy, and XPS characterization are used to examine the degree of intercalation, physical structure, interlayer spacing, delamination, or pre-expanded nature of the GICs and EG filler. Results outlined in this dissertation can provide promising avenues to achieve next-generation high thermal conductivity polymer-graphene composites.

REFERENCES

1 Darrow, C. B., Satcher Jr, J. H., Lane, S. M., Lee, A. P. & Wang, A. W. (Google Patents, 2002).

2 Hou, J. *et al.* Synthesis of a low band gap polymer and its application in highly efficient polymer solar cells. *Journal of the American Chemical Society* **131**, 15586-15587 (2009).

3 Suriyakumar, S., Bhardwaj, P., Grace, A. N. & Stephan, A. M. Role of Polymers in Enhancing the Performance of Electrochemical Supercapacitors: A Review. *Batteries & Supercaps* (2021).

4 Chatterjee, S. G., Chatterjee, S., Ray, A. K. & Chakraborty, A. K. Graphene–metal oxide nanohybrids for toxic gas sensor: A review. *Sensors and Actuators B: Chemical* **221**, 1170-1181 (2015).

5 Okamoto, Y. *et al.* Perfluorodioxolane Polymers for Gas Separation Membrane Applications. *Membranes* **10**, 394 (2020).

6 Henry, A. Thermal transport in polymers. *Annual review of heat transfer* **17** (2014).

7 Muthaiah, R., Tarannum, F., Yedukondalu, N. & Garg, J. First principles investigation of high thermal conductivity in hexagonal boron phosphide. *arXiv preprint arXiv:2201.09430* (2022).

8 Muthaiah, R. & Garg, J. First principles investigation of high thermal conductivity in hexagonal germanium carbide (2H-GeC). *Carbon Trends* **5**, 100113 (2021).

9 Muthaiah, R. & Garg, J. Ultrahigh thermal conductivity in hexagonal BC6N-An efficient material for nanoscale thermal management-A first principles study. *Computational Materials Science* **200**, 110773 (2021).

10 Muthaiah, R. & Garg, J. Thermal conductivity of magnesium selenide (MgSe)–A first principles study. *Computational Materials Science* **198**, 110679 (2021).

11 Muthaiah, R. *et al.* Thermal conductivity of hexagonal BC 2 P–a first-principles study. *RSC advances* **10**, 42628-42632 (2020).

12 Muthaiah, R. & Garg, J. Strain tuned high thermal conductivity in boron phosphide at nanometer length scales–a first-principles study. *Physical Chemistry Chemical Physics* **22**, 20914-20921 (2020).

13 Muthaiah, R. & Garg, J. Temperature effects in the thermal conductivity of aligned amorphous polyethylene—A molecular dynamics study. *Journal of Applied Physics* **124**, 105102 (2018).

14 Tarannum, F. Effect of Alignment on Thermal Conductivity of Polyethylene-Graphene Composites and Comparison with Effective Medium Theory. (2019).

15 Kouters, M., Gubbels, G. & Ferreira, O. D. S. Characterization of intermetallic compounds in Cu–Al ball bonds: Mechanical properties, interface delamination and thermal conductivity. *Microelectronics Reliability* **53**, 1068-1075 (2013).

16 Dreiser, C. & Bart, H.-J. Mineral scale control in polymer film heat exchangers. *Applied thermal engineering* **65**, 524-529 (2014).

17 Mallik, S., Ekere, N., Best, C. & Bhatti, R. Investigation of thermal management materials for automotive electronic control units. *Applied Thermal Engineering* **31**, 355-362 (2011).

18 Lee, J.-K., Lee, Y.-J., Chae, W.-S. & Sung, Y.-M. Enhanced ionic conductivity in PEO-LiClO 4 hybrid electrolytes by structural modification. *Journal of electroceramics* **17**, 941-944 (2006).

19 Huynh, W. U., Dittmer, J. J. & Alivisatos, A. P. Hybrid nanorod-polymer solar cells. *science* **295**, 2425-2427 (2002).

20 Luo, B., Liu, S. & Zhi, L. Chemical approaches toward graphene-based nanomaterials and their applications in energy-related areas. *Small* **8**, 630-646 (2012).

21 Lu, X. & Xu, G. Thermally conductive polymer composites for electronic packaging. *Journal of applied polymer science* **65**, 2733-2738 (1997).

22 Naghibi, S. *et al.* Noncuring graphene thermal interface materials for advanced electronics. *Advanced Electronic Materials* **6**, 1901303 (2020).

23 Muthaiah, R. *et al.* The superior effect of edge functionalization relative to basal plane functionalization of graphene in enhancing the thermal conductivity of polymer–graphene nanocomposites – a combined molecular dynamics and Green's functions study. *Physical Chemistry Chemical Physics*, doi:10.1039/D2CP00146B (2022).

24 Yan, H., Tang, Y., Long, W. & Li, Y. Enhanced thermal conductivity in polymer composites with aligned graphene nanosheets. *Journal of materials science* **49**, 5256-5264 (2014).

25 Wang, Y. *et al.* Enhanced thermal and electrical properties of epoxy composites reinforced with graphene nanoplatelets. *Polymer Composites* **36**, 556-565 (2015).

26 Zhao, Q. *et al.* Expanded-graphite embedded in lithium metal as dendrite-free anode of lithium metal batteries. *Journal of Materials Chemistry A* **7**, 15871-15879, doi:10.1039/C9TA04240G (2019).

27 Wei, P. & Bai, S. Fabrication of a high-density polyethylene/graphene composite with high exfoliation and high mechanical performance via solid-state shear milling. *RSC advances* **5**, 93697-93705 (2015).

28 Zhang, H.-B. *et al.* Electrically conductive polyethylene terephthalate/graphene nanocomposites prepared by melt compounding. *polymer* **51**, 1191-1196 (2010).

29 Kim, H. & Macosko, C. W. Processing-property relationships of polycarbonate/graphene composites. *Polymer* **50**, 3797-3809 (2009).

30 Kim, H., Miura, Y. & Macosko, C. W. Graphene/polyurethane nanocomposites for improved gas barrier and electrical conductivity. *Chemistry of materials* **22**, 3441-3450 (2010).

31 Hazarika, M. & Jana, T. Graphene nanosheets generated from sulfonated polystyrene/graphene nanocomposite. *Composites science and technology* **87**, 94-102 (2013).

32 Tarannum, F. *et al.* Large Enhancement in Thermal Conductivity of Solvent− Cast Expanded Graphite/Polyetherimide Composites. *Nanomaterials* **12**, 1877 (2022).

33 Chen, Z. & Lu, H. Constructing sacrificial bonds and hidden lengths for ductile graphene/polyurethane elastomers with improved strength and toughness. *Journal of Materials Chemistry* **22**, 12479-12490 (2012).

34 Liang, A. *et al.* Recent developments concerning the dispersion methods and mechanisms of graphene. *Coatings* **8**, 33 (2018).

35 Bafekrpour, E. *Advanced Composite Materials: Properties and Applications*. (De Gruyter Open Poland, 2019).

36 Song, M. Graphene functionalization and its application to polymer composite materials. *Nanomaterials and Energy* **2**, 97-111 (2013).

37 Hu, Y. *et al.* Amino-functionalization of graphene sheets and the fabrication of their nanocomposites. *Polymer composites* **31**, 1987-1994 (2010).

38 Balandin, A. A. Phononics of graphene and related materials. *ACS nano* **14**, 5170-5178 (2020).

39 Colonna, S., Battegazzore, D., Eleuteri, M., Arrigo, R. & Fina, A. Properties of Graphene-Related Materials Controlling the Thermal Conductivity of Their Polymer Nanocomposites. *Nanomaterials* **10**, 2167 (2020).

40 Barani, Z. *et al.* Thermal properties of the binary-filler hybrid composites with graphene and copper nanoparticles. *Advanced Functional Materials* **30**, 1904008 (2020).

41 Cui, X. *et al.* Thermal conductive and mechanical properties of polymeric composites based on solution-exfoliated boron nitride and graphene nanosheets: a morphology-promoted synergistic effect. *ACS applied materials & interfaces* **7**, 19068-19075 (2015).

42 Tarannum, F., Muthaiah, R., Annam, R. S., Gu, T. & Garg, J. Effect of Alignment on Enhancement of Thermal Conductivity of Polyethylene–Graphene Nanocomposites and Comparison with Effective Medium Theory. *Nanomaterials* **10**, 1291 (2020).

43 Saeidijavash, M. *et al.* High thermal conductivity through simultaneously aligned polyethylene lamellae and graphene nanoplatelets. *Nanoscale* **9**, 12867-12873 (2017).

44 Tarannum, F. & Garg, J. in *APS March Meeting Abstracts.* K52. 010.

45 Shahil, K. M. & Balandin, A. A. Graphene–multilayer graphene nanocomposites as highly efficient thermal interface materials. *Nano letters* **12**, 861-867 (2012).

46 Xu, Y., Wang, X. & Hao, Q. A mini review on thermally conductive polymers and polymer-based composites. *Composites Communications* **24**, 100617 (2021).

47 Lin, S. & Buehler, M. J. The effect of non-covalent functionalization on the thermal conductance of graphene/organic interfaces. *Nanotechnology* **24**, 165702 (2013).

48 Georgakilas, V. *et al.* Functionalization of graphene: covalent and non-covalent approaches, derivatives and applications. *Chemical reviews* **112**, 6156-6214 (2012).

49 Wang, M., Hu, N., Zhou, L. & Yan, C. Enhanced interfacial thermal transport across graphene–polymer interfaces by grafting polymer chains. *Carbon* **85**, 414-421 (2015).

50 Shen, X. *et al.* Multilayer graphene enables higher efficiency in improving thermal conductivities of graphene/epoxy composites. *Nano Letters* **16**, 3585-3593 (2016).

51 Miao, Z., Li, X. & Zhi, L. Controlled functionalization of graphene with carboxyl moieties toward multiple applications. *RSC advances* **6**, 58561-58565 (2016).

52 Hummers, W. S. & Offeman, R. E. Preparation of Graphitic Oxide. *Journal of the American Chemical Society* **80**, 1339-1339, doi:10.1021/ja01539a017 (1958).

53 Wang, M., Galpaya, D., Lai, Z. B., Xu, Y. & Yan, C. Surface functionalization on the thermal conductivity of graphene–polymer nanocomposites. *International Journal of Smart and Nano Materials* **5**, 123-132 (2014).

54 Konatham, D. & Striolo, A. Thermal boundary resistance at the graphene-oil interface. *Applied Physics Letters* **95**, 163105 (2009).

55 Ganguli, S., Roy, A. K. & Anderson, D. P. Improved thermal conductivity for chemically functionalized exfoliated graphite/epoxy composites. *Carbon* **46**, 806-817 (2008).

56 Teng, C.-C., Ma, C.-C. M., Chiou, K.-C. & Lee, T.-M. in *2010 5th International Microsystems Packaging Assembly and Circuits Technology Conference.* 1-4 (IEEE).

57 Yang, H., Li, J.-S. & Zeng, X. Correlation between molecular structure and interfacial properties of edge or basal plane modified graphene oxide. *ACS Applied Nano Materials* **1**, 2763-2773 (2018).

58 Mungse, H. P., Kumar, N. & Khatri, O. P. Synthesis, dispersion and lubrication potential of basal plane functionalized alkylated graphene nanosheets. *RSC advances* **5**, 25565-25571 (2015).

59 Rezvani Moghaddam, A. *et al.* Tuning the network structure of graphene/epoxy nanocomposites by controlling edge/basal localization of functional groups. *Industrial & Engineering Chemistry Research* **58**, 21431-21440 (2019).

60 Xiang, Z., Dai, Q., Chen, J. F. & Dai, L. Edge functionalization of graphene and two-dimensional covalent organic polymers for energy conversion and storage. *Advanced Materials* **28**, 6253-6261 (2016).

61 Pei, S. & Cheng, H.-M. The reduction of graphene oxide. *Carbon* **50**, 3210-3228 (2012).

62 Compton, O. C. & Nguyen, S. T. Graphene oxide, highly reduced graphene oxide, and graphene: versatile building blocks for carbon-based materials. *small* **6**, 711-723 (2010).

63 Eigler, S., Grimm, S., Enzelberger-Heim, M., Müller, P. & Hirsch, A. Graphene oxide: efficiency of reducing agents. *Chemical Communications* **49**, 7391-7393 (2013).

64 Bagri, A., Grantab, R., Medhekar, N. V. & Shenoy, V. B. Stability and Formation Mechanisms of Carbonyl- and Hydroxyl-Decorated Holes in Graphene Oxide. *The Journal of Physical Chemistry C* **114**, 12053-12061, doi:10.1021/jp908801c (2010).

65 Fugallo, G. *et al.* Thermal conductivity of graphene and graphite: collective excitations and mean free paths. *Nano letters* **14**, 6109-6114 (2014).

66 Mu, X., Wu, X., Zhang, T., Go, D. B. & Luo, T. Thermal transport in graphene oxide–from ballistic extreme to amorphous limit. *Scientific reports* **4**, 1-9 (2014).

67 Shenogin, S., Bodapati, A., Xue, L., Ozisik, R. & Keblinski, P. Effect of chemical functionalization on thermal transport of carbon nanotube composites. *Applied Physics Letters* **85**, 2229-2231 (2004).

68 Wang, G. *et al.* Facile synthesis and characterization of graphene nanosheets. *The Journal of Physical Chemistry C* **112**, 8192-8195 (2008).

69 Choi, Y. S. *et al.* Multifunctional reduced graphene oxide-CVD graphene core–shell fibers. *Nanoscale* **11**, 12637-12642 (2019).

70 Navaee, A. & Salimi, A. Efficient amine functionalization of graphene oxide through the Bucherer reaction: an extraordinary metal-free electrocatalyst for the oxygen reduction reaction. *Rsc Advances* **5**, 59874-59880 (2015).

71 Hussein, A., Sarkar, S., Oh, D., Lee, K. & Kim, B. Epoxy/p-phenylenediamine functionalized graphene oxide composites and evaluation of their fracture toughness and tensile properties. *Journal of Applied Polymer Science* **133** (2016).

72 Han, D., Zhao, Y.-H., Zhang, Y.-F. & Bai, S.-L. Vertically and compactly rolled-up reduced graphene oxide film/epoxy composites: a two-stage reduction method for graphene-based thermal interfacial materials. *RSC advances* **5**, 94426-94435 (2015).

73 Hwang, Y., Heo, Y., Yoo, Y. & Kim, J. The addition of functionalized graphene oxide to polyetherimide to improve its thermal conductivity and mechanical properties. *Polymers for Advanced Technologies* **25**, 1155-1162 (2014).

74 Bernal, M. M. *et al.* Edge-Grafted Molecular Junctions between Graphene Nanoplatelets: Applied Chemistry to Enhance Heat Transfer in Nanomaterials. *Advanced Functional Materials* **28**, 1706954 (2018).

75 Muthaiah, R. *et al.* Superior effect of edge relative to basal plane functionalization of graphene in enhancing polymer-graphene nanocomposite thermal conductivity-A combined molecular dynamics and Greens functions study. *arXiv preprint arXiv:2201.01011* (2022).

76 Balandin, A. A. Thermal properties of graphene and nanostructured carbon materials. *Nature materials* **10**, 569-581 (2011).

77 Zhang, W., Fisher, T. S. & Mingo, N. The Atomistic Green's Function Method: An Efficient Simulation Approach for Nanoscale Phonon Transport. *Numerical Heat Transfer, Part B: Fundamentals* **51**, 333-349, doi:10.1080/10407790601144755 (2007).

78 Yuge, R. *et al.* Site identification of carboxyl groups on graphene edges with Pt derivatives. *ACS nano* **2**, 1865-1870 (2008).

79 Radovic, L. R., Mora-Vilches, C. V., Salgado-Casanova, A. J. & Buljan, A. Graphene functionalization: Mechanism of carboxyl group formation. *Carbon* **130**, 340-349 (2018).

80 GRAPHENE SUPERMARKET, https://www.graphene-supermarket.com/products/graphene-nanopowder-ao-4-60nm-flakes.

81 MilliporeSigma, https://www.sigmaaldrich.com/US/en/product/aldrich/700207.

82 Kang, J. H. *et al.* Hidden second oxidation step of Hummers method. *Chemistry of Materials* **28**, 756-764 (2016).

83 Han, L. *et al.* Green and facile edge-oxidation of multi-layer graphene by sodium persulfate activated with ferrous ions. *RSC Advances* **10**, 30716-30722 (2020).

84 Wu, H. & Drzal, L. T. High thermally conductive graphite nanoplatelet/polyetherimide composite by precoating: Effect of percolation and particle size. *Polymer composites* **34**, 2148-2153 (2013).

85 Marcano, D. C. *et al.* Improved synthesis of graphene oxide. *ACS nano* **4**, 4806-4814 (2010).

86 Yadav, N. & Lochab, B. A comparative study of graphene oxide: Hummers, intermediate and improved method. *FlatChem* **13**, 40-49 (2019).

87 Botas, C. *et al.* The effect of the parent graphite on the structure of graphene oxide. *Carbon* **50**, 275-282 (2012).

88 Bepete, G., Pénicaud, A., Drummond, C. & Anglaret, E. Raman Signatures of Single Layer Graphene Dispersed in Degassed Water,"'Eau de Graphene"'. *The Journal of Physical Chemistry C* **120**, 28204-28214 (2016).

89 Ganguly, A., Sharma, S., Papakonstantinou, P. & Hamilton, J. Probing the thermal deoxygenation of graphene oxide using high-resolution in situ X-ray-based spectroscopies. *The Journal of Physical Chemistry C* **115**, 17009-17019 (2011).

90 Chen, Q. *et al.* Small-Nanostructure-Size-Limited Phonon Transport within Composite Films Made of Single-Wall Carbon Nanotubes and Reduced Graphene Oxides. *ACS Applied Materials & Interfaces* **13**, 5435-5444 (2021).

91 Cao, H., Wu, X., Yin, G. & Warner, J. H. Synthesis of adenine-modified reduced graphene oxide nanosheets. *Inorganic chemistry* **51**, 2954-2960 (2012).

92 Li, J., Zeng, X., Ren, T. & Van der Heide, E. The preparation of graphene oxide and its derivatives and their application in bio-tribological systems. *Lubricants* **2**, 137-161 (2014).

93 Chhabra, V. A., Deep, A., Kaur, R. & Kumar, R. Functionalization of graphene using carboxylation process. *Int. J. Sci. Emerg. Technol* **4**, 13-19 (2012).

94 Krishnamoorthy, K., Veerapandian, M., Yun, K. & Kim, S.-J. The chemical and structural analysis of graphene oxide with different degrees of oxidation. *Carbon* **53**, 38-49 (2013).

95 Shahriary, L. & Athawale, A. A. Graphene oxide synthesized by using modified hummers approach. *Int. J. Renew. Energy Environ. Eng* **2**, 58-63 (2014).

96 Muzyka, R., Drewniak, S., Pustelny, T., Chrubasik, M. & Gryglewicz, G. Characterization of graphite oxide and reduced graphene oxide obtained from different graphite precursors and oxidized by different methods using Raman spectroscopy. *Materials* **11**, 1050 (2018).

97 Suhaimin, N. S. *et al.* Tuning the oxygen functional groups in graphene oxide nanosheets by optimizing the oxidation time. *Physica E: Low-dimensional Systems and Nanostructures* **131**, 114727 (2021).

98 Lerf, A., He, H., Forster, M. & Klinowski, J. Structure of graphite oxide revisited. *The Journal of Physical Chemistry B* **102**, 4477-4482 (1998).

99 Tabish, T. A. *et al.* Graphene oxide-based targeting of extracellular cathepsin D and cathepsin L as a novel anti-metastatic enzyme cancer therapy. *Cancers* **11**, 319 (2019).

100 Park, J., Kim, Y. S., Sung, S. J., Kim, T. & Park, C. R. Highly dispersible edge-selectively oxidized graphene with improved electrical performance. *Nanoscale* **9**, 1699-1708 (2017).

101 Hack, R., Correia, C. H. G., Zanon, R. A. d. S. & Pezzin, S. H. Characterization of graphene nanosheets obtained by a modified Hummer's method. *Matéria (Rio de Janeiro)* **23** (2018).

102 Aliyev, E. *et al.* Structural characterization of graphene oxide: Surface functional groups and fractionated oxidative debris. *Nanomaterials* **9**, 1180 (2019).

103 Stobinski, L. *et al.* Graphene oxide and reduced graphene oxide studied by the XRD, TEM and electron spectroscopy methods. *Journal of Electron Spectroscopy and Related Phenomena* **195**, 145-154 (2014).

104 Drewniak, S. *et al.* Studies of reduced graphene oxide and graphite oxide in the aspect of their possible application in gas sensors. *Sensors* **16**, 103 (2016).

105 Liu, Q., Tian, B., Liang, J. & Wu, W. Recent advances in printed flexible heaters for portable and wearable thermal management. *Materials Horizons* **8**, 1634-1656 (2021).

106 Qin, Z., Li, M., Flohn, J. & Hu, Y. Thermal management materials for energy-efficient and sustainable future buildings. *Chemical Communications* **57**, 12236-12253 (2021).

107 Vadivelu, M., Kumar, C. R. & Joshi, G. M. Polymer composites for thermal management: a review. *Composite Interfaces* **23**, 847-872 (2016).

108 Wang, K. *et al.* Advanced functional polymer materials. *Materials Chemistry Frontiers* **4**, 1803-1915 (2020).

109 Lewis, J. S., Perrier, T., Barani, Z., Kargar, F. & Balandin, A. A. Thermal interface materials with graphene fillers: review of the state of the art and outlook for future applications. *Nanotechnology* **32**, 142003, doi:10.1088/1361-6528/abc0c6 (2021).

110 Sudhindra, S. *et al.* Specifics of Thermal Transport in Graphene Composites: Effect of Lateral Dimensions of Graphene Fillers. *ACS Applied Materials & Interfaces* **13**, 53073-53082, doi:10.1021/acsami.1c15346 (2021).

111 Sudhindra, S., Kargar, F. & Balandin, A. A. Noncured Graphene Thermal Interface Materials for High-Power Electronics: Minimizing the Thermal Contact Resistance. *Nanomaterials* **11**, doi:10.3390/nano11071699 (2021).

112 Bernal, M. M. *et al.* Edge-Grafted Molecular Junctions between Graphene Nanoplatelets: Applied Chemistry to Enhance Heat Transfer in Nanomaterials. *Advanced Functional Materials* **28**, 1706954, doi:https://doi.org/10.1002/adfm.201706954 (2018).

113 Barani, Z. *et al.* Thermal Properties of the Binary-Filler Hybrid Composites with Graphene and Copper Nanoparticles. *Advanced Functional Materials* **30**, 1904008, doi:https://doi.org/10.1002/adfm.201904008 (2020).

114 An, F. *et al.* Vertically Aligned High-Quality Graphene Foams for Anisotropically Conductive Polymer Composites with Ultrahigh Through-Plane Thermal Conductivities. *ACS Applied Materials & Interfaces* **10**, 17383-17392, doi:10.1021/acsami.8b04230 (2018).

115 Saeidijavash, M. *et al.* High thermal conductivity through simultaneously aligned polyethylene lamellae and graphene nanoplatelets. *Nanoscale* **9**, 12867-12873, doi:10.1039/C7NR04686C (2017).

116 Wu, S. *et al.* Aligning multilayer graphene flakes with an external electric field to improve multifunctional properties of epoxy nanocomposites. *Carbon* **94**, 607-618, doi:https://doi.org/10.1016/j.carbon.2015.07.026 (2015).

117 Liao, Q., Liu, Z., Liu, W., Deng, C. & Yang, N. Extremely High Thermal Conductivity of Aligned Carbon Nanotube-Polyethylene Composites. *Scientific Reports* **5**, 16543, doi:10.1038/srep16543 (2015).

118 Lian, G. *et al.* Vertically Aligned and Interconnected Graphene Networks for High Thermal Conductivity of Epoxy Composites with Ultralow Loading. *Chemistry of Materials* **28**, 6096-6104, doi:10.1021/acs.chemmater.6b01595 (2016).

119 Li, Q. *et al.* Ultrahigh Thermal Conductivity of Assembled Aligned Multilayer Graphene/Epoxy Composite. *Chemistry of Materials* **26**, 4459-4465, doi:10.1021/cm501473t (2014).

120 Kargar, F. *et al.* Thermal Percolation Threshold and Thermal Properties of Composites with High Loading of Graphene and Boron Nitride Fillers. *ACS Applied Materials & Interfaces* **10**, 37555-37565, doi:10.1021/acsami.8b16616 (2018).

121 Nguyen, G. T., Hwang, H. S., Lee, J. & Park, I. Azelaic Acid/Expanded Graphite Composites with High Latent Heat Storage Capacity and Thermal Conductivity at Medium Temperature. *ACS Omega* **6**, 8469-8476, doi:10.1021/acsomega.1c00265 (2021).

122 Deng, S. *et al.* Preparation of polyvinylidene fluoride/expanded graphite composites with enhanced thermal conductivity via ball milling treatment. *RSC advances* **6**, 45578-45584 (2016).

123 Kim, H. S. *et al.* Volume control of expanded graphite based on inductively coupled plasma and enhanced thermal conductivity of epoxy composite by formation of the filler network. *Carbon* **119**, 40-46 (2017).

124 Lin, X., Zhang, X., Liu, L., Liang, J. & Liu, W. Polymer/expanded graphite-based flexible phase change material with high thermal conductivity for battery thermal management. *Journal of Cleaner Production* **331**, 130014 (2022).

125 Nayak, S. K., Mohanty, S. & Nayak, S. K. A new way synthesis of expanded graphite as a thermal filler to enhance the thermal conductivity of DGEBA resin as thermal interface material. *High Performance Polymers* **32**, 506-523, doi:10.1177/0954008319884616 (2019).

126 Raza, G., Shi, Y. & Deng, Y. in *2016 13th International Bhurban Conference on Applied Sciences and Technology (IBCAST)*. 1-12.

127 Moon, S., Choi, J. & Farris, R. J. Preparation of aligned polyetherimide fiber by electrospinning. *Journal of applied polymer science* **109**, 691-694 (2008).

128 Sato, D. M., Guerrini, L. M., De Oliveira, M. P., de Oliveira Hein, L. R. & Botelho, E. C. Production and characterization of polyetherimide mats by an electrospinning process. *Materials Research Express* **5**, 115302 (2018).

129 Khanbareh, H., Hegde, M., Bijleveld, J., Van Der Zwaag, S. & Groen, P. Functionally graded ferroelectric polyetherimide composites for high temperature sensing. *Journal of Materials Chemistry C* **5**, 9389-9397 (2017).

130 Preethika, M., Shetty, B. H., Govindasamy, M. & Sundramoorthy, A. K. Recent Trends in the Applications of Thermally Expanded Graphite for Energy Storage and Sensors–A Review. *Nanoscale Advances* (2021).

131 Huang, J. *et al.* Preparation of highly dispersed expandable graphite/polystyrene composite foam via suspension polymerization with enhanced fire retardation. *Carbon* **146**, 503-512 (2019).

132 Chen, W. *et al.* SiO2 hydrophilic modification of expanded graphite to fabricate form-stable ternary nitrate composite room temperature phase change material for thermal energy storage. *Chemical Engineering Journal* **413**, 127549 (2021).

133 Li, C., Zhang, B. & Liu, Q. N-eicosane/expanded graphite as composite phase change materials for electro-driven thermal energy storage. *Journal of Energy Storage* **29**, 101339 (2020).

134 Xu, T. *et al.* In situ synthesis of porous Si dispersed in carbon nanotube intertwined expanded graphite for high-energy lithium-ion batteries. *Nanoscale* **10**, 16638-16644, doi:10.1039/C8NR04587A (2018).

135 Manea, F. *et al.* Simultaneous Determination of 4-Chlorophenol and Oxalic Acid Using an Expanded Graphite-Epoxy Composite Electrode. *Electroanalysis: An International Journal Devoted to Fundamental and Practical Aspects of Electroanalysis* **20**, 1719-1722 (2008).

136 Dhakate, S., Sharma, S., Borah, M., Mathur, R. & Dhami, T. Expanded graphite-based electrically conductive composites as bipolar plate for PEM fuel cell. *international journal of hydrogen energy* **33**, 7146-7152 (2008).

137 Chen, X. *et al.* Three-dimensional catalyst systems from expanded graphite and metal nanoparticles for electrocatalytic oxidation of liquid fuels. *Nanoscale* **11**, 7952-7958 (2019).

138 Zhao, Y., Ma, C., Li, Y., Chen, H. & Shao, Z. Self-adhesive Co3O4/expanded graphite paper as high-performance flexible anode for Li-ion batteries. *Carbon* **95**, 494-496 (2015).

139 Dong, L. *et al.* Building vertically-structured, high-performance electrodes by interlayer-confined reactions in accordion-like, chemically expanded graphite. *Nano Energy* **70**, 104482 (2020).

140 Xiong, C. *et al.* Fabrication of 3D expanded graphite-based (MnO2 nanowalls and PANI nanofibers) hybrid as bifunctional material for high-performance supercapacitor and sensor. *Journal of The Electrochemical Society* **166**, A3965 (2019).

141 He, J. *et al.* Fabrication of MoS2 loaded on expanded graphite matrix for high-efficiency pH-universal hydrogen evolution reaction. *Journal of Alloys and Compounds* **828**, 154370 (2020).

142 Wu, S. *et al.* Thermal conductivity measurement of an individual millimeter-long expanded graphite ribbon using a variable-length T-type method. *International Journal of Heat and Mass Transfer* **171**, 121115, doi:https://doi.org/10.1016/j.ijheatmasstransfer.2021.121115 (2021).

143 Tao, Z., Wang, H., Li, X., Liu, Z. & Guo, Q. Expanded graphite/polydimethylsiloxane composites with high thermal conductivity. *Journal of Applied Polymer Science* **134** (2017).

144 Zhao, Y. *et al.* Expanded graphite–Paraffin composite phase change materials: Effect of particle size on the composite structure and properties. *Applied Thermal Engineering* **171**, 115015 (2020).

145 Song, Z., Deng, Y., Li, J. & Nian, H. Expanded graphite for thermal conductivity and reliability enhancement and supercooling decrease of MgCl2·6H2O phase change material. *Materials Research Bulletin* **102**, 203-208, doi:https://doi.org/10.1016/j.materresbull.2018.02.024 (2018).

146 Wei, B. & Yang, S. Polymer composites with expanded graphite network with superior thermal conductivity and electromagnetic interference shielding performance. *Chemical Engineering Journal* **404**, 126437 (2021).

147 Che, J., Wu, K., Lin, Y., Wang, K. & Fu, Q. Largely improved thermal conductivity of HDPE/expanded graphite/carbon nanotubes ternary composites via filler network-network synergy. *Composites Part A: Applied Science and Manufacturing* **99**, 32-40, doi:https://doi.org/10.1016/j.compositesa.2017.04.001 (2017).

148 Yang, S., Li, W., Bai, S. & Wang, Q. High-performance thermal and electrical conductive composites from multilayer plastic packaging waste and expanded graphite. *Journal of Materials Chemistry C* **6**, 11209-11218 (2018).

149 Termentzidis, K. *et al.* Enhanced thermal conductivity in percolating nanocomposites: a molecular dynamics investigation. *Nanoscale* **10**, 21732-21741, doi:10.1039/C8NR05734F (2018).

150 Ghossoub, M. G., Lee, J.-H., Baris, O. T., Cahill, D. G. & Sinha, S. Percolation of thermal conductivity in amorphous fluorocarbons. *Physical Review B* **82**, 195441, doi:10.1103/PhysRevB.82.195441 (2010).

151 Jang, J.-u. *et al.* Thermal Percolation Behavior in Thermal Conductivity of Polymer Nanocomposite with Lateral Size of Graphene Nanoplatelet. *Polymers* **14**, doi:10.3390/polym14020323 (2022).

152 Konatham, D., Papavassiliou, D. V. & Striolo, A. Thermal boundary resistance at the graphene–graphene interface estimated by molecular dynamics simulations. *Chemical Physics Letters* **527**, 47-50, doi:https://doi.org/10.1016/j.cplett.2012.01.007 (2012).

153 Krauklis, A. E. & Echtermeyer, A. T. Mechanism of yellowing: Carbonyl formation during hygrothermal aging in a common amine epoxy. *Polymers* **10**, 1017 (2018).

154 Tarannum, F. *et al.* Chemically Edge-Carboxylated Graphene Enhances the Thermal Conductivity of Polyetherimide–Graphene Nanocomposites. *ACS Applied Materials & Interfaces* **14**, 14753-14763, doi:10.1021/acsami.1c25279 (2022).

155 Chen, J. & Li, L. Effect of oxidation degree on the thermal properties of graphene oxide. *Journal of Materials Research and Technology* **9**, 13740-13748 (2020).

156 Sun, Z. *et al.* Temperature-dependent mechanical properties of polyetherimide composites reinforced by graphene oxide-coated short carbon fibers. *Composite Structures* **270**, 114075 (2021).

157 Huang, J. *et al.* Green preparation of expandable graphite and its application in flame-resistance polymer elastomer. *Industrial & Engineering Chemistry Research* **56**, 5253-5261 (2017).

158 Tarannum, F. *et al.* Thermally expanded graphite polyetherimide composite with superior electrical and thermal conductivity. *arXiv preprint arXiv:2204.12075* (2022).

159 Kuan, C. F. *et al.* Preparation of expandable graphite via H2O2-hydrothermal process and its effect on properties of high-density polyethylene composites. *Polymer composites* **33**, 872-880 (2012).

160 Graphite store, https://www.graphitestore.com/gs-3570-expandable-graphite.

161 GRAPHENE SUPERMARKET, https://www.graphene-supermarket.com/products/graphene-nanopowder-ao-4-60nm-flakes.

162 HEXION, https://www.hexion.com/en-us/chemistry/epoxy-resins-curing-agents-modifiers/system-recommendations/wind-composites.

163 Alfa Aesar, https://www.alfa.com/en/catalog/A10924/.

164 MilliporeSigma, https://www.sigmaaldrich.com/US/en/product/aldrich/700207.

165 Mokhtari, M., Archer, E., Bloomfield, N., Harkin-Jones, E. & McIlhagger, A. High-performance and cost-effective melt blended poly (ether ether ketone)/expanded graphite composites for mass production of antistatic materials. *Polymer International* (2021).

166 Wu, K. *et al.* Design and preparation of a unique segregated double network with excellent thermal conductive property. *ACS applied materials & interfaces* **9**, 7637-7647 (2017).

167 Feng, C., Ni, H., Chen, J. & Yang, W. Facile method to fabricate highly thermally conductive graphite/PP composite with network structures. *ACS applied materials & interfaces* **8**, 19732-19738 (2016).

168 Sun, W. *et al.* Tuning the oxidation degree of graphite toward highly thermally conductive graphite/epoxy composites. *Chemistry of Materials* **30**, 7473-7483 (2018).

169 Wu, M., Huang, H.-X., Tong, J. & Ke, D.-Y. Enhancing thermal conductivity and mechanical properties of poly (methyl methacrylate) via adding expanded graphite and injecting water. *Composites Part A: Applied Science and Manufacturing* **102**, 228-235 (2017).

170 Kratochvíla, J., Boudenne, A. & Krupa, I. Effect of filler size on thermophysical and electrical behavior of nanocomposites based on expanded graphite nanoparticles filled in low-density polyethylene matrix. *Polymer composites* **34**, 149-155 (2013).

171 Wang, W., Yang, X., Fang, Y., Ding, J. & Yan, J. Preparation and thermal properties of polyethylene glycol/expanded graphite blends for energy storage. *Applied Energy* **86**, 1479-1483 (2009).

172 Sun, Z. *et al.* Mechanical, tribological and thermal properties of injection molded short carbon fiber/expanded graphite/polyetherimide composites. *Composites Science and Technology* **201**, 108498 (2021).

173 Su, Y., Li, J. J. & Weng, G. J. Theory of thermal conductivity of graphene-polymer nanocomposites with interfacial Kapitza resistance and graphene-graphene contact resistance. *Carbon* **137**, 222-233, doi:https://doi.org/10.1016/j.carbon.2018.05.033 (2018).

174 Nika, D. L. & Balandin, A. A. Phonons and thermal transport in graphene and graphene-based materials. *Reports on Progress in Physics* **80**, 036502, doi:10.1088/1361-6633/80/3/036502 (2017).

175 Valapa, R. B., Pugazhenthi, G. & Katiyar, V. Effect of graphene content on the properties of poly (lactic acid) nanocomposites. *Rsc Advances* **5**, 28410-28423 (2015).

176 Chen, G. *et al.* Preparation and characterization of graphite nanosheets from ultrasonic powdering technique. *Carbon* **42**, 753-759 (2004).

177 Bourbigot, S. & Fontaine, G. Flame retardancy of polylactide: an overview. *Polymer Chemistry* **1**, 1413-1422 (2010).

178 Xiang, H. *et al.* Graphene/nanosized silicon composites for lithium battery anodes with improved cycling stability. *Carbon* **49**, 1787-1796 (2011).

179 Lin, Y. *et al.* Mildly expanded graphite for anode materials of lithium ion battery synthesized with perchloric acid. *Electrochimica Acta* **116**, 170-174 (2014).

180 Zhao, H. & Lin, R. Preparation of boric acid modified expandable graphite and its influence on polyethylene combustion characteristics. *Journal of the Chilean Chemical Society* **61**, 2767-2771 (2016).

181 Tao, S., Wei, S. & Yulan, Y. Characterization of expanded graphite microstructure and fabrication of composite phase-change material for energy storage. *Journal of Materials in Civil Engineering* **27**, 04014156 (2015).

182 Wang, P. *et al.* Interlayer polymerization in chemically expanded graphite for preparation of highly conductive, mechanically strong polymer composites. *Chemistry of Materials* **29**, 3412-3422 (2017).

183 Zhang, H. *et al.* The graphite foam/erythritol composites with ultrahigh thermal conductivity for medium temperature applications. *Solar Energy Materials and Solar Cells* **230**, 111135 (2021).

184 Peng, T., Liu, B., Gao, X., Luo, L. & Sun, H. Preparation, quantitative surface analysis, intercalation characteristics and industrial implications of low temperature expandable graphite. *Applied Surface Science* **444**, 800-810 (2018).

185 Malard, L., Pimenta, M. A., Dresselhaus, G. & Dresselhaus, M. Raman spectroscopy in graphene. *Physics reports* **473**, 51-87 (2009).

186 Xia, Z., Bellani, V., Sun, J. & Palermo, V. Electrochemical exfoliation of graphite in H2SO4, Li2SO4 and NaClO4 solutions monitored in situ by Raman microscopy and spectroscopy. *Faraday Discussions* **227**, 291-305 (2021).

187 Wen, P., Gong, P., Mi, Y., Wang, J. & Yang, S. Scalable fabrication of high quality graphene by exfoliation of edge sulfonated graphite for supercapacitor application. *RSC advances* **4**, 35914-35918 (2014).

188 Kaur, G., Adhikari, R., Cass, P., Bown, M. & Gunatillake, P. Electrically conductive polymers and composites for biomedical applications. *Rsc Advances* **5**, 37553-37567 (2015).

189 Huang, X., Jiang, P. & Tanaka, T. A review of dielectric polymer composites with high thermal conductivity. *IEEE Electrical Insulation Magazine* **27**, 8-16 (2011).

190 El-Kady, M. F. & Kaner, R. B. Scalable fabrication of high-power graphene micro-supercapacitors for flexible and on-chip energy storage. *Nature communications* **4**, 1-9 (2013).

191 Wei, Y. *et al.* Highly stable and sensitive paper-based bending sensor using silver nanowires/layered double hydroxides hybrids. *ACS applied materials & interfaces* **7**, 14182-14191 (2015).

192 Yan, D. X. *et al.* Structured reduced graphene oxide/polymer composites for ultra-efficient electromagnetic interference shielding. *Advanced Functional Materials* **25**, 559-566 (2015).

193 Paton, K. R. *et al.* Scalable production of large quantities of defect-free few-layer graphene by shear exfoliation in liquids. *Nature materials* **13**, 624-630 (2014).

194 Masoud, E. M., El-Bellihi, A.-A., Bayoumy, W. A. & Mohamed, E. A. Polymer composite containing nano magnesium oxide filler and lithiumtriflate salt: an efficient polymer electrolyte for lithium ion batteries application. *Journal of Molecular Liquids* **260**, 237-244 (2018).

195 Guo, C. X., Wang, M., Chen, T., Lou, X. W. & Li, C. M. A Hierarchically Nanostructured Composite of MnO2/Conjugated Polymer/Graphene for High-Performance Lithium Ion Batteries. *Advanced Energy Materials* **1**, 736-741 (2011).

196 El-Kady, M. F., Strong, V., Dubin, S. & Kaner, R. B. Laser scribing of high-performance and flexible graphene-based electrochemical capacitors. *Science* **335**, 1326-1330 (2012).

197 Shown, I., Ganguly, A., Chen, L. C. & Chen, K. H. Conducting polymer-based flexible supercapacitor. *Energy Science & Engineering* **3**, 2-26 (2015).

198 Jaidev, L., Kumar, S. & Chatterjee, K. Multi-biofunctional polymer graphene composite for bone tissue regeneration that elutes copper ions to impart angiogenic, osteogenic and bactericidal properties. *Colloids and Surfaces B: Biointerfaces* **159**, 293-302 (2017).

199 Han, J. *et al.* Bio-functional electrospun nanomaterials: From topology design to biological applications. *Progress in Polymer Science* **91**, 1-28 (2019).

200 Taherian, R. Experimental and analytical model for the electrical conductivity of polymer-based nanocomposites. *Composites Science and Technology* **123**, 17-31 (2016).

201 Wajid, A. S. *et al.* High-performance pristine graphene/epoxy composites with enhanced mechanical and electrical properties. *Macromolecular Materials and engineering* **298**, 339-347 (2013).

202 Chandrasekaran, S., Seidel, C. & Schulte, K. Preparation and characterization of graphite nano-platelet (GNP)/epoxy nano-composite: Mechanical, electrical and thermal properties. *European Polymer Journal* **49**, 3878-3888 (2013).

203 Fan, Z., Zheng, C., Wei, T., Zhang, Y. & Luo, G. Effect of carbon black on electrical property of graphite nanoplatelets/epoxy resin composites. *Polymer Engineering & Science* **49**, 2041-2045 (2009).

204 Lima, T. B., Silva, V. O., Araujo, E. S. & Araujo, P. L. in *Macromolecular symposia.* 1800051 (Wiley Online Library).

205 Bansala, T., Joshi, M. & Mukhopadhyay, S. Electromagnetic interference shielding behavior of chemically and thermally reduced graphene based multifunctional polyurethane nanocomposites: A comparative study. *Journal of Applied Polymer Science* **136**, 47666 (2019).

206 Thorpe, M. Geometrical percolation threshold of overlapping ellipsoids E. J. Garboczi, 1 KA Snyder, 1 and JF Douglas2. *PHYSICAL REVIEW E* **52** (1995).

207 Zhang, W. *et al.* Binder-free graphene foams for O 2 electrodes of Li–O 2 batteries. *Nanoscale* **5**, 9651-9658 (2013).

208 He, Y. *et al.* Freestanding three-dimensional graphene/MnO2 composite networks as ultralight and flexible supercapacitor electrodes. *ACS nano* **7**, 174-182 (2013).

209 Loeblein, M., Tay, R. Y., Tsang, S. H., Ng, W. B. & Teo, E. H. T. Configurable Three-Dimensional Boron Nitride–Carbon Architecture and Its Tunable Electronic Behavior with Stable Thermal Performances. *Small* **10**, 2992-2999 (2014).

210 Pettes, M. T., Ji, H., Ruoff, R. S. & Shi, L. Thermal transport in three-dimensional foam architectures of few-layer graphene and ultrathin graphite. *Nano letters* **12**, 2959-2964 (2012).

211 Worsley, M. A. *et al.* Ultralow density, monolithic WS2, MoS2, and MoS2/graphene aerogels. *ACS nano* **9**, 4698-4705 (2015).

212 Kashi, S., Gupta, R. K., Baum, T., Kao, N. & Bhattacharya, S. N. Phase transition and anomalous rheological behaviour of polylactide/graphene nanocomposites. *Composites Part B: Engineering* **135**, 25-34 (2018).

213 Chung, D. Exfoliation of graphite. *Journal of materials science* **22**, 4190-4198 (1987).

214 Inagaki, M. Applications of graphite intercalation compounds. *Journal of Materials Research* **4**, 1560-1568 (1989).

215 Yakovlev, A., Finaenov, A., Zabud'Kov, S. & Yakovleva, E. Thermally expanded graphite: Synthesis, properties, and prospects for use. *Russian journal of applied chemistry* **79**, 1741-1751 (2006).

216 Steurer, P., Wissert, R., Thomann, R. & Mülhaupt, R. Functionalized graphenes and thermoplastic nanocomposites based upon expanded graphite oxide. *Macromolecular rapid communications* **30**, 316-327 (2009).

217 Zheng, G., Wu, J., Wang, W. & Pan, C. Characterizations of expanded graphite/polymer composites prepared by in situ polymerization. *Carbon* **42**, 2839-2847 (2004).

218 Deng, S. *et al.* Effect of chain structure on the thermal conductivity of expanded graphite/polymer composites. *RSC advances* **6**, 10185-10191 (2016).

219 Yasmin, A., Luo, J.-J. & Daniel, I. M. Processing of expanded graphite reinforced polymer nanocomposites. *Composites Science and Technology* **66**, 1182-1189 (2006).

220 Tong, J., Li, W., Chen, H. C. & Tan, L. C. Improving Properties of Poly (vinylidene fluoride) by Adding Expanded Graphite without Surface Modification via Water-Assisted Mixing Extrusion. *Macromolecular Materials and Engineering* **305**, 2000270 (2020).

221 Wong, S.-C., Sutherland, E. M. & Uhl, F. M. Materials processes of graphite nanostructured composites using ball milling. *Materials and manufacturing processes* **21**, 159-166 (2006).

222 Mutlay, İ. & Tudoran, L. B. Percolation behavior of electrically conductive graphene nanoplatelets/polymer nanocomposites: theory and experiment. *Fullerenes, Nanotubes and Carbon Nanostructures* **22**, 413-433 (2014).

223 Stoller, M. D., Park, S., Zhu, Y., An, J. & Ruoff, R. S. Graphene-based ultracapacitors. *Nano letters* **8**, 3498-3502 (2008).

224 She, Y., Chen, G. & Wu, D. Fabrication of polyethylene/graphite nanocomposite from modified expanded graphite. *Polymer International* **56**, 679-685 (2007).

225 Piao, M., Kim, G., Kennedy, G. P., Roth, S. & Dettlaff-Weglikowska, U. Preparation and characterization of expanded graphite polymer composite films for thermoelectric applications. *physica status solidi (b)* **250**, 2529-2534 (2013).

226 Yoonessi, M. *et al.* Fabrication of graphene–polyimide nanocomposites with superior electrical conductivity. *ACS applied materials & interfaces* **9**, 43230-43238 (2017).

227 Li, Y., Li, R. & Tjong, S. C. Fabrication and properties of PVDF/expanded graphite nanocomposites. *e-Polymers* **9** (2009).

228 Sarı, A. & Karaipekli, A. Thermal conductivity and latent heat thermal energy storage characteristics of paraffin/expanded graphite composite as phase change material. *Applied thermal engineering* **27**, 1271-1277 (2007).

229 Wu, H. & Drzal, L. T. Graphene nanoplatelet-polyetherimide composites: Revealed morphology and relation to properties. *Journal of Applied Polymer Science* **130**, 4081-4089 (2013).

230 Ling, J. *et al.* Facile preparation of lightweight microcellular polyetherimide/graphene composite foams for electromagnetic interference shielding. *ACS applied materials & interfaces* **5**, 2677-2684 (2013).

231 Graphitestore, https://www.graphitestore.com/gs-3772-expandable-graphite.

232 Alfa Aesar, https://www.alfa.com/en/catalog/043319/.

233 Chen, X. Y. *et al.* in *Functionalized Graphene Nanocomposites and their Derivatives* 121-155 (Elsevier, 2019).

234 Zhong, J. & Isayev, A. I. Properties of polyetherimide/graphite composites prepared using ultrasonic twin-screw extrusion. *Journal of Applied Polymer Science* **132** (2015).

235 Song, L., Xiao, M. & Meng, Y. Electrically conductive nanocomposites of aromatic polydisulfide/expanded graphite. *Composites science and technology* **66**, 2156-2162 (2006).

236 Zheng, W., Lu, X. & Wong, S. C. Electrical and mechanical properties of expanded graphite-reinforced high-density polyethylene. *Journal of Applied Polymer Science* **91**, 2781-2788 (2004).

237 Sever, K. *et al.* Electrical and mechanical properties of expanded graphite/high density polyethylene nanocomposites. *Composites Part B: Engineering* **53**, 226-233 (2013).

238 Ramanujam, B. & Gopalakrishnan, C. Investigations of structure development, electrical and thermal properties of polyvinylidene fluoride-expanded graphite nanocomposites. *Bulletin of Materials Science* **44**, 1-10 (2021).

239 Zhao, B. *et al.* Incorporating a microcellular structure into PVDF/graphene–nanoplatelet composites to tune their electrical conductivity and electromagnetic interference shielding properties. *Journal of Materials Chemistry C* **6**, 10292-10300 (2018).

240 Yan, D.-X. *et al.* Efficient electromagnetic interference shielding of lightweight graphene/polystyrene composite. *Journal of Materials Chemistry* **22**, 18772-18774 (2012).

241 Singh, A. P. *et al.* Phenolic resin-based composite sheets filled with mixtures of reduced graphene oxide, γ-Fe2O3 and carbon fibers for excellent electromagnetic interference shielding in the X-band. *Carbon* **50**, 3868-3875 (2012).

242 Gao, W. *et al.* High-efficiency electromagnetic interference shielding realized in nacre-mimetic graphene/polymer composite with extremely low graphene loading. *Carbon* **157**, 570-577 (2020).

243 Xia, X., Hao, J., Wang, Y., Zhong, Z. & Weng, G. J. Theory of electrical conductivity and dielectric permittivity of highly aligned graphene-based nanocomposites. *Journal of Physics: Condensed Matter* **29**, 205702 (2017).

244 Wang, Y., Weng, G. J., Meguid, S. A. & Hamouda, A. M. A continuum model with a percolation threshold and tunneling-assisted interfacial conductivity for carbon nanotube-based nanocomposites. *Journal of Applied Physics* **115**, 193706 (2014).

245 Wang, Y., Shan, J. W. & Weng, G. J. Percolation threshold and electrical conductivity of graphene-based nanocomposites with filler agglomeration and interfacial tunneling. *Journal of Applied Physics* **118**, 065101 (2015).

246 Lee, H. L. *et al.* Thermal conductivity improvement of surface-enhanced polyetherimide (PEI) composites using polyimide-coated h-BN particles. *Physical Chemistry Chemical Physics* **16**, 20041-20046 (2014).

247 Chia, C. H. *et al.* Microstructural characterization of white charcoal. *Journal of Analytical and Applied Pyrolysis* **109**, 215-221 (2014).

248 Mohammad, H., Stepashkin, A. A. & Tcherdyntsev, V. V. Effect of Graphite Filler Type on the Thermal Conductivity and Mechanical Behavior of Polysulfone-Based Composites. *Polymers* **14**, 399 (2022).

249 Kim, Y. *et al.* Breakdown of the interlayer coherence in twisted bilayer graphene. *Physical Review Letters* **110**, 096602 (2013).

250 Bodzenta, J., Mazur, J. & Kaźmierczak-Bałata, A. Thermal properties of compressed expanded graphite: photothermal measurements. *Applied Physics B* **105**, 623-630 (2011).

251 Yoshida, A., Hishiyama, Y. & Inagaki, M. Exfoliated graphite from various intercalation compounds. *Carbon* **29**, 1227-1231 (1991).

252 Wei, L., Zhang, Y., Yang, Y., Ye, M. & Li, C. C. Manipulating the Electronic Structure of Graphite Intercalation Compounds for Boosting the Bifunctional Oxygen Catalytic Performance. *Small*, 2107667 (2022).

253 Enoki, T., Suzuki, M. & Endo, M. *Graphite intercalation compounds and applications*. (Oxford University Press, 2003).

254 Grüneis, A. *et al.* Electronic structure and electron-phonon coupling of doped graphene layers in KC 8. *Physical Review B* **79**, 205106 (2009).

255 Belash, I., Bronnikov, A., Zharikov, O. & Pal'nichenko, A. Superconductivity of graphite intercalation compound with lithium C2Li. *Solid state communications* **69**, 921-923 (1989).

256 Wang, T., Quinn, M. D. & Notley, S. M. Enhanced electrical, mechanical and thermal properties by exfoliating graphene platelets of larger lateral dimensions. *Carbon* **129**, 191-198 (2018).

257 Kim, J. *et al.* Extremely large, non-oxidized graphene flakes based on spontaneous solvent insertion into graphite intercalation compounds. *Carbon* **139**, 309-316 (2018).

258 Wu, W. *et al.* Fast chemical exfoliation of graphite to few-layer graphene with high quality and large size via a two-step microwave-assisted process. *Chemical Engineering Journal* **381**, 122592 (2020).

259 Liang, B. *et al.* Improved efficiency of liquid-phase shear exfoliation of expanded graphite with mica plates as bifunctional additives. *Journal of Materials Chemistry A* **9**, 27586-27595 (2021).

260 Cai, M., Thorpe, D., Adamson, D. H. & Schniepp, H. C. Methods of graphite exfoliation. *Journal of Materials Chemistry* **22**, 24992-25002 (2012).

261 Chung, D. A review of exfoliated graphite. *Journal of materials science* **51**, 554-568 (2016).

262 Dresselhaus, M. S. & Dresselhaus, G. Intercalation compounds of graphite. *Advances in physics* **51**, 1-186 (2002).

263 Dimiev, A. M. *et al.* Direct real-time monitoring of stage transitions in graphite intercalation compounds. *ACS nano* **7**, 2773-2780 (2013).

264 Noel, M. & Santhanam, R. Electrochemistry of graphite intercalation compounds. *Journal of Power Sources* **72**, 53-65 (1998).

265 Wang, G., Yu, M. & Feng, X. Carbon materials for ion-intercalation involved rechargeable battery technologies. *Chemical Society Reviews* **50**, 2388-2443 (2021).

266 Van Heerden, X. & Badenhorst, H. The influence of three different intercalation techniques on the microstructure of exfoliated graphite. *Carbon* **88**, 173-184 (2015).

267 Rüdorff, W. in *Advances in Inorganic Chemistry and Radiochemistry* Vol. 1 223-266 (Elsevier, 1959).

268 Camino, G. *et al.* (ACS Publications, 2001).

269 Duquesne, S. *et al.* Thermal degradation of polyurethane and polyurethane/expandable graphite coatings. *Polymer degradation and stability* **74**, 493-499 (2001).

270 Xia, Z., Bellani, V., Sun, J. & Palermo, V. Electrochemical exfoliation of graphite in H 2 SO 4, Li 2 SO 4 and NaClO 4 solutions monitored in situ by Raman microscopy and spectroscopy. *Faraday Discussions* **227**, 291-305 (2021).

271 Yu, P., Lowe, S. E., Simon, G. P. & Zhong, Y. L. Electrochemical exfoliation of graphite and production of functional graphene. *Current opinion in colloid & interface science* **20**, 329-338 (2015).

272 Su, C.-Y. *et al.* High-quality thin graphene films from fast electrochemical exfoliation. *ACS nano* **5**, 2332-2339 (2011).

273 Calandra, M. & Mauri, F. Origin of superconductivity of CaC6 and of other intercalated graphites. *physica status solidi (b)* **243**, 3458-3463 (2006).

274 Chacón-Torres, J. C., Wirtz, L. & Pichler, T. Raman spectroscopy of graphite intercalation compounds: Charge transfer, strain, and electron–phonon coupling in graphene layers. *physica status solidi (b)* **251**, 2337-2355 (2014).

275 Hong, Y., Wang, Z. & Jin, X. Sulfuric acid intercalated graphite oxide for graphene preparation. *Scientific reports* **3**, 1-6 (2013).

276 Salvatore, M. *et al.* Synthesis and characterization of highly intercalated graphite bisulfate. *Nanoscale Research Letters* **12**, 1-8 (2017).

277 Parvez, K. *et al.* Electrochemically exfoliated graphene as solution-processable, highly conductive electrodes for organic electronics. *ACS nano* **7**, 3598-3606 (2013).

278 Liu, C. *et al.* 3D Expanded Graphite Frameworks for Dual-Functional Polymer Composites with Exceptional Thermal Conductive and Electromagnetic Interference Shielding Capabilities. *ACS Applied Electronic Materials* (2022).

279 Udod, I., Orman, H. & Genchel, V. The sodium-graphite system under high-pressure conditions: the comparison with the lithium-graphite system. *Carbon* **32**, 101-106 (1994).

280 Kang, Y.-J., Jung, S. C., Choi, J. W. & Han, Y.-K. Important role of functional groups for sodium ion intercalation in expanded graphite. *Chemistry of Materials* **27**, 5402-5406 (2015).

281 Wen, Y. *et al.* Expanded graphite as superior anode for sodium-ion batteries. *Nature communications* **5**, 1-10 (2014).

282 Vittore, A., Acocella, M. R. & Guerra, G. Edge-oxidation of graphites by hydrogen peroxide. *Langmuir* **35**, 2244-2250 (2019).

283 Brodie, B. C. XIII. On the atomic weight of graphite. *Philosophical transactions of the Royal Society of London*, 249-259 (1859).

284 Shin, H. J. *et al.* Efficient reduction of graphite oxide by sodium borohydride and its effect on electrical conductance. *Advanced Functional Materials* **19**, 1987-1992 (2009).

285 Yap, R. C. C. *et al.* Identifying the mechanisms of p-to-n conversion in unipolar graphene field-effect transistors. *Nanotechnology* **24**, 195202 (2013).

286 Kawashima, Y. & Katagiri, G. Fundamentals, overtones, and combinations in the Raman spectrum of graphite. *Physical Review B* **52**, 10053 (1995).

287 Chakrabarti, A. *et al.* Conversion of carbon dioxide to few-layer graphene. *Journal of Materials Chemistry* **21**, 9491-9493 (2011).

288 Ferrari, A. C. *et al.* Raman spectrum of graphene and graphene layers. *Physical review letters* **97**, 187401 (2006).

289 Ali, M. (2015).

290 Yang, Y. *et al.* Thermal conductivity of defective graphene oxide: a molecular dynamic study. *Molecules* **24**, 1103 (2019).

291 Méndez-Romero, U. A., Pérez-García, S. A., Fan, Q., Wang, E. & Licea-Jiménez, L. Lateral size reduction of graphene oxide preserving its electronic properties and chemical functionality. *RSC Advances* **10**, 29432-29440 (2020).

292 Kumar, R., Mohanty, S. & Nayak, S. K. Study on epoxy resin-based thermal adhesive filled with hybrid expanded graphite and graphene nanoplatelet. *SN Applied Sciences* **1**, 1-13 (2019).

293 Jiao, X., Qiu, Y., Zhang, L. & Zhang, X. Comparison of the characteristic properties of reduced graphene oxides synthesized from natural graphites with different graphitization degrees. *RSC advances* **7**, 52337-52344 (2017).